Constraining Drivers of the Southern Ocean Carbon Cycle with Autonomous Observations and Numerical Simulations

Jade Sauve

A dissertation
submitted in partial fulfillment of the
requirements for the degree of

Doctor of Philosophy

University of Washington
2025

Reading Committee:
Alison R. Gray, Co-Chair
Stephen C. Riser, Co-Chair
Frank J.Pavia

Program Authorized to Offer Degree:
School of Oceanography

Jade Sauve

University of Washington

Abstract

Constraining Drivers of the Southern Ocean Carbon Cycle with Autonomous Observations and Numerical Simulations

Jade Sauve

Co-chairs of the Supervisory Committee:

Alison R. Gray
School of Oceanography

Stephen C. Riser
School of Oceanography

The Southern Ocean plays a central role in the global carbon cycle, yet the processes that govern its air-sea carbon exchange remain incompletely understood. This dissertation advances our process-based understanding of dissolved inorganic carbon (DIC) variability, a key determinant of surface ocean $p\mathrm{CO}_2$ and air-sea carbon fluxes. A circumpolar DIC budget framework is developed and applied to both biogeochemical observations and global ocean models to quantify the drivers of mixed layer DIC variability. The approach is further refined through a closed budget analysis in a high-resolution, data-assimilating model, enabling more detailed process-level insight into the Southern Ocean carbon cycle.

Chapter 2 constructs the first observation-based, monthly resolved mixed layer DIC budget for the circumpolar Southern Ocean, using six years of autonomous biogeochemical float data. Analysis of two regions, the Sea Ice Zone (SIZ) and the Antarctic Southern Zone (ASZ), shows that biological processes dominate seasonal DIC variability, with northward Ekman transport playing a secondary but important role. On annual scales, vertical mixing supplies DIC to the mixed layer in both regions, but the fate of this DIC diverges: in the ASZ it is either consumed by biological production or outgassed, while in the SIZ it is exported northward. This wind-driven DIC redistribution emerges as a key mechanism supporting carbon

outgassing, with implications for future changes under reduced sea ice cover. The results also provide a robust observational benchmark for evaluating climate models.

Chapter 3 extends the DIC budget framework to evaluate seasonal carbon fluxes across multiple models, including OMIP simulations, the B-SOSE data-assimilating model, and observations. All datasets identify vertical mixing as the primary DIC source and biological uptake as the main sink, but models consistently underestimate and delay the biological drawdown, leading to a negative entrainment flux, opposite in sign to observational estimates. Advection shows the largest model spread, reflecting differences in simulated circulation. These results highlight that even models performing well in global metrics can misrepresent key seasonal processes, emphasizing the value of process-based diagnostics to improve model fidelity.

Chapter 4 shifts focus to zonal variability, revealing that zonal asymmetries in the physical drivers of carbon flux are central to explaining spatial variability in Southern Ocean air-sea carbon exchange. Using a closed budget in the B-SOSE model, the analysis identifies carbon outgassing hotspots in the Indo-Pacific ASZ linked to intense vertical mixing downstream of topographic features. Zonal advection spreads this DIC eastward, sustaining outgassing further along the path of the ACC. Regional variation in mixing, entrainment, and advection explains much of the zonal variability in air-sea carbon exchange, underscoring the limitations of zonally averaged approaches and the necessity of resolving regional processes in both models and diagnostics.

Across all chapters, this dissertation demonstrates that carbon fluxes in the Southern Ocean result from tightly coupled physical and biological processes whose variability plays out across both space and time. It highlights the importance of moving beyond global and annual averages to resolve seasonal and regional dynamics, which are critical for understanding and predicting carbon cycle behavior. Looking forward, extending the budget framework to additional float data, higher-resolution models, and climate projections will help clarify how DIC fluxes and carbon outgassing may evolve in a warming world. These advances are essential for improving Earth system models and supporting more reliable climate policy.

Acknowledgements

The research in this dissertation was supported through National Science Foundation grants OPP-193622 (SOC-795 COM) and awards 1946578 (GO-BGC) and 2110258 (GO-BGC Operational Support). Additionally, we acknowledge the generous continuing support of NOAA through grant NA20OAR4320271 (US Argo). Chapter 2 was also partly supported by a University of Washington Program on Climate Change fellowship. Chapter 1 was coauthored by Alison R. Gray, Channing J. Prend, Seth M. Bushinsky and Stephen C. Riser. Chapter 2 was coauthored by Alison R. Gray, Cara Nissen, Nicole Lovenduski and Matthew Mazloff. Chapter 3 was coauthored by Alison R. Gray and Matthew Mazloff.

Profiling float data were collected and made freely available by the Southern Ocean Carbon and Climate Observations and Modeling (SOCCOM) Project funded by the National Science Foundation, Division of Polar Programs (NSF PLR-1425989), supplemented by NASA (NNX14AP49B), and by Argo and the NOAA programs that contribute to it. The Argo data were collected and made freely available by the International Argo Program and the national programs that contribute to it. (http://www.argo.ucsd.edu, http://argo.jcommops.org). The Argo Program is part of the Global Ocean Observing System. Generated using Copernicus Climate Change Service information [2021].

We would like to acknowledge computing support from the Casper system (https://ncar.pub/casper) provided by the NSF National Center for Atmospheric Research (NCAR), sponsored by the National Science Foundation. We also would like to acknowledge the data access and computing support provided by the NCAR CMIP Analysis Platform (doi:10.5065/D60R9MSP). We acknowledge the World Climate Research Programme, which, through its Working Group on Coupled Modelling, coordinated and promoted CMIP6. We thank the climate modeling groups for producing and making available their model output, the Earth System Grid Federation (ESGF) for archiving the data and providing access, and the multiple funding agencies who support CMIP6 and ESGF. Computational resources for the B-SOSE were provided by NSF XSEDE resource grant OCE130007 and SOCCOM NSF award PLR-1425989.

Input from B. Carter and N. Williams is gratefully acknowledged. I gratefully thank Carolina Dufour for sharing code to compute horizontal transport across a front for gridded data.

This research took place on the ancestral territory of the Coast Salish peoples. I acknowledge with gratitude their stewardship of these lands and waters since time immemorial.

Many people have contributed to making this thesis possible. I am especially grateful to Carolina Dufour, who gave me my first opportunity in oceanography and shared her love of the Southern Ocean with me—thank you for opening that door. I owe immense thanks to my advisors, Alison Gray and Steve Riser, for taking a chance on me and supporting me over these last seven years. Alison, your steadfast support of my professional goals, your endless well of ideas, and your calm encouragement when I felt stuck made this work possible. Thank you for your kindness, your trust, and for helping me grow into an independent researcher.

Thank you to my committee members—Randie Bundy, Abby Swan, LuAnne Thompson, and Frankie Pavia—for your guidance and encouragement over the years. I have truly appreciated your thoughtful questions and the engaging conversations we've had along the way.

A special thank you to Channing Prend, who was incredibly generous with his time and helped me navigate the writing and publishing of my first paper. You taught me that scientific writing is a form of storytelling—an idea that shaped the way I approached this thesis. I also owe a deep debt of gratitude to Arthur Nowell, my writing mentor, who helped me with so many parts of this thesis. Your advice kept the writing curl low and the progress vectors straight. Our conversations were a joy.

I feel lucky to have collaborated with the wonderful team at CETI during my Climate Change capstone. You exemplify the rare and precious mix of meaningful work and exceptional people.

To my labmates in the Gray and Riser groups, past and present—Earle Wilson, Rosalind Echols, Ethan Campbell, Katy Christensen, Song Sagmin, Nina Buzby, Kristen Falcinelli, Jannes Koelling, Dhruv Balwada, and others—thank you for your unwavering support and the thoughtful, judgment-free environment you helped create. I learned so much from your feedback, which consistently helped me improve my work.

Throughout graduate school, I've been surrounded by a vibrant and supportive community of fellow students. I can honestly say I haven't had a single bad experience with any of you—thank you for making UW such a positive place to be. I'm especially grateful to my 2018 cohort, and within it, to my physical oceanography peers Laura Crews and Erin Broatch. It was a delight to share an office with you both. Erin, thank you for being an incredible officemate and close friend. You've been a generous listener and a tireless source of insight—whether about science, math, or the mysterious workings of UW administration. I'm so grateful to have found such a kindred spirit.

To my friends near and far, thank you for growing alongside me—sharing laughter, meals, and companionship with you made even the hardest days worthwhile. To my family, thank you for always being in my corner and for welcoming me with open arms every time I returned home. I am especially grateful to my parents, Normand Sauvé and Josée Duchesneau. You planted the seeds of everything I've accomplished, and your constant encouragement has never wavered. I carry your love and faith with me every day.

Finally, thank you to my love and partner, Andres Sheikh. You've been by my side since the beginning of this journey—drying my tears, cheering my successes, and sharing in every step along the way. With you, even the hardest parts were bearable. Without you, this would have been a much more perilous climb.

Parmi les vains désirs, à l'avance déçus,
N'est-ce pas le plus fou, celui dont je me vante,
De faire dans des mots tenir la mer vivante
Avec tous ses secrets que nul n'a jamais sus ?

Sans doute. Mais pourtant, auprès d'elle, et dessus,
J'ai passé de longs jours d'extase captivante.
J'en ai bu la tendresse et mangé l'épouvante.
C'est ce que j'ai senti dont mes vers sont tissus.

Pour un si grand tableau, certes, l'étoffe est brève
Ah ! tout ce qu'on entend, ce qu'on voit, ce qu'on rêve
Devant cet infini qui change incessamment !

JEAN RICHEPIN
La Mer

Contents

List of Figures

List of Tables

Chapter 1

Introduction

The exchange of carbon between the atmosphere and the ocean forms an important component of the global climate system. While about 25% of the anthropogenic carbon dioxide that enters the atmosphere is absorbed by the ocean [DeVries, 2014], this flux only constitutes a small fraction of the total carbon stored in the oceans. In fact, the ocean comprises the largest labile carbon reservoir on our planet [Ciais et al., 2013]. Small changes in ocean circulation or biology therefore have the potential to significantly alter atmospheric CO_2. In order to predict future climate, we need to better understand the mechanisms by which carbon moves between atmospheric and oceanic reservoirs. The Southern Ocean, which surrounds Antarctica, plays a particularly important role in the global carbon cycle due to its unique circulation, which acts as a conduit between the atmosphere and the deep ocean. Indeed, this region is responsible for the absorption of about 40% of the anthropogenic carbon taken up by the ocean despite only representing about 20% of the global ocean surface [DeVries, 2014]. About two thirds of the carbon entering the ocean in the Southern Ocean is stored within the region while a third is transported to the thermoclines of the midlatitudes [Bopp et al., 2015; DeVries, 2014].

The Southern Ocean refers to the sections of the Atlantic, Pacific and Indian Oceans that are located south of about 35°S. Its circulation is dominated by the Antarctic Circumpolar Current (ACC), the world's strongest ocean current in terms of mass transport, which encircles the continent of Antarctica on an uninterrupted path. The ACC is a significant obstacle to meridional exchanges of heat, salt and other tracers. Consequently, the Southern Ocean circulation is characterized by distinct fronts with strong meridional property gradients [Orsi et al., 1995]. For example, the Subtropical Front delineates the separation between the cold Southern Ocean waters and the warmer, saltier waters of the subtropics. The Subantarctic Front, found around 48°S, forms the northern boundary of the ACC. The Polar Front, located at about 60°S, defines the northern boundary of the high-latitude Southern Ocean (HLSO). The HLSO can be further separated into two zones corresponding to different oceanic regimes, as noted in previous studies [Bushinsky et al., 2019; Gray et al., 2018; Orsi et al., 1995]. The southernmost zone, the sea ice zone (SIZ), is bounded by the September 15% sea ice concentration contour. This seasonally ice-covered region undergoes the strongest seasonal salinity variations and has the coldest surface temperatures. The Antarctic Southern Zone (ASZ) corresponds to the southern part of the ACC and can be found between the Polar Front and the SIZ.

The strong westerly winds that drive the ACC also support a meridional overturning circulation. Surface divergence due to Ekman transport drives strong upwelling south of the Polar front bringing deep water up to the surface. This old water is rich in dissolved inorganic carbon (DIC) from organic matter remineralization and dissolution of biogenic $CaCO_3$. Because these waters have been at depth since before the industrial revolution, they contain virtually no anthropogenic carbon associated with the burning of fossil fuels. At the surface, some of the upwelled water moves towards the Antarctic coast and sink, becoming Antarctic Bottom Water. However, ocean-atmosphere exchanges are mostly blocked by the presence of sea ice. The remainder of the upwelled water travels north and undergoes considerable outgassing due to a weak biological pump that fails to consume all the available natural carbon. At about 44°S, where subtropical waters are cooling as they move south near the surface, there is strong uptake of carbon by the ocean because the solubility of CO_2 is inversely proportional to water temperature. Superimposed on these natural processes is an uptake of anthropogenic CO_2 by the ocean over the totality of the ocean south of 35°S. This uptake is strongest in the region of the ACC, mostly due to high wind speeds and low initial concentrations of anthropogenic DIC in the waters of this region. The sum of processes involving both natural and anthropogenic carbon leads to a net uptake of CO_2 by the ocean between 35°S and 55°S. However, there is still substantial uncertainty in the estimates of carbon air-sea fluxes, particularly south of 55°S, in the HLSO [Gruber et al., 2019].

Takahashi et al. [2009] provide an estimate of HLSO carbon air-sea flux based on their global gridded climatology of surface ocean $p\text{CO}_2$. They find a small amount of net outgassing in both the ASZ and the SIZ. Their estimate is based on 3 million shipboard measurements taken between 1970 and 2007 which were then interpolated to a global 4°x5° grid. Since the Southern Ocean is dramatically under-sampled, data from neighboring pixels must be used to fill in the gaps. Moreover, there is only year-round data in the vicinity of Drake Passage. Landschützer et al. [2014] use a neural-network approach to map global shipboard measurements of surface ocean $p\mathrm{CO}_2$ to a monthly 1°x1° grid (1998-2011). They find a small amount of annual uptake of carbon by the ocean though they do acknowledge that the Southern Ocean is strongly under-sampled compared to other ocean basins. Both Landschützer et al. [2014] and Takahashi et al. [2009] use the same shipboard observations for their estimate.

Since the 1960s, the long-term trend of the ocean carbon sink has been keeping pace with the increasing anthropogenic CO_2 emissions, more than tripling from the 1960s to the 2010s [Friedlingstein et al., 2022]. However, the annual mean carbon sink for any particular year has varied away from the long-term tendency by as much as 20% [Gruber et al., 2023; Ritter et al., 2017]. For example, several studies based on pCO_2 measurements have found a weakening ocean carbon sink in the 1990s followed by a reinvigoration in the early 2000s, reaching its expected magnitude once more by 2010 [Gruber et al., 2023]. However, simulations by biogeochemical models find decadal variations in the ocean carbon sink of smaller magnitude [Hauck et al., 2020; DeVries et al., 2019]. Several studies have shown that the strongest inter-decadal variations in the ocean carbon sink occur in the Southern Ocean [Gruber et al., 2019; Landschützer et al., 2016, 2015]. However, the uncertainty of the ocean carbon sink is highest in the Southern Ocean [Friedlingstein et al., 2022; Gloege et al., 2021] and the discrepancy between models and observations is also most significant there compared to other ocean basins [Hauck et al., 2020].

One reason for this increased uncertainty is that the Southern Ocean is a remote and harsh environment where collecting measurements is challenging. Instruments must survive the polar darkness, high winds, strong waves and drifting sea ice, and consequently there are few moorings or free-drifting instruments [Bourassa et al., 2013]. The frequent cloud cover, the presence of sea ice and the polar night also all make retrieving continuous satellite data challenging [Castro et al., 2016; Bourassa et al., 2013]. Furthermore, the circulation in this region is unique such that physical understanding developed in temperate locations does not necessarily apply to high latitude systems. This is primarily due to the presence of sea ice, frequent high wind speeds, low winter temperatures and significant mesoscale and submesoscale activity [Bourassa et al., 2013]. The Southern Ocean is also challenging to model because of the interplay between the three climate system components (atmosphere, ocean, sea ice) and the fundamental role of mesoscale and submesoscale eddy fluxes in Southern Ocean dynamics [Newman et al., 2019]. Thus, we cannot rely solely on modeling studies to make-up for the sparseness of available data.

Year-round and spatially distributed observations of carbonate system parameters have only recently become available in regions other than in the Drake passage [Bushinsky et al., 2019]. The Southern Ocean Carbon and Climate Observation and Modeling (SOCCOM) project has been responsible for releasing more than 300 autonomous biogeochemical floats in the Southern Ocean starting in 2014. These floats are equipped to measure below the sea ice and measure biogeochemical variables that allow us to estimate carbonate system parameters [Riser et al., 2018; Johnson et al., 2017b; Wanninkhof et al., 2016]. Using these year-round float observations from 2014-2017, Gray et al. [2018] found carbon outgassing in the ASZ of heretofore undetected magnitude, dominated by a strong winter outgassing signal. In the SIZ, the authors found that significant summer carbon uptake was nearly balanced by winter outgassing. In a follow-up study using both the ship and float observations, Bushinsky et al. [2019] found that the HLSO winter outgassing signal is still present and that net outgassing is still predicted for the ASZ. However, a recent study used atmospheric observations of vertical and horizontal CO_2 gradients to constrain atmospheric transport models and estimate the Southern Ocean carbon air-sea flux [Long et al., 2021]. While they only provide an estimate of the carbon air-sea flux for the Southern Ocean as a whole, their result, a strong carbon sink, does not agree with the float-based estimate. Thus, there is still considerable uncertainty, even on the sign, of the HLSO air-sea carbon flux.

Air-sea carbon fluxes are computed from the difference in CO_2 partial pressure between the atmosphere and the ocean multiplied by a gas transfer velocity and the solubility of CO_2 in the ocean [Gruber et al., 2019; Gray et al., 2018]. Since these last two parameters are strictly positive, the sign of the air-sea flux depends solely on the air-sea gradient in $p\mathrm{CO}_2$. Spatio-temporal variability in atmospheric CO_2 is small compared to surface ocean $p\mathrm{CO}_2$ [Takahashi et al., 1997]. Therefore, the spatial and seasonal variation in oceanic $p\mathrm{CO}_2$ primarily determines seasonal and regional variations in air-sea carbon fluxes [Takahashi et al., 2002].

The dominant mode of variability for both surface ocean $p\mathrm{CO}_2$ and air-sea carbon flux is the seasonal cycle [Gruber et al., 2019]. It has also been shown that the inter-annual to inter-decadal variability in the

$p\mathrm{CO}_2$ difference between the atmosphere and the ocean ($\delta p\mathrm{CO}_2$) are embedded in its seasonal cycle [Gregor et al., 2018]. In the high latitude Southern Ocean, uptake of CO_2 is stronger in summer than in winter. In winter, mixing and entrainment of DIC-rich water dominate and lead to elevated surface ocean $p\mathrm{CO}_2$ and potentially outgassing [Takahashi et al., 2009]. In summer, reduced wind speeds and surface freshening lead to stratification, allowing for more biological production which decreases surface $p\mathrm{CO}_2$ [Thomalla et al., 2011].

To formalize our understanding of the processes driving seasonal changes in ocean $p\mathrm{CO}_2$, we can separate the signal into thermal and non-thermal components using the well-known thermal sensitivity of $p\mathrm{CO}_2$ [Takahashi et al., 1993]. The thermal component is in phase with seasonal temperature changes. Colder waters have a higher dissolved carbon solubility leading to smaller $p\mathrm{CO}_2$ for the same amount of DIC. While the temperature effect is very strong and dominates over most of the world oceans, south of the Subantarctic front, $p\mathrm{CO}_2$ seasonality is driven primarily by the non-thermal component [Prend et al., 2022a; Gruber et al., 2019; Takahashi et al., 2002]. The non-thermal component is dominated by changes in DIC concentration at the surface. Thus, surface DIC variability is central to understanding HLSO air-sea carbon fluxes. However, there are still several unanswered questions about the mechanisms driving mixed layer DIC variability. This work aims to further our understanding of the processes driving the Southern Ocean carbon cycle to facilitate future projections of global climate change.

Together, these observations highlight major open questions in our understanding of carbon cycling in the Southern Ocean, motivating the following guiding questions for this dissertation:

1. What drives variability in mixed layer DIC on seasonal and annual time scales in the high latitude Southern Ocean?
2. Are those drivers consistent across different global circulation models used to make climate change predictions?
3. What is the role of zonal asymmetries in driving mixed layer DIC variability in the high latitude Southern Ocean?

This dissertation is structured around 3 independent chapters that build sequentially in the application of the method. In this work, we use both observations and models to quantify mixed layer DIC fluxes within a budget framework in order to understand how carbon content varies in time and space. First, Chapter 1 will seek to answer Question 1 using observations from autonomous biogeochemical floats to characterize the variability in mixed layer carbon fluxes. Building on this for Chapter 2, we evaluate the drivers of DIC variability in an ensemble of low resolution ocean-sea ice-biogeochemistry models used in the OMIP component of the CMIP6 project. In this chapter, we address Question 1 from the modeling perspective as well as Question 2, building on the observational insights from Chapter 1. Finally, Chapter 3 investigates the zonal asymmetry of mixed layer carbon fluxes (Question 3) in a higher resolution ocean model with a biogeochemical component.

Chapter 2

Carbon Outgassing in the Antarctic Circumpolar Current is Supported by Ekman Transport from the Sea Ice Zone in an Observation-based Seasonal Mixed-layer Budget

This chapter includes materials originally published in Sauvé, J., Gray, A. R., Prend, C. J., Bushinsky, S. M., & Riser, S. C. (2023). Carbon outgassing in the Antarctic Circumpolar Current is supported by Ekman transport from the sea ice zone in an observation-based seasonal mixed-layer budget. Journal of Geophysical Research: Oceans, 128, e2023JC019815. `https://doi.org/10.1029/2023JC019815`

Abstract

Despite its importance for the global cycling of carbon, there are still large gaps in our understanding of the processes driving annual and seasonal carbon fluxes in the high-latitude Southern Ocean. This is due in part to a historical paucity of observations in this remote, turbulent, and seasonally ice-covered region. Here, we use autonomous biogeochemical float data spanning 6 full seasonal cycles and with circumpolar coverage of the Southern Ocean, complemented by atmospheric reanalysis, to construct a monthly climatology of the mixed layer budget of dissolved inorganic carbon (DIC). We investigate the processes that determine the annual mean and seasonal cycle of DIC fluxes in two different zones of the Southern Ocean - the Sea Ice Zone (SIZ) and Antarctic Southern Zone (ASZ). We find that, annually, mixing with carbon-rich waters at the base of the mixed layer supplies DIC which is, in the ASZ, either used for net biological production or outgassed to the atmosphere. In contrast, in the SIZ, where carbon outgassing and the biological pump are weaker, the surplus of DIC is instead advected northward to the ASZ. In other words, carbon outgassing in the southern Antarctic Circumpolar Current (ACC), which has been attributed to remineralized carbon from deep water upwelled in the ACC, is also due to the wind-driven transport of DIC from the SIZ. These results stem from the first observation-based carbon budget of the circumpolar Southern Ocean and thus provide a useful benchmark to evaluate climate models, which have significant biases in this region.

2.1 Introduction

The Southern Ocean plays a significant role in the global carbon cycle. Around 40% of oceanic uptake of anthropogenic carbon dioxide (CO_2) occurs in the waters south of 35°S [DeVries, 2014]. Ekman divergence driven by strong westerly winds leads to a combination of upwelling and downwelling of natural and anthropogenic carbon, respectively. Consequently, the Southern Ocean is a strong CO_2 sink between 35-55°S, although the picture is not as clear at higher latitudes [Gruber et al., 2019]. Historically, observations from this remote region have been strongly biased towards summer and limited spatially, particularly in the seasonally ice-covered areas. Data from autonomous biogeochemical floats deployed by the Southern Ocean Carbon and Climate Observations and Modeling (SOCCOM) project showed a stronger wintertime outgassing of carbon dioxide at high latitudes than expected, leading to a low Southern Ocean annual mean carbon uptake [Gray et al., 2018; Bushinsky et al., 2019]. However, another recent study based on airborne measurements found strong Southern Ocean annual mean carbon uptake [Long et al., 2021].

Air-sea carbon fluxes are computed from the difference in CO_2 partial pressure ($p\mathrm{CO}_2$) between the atmosphere and the ocean multiplied by a gas transfer velocity and the solubility of CO_2 in the ocean [Gruber et al., 2019; Gray et al., 2018]. Since these last two parameters are strictly positive, the sign of the air-sea flux depends solely on the air-sea gradient in $p\mathrm{CO}_2$. Spatio-temporal variability in atmospheric CO_2 is small compared to surface ocean $p\mathrm{CO}_2$ [Takahashi et al., 1997]. Therefore, oceanic $p\mathrm{CO}_2$ primarily determines seasonal and regional variations in air-sea carbon fluxes [Takahashi et al., 2002].

The dominant mode of variability for both surface ocean $p\mathrm{CO}_2$ and air-sea carbon flux is the seasonal cycle [Gruber et al., 2019]. Seasonal changes in ocean $p\mathrm{CO}_2$ can be separated into thermal and non-thermal components using the well-known thermal sensitivity of $p\mathrm{CO}_2$ [Takahashi et al., 1993]. The thermal component is in phase with seasonal temperature changes. Colder waters have a higher dissolved carbon solubility leading to lower $p\mathrm{CO}_2$ for the same amount of dissolved carbon dioxide. The non-thermal component is dominated by changes in dissolved inorganic carbon (DIC), and thus peaks in winter due to respiration and entrainment of subsurface carbon [Takahashi et al., 2002]. South of the Sub-Antarctic front, $p\mathrm{CO}_2$ seasonality is driven primarily by the non-thermal component [Gruber et al., 2019; Prend et al., 2022b]. Therefore, surface DIC variability is central to understanding high-latitude Southern Ocean air-sea carbon fluxes.

In order to understand air-sea carbon flux variations, it is useful to quantify the processes that alter mixed-layer DIC concentration. A range of tracer budgets have been used for this purpose across diverse space and time scales. As the necessary data is more readily available, there have been numerous DIC budgets constructed from model output, including from coupled models [Levy et al., 2013; Dufour et al., 2013; Hauck et al., 2013], idealized models [Bronselaer et al., 2018] and data-assimilating models [Carroll et al., 2022; Jersild and Ito, 2020; DeVries, 2014; Rosso et al., 2017]. However, these model-based budgets often average the entire ocean south of a given latitude (usually 44°S) and are computed over a fixed depth. These modelling studies show that both biological and physical processes drive DIC variations, but no clear quantitative agreement has been reached about the leading order terms. In the high-latitude Southern Ocean, a small number of observation-based DIC budgets have been constructed using mooring data [Yang et al., 2021], shipboard sections [Brown et al., 2015; Munro et al., 2015; Jouandet et al., 2008; McNeil and Tilbrook, 2009], autonomous float data [Williams et al., 2018; Prend et al., 2022a] or a combination of methods [Shadwick et al., 2015; Merlivat et al., 2015]. However, the limited number of studies, as well as the different characteristics of the budgets constructed, preclude any specific conclusions aside from the strong seasonality in the processes driving mixed layer DIC variations. Furthermore, no previous study has provided a large-scale view of Southern Ocean DIC fluxes based on year-round and circumpolar observations.

Recognizing the paucity of year-round biogeochemical data in the Southern Ocean, the SOCCOM project began deploying sea ice-enabled autonomous biogeochemical profiling floats in 2014. Since then, a new database has been growing that can be used to shed light on the carbon cycle in this hard-to-reach environment. In this study, we build a monthly mixed layer DIC budget using SOCCOM float data, complemented with atmospheric reanalysis. This framework allows us to investigate the processes that determine the seasonal cycle of carbon fluxes in different regions; namely, the Sea Ice Zone (SIZ) and Antarctic Southern Zone (ASZ), which are delimited by the Polar Front (PF) and winter sea ice edge (SIE) (Figure 2.1 a). Section 2.2 covers the datasets used in this study. Section 2.3 elaborates on the budget framework, Section 2.4 presents the results on both annual and seasonal scales, and Section 2.5 discusses the implications of our results.

2.2 Datasets

2.2.1 Float Data

In this study, we use in situ data from the December 2020 snapshot of the SOCCOM Project dataset (`doi.org/10.6075/J0B27ST5`). This snapshot covers the period from January 2014 to December 22, 2020 and contains data from 201 autonomous biogeochemical profiling floats. SOCCOM floats measure temperature (T), pressure (P) and salinity (S) over the top 2000 m of the water column, every 10 days, similar to a typical Argo float. However, they also carry sensors for dissolved oxygen (O_2), nitrate, pH, chlorophyll fluorescence, and optical backscatter. Floats sample unevenly in the vertical, so all profiles are linearly interpolated onto a regular depth axis with 5 m resolution in the upper 500 m, 10 m resolution from 500-1000 m, 50 m resolution from 1000-1500 m, and 100 m resolution from 1500-2000 m. We only consider profiles with good pH data (i.e. where DIC content can be estimated), which leaves us with 7029 profiles from 132 floats, reasonably well spatially distributed in the Southern Ocean (Figure 2.1). We separate profiles according to the month and the zone (see Section 2.3.2) and obtain about 100 profiles per category (Figure 2.1 b)). We download a delayed-mode quality-controlled snapshot of the SOCCOM data [Maurer et al., 2021] and keep only the data flagged “Good" except for latitude and longitude, where we additionally keep under-ice

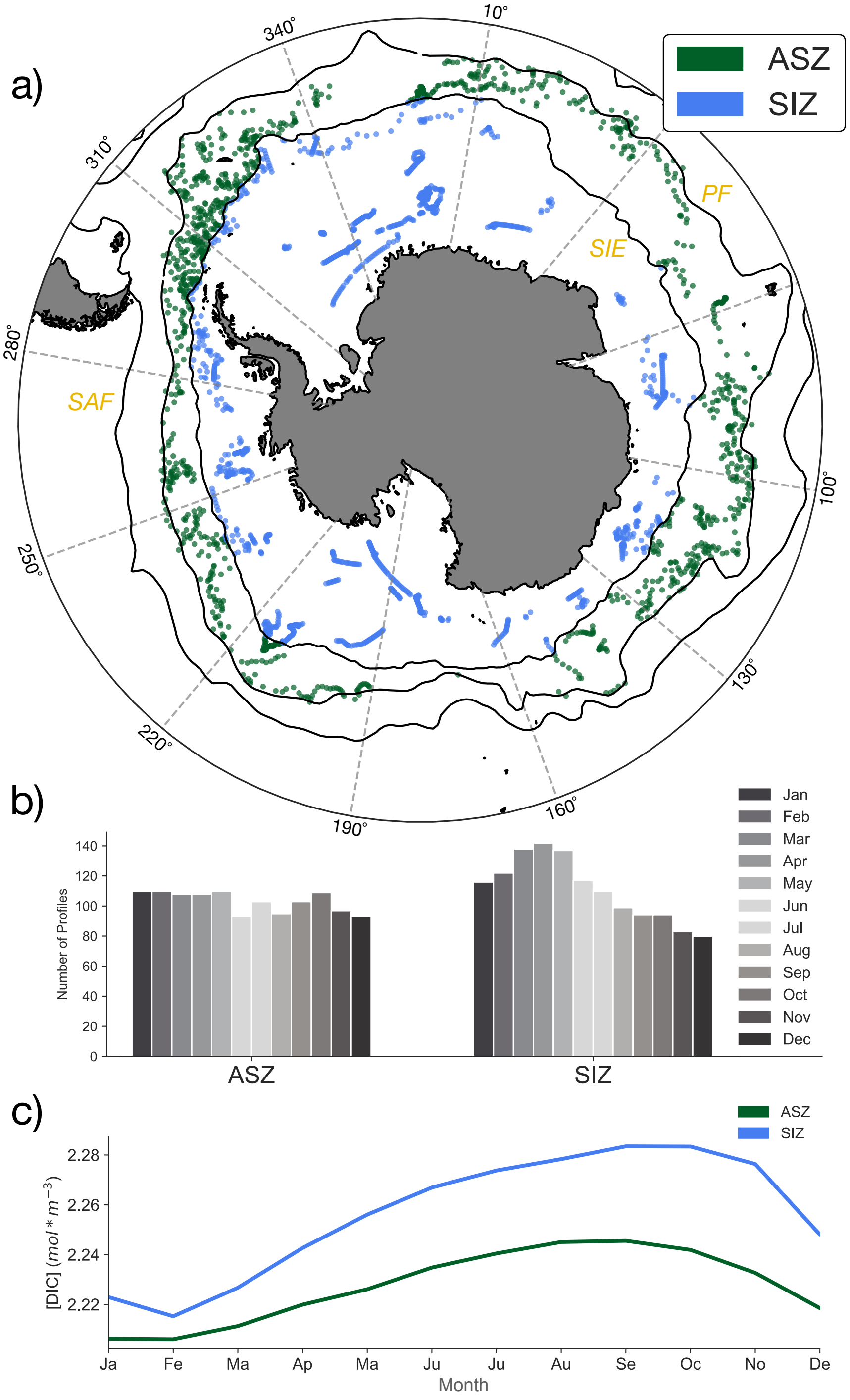

Figure 2.1: a) Location of available float profiles with good pH data (i.e. where DIC can be estimated), colored by zone (SIE: Sea Ice Edge, PF: Polar Front, SAF: Subantarctic Front). b) Number of profiles available for analysis per month and per zonal region c) Monthly and spatially averaged DIC concentration for the ASZ and SIZ (ASZ: Antarctic Southern Zone, SIZ: Sea Ice Zone).

data labeled “Questionable."

2.2.2 Ancillary Data

Monthly composites of the ERA5 reanalysis product, covering the period of January 2014 to December 2020, are used to create climatological seasonal cycles of eastward and northward wind stress, sea ice fraction, and evaporation and total precipitation rate [Hersbach et al., 2020]. Monthly composites of the ORAS5 global ocean reanalysis product, also covering the period of January 2014 to December 2020, are used to create climatological seasonal cycles of eastward and northward sea ice velocity, sea ice fraction, and sea ice thickness [Zuo et al., 2019]. Monthly fields from the Roemmich-Gilson Argo Climatology (RGAC) for the period of January 2014 to December 2020 are used to compute an average monthly climatology of potential temperature, which is used to estimate frontal positions [Roemmich and Gilson, 2009]. A gridded product of geostrophic velocity updated from Gray and Riser (2014) with improved mapping and additional data points is used in the geostrophic transport calculations (see Section 2.3.3). Finally, we use the bathymetry from the ETOPO1 Global Relief Model [Amante and Eakins, 2009].

2.3 Budget Framework and Analysis Methods

In order to create a monthly climatology of the mixed layer budgets of carbon and oxygen, we use a box model framework with boxes defined by the Polar Front and the maximum sea ice extent. Thus, averaging over a region is roughly equivalent to applying a zonal average. Consequently, horizontal fluxes of carbon and oxygen need only be defined at the box’s northern and southern edges (Figure 2.1 a). Available float data are selected for a particular box (i.e. zonal region) and then averaged for each month, combining all available years to get a climatological seasonal cycle for each zone. We derive the mixed layer budget equation by volume integrating the tracer conservation equation for an arbitrary tracer, X, in this case DIC or O_2. The volume of the box can be converted to the product of the mixed layer depth (h) by the ocean surface area (A) of the box.

$$\int_A \int_{-h(t)}^{0} \left[\frac{\partial(\rho[X])}{\partial t} + \vec{u} \cdot \nabla(\rho[X]) = f_{air-sea} + \kappa_z \frac{\partial^2(\rho[X])}{\partial z^2} \right] dz dA \tag{2.1}$$

After solving and applying the appropriate assumptions, we obtain the final form of the budget equation (see Section 3.3 and Supplementary Information for details).

$$
\begin{aligned}
\frac{\partial(\rho[X]h)}{\partial t} = \\
&\rho[X]\big|_{-h}\frac{dh}{dt} - \frac{1}{A}\left[(\rho[X]V_{ek})\big|_{N} - (\rho[X]V_{ek})\big|_{S} + (\rho[X]V_{geo})\big|_{N} - (\rho[X]V_{geo})\big|_{S}\right] + \\
&\qquad w\rho[X]\big|_{-h} + F_{air-sea} - \kappa\frac{\partial(\rho[X])}{\partial z}\bigg|_{-h} + F_{bio} \qquad (2.2)
\end{aligned}
$$

In this form, we have canceled out the ocean surface area of the zonal region. However, multiplying any term by this area will return units of mol time^{-1}, which properly reflects the fact that our budget tracks the total quantity of DIC in the mixed layer over time. Each term of Eq. 2.2 represents a different process that can cause an increase or decrease in tracer mixed layer molar concentration (mol m^{-3}). Eq. 2.2 can be expressed in terms of the different fluxes at play, namely

$$\text{TEND} = F_{entrain} + F_{horiz-adv} + F_{vert-adv} + F_{air-sea} + F_{mixing} + F_{bio} \qquad (2.3)$$

In Section 2.3.3, we give a detailed overview of each term and its derivation.

2.3.1 Initial Processing of the Float Data

We follow the method used by the SOCCOM project to determine DIC from the float data [Johnson et al., 2017a; Wanninkhof et al., 2016]. We estimate total alkalinity (TA) by using float-derived T, S, and O_2 as inputs to the LIAR algorithm [Carter et al., 2018]. To estimate DIC, we use the CO_2 System Calculator for Python (PyCO2SYS) which requires two carbonate system parameters, TA and in situ pH, as well as measured T, S, and P [Humphreys et al., 2021]. We also provide total silicate and total phosphate concentrations estimated using stochiometric ratios of float-derived nitrate concentration. We use the equilibrium constant parameterizations of Lueker et al. [2000] to model carbonic acid dissociation, Dickson [1990] for bisulfate ion dissociation, Perez and Fraga [1987] for hydrogen fluoride dissociation, and Lee et al. [2010] for the boron:salinity relationship to estimate total borate.

We take the quality-controlled float data and average the relevant quantities in the mixed layer. To estimate the mixed layer depth (MLD), we find the absolute salinity and the conservative temperature using the Gibbs Sea-Water Oceanographic Toolbox for Python [McDougall and Barker, 2011]. From those, we estimate the in-situ density (ρ) and the potential density anomaly with reference pressure of 0. We then interpolate the potential density anomaly to 0.01 dbar increments and use a density variation threshold of 0.03 kg m^{-3} from a reference pressure of 10 dbar from the surface to identify an approximate pressure for the base of the mixed layer [de Boyer Montégut et al., 2004; Holte and Talley, 2009]. Note that the mixed layer pressure identified with this method includes the contribution of any sea ice present at the surface of the water column.

We select profiles which have at least one value in the top 30 dbar and at least 2 values in the top 1000 dbar, though only 1% of the DIC profiles have less than 50 data points. We fit a curve to each profile using a Piecewise Cubic Hermite Interpolating Polynomials (pchip) interpolator as they have been shown to be more accurate than linear interpolation schemes at representing the curvature found in vertical profiles of oceanographic data [Li et al., 2022]. We then find the average concentration in the mixed layer. This averaging is executed for the biogeochemical tracers' molality (concentration of tracer in mol kg^{-1} of seawater) multiplied by ρ to obtain the average mixed layer molar concentration of each variable (mol m^{-3}, called concentration for the remainder of this study). We also find the vertical gradient below the mixed layer by fitting a straight line through the data between the mixed layer pressure and 20 dbar deeper, finding its slope and converting to depth units by multiplying by $-g\rho 10^{-4}$. We then average the float data monthly and by zonal region, multiplying by h beforehand as the budget equation requires.

2.3.2 Zonal Regions

We sort profiles into two different zones, shaped like concentric circles around the continent of Antarctica (Figure 2.1 a) based on the Polar Front (PF), the sea ice edge (SIE) and the 1000m isobath. The sea ice zone (SIZ) is defined as the region south of the SIE where waters are at least 1000 m deep. The Antarctic Southern zone (ASZ) can be found north of the SIE and south of the PF. This is similar to a number of previous papers [Gray et al., 2018; Bushinsky et al., 2019]. We define the PF using the 2°C contour at the minimum potential temperature of the top 200 m. We compute the position of the front at monthly resolution by applying the

Orsi et al. [1995] criteria to the RGAC monthly climatology of potential temperature (Figure C.1). We use the 15% sea ice concentration contour in September to identify the Sea Ice Edge (SIE).

2.3.3 Budget Terms

The following section will provide details about the different terms of the mixed layer budget and their derivation.

Tendency and Entrainment Flux

The left-hand side, or tendency (TEND), of Eq. 2.2 corresponds to the time rate of change of the tracer concentration (mol m^{-3}) in the box. The entrainment flux is due to the processes by which the base of the mixed layer deepens or shoals. During mixed layer deepening, water below the mixed layer is integrated into the surface layer leading to mixed layer volume and tracer content increasing, proportionally to the amount of tracer in the waters just below the base of the mixed layer. During mixed layer shoaling, mixed layer volume decreases and so does the amount of tracer in the mixed layer, proportionally to the mixed layer concentration. Both the TEND and $F_{entrain}$ can be estimated from float-derived molality, the thickness of the mixed layer (h) and ρ, using a centered difference calculation. Integrating the first component of Eq. 2.1 over a time-varying $h(t)$ produces two terms, the tendency term (the rate of change of the total tracer amount) and the entrainment term (proportional to the rate of change of the MLD) (see Supplementary Information for details). The tendency term is given by

$$\text{TEND} = \frac{\partial(\rho[X]h)}{\partial t} \tag{2.4}$$

and the entrainment term is expressed as

$$F_{entrain} = \rho_{-h}[X]_{-h}\frac{dh}{dt} \quad \text{if } \frac{dh}{dt} > 0 \tag{2.5}$$

$$F_{entrain} = \rho[X]\frac{dh}{dt} \quad \text{if } \frac{dh}{dt} < 0 \tag{2.6}$$

both terms having been divided by the area to be consistent with Eq. 2.3.

It is important to note that the subtraction of the entrainment flux from the tendency is equivalent to the rate of change of the concentration multiplied by the mixed layer depth (h). This will be used in the presentation of the results.

$$\frac{\partial(\rho[X]h)}{\partial t} - (\rho[X])_{-h}\frac{dh}{dt} = h\frac{\partial(\rho[X])}{\partial t} \tag{2.7}$$

Air-Sea Flux

We estimate the air-sea fluxes of carbon using the method from Gray et al. [2018]. Using float-measured pH and a float-based estimate of alkalinity, we compute $p\text{CO}_2$ at the surface of the ocean. We then use monthly observations of the mole fraction of CO_2 in dry air from air samples at the Cape Grim Observatory in Tasmania which we interpolate to a 6-hourly timescale. To derive atmospheric $p\text{CO}_2$, we combine these measurements with estimates of the mean sea level pressure at each profile location, corrected for water vapor pressure using the method of Zeebe and Wolf-Gladrow [2001]. The air-sea flux of carbon can then be estimated using the following equation, where k_g is the gas transfer velocity and K_0 is the solubility of CO_2:

$$f_{air-sea} = k_g K_0 (p\text{CO}_2^{ocn} - p\text{CO}_2^{atm}). \tag{2.8}$$

We use a squared wind speed-dependent parameterization to compute k_g from the Schmidt number and an estimate of the 10-m wind speed [Wanninkhof, 2014]. Because carbon dioxide is highly soluble in seawater, we do not need to account for the effect of bubble fluxes. If sea ice is present at the surface, we find the sea ice concentration (C_{si}) at a particular profile location from satellite observations. We then apply a correction factor of (1-C_{si}) to the flux value. If $\text{C}_{si} > 95\%$, we set C_{si} equal to 95% to account for the presence of leads in sea ice.

We estimate the oxygen air-sea fluxes following Bushinsky et al. [2017]. Contrarily to carbon, oxygen is a relatively insoluble gas, and bubble fluxes must be taken into account. The total air-sea flux is thus made up of three components: F_s is the diffusive component, F_c accounts for small bubbles that collapse while under water, and F_p accounts for big bubbles that partly escape the water column. β is the tuning parameter.

$$f_{air-sea} = F_s + \beta F_c + \beta F_p \tag{2.9}$$

To obtain the form of the air-sea flux that is consistent with Eq. 2.3 ($F_{air-sea}$), we compute the air-sea flux ($f_{air-sea}$) at high frequency (6-hourly) and then find the average air-sea flux of tracer per meter squared (mol m^{-2} day^{-1}) for each zonal region.

Advective Flux

The advective fluxes originate from the second term of Eq. 2.1, which we separate into a horizontal and a vertical component. We consider the horizontal advection crossing the zonal boundaries at the northern and southern edges of the box only. In the Southern Ocean, cross-front (largely meridional) advection at the surface is mostly due to Ekman transport, which is northward due to the strong westerly winds. Additional contributions to the cross-front advection come from the geostrophic flow, which can be decomposed into low-frequency (mean and seasonal cycle) and high-frequency (eddying) components. In the context of this work, we neglect the cross-front advection due to eddies because it has been shown to be more than 50% smaller than the time mean component in the Ekman layer [Dufour et al., 2015]. Defining V_{ek} and V_{geo} as the Ekman and geostrophic mass transports, the final form of the horizontal advection term equation, as consistent with Eq. 2.3, becomes

$$F_{horiz-adv} = -\frac{1}{A}\left[\left(\rho[X]V_{ek}\right)\big|_N - \left(\rho[X]V_{ek}\right)\big|_S + \left(\rho[X]V_{geo}\right)\big|_N - \left(\rho[X]V_{geo}\right)\big|_S\right] \tag{2.10}$$

(see Supplementary Information for details). Here, $\rho[X]\big|_N$ ($\rho[X]\big|_S$) corresponds to the tracer concentration of the source water of the horizontal advection at the northern (southern) boundary. This will change depending on the direction of mass flux (northward or southward). For example, Ekman transport in this region is northward. Consequently, we multiply the Ekman mass transport at the northern (southern) boundary of the zone by the concentration of tracer in (just South of) the zonal region (Figure C.4).

We can compute the Ekman mass transport (V_{ek}) using ERA5 wind stress data. We take the monthly averaged wind stress and interpolate the data to each (latitude, longitude) points defining the boundaries of the zones. Using both the zonal and the meridional wind stress, we compute the component of the wind stress parallel to each segment of the boundary, defined by two (latitude, longitude) points. Taking the along-boundary wind stress, we convert it to the depth integrated Ekman velocity across the boundary using the Coriolis equation (Eq. B.10). Integrating further zonally around the boundary, we obtain the Ekman transport across the boundary of the zone (m^3 time^{-1}) (see Appendix A.1).

The geostrophic mass transport is computed using an updated version of the geostrophic velocity product from Gray and Riser [2014]. Similarly to the process for Ekman transport, the data is interpolated to boundary locations and the across-boundary geostrophic velocity is identified at each segment of the boundaries of the zones. This geostrophic velocity is then integrated zonally along the boundary before being integrated further in depth to the mixed layer depth of the zone being considered (see Appendix A.1).

The vertical advection at the base of the mixed layer depends on the vertical velocity at the base of the mixed layer (w_{-h}) as well as on the concentration of tracer ($\rho[X]\big|_{-h}$) in the downwelled or upwelled waters depending on the sign of w$_{-h}$.

$$F_{vert-adv} = (w\rho[X])\big|_{-h} \tag{2.11}$$

Vertical velocity is more challenging to determine from satellite products as it is comparatively small. We use a mixed layer mass budget to determine the monthly-mean vertical velocity averaged across each zone. The equation for the mixed layer mass budget is determined by integrating the advection-diffusion equation for density over the mixed layer volume in a process similar to the derivation for the tracer conservation equation. The resulting equation has many of the same terms as the biogeochemical budget equation.

$$\frac{d(A\rho h)}{dt} = F_{entrain} + F_{surface} + F_{horiz-adv} + F_{vert-adv} \tag{2.12}$$

The rate of change with time of the mass of water in the mixed layer as well as the entrainment flux of water can both be determined from float-derived data following Eq. 2.7 applied to the density (kg m^{-3}) instead of the concentration of tracer (mol m^{-3}). Similarly, the horizontal mass advection can be determined following Eq. 2.10. We use ERA5 precipitation, evaporation, and sea ice concentration data to estimate surface fluxes of mass ($F_{surface}$). For the sea ice contribution, we take the centered difference of the sea ice area combined with an estimated seasonal sea ice thickness [Li et al., 2018] to find the rate of change with time of the sea ice volume for each month. We use ORAS5 sea ice velocity and sea ice thickness to estimate the sea ice transport across each zonal boundary with the same method as for the Ekman and geostrophic transports. We subtract the volume of sea ice advected into the zone from the rate of change of the sea ice volume to get the sea ice contribution to the surface mass flux. Since the mass budget doesn't have biological fluxes or fluxes due to mixing, there is only one unknown, w_{-h}, which we solve for (Figure C.3) (see Appendix A.2).

Mixing Flux

Vertical mixing represents multiple processes involving the gradient of tracer concentration between the mixed layer and the waters underlying it. It differs from vertical advection because there is no exchange of mass. It is typically parameterized in terms of a vertical eddy diffusivity (κ_z), which ideally is tuned to observations. The mixing flux term corresponds to the last term of Eq. 2.1,

$$F_{mixing} = -\kappa_z \frac{\partial(\rho[X])}{\partial z}\bigg|_{-h} \tag{2.13}$$

(see Supplementary Information for details). There are very few observations of the vertical eddy diffusivity in the Southern Ocean and few observations at the base of the mixed layer. Law et al. [2003] estimate that the mean effective vertical diffusivity is less than 0.3×10^{-4} m^2 s^{-1} in the Antarctic Circumpolar Current (ACC) region (61°S, 140°E) using a tracer dispersion experiment. Cronin et al. [2015] used data from moorings, satellites, and Argo floats to construct mixed layer budgets of heat and salt and estimate the residual diffusive flux of heat or salt across the base of the mixed layer. This residual flux implies a vertical eddy diffusivity of 1 to 3 $\times$ 10^{-4} m^2 s^{-1} in summer and spring for an open ocean location in the Northeast Pacific subpolar gyre. Please refer to section 2.3.4 for details on how we estimate this parameter for the budgets presented here.

Biological Flux

The net contribution of all biological activity to changes in the concentration of tracer in the mixed layer of each zone is represented by the biological flux term (F_{bio}). Also included in this quantity are any non-explicitly represented physical processes. In the following section, we detail the method used to estimate both this term and the unknown eddy diffusivity parameter necessary for the mixing flux.

2.3.4 Optimization of the Coupled DIC and O$_2$ Budgets

To find the few parameters that cannot be easily estimated from float or reanalysis data, we define, for each zonal region, a system of 24 non-linear coupled equations (the monthly equations for the DIC and O$_2$

budgets) with 14 unknowns, where Y_X represents all terms that can be estimated from float or reanalysis data.

$$Y_{DIC} = -\kappa_z \frac{\partial \rho [C]}{dz}\bigg|_{-h} + F_{biology-DIC} \tag{2.14}$$

$$Y_{O_2} = -\kappa_z \frac{\partial \rho [O_2]}{dz}\bigg|_{-h} + R_{O_2/C} F_{biology-DIC} \tag{2.15}$$

We assume a single value of eddy diffusivity (κ_z) for all months in a zonal region. We use the respiration quotient ($R_{O_2/C}$) to link the biological flux of DIC and O_2 and assume that this ratio doesn't change from month to month in a particular zone. This leaves us with 12 monthly carbon biological fluxes, one value of κ_z and one value of $R_{O_2/C}$ as the unknowns for each region. Using our system of equations, we construct a cost function that we minimize to determine the missing parameters. We use the Trust Region Reflective algorithm as part of a non-linear problem solver, to which we provide a Jacobian, to find a local minimum of our cost function [Branch et al., 1999] (See Appendix A.3).

2.3.5 Uncertainty estimation

Unlike model budgets which can be closed exactly, our budget framework is based on several observational products, which each have their own uncertainties. Furthermore, we have used an optimization method to find the value of some parameters. As such, the budget has a non-zero residual (Figure C.8 and C.9). The residual is small compared to the other monthly carbon fluxes (about 1-2% of the average value of the flux for each month, except February and September in the SIZ where the fluxes are small and the residual is proportionally bigger), which gives us more confidence in our results. We also estimate an uncertainty for each monthly budget term.

To estimate the uncertainty associated with the results of the mixed layer budgets, we use a Monte Carlo simulation with 1500 iterations. The uncertainty and degree of correlation of each data variable used in the simulation can be found in Table A.1 (see Appendix A.4). The uncertainty associated with each budget result is set to one standard deviation of the mean of the 1500 simulations. We use a uniform distribution for the error in T,S,P and a normal distribution for all other variables. To estimate the uncertainty on the monthly composite of wind stress from ERA5, we interpolate the x- and y-direction wind stress at each boundary location for each ensemble member available from ERA5. We set the uncertainty as one standard deviation from the mean of the ensemble members. Similarly for the sea ice fraction from ERA5, we set the uncertainty of the change in sea ice fraction over a month as one standard deviation from the mean of the ensemble members. We use the uncertainty estimates provided by the LIAR algorithm for the uncertainty in TA [Carter et al., 2018]. We set the uncertainty of the geostrophic velocity interpolated at each (latitude, longitude) location of the zone boundaries to be 20% of the velocity, which is a conservative estimate based on the methodology [Gray and Riser, 2014]. We also set the uncertainty of the sea ice transport and the sea ice thickness to be 20% since sea ice thickness estimates tend to vary depending on which product is used (see Kern and Spreen [2015] for example). The uncertainty on the air-sea fluxes of carbon and oxygen was estimated separately following the methods of Gray et al. [2018] and Bushinsky et al. [2017], then used in the Monte Carlo.

Among the 1500 iterations of the Monte Carlo simulation, 15% (16%) of the eddy diffusivities (or κ_z) identified by the optimization scheme are negative for the ASZ (SIZ). This indicates up-gradient eddy diffusion of carbon which is not expected. However, when taking all iterations together, the averaged value of κ_z does converge to a positive value of the expected magnitude, as is also the case when running the budget with no uncertainty added. The presence of negative κ_z values points toward the fact that this system is physically fragile and may flip to a different, maybe non physically realistic, state easily. This fragility probably originates from the identification of the MLD, which is sensitive to the addition of uncertainties to the temperature and salinity profiles.

The budget framework assumes that the biological processes taking up or releasing DIC in the mixed layer are only photosynthesis and respiration. However, formation and dissolution of calcium carbonate by certain phytoplankton species also changes the mixed layer DIC and alkalinity content while not influencing the oxygen content [Krumhardt et al., 2020]. This process is not accounted for in our budget, which is a reasonable assumption for the ASZ and SIZ where there is low abundance of calcifying organisms [Balch et al., 2016] and the mixed layer DIC consumption attributed to particulate inorganic carbon production, like calcium carbonate, is relatively low compared to organic carbon production [Huang et al., 2023].

In this study, DIC concentration is calculated from in situ pH and empirically-estimated alkalinity. Most of the uncertainty in the DIC concentration arises from the uncertainty in TA provided by the LIAR algorithm, which is defined for each depth and latitude-longitude position. We then propagate this uncertainty through the Monte-Carlo simulation, assuming that the uncertainty is random to avoid introducing spurious variability in our results. We should note, however, that the TA uncertainty may be correlated in time, at least seasonally. Testing the algorithm against seasonally resolved measurements would be required to determine how much of the uncertainty is correlated in time. As such, the uncertainty on the DIC fluxes may be underestimated here.

2.4 Results

2.4.1 Drivers of the annual-mean mixed layer carbon budget

We first consider the drivers of the annually integrated air-sea flux of carbon in the high-latitude Southern Ocean (Figure 2.2 a). Note that the tendency term of Eq. 2.3 integrates to 0 by definition and does not appear in the annually integrated results. We find a net outgassing of carbon in both zones. In the ASZ, the outgassed carbon enters the mixed layer by mixing with carbon-rich waters from the interior. This mixing flux comprises eddy-driven processes that can transfer DIC across the mixed layer base without any exchange of fluid. The DIC mixed in from below is then either consumed by net community production or outgassed to the atmosphere. The magnitudes of the annual advective and entrainment fluxes are small. In the SIZ, the annual fluxes of DIC are of smaller magnitude in general than those in the ASZ. Similarly to the more northerly region, the annually-averaged contribution from the entrainment flux is small, and DIC principally enters the mixed layer due to mixing from below. However, since the outgassing signal and the annual biological flux are weaker, the surplus of carbon is carried north to the ASZ by net Ekman transport.

This flux of DIC from the SIZ supports an outgassing signal in the ASZ by providing an additional source of carbon to the mixed layer. Since the magnitudes of the individual advective fluxes are so much greater than the net DIC advection (Figure 2.2 b), small changes in the individual components of the advective flux could significantly alter the sign and magnitude of the net advective flux. For example, if sea ice retreats under climate change, it could decrease the capping effect of sea ice in the SIZ which is currently acting to prevent carbon outgassing in winter. This could lead to a decrease in the flux of DIC to the ASZ and the location of CO_2 outgassing could move south into the SIZ. In this way, changes in the transport at the southern boundary of the ASZ may be critical in determining the net air-sea flux of carbon dioxide in this

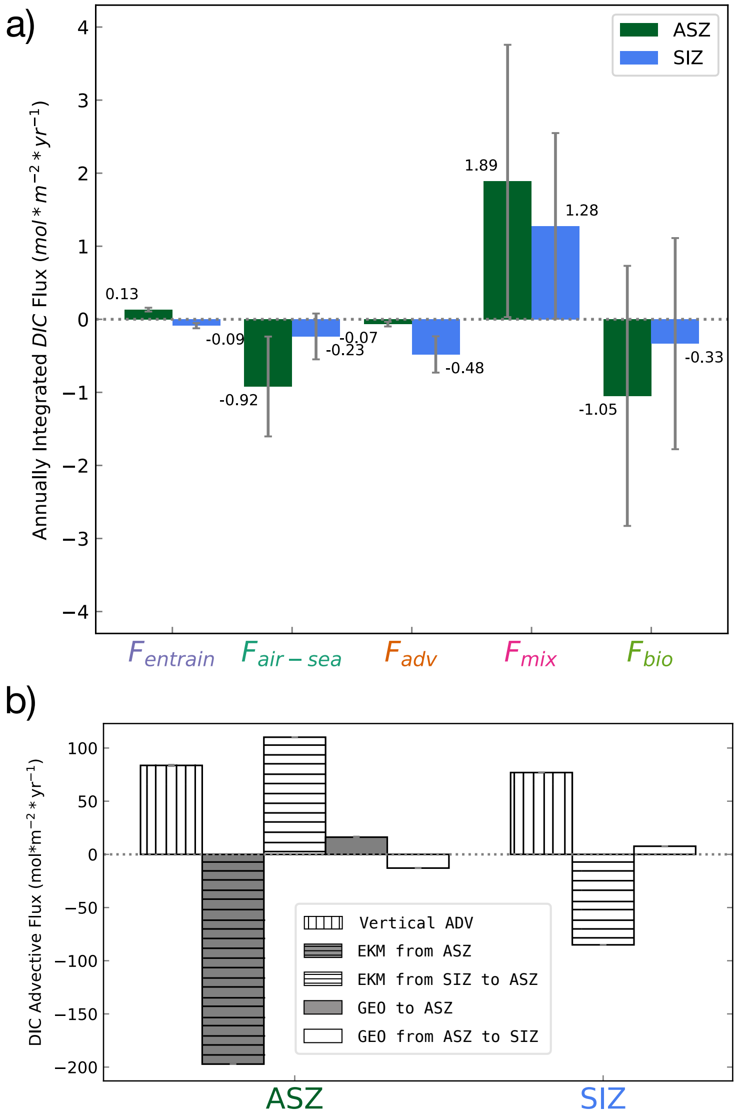

Figure 2.2: a) Annually integrated fluxes of DIC and their uncertainty indicated by the gray bars. Negative values indicate that DIC is being removed from the mixed layer of the zone in question ($F_{entrain}$: Entrainment flux, $F_{air-sea}$: Air-sea flux, F_{adv}: Advective flux, F_{mix}: Mixing flux, F_{bio}: Biological flux) b) Annually integrated advective fluxes of DIC which add up to F_{adv} from panel a (uncertainty is not shown because error bars are too small). "EKM from SIZ to ASZ" is the northward Ekman transport of DIC across the boundary separating the SIZ and the ASZ. Since the budget is computed per m^2, this term has a different magnitude when considered for the SIZ or the ASZ as the area of the zones are different. (Vertical ADV: vertical advection of DIC, EKM from ASZ: Ekman advection of DIC from the ASZ northward to the PFZ, EKM from SIZ to ASZ: Ekman advection of DIC from the SIZ northward to the ASZ, GEO to ASZ: geostrophic advection of DIC southward from the PFZ to the ASZ, GEO from ASZ to SIZ: geostrophic advection of DIC southward from the ASZ to the SIZ) (PFZ: Polar Frontal Zone, ASZ: Antarctic Southern Zone, SIZ: Sea Ice Zone)

region.

2.4.2 Seasonally-varying fluxes of carbon in the mixed layer

The monthly-averaged fluxes reveal similar seasonal patterns in air-sea carbon flux across both high-latitude regions, with carbon uptake by the ocean in summer partly opposing carbon outgassing during the rest of the year (Figure 2.3 and 2.4). In the ASZ, the air-sea flux is stronger and peaks at the end of winter (September), while in the SIZ carbon outgassing is strongly modulated by sea ice concentration and peaks in May [Butterworth and Miller, 2016].

We find that the seasonal variations in carbon air-sea flux lag one to two months behind the contribution from the term obtained by subtracting the entrainment from the tendency term (TEND$-F_{entrain}$, Figure 2.3a and 2.4a). This relationship is confirmed by a strong anticorrelation of -0.93 (-0.87) or -0.88 (-0.83) at one or two months lag for the ASZ (SIZ). The TEND$-F_{entrain}$ term is equivalent to the time rate of change of the mixed layer concentration multiplied by the mixed layer depth (see Eq. 2.7). Both the TEND and $F_{entrain}$ are two orders of magnitude larger than the other fluxes (not shown). However, their net effect is much smaller and comparable to the other processes that change the mixed layer DIC. Since the seasonal cycle in mixed layer depth is only weakly correlated to the seasonal cycle in TEND$-F_{entrain}$ (0.39 and 0.45 for the ASZ and SIZ respectively, Figure C.2), we interpret seasonal variations in TEND$-F_{entrain}$ to be caused by variations in the rate of change of mixed layer DIC concentration. Periods of carbon outgassing (uptake) tend to follow periods of concentration increase (decrease) by about one month, suggesting that changes in mixed layer DIC concentration are driving the air-sea fluxes of carbon in the zonal regions under study [Gruber et al., 2019]. To support the link between carbon air-sea fluxes and surface DIC concentration, we examine the drivers of $p\mathrm{CO}_2$ seasonal variability by computing $p\mathrm{CO}_2$ in pyCO2SYS while varying only one variable at a time. We find that in the high-latitude Southern Ocean, nearly all variability is due to seasonal changes in pH and thus to changes in DIC (Figure C.17).

Seasonal variations in the mixed layer DIC concentration change are driven chiefly by changes in the biological flux term in both zones (Figure 2.3 a and 2.4a), as confirmed by a strong correlation of 0.97 and 0.95 at no lag for the ASZ and SIZ, respectively. Biological activity adds carbon to the mixed layer when DIC concentration is increasing, probably due to net respiration, and the biological flux removes carbon from

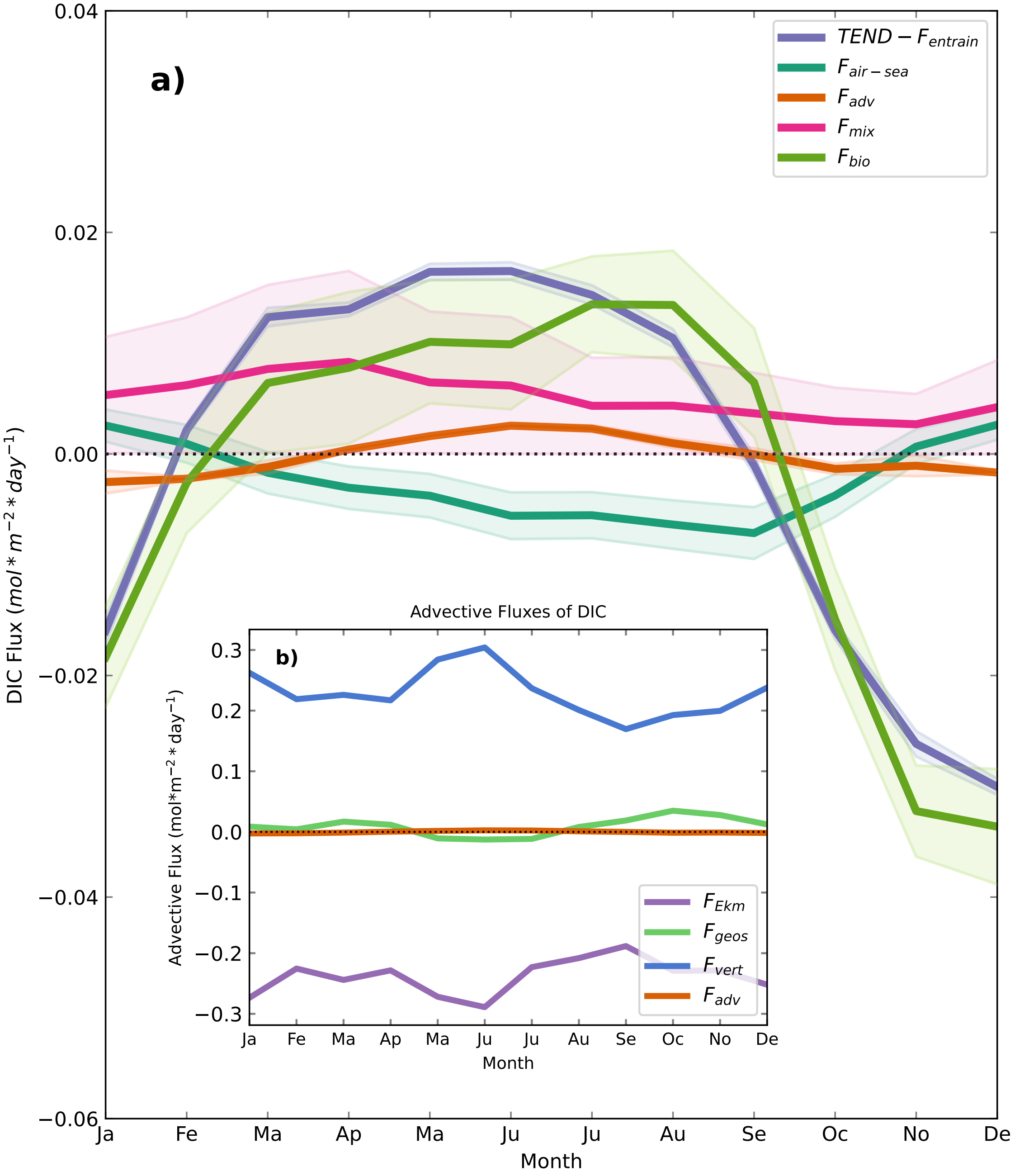

Figure 2.3: Monthly averaged fluxes of DIC to and from the ASZ mixed layer. a) DIC fluxes are presented with their uncertainty of one standard deviation (TEND: Tendency, $F_{entrain}$: Entrainment flux, $F_{air-sea}$: Air-sea flux, F_{adv}: Advective flux, F_{mix}: Mixing flux, F_{bio}: Biological flux) b) The components of the advective flux are presented: the flux of DIC due to Ekman advection (F_{Ekm}), geostrophic advection (F_{geos}), vertical advection (F_{vert}), as well as the net advective flux of DIC (F_{adv}). Uncertainty on the components of the advective flux is very small. Negative (positive) fluxes remove (add) carbon from (to) the mixed layer. (ASZ: Antarctic Southern Zone)

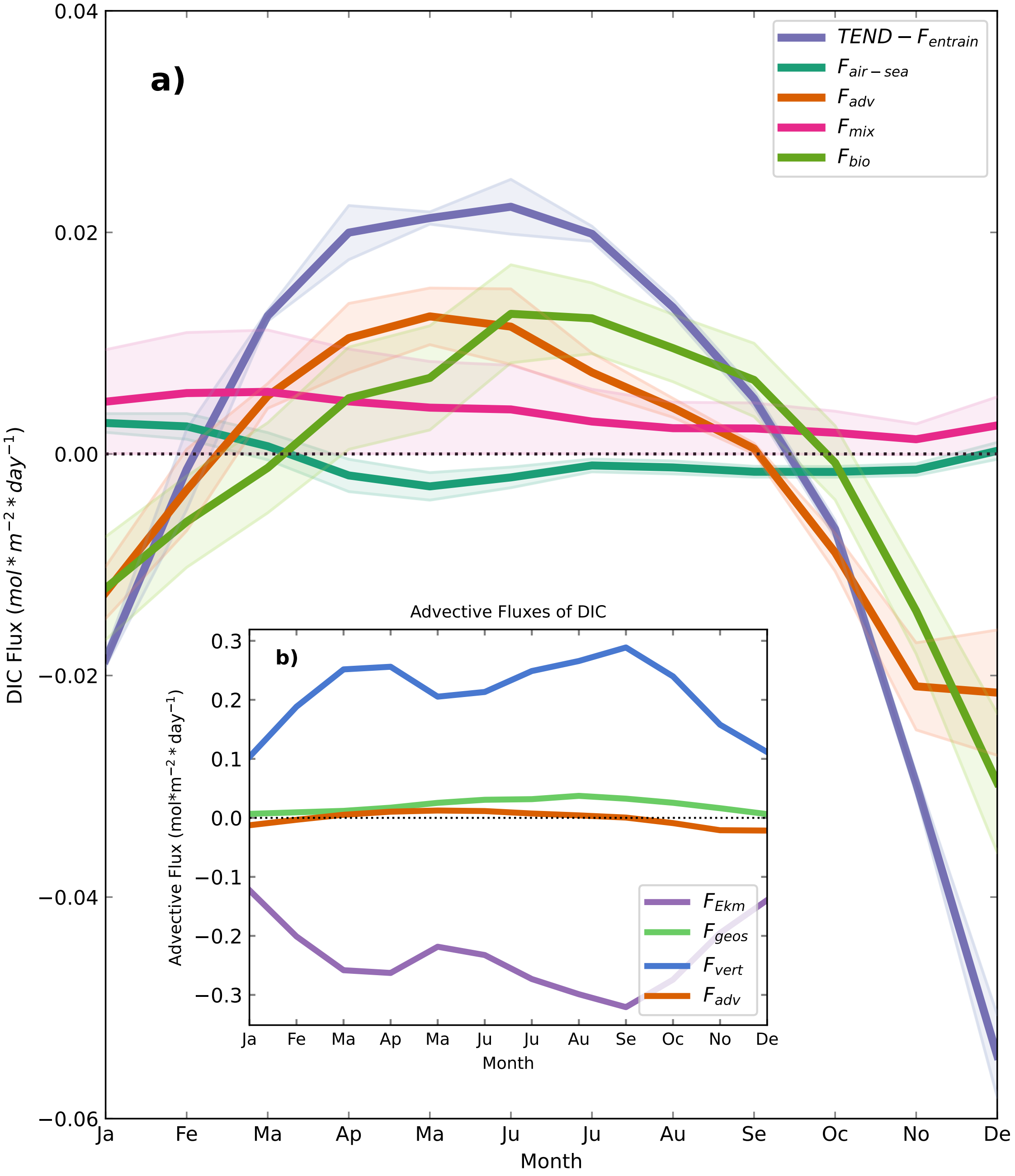

Figure 2.4: Monthly averaged fluxes of DIC to and from the SIZ mixed layer. a) DIC fluxes are presented with their uncertainty of one standard deviation (TEND: Tendency, $F_{entrain}$: Entrainment flux, $F_{air-sea}$: Air-sea flux, F_{adv}: Advective flux, F_{mix}: Mixing flux, F_{bio}: Biological flux) b) The components of the advective flux are presented: the flux of DIC due to Ekman advection (F_{Ekm}), geostrophic advection (F_{geos}), vertical advection (F_{vert}), as well as the net advective flux of DIC (F_{adv}). Uncertainty on the components of the advective flux is very small. Negative (positive) fluxes remove (add) carbon from (to) the mixed layer. (SIZ: Sea Ice Zone)

the mixed layer during the spring and summer phytoplankton bloom. The strength of this bloom is greater in the ASZ, as can be seen by the strong drop in the biological flux between September and November. In the SIZ, the seasonal cycle of the advective flux (Figure 2.4 a) is just as important as variations in the biological flux in driving changes in mixed layer DIC concentration (correlation of 0.97 at no lag).

The net advective flux is the sum of the Ekman, vertical and geostrophic components (Figure 2.4 b). We assume that the contribution from eddy-driven advection is small in the mixed layer for the timescales considered here. The individual advective components dominate over the other DIC fluxes (Figure C.13 and C.14), but the Ekman and vertical components largely compensate so that the net advection is of smaller magnitude. We find a net positive advective flux of DIC in fall and winter, indicating a dominance of vertical advection over the net meridional advection, while the opposite occurs in summer and spring. In the ASZ, the magnitude of the advective flux is much smaller than the biological flux (Figure 2.3 a), though we do observe a sign reversal similar to the SIZ, from net positive flux in winter to net negative flux in summer. In both zones, the flux of DIC from diffusive mixing with carbon-rich waters at the mixed layer base always acts to bring DIC into the mixed layer (Figure 2.3 a and 2.4 a). In both regions, the seasonal variations of the mixing flux are not strongly correlated with the change in DIC concentration.

In both zones, seasonal variations in the net advective flux of DIC can be attributed to a combination of changes in the Ekman flux of DIC from the SIZ to the ASZ and changes in the vertical advection signal, though the months where one or the other dominates are not the same across the study region (Figure 2.5). Changes in the southward geostrophic transport of DIC are also correlated with changes in the net advection, but the magnitude of the geostrophic advection is one order of magnitude smaller than the Ekman and vertical advections (Figure C.13).

By comparing the period of carbon outgassing (April to August) to the period of carbon uptake (December to January), we gain further insight into what drives the seasonal fluxes in this region. During wintertime outgassing, the mixed layer DIC concentration is increasing (positive value of TEND$-F_{entrain}$, Figure 2.3 a and 2.4a) because net respiration, eddy-driven mixing from below, and net vertical advection bring DIC into the mixed layer. Some of this DIC is then outgassed to the atmosphere (Figure 2.3 a and 2.4 a). During the summer period of oceanic carbon uptake, the mixed layer DIC concentration is decreasing due to strong net photosynthesis and a net Ekman northward advection of DIC. This superposition of processes leads to car-

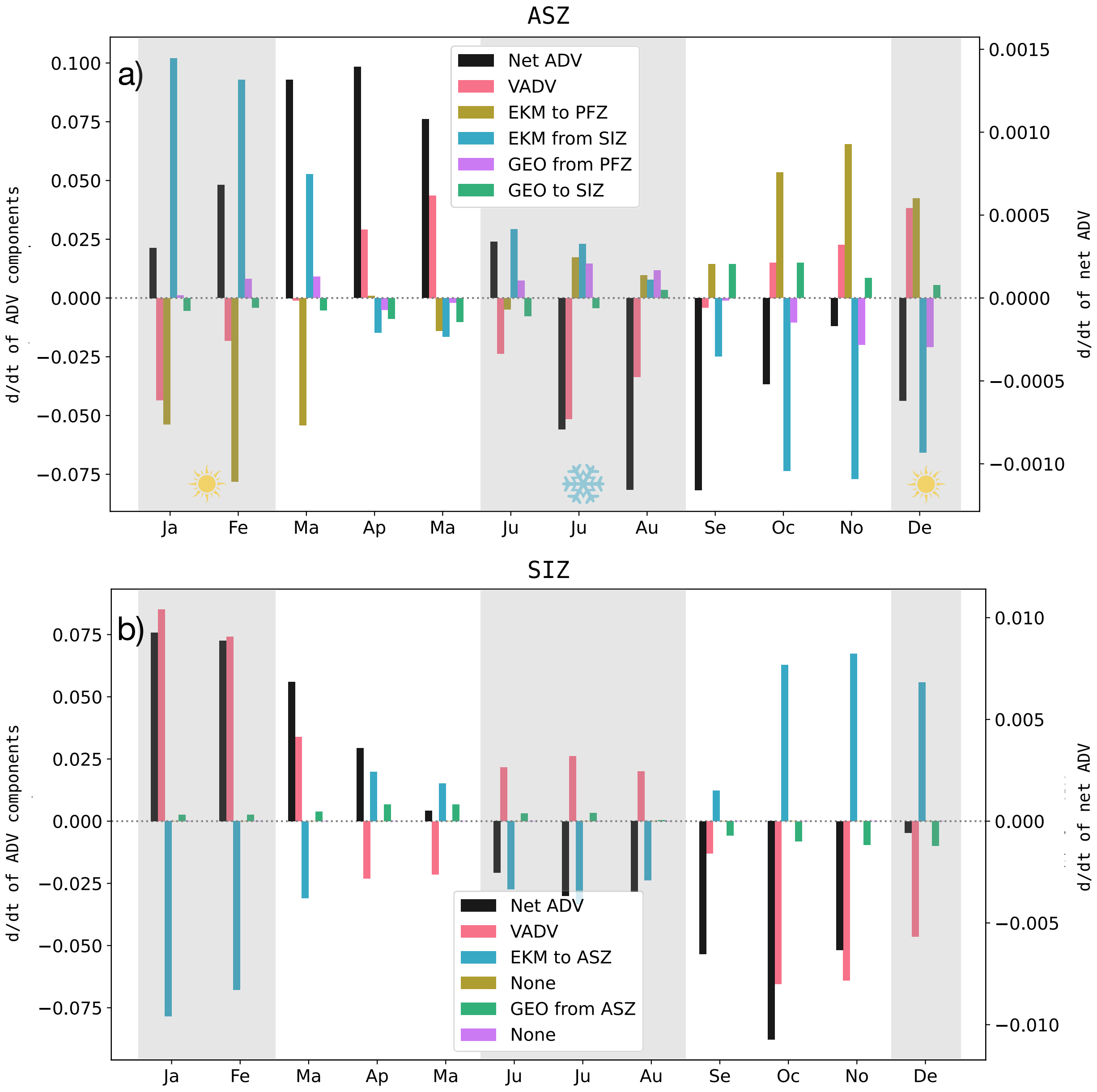

Figure 2.5: First time-derivative of the monthly averaged advective fluxes of DIC for a) the ASZ and b) the SIZ (mol m^{-2} day^{-1} month^{-1}). Note that the net advective flux (Net ADV) is plotted on its own axis (right) and the components of the net advective flux (Ekman (EKM), geostrophic (GEO) and vertical (VADV) advective fluxes of DIC) are plotted on the left axis. The gray shading indicates the summer and winter months.(PFZ: Polar Frontal Zone, ASZ: Antarctic Southern Zone, SIZ: Sea Ice Zone)

bon uptake from the atmosphere (Figure 2.3 a and 2.4 a). However, mixing with carbon-rich waters below is still bringing DIC into the mixed layer, which may contribute to the observed net outgassing signal over a full seasonal cycle.

The shift from carbon outgassing to uptake corresponds to a shift from respiration to photosynthesis and from net positive to net negative advection (Figure 2.3 a and 2.4 a). In the ASZ, the net advective flux of DIC primarily changes sign because of transport at the southern boundary; namely, Ekman advection of DIC from the SIZ (Figure C.13 and C.14) decreases significantly from winter to summer (by 53% on average), while the vertical advective flux and Ekman transport at the northern boundary stay relatively constant (decreases by 15% and 28% respectively). In the SIZ, most components of the advective flux decrease by approximately half during months of carbon uptake compared to months of outgassing.

The seasonal change in the Ekman advective flux of DIC at the sea ice edge is due to changes in Ekman mass transport driven by wind variations, rather than changes in the DIC concentration of the SIZ. We observe that the seasonal cycle in the Ekman mass advection and its components is very similar to that of the Ekman DIC advection (Figure C.13 to C.16). Furthermore, the amplitude of seasonal variations of the Ekman mass advection at the SIE is 74% (83%) for the ASZ (SIZ) which compares well to the amplitude of seasonal change of the Ekman DIC advection at the SIE (76% (85%) for the ASZ (SIZ)), while the amplitude of seasonal variations in the mixed layer DIC concentration of the SIZ used to convert mass transport to DIC advection is only 3% in both zones.

2.5 Discussion

The Southern Ocean is an essential part of the global climate system because of its important contribution to the total oceanic uptake of anthropogenic carbon. However, the uncertainty of the ocean carbon sink is highest in the Southern Ocean [Friedlingstein et al., 2022; Fay and McKinley, 2021; Gloege et al., 2021] and the discrepancy between models and observations is also most significant there compared to other ocean basins [Hauck et al., 2020]. There is also discrepancy between observational estimates of the Southern Ocean carbon sink, or the carbonate parameters necessary to determine it, based on the method or dataset used [Bushinsky and Cerovečki, 2023; Coggins et al., 2023; Wu et al., 2022; Wu and Qi, 2022; Mackay and Watson, 2021; Long et al., 2021]. Further, sampling alias linked to the spatial distribution of available observations has been shown to be significant [Hauck et al., 2023]. For this reason, it is essential to better understand the processes driving surface ocean $p\mathrm{CO}_2$, and thus the air-sea carbon flux, in order to improve the representation of the Southern Ocean carbon sink in models. The mixed layer budget presented in this study provides a useful framework for understanding the relative roles of the mechanisms that drive air-sea carbon fluxes at seasonal and annual timescales in the high-latitude Southern Ocean.

Using a monthly mean climatology of the mixed layer carbon budget, we show that small-scale mixing at the base of the mixed layer provides DIC to the surface layer year-round. In the ASZ, most of this DIC is then consumed by net biological production, while the net biological flux is weaker in the SIZ. On an annual timescale, the surplus of DIC in the mixed layer from the balance of these two processes is either advected from the SIZ to the ASZ by Ekman divergence or outgassed to the atmosphere in the ASZ. Physical transport of carbon, in concert with the transition from net production to net respiration, also explains the difference between seasonal periods of carbon outgassing (fall to spring) and uptake (summer).

Values for the vertical eddy diffusivity at the base of the mixed layer are sparse in the literature. Still, the magnitude of the diffusivity obtained from our optimization scheme (between 2.95 and 6.83×10^{-5} m^2 s-1) is similar to the only comparable published value in the Southern Ocean (less than 3×10^{-5} m^2 s^{-1}) [Law et al., 2003]. The ASZ makes up the southern part of the ACC, where wind-driven upwelling brings carbon-rich isopycnals to the near-surface. The high-latitude Southern Ocean also exhibits strong vertical DIC gradients [Dove et al., 2022]; therefore, it is not surprising that subsurface mixing plays a strong role in supplying DIC to the mixed layer. In the SIZ, there is also upwelling of carbon-rich deep waters. However, the SIZ is characterized by multiple gyre circulations as well as sea ice cover, which can act to isolate the surface ocean from the atmosphere and may be a barrier to momentum transfer [Shadwick et al., 2021; Vihma and Haapala, 2009]. Indeed, we find a stronger mixing flux of DIC in the ASZ compared to the SIZ due to differences in the eddy diffusivity (see Section A.3), consistent with more wind energy input in the ASZ resulting from stronger winds and lack of ice cover. However, the vertical gradient of DIC near the base of the mixed layer is stronger in the SIZ, most probably due to gyre dynamics allowing respired DIC to accumulate in the surface waters [MacGilchrist et al., 2019].

We find that inorganic carbon entering the mixed layer through eddy processes is mostly consumed by biological production. This is similar to previous results by Hauck et al. [2013], who found that biological processes remove more DIC from the mixed layer than air-sea fluxes. In the ASZ specifically, net production is the dominant sink of DIC in the mixed layer at annual timescales. We find annual net production of 1.05 mol C m^{-2} yr^{-1} in this region, consistent with previous float-based annual net community production estimates at similar latitudes (about 1-2 mol C m^{-2} yr^{-1}) [Arteaga et al., 2019]. In the SIZ, we also find annual net production, which agrees with model-based results [Carroll et al., 2022]. Note though that, in both zones, error bars are large and extend to a value of net respiration. This agrees with the analysis of Briggs et al. [2018] who found that respiration in winter nearly balanced out biological production. Still, in both zones, we find an important net production signal in spring and summer and that the DIC tendency typically follows the biological flux, as has been reported in past studies [Carroll et al., 2022; Yang et al., 2021; Williams et al., 2018; Munro et al., 2015]. In winter in both zones, we find net respiration of the same order of magnitude as the seasonal photosynthesis signal, due to low light availability (even more significant for the SIZ).

In the SIZ, the role of DIC advection is as important as the biological flux in both the seasonal and annual budgets. In the annual view, a large fraction of the surplus of DIC from subsurface mixing is advected to the ASZ by the Ekman transport component, with the rest either consumed by the net biological flux or outgassed. This is likely due, in part, to the wintertime ice cover preventing (or limiting) outgassing, as the surface ocean $p\mathrm{CO}_2$ values alone imply a stronger outgassing than is observed. Indeed, a sea ice capping effect has been reported on the continental shelf [Shadwick et al., 2021] and in idealized models [Gupta et al., 2020]. Still, without physical transport removing available DIC from the region in winter, there would be less potential for carbon uptake in summer after the sea ice melts. As such, seasonal variability in the net advective flux is important for explaining the low annual outgassing signal in the SIZ. Throughout the year, vertical advection supplies carbon to the mixed layer, while horizontal advection (dominated by Ekman divergence) removes DIC from the region. Net advection is the smaller residual of these two opposing processes. In fall and winter, the DIC flux due to vertical advection dominates over the Ekman transport (Figure C.14). In winter, however, stronger winds drive an increase in the Ekman flux of DIC, which continues until the net advection of DIC changes sign around the beginning of spring.

In the ASZ, seasonal variability in the advective flux of DIC from the SIZ is essential to explain the carbon air-sea fluxes in the region. In the annually-integrated view, the net advective flux in the ASZ is the residual between DIC removal from lateral advection at the northern front and DIC supply by both vertical advection and horizontal advection from the SIZ (Figure 2.3). The different components of the advective flux depend on both the circulation and the DIC concentration of the source waters. These two aspects are connected but could evolve independently under future warming. For example, ice retreat could increase wintertime outgassing in the SIZ, subsequently reducing the northward Ekman flux of DIC and carbon outgassing in the ASZ. In the seasonal picture, the net advective flux of DIC is smaller in magnitude than some of the other fluxes (Figure 2.3). Still, the change in sign of the net advection from periods of outgassing to uptake, which is due to a decrease in the amount of DIC entering from the SIZ by Ekman transport (Figure C.13), implies that wind-driven advection of DIC from the seasonal ice zone plays an important role in driving carbon outgassing in the ACC.

It is challenging to compare these results with previous work as there has been no other observation-based circumpolar mixed layer DIC budget in the Southern Ocean. However, a regional study of the Weddell Gyre (part of the SIZ) based on shipboard data and an inverse model found that DIC entrained from below mostly exits the gyre through northward transport to the ACC frontal region (equivalent to the ASZ) or becomes deep water at the gyre edges [Brown et al., 2015]. Using the same biogeochemical float dataset as this work, Prend et al. [2022a] find a strong role of the entrainment of carbon-rich waters into the mixed layer to explain spatial variability in carbon outgassing. However, they focus on inter-basin variations in air-sea fluxes, and specifically the period of obduction (the two months preceding the maximum mixed layer depth). Comparison to model-based DIC budgets is also difficult since they are typically computed over fixed depths, and many models have seasonal variations in air-sea carbon fluxes that are inconsistent with observations [Mongwe et al., 2018]. Still, two recent papers found that the advective flux of DIC plays an important role in the carbon budget of the region [Rosso et al., 2017; Carroll et al., 2022]. For example, Carroll et al. [2022] find that the DIC tendency and interannual variability in their SIZ biome is dominated by net advection, although they do not show the contribution from the different advective components. Rosso et al. [2017] do separate the advection into vertical, geostrophic and ageostrophic components, however, they compute their budget down to 650 m, which implicitly reduces the relative importance of Ekman transport (which only occurs in the top $\sim$80 m). One study did find, using a high-resolution model, that Ekman transport was the primary mechanism for the zonally integrated, cross-frontal transport of anthropogenic

CO_2 and its intra-annual variability, particularly across the Polar Front [Ito et al., 2010].

While these studies support our own results, they do not directly confirm the importance of Ekman transport from the SIZ in driving carbon outgassing in the southern ACC. In fact, while estimates based on biogeochemical float data find net outgassing in the high-latitude Southern Ocean that peaks in winter [Gray et al., 2018], this result disagrees with data products based on $p\mathrm{CO}_2$ measurements from the Surface Ocean CO_2 Atlas (SOCAT) dataset [Takahashi et al., 2009; Landschützer et al., 2014], airborne measurements [Long et al., 2021] and ocean biogeochemical circulation models [Hauck et al., 2020]. We use the carbon air-sea flux estimates from the SeaFlux ensemble, which is based on 6 $f\mathrm{CO}_2$ observation-based data products [Fay et al., 2021; Gregor and Fay, 2021], as input in our analysis in order to further investigate how a carbon uptake signal would combine with the subsurface carbon fluxes provided by the depth-resolved float data, in the optimization process (see Section 2.3.4). The SeaFlux ensemble includes three neural network-derived products, a mixed layer scheme, a multiple linear regression and a machine learning ensemble, all of which are based on the SOCAT observations.

Inputting the SeaFlux-based air-sea fluxes into our mixed-layer budget leads to mixing and biological fluxes, identified by the optimization scheme, that are not in line with previously published estimates (Figure C.10, C.11 and C.12). In the SIZ, the mixing flux is very small due to a vertical eddy diffusivity that is one order of magnitude smaller than for the ASZ. The error bar also extend significantly into negative values which would indicate diffusive mixing towards regions of higher concentration. In the ASZ, the annually-integrated biological flux at 2.65 mol C m^{-2} yr^{-1} is higher than expected based on previous estimates (Figure C.10) [Arteaga et al., 2019]. These results seem to imply that carbon uptake of the magnitude found in the SeaFlux-based air-sea fluxes is not consistent with the subsurface DIC fluxes, as well as with the surface and subsurface O_2 fluxes provided by the floats. This discrepancy could be due, at least in part, to the availability of year-round float data, whereas SOCAT observations tend to be seasonally-biased except in Drake Passage. As carbon air-sea fluxes have been shown to be zonally asymmetric in the Southern Ocean [Prend et al., 2022a; MacGilchrist et al., 2019; Gregor et al., 2018], differences in the spatial sampling between datasets could also lead to this discrepancy. For example, it is possible that the float dataset is capturing different scales of variability that are not resolved in the SOCAT based products. As such, it would be useful to quantify the mixed layer DIC budget in this region on smaller spatial scales (e.g. inter-basin comparisons). However, this is not possible using the approach presented here with the current data coverage, and is a limitation of this study. Determining the mechanisms that drive carbon air-sea flux variability is necessary to understand the discrepancies between different estimates of the Southern Ocean carbon sink from observation-based products and models. Float data, and the subsurface information they provide, are thus an invaluable tool to investigate the drivers of air-sea carbon flux on annual to seasonal timescales.

2.6 Conclusion

This study uses six years of under-ice capable autonomous biogeochemical float data to construct a monthly mixed layer carbon budget in two regions of the high-latitude Southern Ocean. We find that the monthly changes in the mixed layer DIC concentration closely corresponds to the seasonal variations in the biological flux of DIC. However, northward Ekman transport from the SIZ is also significant in setting the seasonal changes in DIC concentration. On annual timescales, mixing with carbon-rich waters from below the mixed layer leads to carbon outgassing in both regions under study (Figure 2.6). However, in the SIZ, where ice cover damps air-sea exchange and primary production is heavily light-limited, most of the carbon injected from below the mixed layer is transported northward to the ASZ by Ekman advection. In other words, Ekman transport of DIC from the seasonal ice zone contributes to carbon outgassing in the southern portion of the ACC. This has implications for the response of the Southern Ocean carbon cycle to anthropogenic forcing, since reduced ice cover under ocean warming could potentially lead to a redistribution of carbon outgassing from the ASZ to the SIZ.

These results comprise the first observation-based carbon budget spanning large spatial scales and at monthly resolution in the high-latitude Southern Ocean. Strong seasonal variability in air-sea fluxes, as well as biological and advective fluxes of carbon, highlight the importance of year-round measurements in understanding carbon cycling in the region. These results also provide a much-needed observational baseline to evaluate the performance of climate models, which are notably unsuccessful in reproducing the Southern Ocean carbon cycle [Hauck et al., 2020]. Improved understanding of these processes is crucial given the key role of the Southern Ocean in the global climate system.

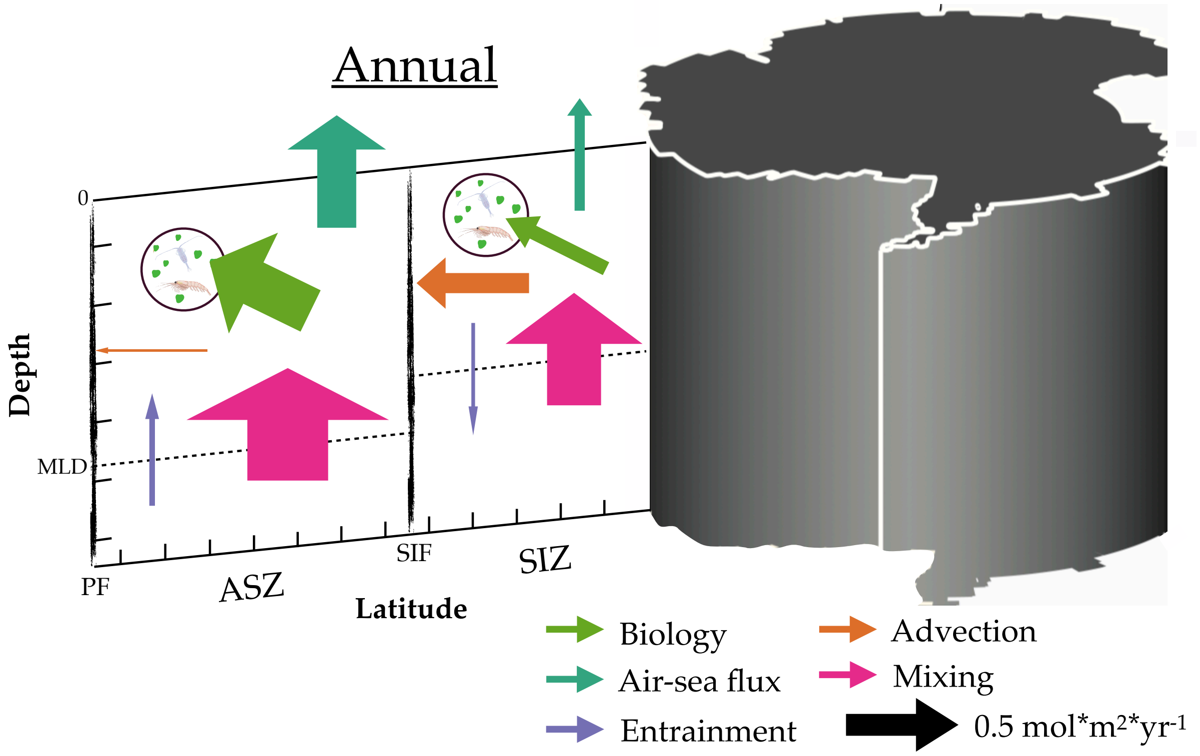

Figure 2.6: Schematic of the annually integrated fluxes of carbon where each colored arrow correspond to a different process by which the DIC content of the mixed layer can be modified. The green arrow represents the net effect of biological activity on mixed layer DIC content or the transfer of carbon between the inorganic and organic carbon (represented by the symbols in the circle) content of the mixed layer. The teal arrow represents the air-sea flux of carbon. The purple arrow corresponds to the entrainment flux of DIC. The orange arrow represents the net advective flux of DIC by Ekman, geostrophic and vertical advection. The pink arrow represents the eddy-driven mixing flux of DIC. The width of each arrow scales with the magnitude of the flux. (ASZ: Antarctic Southern Zone, SIZ: Sea Ice Zone)

Data availability statement

The Southern Ocean Carbon and Climate Observations and Modeling (SOCCOM) snapshot of quality-controlled data from 22 December 2020 [Southern Ocean Carbon and Climate Observations and Modeling Project, 2021] is available from the SOCCOM project at `http://doi.org/10.6075/J0B27ST5`. We also utilize the European Centre for Carbon Medium-Range Weather Forecasts (ECMWF) ERA5 atmospheric reanalysis product [Hersbach et al., 2021]and the Ocean Reanalysis System 5 (ORAS5)[Copernicus Climate Change Service, 2021] both available at `https://cds.climate.copernicus.eu/`. Other datasets used include the SeaFlux harmonized sea-air CO_2 fluxes [Gregor and Fay, 2021] available at `https://doi.org/10.5281/zenodo.5482547`, the Roemmich-Gilson Argo Climatology [Roemmich and Gilson, 2009], available at `https://sio-argo.ucsd.edu/RG_Climatology.html` and based on the Argo data [Argo, 2021], and the ETOPO1 Global Relief Model [NOAA National Geophysical Data Center, 2009] available at `http://dx.doi.org/10.7289/V5C8276M`.

Acknowledgments

This work was supported through National Science Foundation grants OPP-193622 (SOCCOM) and awards 1946578 (GO-BGC) and 2110258 (GO-BGC Operational Support). Additionally, we acknowledge the generous continuing support of NOAA through grant NA20OAR4320271 (US Argo). JS was also partly supported by a University of Washington Program on Climate Change fellowship. CJP also received funding through a NOAA Climate & Global Change Postdoctoral Fellowship. ARG acknowledges additional support from NSF through award OCE-1756882 and from the Department of Energy through Award DE-SC0022243. Profiling float data were collected and made freely available by the Southern Ocean Carbon and Climate Observations and Modeling (SOCCOM) Project funded by the National Science Foundation, Division of Polar Programs (NSF PLR-1425989), supplemented by NASA (NNX14AP49B), and by Argo and the NOAA programs that contribute to it. The Argo data were collected and made freely available by the International Argo Program and the national programs that contribute to it. (http://www.argo.ucsd.edu, http://argo.jcommops.org). The Argo Program is part of the Global Ocean Observing System. Generated using Copernicus Climate Change Service information [2021]. Input from B. Carter and N. Williams is gratefully acknowledged.

Chapter 3

Model Intercomparison and Observational Constraints for the Drivers of Southern Ocean Mixed-layer Carbon Fluxes

Abstract

The high latitude Southern Ocean plays a pivotal role in the global carbon cycle, acting as a key conduit for the exchange of carbon between the atmosphere and the deep ocean, yet it remains a region of pronounced uncertainty in both observational estimates and model predictions of air-sea carbon fluxes. Understanding the processes that underpin mixed-layer dissolved inorganic carbon (DIC) variability, the main driver of ocean $p\text{CO}_2$ in this region, is critical for improving Earth system models and projections of the global carbon cycle under climate change. In this study, we apply a process-based analysis of the seasonal cycle of mixed-layer DIC to a suite of global ocean biogeochemical models, a data-assimilating model (B-SOSE), and an observation-derived estimate from Argo floats using the framework of Sauvé et al. [2023]. By reconstructing mixed-layer budgets from standard model outputs, we directly compare modeled and observed drivers of DIC variability over the seasonal cycle. Across all datasets, vertical mixing consistently emerges as the dominant source of DIC to the mixed layer, while biological production acts as the primary sink. However, a key model bias is the weaker and delayed spring/summer biological drawdown of DIC relative

to observations, which results in a negative annually integrated entrainment flux in all models, opposite in sign to that inferred from float-based estimates. Though smaller in magnitude than mixing or biological terms, advective fluxes exhibit the greatest variability across models. These differences stem largely from the non-Ekman component of advection and can reverse the direction of vertical and horizontal transports, contrary to expectations based on known regional circulation patterns. Furthermore, we find that a stronger supply of DIC to the mixed layer is generally associated with enhanced DIC-driven $p\mathrm{CO}_2$ variability and, in some cases, increased air-sea carbon fluxes, though this relationship is strongly modulated by biological activity. These results underscore the need for models to accurately represent both physical transport and biogeochemical processes, particularly in the Southern Ocean, where persistent biases may otherwise compromise future climate projections. Our findings also highlight the value of seasonal, process-based diagnostics in revealing discrepancies that remain hidden in global or annual mean evaluations, offering a pathway toward improving the fidelity of Earth system models.

3.1 Introduction

The Southern Ocean, which surrounds Antarctica, plays a particularly important role in the global carbon cycle due to its unique circulation, which acts as a conduit between the atmosphere and the deep ocean. Indeed, this region is responsible for the absorption of about 40% of the anthropogenic carbon taken up by the ocean despite only representing about 20% of the global ocean surface [DeVries, 2014; Hauck et al., 2023; DeVries et al., 2023]. However, the uncertainty of the ocean carbon sink is highest in the Southern Ocean [Friedlingstein et al., 2025; Gloege et al., 2021], and the discrepancy between models and observations is also most significant there compared to other ocean basins [Hauck et al., 2020].

Models characterizing the processes coupling different components of the Earth system are essential to make predictions about the state of the climate system. They traditionally combine ocean, atmosphere, and sea ice components and are used to understand and predict the effects of physical processes. However, the biogeochemical processes that influence the exchange of carbon between the atmosphere, the land, and the ocean also play an important role in the global climate system. To predict future climate, we need to better understand the mechanisms by which carbon moves between these reservoirs. Earth System Models (ESMs) address this by explicitly simulating the cycling of biogeochemical tracers, such as carbon, through land ecology and ocean biogeochemistry components.

As part of the Coupled Model Intercomparison Project Version 6 (CMIP6) [Eyring et al., 2016], the Ocean Model Intercomparison Project (OMIP) provides a coordinated framework for evaluating ocean–sea ice models and their biogeochemical components. In OMIP, participating modeling centers force a coupled ocean–sea ice model of their choice with a common prescribed atmospheric dataset, ensuring consistency across simulations [Tsujino et al., 2020]. The atmospheric forcing, spanning 1948–2009 for OMIP1 and 1958–2018 for OMIP2, is applied repeatedly until the model fields stabilize [Griffies et al., 2016]. When biogeochemical components are included, models are also forced with historical atmospheric CO_2 concentrations and other tracers, following CMIP6 protocols and standardized guidelines for gas exchange and carbonate chemistry [Orr et al., 2017]. A key goal of OMIP is to assess how well models reproduce present-day variability in the carbon cycle and the mechanisms driving it, an essential step before examining how air–sea carbon fluxes may respond to climate change. By using prescribed atmospheric forcing, OMIP enables researchers to isolate and evaluate biases arising from the ocean and sea ice components directly, without the added complexity of a coupled, freely-evolving atmosphere. In doing so, OMIP complements fully coupled CMIP experiments and contributes to advancing climate research.

However, CMIP6 ESMs still suffer from several well-known biases found across most submitted models, particularly in the Southern Ocean. Biases in biogeochemical parameters are of particular interest for the study of carbon fluxes. In the Southern Ocean, these include overestimating surface chlorophyll, large errors in mean surface silicic acid [Séférian et al., 2020] and the broad range in predictions of biological primary production [Fisher et al., 2023]. Systematic biases in the surface ocean temperature and salinity [Beadling et al., 2020], as well as large errors in the sea ice extent, have also been identified. There have been very few studies of how these physical biases impact the modeling of carbon cycling in the Southern Ocean [Mongwe et al., 2018; Terhaar et al., 2021].

The evaluation of model skill is often based on the model mean state [Beadling et al., 2020]; however, there is evidence of important model biases in seasonal and inter-annual variability. Qu et al. [2022] found that inter-annual variability in carbon air-sea flux deviated most from observations in the Southern Ocean. While CMIP Phase 5 (CMIP5) models agree with observations on the annual mean CO_2 sink, they disagree with observations on the phasing of the seasonal cycle of air-sea carbon flux [Anav et al., 2013]. Further investigation by Mongwe et al. [2018] found that the cause of the discrepancy varied among models, with most suffering from exaggerated seasonal variations in surface temperature that were counterbalanced in some models by an exaggerated biological production.

The seasonal and regional variations in the ocean-atmosphere flux of carbon are primarily determined by oceanic $p\text{CO}_2$ [Takahashi et al., 2002]. Variations in ocean $p\text{CO}_2$ can be separated into a thermal and non-thermal component. While the temperature effect is very strong and dominates over most of the world oceans, south of the Subantarctic front, $p\text{CO}_2$ seasonality is driven primarily by the non-thermal component [Prend et al., 2022a; Gruber et al., 2019; Takahashi et al., 2002]. The non-thermal component is dominated by changes in dissolved inorganic carbon (DIC) concentration at the surface. Thus, mixed layer DIC (DIC_{ml}) variability is directly linked to high-latitude Southern Ocean air-sea carbon fluxes. Furthermore, it is essential to gain process understanding about the drivers of DIC variability in models in order to make progress towards their accurate representation.

Carbon budgets can be used to quantify the relative importance of different processes that drive DIC_{ml} variability. Budgets tracking the drivers of biogeochemical tracers (including DIC) have been constructed from model output, including from coupled models [Dufour et al., 2013; Hauck et al., 2013; Levy et al., 2013], ocean-only models [Nissen et al., 2021], idealized models [Bronselaer et al., 2018] and data-assimilating models [Carroll et al., 2022; Rosso et al., 2017; DeVries, 2014]. However, these model-based budgets often average the entire ocean south of a given latitude (usually 44°S). They are also computed over a fixed depth, frequently much deeper than the mixed layer, which limits their use for understanding the drivers of air-sea fluxes as the mixed layer is the part of the water column that can interact with the atmosphere. These modeling studies show that both biological and physical processes drive DIC variations, but no clear quantitative agreement has been reached about the leading order terms.

Of specific note, few studies have looked at modeled DIC seasonal variability. This knowledge gap may be partially explained by the rarity of seasonally resolved observations of DIC_{ml} and its fluxes. Most previous work involving more than one model only considered the annual mean or seasonal variability of carbon air-sea fluxes [Li et al., 2022; Qu et al., 2022; Mongwe et al., 2018]. The few studies that have looked at Southern Ocean DIC mostly looked at surface DIC [Lerner et al., 2021] or the annual or multi-year averaged DIC in a single model [Yool et al., 2021; Tjiputra et al., 2020]. However, no studies have taken a process-based approach to evaluate the OMIP or CMIP ensemble of models in terms of mixed-layer DIC fluxes.

The observation-based budget framework developed by Sauvé et al. [2023] offers a unique opportunity to investigate the processes driving mixed-layer biogeochemical tracer variability in CMIP-class ocean models. By combining profiling Argo float data with a mixed-layer budget approach, this framework estimates the different fluxes that contribute to seasonal changes in DIC$_{ml}$. Importantly, the framework can also be applied to model output. Usually, biogeochemical tracer budgets based on model output require online flux computation for each tracer. When available, this output can be used to compute a closed tracer budget, where each flux is accounted for to machine precision (with additional loss of precision due to any averaging from the original model time step). However, tracer budget output is not always available, especially for biogeochemical variables, and cannot be extracted offline. The framework from Sauvé et al. [2023] requires only standard model output provided by most OMIP or CMIP participants (Table D.1 for required output).

In this study, we use this framework to compare seasonal carbon budgets across a suite of OMIP models, a data-assimilating model (B-SOSE), and an observation-derived mixed-layer DIC budget based on profiling float data from Sauvé et al. [2023]. By examining the full seasonal cycle, we aim to disentangle the respective roles of physical and biological processes in controlling DIC variability and to assess whether the drivers of DIC changes are consistent across models and with observations. Ultimately, this process-based comparison seeks to advance our understanding of what controls mixed-layer DIC variability on seasonal to annual timescales in the Southern Ocean and how faithfully these drivers are represented in the models that underpin climate change projections. We find that while mixing and biological production are respectively the largest source and sink of DIC to the mixed layer in all datasets, models differ from observations in the sign of the entrainment flux, due in part to a weaker and delayed spring phytoplankton bloom. Furthermore, the largest intermodel spread is found in the advection and the air-sea flux.

3.2 Methods

3.2.1 Study Region

The tracer content budget is estimated for two distinct Southern Ocean zones defined by an Antarctic Circumpolar Current (ACC) front, maximum sea ice extent, and bathymetry (Figure 3.1). The Antarctic Southern Zone (ASZ) encompasses the southern half of the ACC, bounded by the Polar Front to the north and the September 15% sea ice area contour to the south (the sea ice edge (SIE)). The Sea Ice Zone (SIZ), which experiences seasonal ice cover, lies south of the sea ice edge but excludes Antarctic coastal areas (as defined by the 1000 m isobath). This zonal definition aligns with previous studies [Gray et al., 2018; Bushinsky et al., 2019; Prend et al., 2022a; Dufour et al., 2015].

The Polar front is often defined based on the Orsi et al. [1995] criteria which uses the 2 °C contour at the minimum potential temperature of the top 200 m. To account for model-to-model variability in temperature, we employ a new method for determining the Polar Front, combining the Orsi et al. [1995] temperature criteria and sea surface height (SSH) gradients as seen in the work of Dufour et al. [2015] and Le Chevère et al. (under review). We identify the maximum SSH gradient within 4 ° of latitude north of the 2 °C isotherm, for 10 topographically-constrained locations where the Polar Front exhibits strong SSH gradients (labeled longitudes in Figure 3.1). We average the SSH values at these 10 locations and use the contour of the resulting mean SSH to define the PF. Unlike Sauvé et al. [2023], we apply this approach to annually-averaged data to maintain constant zone areas throughout the analysis period.

3.2.2 Ocean Biogeochemical Models

We analyze output from four OMIP models (Table 3.1) and one state estimate (Table 3.2): the Meteorological Research Institute Earth System Model Version 2.0 (MRI-ESM2.0) [YUKIMOTO et al., 2019], the Australian Community Climate and Earth System Simulation Ocean Model Version 2 (ACCESS-OM2) [Kiss et al., 2020], the Canadian Earth System Model Version 5 (CanESM5) [Swart et al., 2019], the Norwegian Earth System Model Version 2 Low Resolution (NorESM2-LM) [Tjiputra et al., 2020], and the Biogeochemical Southern Ocean State Estimate (B-SOSE) [Verdy and Mazloff, 2017]. All OMIP models are 1 ° resolution coupled ocean-sea ice systems with ocean biogeochemical cycling components, forced

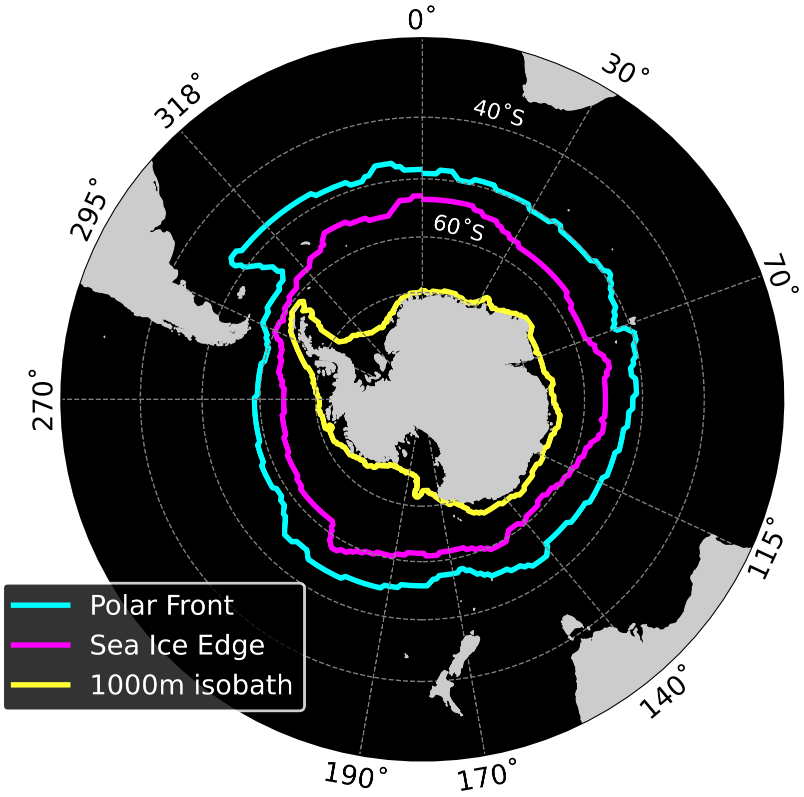

Figure 3.1: Map of the study region. The Polar front (PF - cyan) defines the northern edge of the Antarctic Southern Zone (ASZ) and the sea ice egde (SIE - magenta), its southern edge. The Sea Ice Zone is located between the SIE and the 1000 m isobath (yellow). The longitude values labelled on the map correspond to topographically-constrained locations where the Polar Front exhibits strong SSH gradients, which we use to determine the position of the Polar front following Dufour et al. [2015] (see Section 3.2.1). Note that the PF and SIE plotted are from CanESM5 (Figure F.2 for all models).

with atmospheric reanalysis and following standardized spin-up and initializing protocols [Griffies et al., 2016; Orr et al., 2017]. All OMIP models analyzed have relatively simple biogeochemical components (Table 3.1). We selected these models because they provide all required outputs in a regularly gridded format compatible with our budget framework.

We utilize OMIP1 (CanESM5, MRI-ESM2-0 and NorESM2-LM) and OMIP2 (ACCESS-OM2, MRI-ESM2-0 and NorESM2-LM) outputs, which follow similar protocols with key differences in forcing datasets [Tsujino et al., 2020]. OMIP1 requires five repeated cycles of the 62-year CORE forcing (1948-2009) from Large and Yeager [2009], while OMIP2 requires six cycles of the 1958-2018 JRA55-do forcing dataset v1.4.0 [Tsujino et al., 2020]. Additional differences include varied sea surface salinity restoration baselines and possible differences in the magnitude of the relative wind (the difference between ocean and atmospheric current at the surface) that is used for flux calculations. By analyzing both OMIP1 and OMIP2 simulations, we assess the influence of forcing datasets and simulation years on our results, allowing for a broader and more robust interpretation.

Model output availability varies between OMIP1 and OMIP2 participants. For OMIP2 (available monthly until 2018), we average over 2014-2018 to reduce natural variability effects and align with available B-SOSE output. For OMIP1 (available until 2009), we use the 2005-2009 period. To assess how different averaging periods affected our results, we examined the OMIP2 submissions of NorESM2-LM and MRI-ESM2-0 for 2005-2009 (Figure F.24). We found that the differences between OMIP1 and OMIP2 were larger than the differences caused by using different time periods. We attribute this to differences in model setup between OMIP1 and OMIP2 and, therefore, treat the OMIP1 and OMIP2 submissions as distinct models.

In addition to OMIP models, we utilize output from the Biogeochemical Southern Ocean State Estimate (B-SOSE) [Verdy and Mazloff, 2017], a 1/6 ° physical-biogeochemical data-assimilating model of the Southern Ocean covering 2013 to 2023, and forced by 6-hourly ERA5 reanalysis [Hersbach et al., 2020]. B-SOSE assimilates observational data and maintains closed tracer budgets through the adjoint method, minimizing weighted least-squares misfits between model solutions and observations. Data sources include biogeochemical Argo floats [Riser et al., 2016, 2018], instrumented Southern elephant seals [Charrassin et al., 2010] and other platforms [Rosso et al., 2017], and assimilated variables include temperature, salinity, oxygen, nitrate and pH. B-SOSE has a biogeochemical component of intermediate-complexity with 3

Table 3.1: Model descriptions for the four OMIP models used in this study, including grid details, biogeochemical components, and references.

Model name	**MRI-ESM2.0**	**ACCESS-OM2**	**CanESM5**	**NorESM2-LM**
Label	MRIo1, MRIo2	ACCo2	CANo1	NORo1, NORo2
Institution	Meteorological Research Institute (Japan)	Consortium for Ocean-Sea Ice Modelling in Australia	Canadian Centre for Climate Modelling and Analysis	Norwegian Climate Center
Time period for analysis	2005–2009[1], 2014–2018[2]	2014–2018[2]	2005–2009[1]	2005–2009[1], 2014–2018[2]
Horizontal Grid	Structured (B) tripolar	Structured (C) tripolar	Structured (C) tripolar	Structured (C) tripolar
Ocean-sea ice model	MRICOM4	MOM5 and CICE5	canNEMO and LIM2	BLOM and CICE5
Ocean Resolution	1° lon × 0.5° lat	1° lon × 1° lat	1° lon × 1° lat	1° lon × 1° lat
Ocean vertical coord.	Free-surface (z*) with 60 levels	Free-surface (z*) with 50 levels	Free surface (z) with 45 levels	51 isopycnal layers; Hybrid z–s2 with 53 levels
BGC model	NPZD (1P,1Z) (NO_3, PO_4)	WOMBAT, NPZD (1P,1Z) (NO_3, PO_4, Fe)	CMOC (1P,1Z) (NO_3)	iHAMOCC, NPZD (1P,1Z) (NO_3, PO_4, SiO_4, Fe)
Atmospheric forcing	6-hourly Large and Yeager (2009)[1], 3-hourly JRA55-do atmospheric reanalysis[2]	3-hourly JRA55-do atmospheric reanalysis[2]	6-hourly Large and Yeager (2009)[1]	6-hourly Large and Yeager (2009)[1], 3-hourly JRA55-do atmospheric reanalysis[2]
Variant label	r1i1p1f1[1,2]	r1i1p1f1[2]	r1i1p2f1[1]	r1i1p1f1[1,2]
References	YUKIMOTO et al. [2019]	Kiss et al. [2020]	Swart et al. [2019]	Tjiputra et al. [2020]; Seland et al. [2020]
Necessary model output	areacello, deptho, thetao, so, dissic, o2, siconc, zos, fgco2, fgo2, wfo, umo, vmo, tauuo, tauvo (Table D.1 for more details).			

[1] OMIP1, [2] OMIP2

Table 3.2: Model description for B-SOSE, including grid details, biogeochemical components, and references.

Model name	**B-SOSE**
Organization	The Southern Ocean Carbon and Climate Observations and Modeling (SOCCOM) Project
Time period for analysis	2018^1, $2014–2018^2$
Grid extent	30°S – 78°S
Horizontal Grid	Mercator
Ocean-sea ice model	MITgcm and ECCO
Ocean Resolution	1/6° lon × 1/6° lat
Ocean vertical coord.	52 levels
BGC model	N-BLING (3P, 9PT)
Atmospheric forcing	6-hourly ERA5 [Hersbach et al., 2020]
References	Verdy and Mazloff [2017]

[1] For method validation (see Section 3.3).

[2] For comparison with OMIP models (see Section 3.4).

phytoplankton groups and 9 prognostic tracers. We use B-SOSE for two purposes: (1) validating our budget framework methodology by leveraging its closed budget term outputs, and (2) comparing with OMIP models for the 2014-2018 period. As a data-assimilating model, B-SOSE bridges the gap between lower-resolution OMIP models and the observation-based budget framework of Sauvé et al. [2023].

Both OMIP models and B-SOSE offer complementary strengths for our analysis. OMIP simulations follow international protocols, though these protocols may limit output availability. B-SOSE, while limited to the Southern Ocean, assimilates biogeochemical data and provides comprehensive output for closed biogeochemical budgets. We gain broader insights into Southern Ocean biogeochemical dynamics by utilizing both approaches.

3.2.3 Budget Framework

Compared to float observations, the comprehensive spatial coverage of model output enables several framework improvements over the original Sauvé et al. [2023] approach which we describe in this section. The framework provides an estimate of the change in DIC_{ml} and oxygen (O_2) content over time (the tendency (*Tend*)) and quantifies contributions from various physical and biological processes (Eq. 3.1). Note that the framework requires coupled DIC and O_2 budgets in order to estimate parameters which are challenging to estimate directly from model output.

$$\text{Tend} = F_{entrain} + F_{horiz-adv} + F_{vert-adv} + F_{air-sea} + F_{mixing} + F_{bio} \tag{3.1}$$

The processes represented in Eq. 3.1 can be categorized as physical or biological. Physical processes include gaseous exchange with the atmosphere ($F_{air-sea}$), vertical ($F_{vert-adv}$) and horizontal advection ($F_{horiz-adv}$) of tracer-rich waters into/out of the mixed layer, entrainment/detrainment of water during mixed layer deepening/shoaling ($F_{entrain}$), and eddy-driven mixing across the mixed layer base (F_{mixing}) [Levy et al., 2013]. Biological processes involve DIC or oxygen O_2 transformation through photosynthesis and organic matter remineralization by (F_{bio}). The framework does not include calcium carbonate formation/dissolution effects on DIC_{ml} content.

We estimate averaged contributions of different mixed layer fluxes across entire frontal regions to leverage available model output and to obtain process-based insight applicable to a broad spatial and time scale.

We adapt the approach of Sauvé et al. [2023] by treating each horizontal model cell as a float profile and calculating mixed layer averages at each cell location. For each model cell and for each month, we calculate density using the Gibbs Sea-Water Oceanographic Toolbox for Python [McDougall and Barker, 2011], first determining the absolute salinity and conservative temperature. We compute in-situ density (ρ) and potential density anomaly from these values with a reference pressure of 0 dbar. We use the mixed layer depth output, calculated online based on a density criteria and provided by each modeling center.

The tendency term (*Tend*) represents the time rate of change of tracer content within the mixed layer. The entrainment flux ($F_{entrain}$) captures the impact of mixed layer depth changes: deepening incorporates underlying water and increases tracer content proportionally to concentrations below the mixed layer, while shoaling reduces mixed layer volume and tracer content proportionally to mixed layer concentration. Both tendency and entrainment are calculated using centered differences.

We refine the entrainment calculation method of Sauvé et al. [2023] to better align with the tendency estimation in the model. This refinement accounts for the dominance of the tendency and entrainment terms over other fluxes, reflecting the fact that much of the mixed layer tracer content change is driven by volume changes during entrainment and detrainment. As a result, examining the difference between the tendency and entrainment terms, which corresponds to the time rate of change of mixed layer tracer concentration multiplied by mixed layer depth (see Sauvé et al. [2023], Eq. 7), allows for comparison on a scale more directly comparable to other flux terms. For tendency calculations, the approach Sauvé et al. [2023] calls for multiplying mixed layer averaged tracer concentration by mixed layer depth on a cell-by-cell basis before spatial averaging and time differentiation. We modify the method for entrainment to align with this. We multiply the time derivative of mixed layer depth by the tracer concentration of entrained/detrained waters for each cell before zonal averaging, unlike Sauvé et al. [2023] who used zonally-averaged mixed layer depth and tracer concentration profiles. Because cell-by-cell entrainment cannot be computed from the float data, we keep the original method for the observation-based results shown in Section 3.4. For the models, these refinements ensure a more accurate representation of the critical balance between the tendency and entrainment terms, capturing the same scales of variability and the same spatial extent.

In the Southern Ocean, cross-frontal (largely meridional) horizontal advection ($F_{horiz-adv}$) includes Ekman transport (northward due to strong westerly winds) and geostrophic flow contributions. Using total mass transport model output, we integrate cross-front mass flux along frontal boundaries and multiply the resulting total mass transport by the averaged tracer concentrations at the front rather than using zone-averaged source water concentrations like in Sauvé et al. [2023]. This modification significantly improves accuracy for O_2 advection at the sea ice edge, where front-averaged and zone-averaged seasonal cycles vary substantially. We use wind stress output from each model to determine the integrated total Ekman transport across the front and use it to separate the Ekman and non-Ekman components of the advection. Note that for the observation-based estimate, we use an updated version of the gridded product of geostrophic velocity used by Sauvé et al. [2023] (in prep, available on request to Alison R. Gray) to determine the geostrophic transport across the front, which we add to an estimate of the Ekman transport based on wind stress. The updated geostrophic velocity product incorporates satellite-derived surface geostrophic velocities from altimetry, along with an improved mapping method. It also integrates trajectory velocities following Zilberman et al. [2023] and expands the dataset to include the most recent observations.

Vertical advection ($F_{vert-adv}$) at the mixed layer base depends on vertical velocity and tracer concentration of advected waters. For consistency with the observation-based budget and to ensure that the mass budget closes, we determine zone-averaged monthly-mean vertical velocity using a mixed layer mass budget derived from the density advection-diffusion equation, which shares many terms with the biogeochemical budget equation:

$$\text{Tend} = F_{entrain} + F_{surface} + F_{horiz-adv} + F_{vert-adv} \tag{3.2}$$

The surface flux of mass ($F_{surface}$) depends on precipitation, evaporation, and sea ice melt and freeze. We enhance vertical advection estimates by calculating tracer concentration below the mixed layer cell-by-cell before zonal averaging, rather than using a zone-averaged profile and mixed layer depth as in Sauvé et al. [2023].

The air-sea flux ($F_{air-sea}$) is calculated as the average ocean-atmosphere tracer exchange per unit area (mol m^{-2} day^{-1}) for each frontal region. Vertical mixing (F_{mixing}) represents processes involving tracer concentration gradients between the mixed layer and underlying waters, typically parameterized using vertical eddy diffusivity (κ). It differs from vertical advection because there is no exchange of mass. Finally, the biological flux term (F_{bio}) captures the net contribution of all biological activity, i.e. photosynthesis and respiration, on mixed layer tracer concentrations.

Without direct model output for biological and mixing processes, we use a system of 24 equations (12 monthly budget equations, each for DIC and O_2) to solve for missing parameters as in Sauvé et al. [2023]. We couple these equations by assuming an annually constant vertical eddy diffusivity at the mixed layer base for both tracers. We also couple both sets of 12 equations using the respiratory quotient which allows us to convert the biological flux of oxygen to the biological flux of carbon [Robinson, 2019]. We have modified the solution method for the 24-equation system used to determine vertical eddy diffusivity and monthly biological flux. While Sauvé et al. [2023] employed a standard least-squares formulation, we instead normalize the error in our system using a block-normalized mean squared error (NMSE), calculated separately for oxygen and carbon to account for differences in their magnitudes and distribute any error more evenly between the two tracers. We constrain the monthly biological flux of carbon to be negative, effectively assuming no net respiration occurs in the mixed layer. This assumption aligns with the B-SOSE closed budget. We validate this assumption for each OMIP model, by examining (when output is available) the wintertime total primary production of organic carbon by all phytoplankton and the total phytoplankton expressed as chlorophyll concentration (Figure F.12) and find that biological activity is near zero in winter (Section 3.4.1).

We minimize the block NMSE using the Limited Memory Broyden–Fletcher–Goldfarb–Shanno algorithm for bound-constrained optimization (L-BFGS-B) [Byrd et al., 1995], implemented via the Python SciPy package. L-BFGS-B is a gradient-based method that efficiently handles problems with simple bounds and performs well with smooth, deterministic objective functions, reducing the risk of convergence to local minima, a common issue with derivative-free methods. In practice, we find that our optimization results are consistent across different initial conditions for all models.

In contrast to Sauvé et al. [2023], we fix the value of the respiratory quotient, which links biological fluxes of oxygen and carbon, to –1.4 rather than treating it as an unknown. This value closely approximates the Redfield ratio (–138/106 = –1.3) and corresponds to the effective respiratory quotient in the B-SOSE closed budget as well as in three other models [Paulmier et al., 2009]. We find that the optimization outcomes are sensitive to the specified respiratory quotient. Although observation-based respiratory quotients can range from -1.6 to –0.8 [Moreno et al., 2020], most coupled biogeochemical circulation models assume constant stoichiometric elemental ratios [Paulmier et al., 2009]. Since we are less certain of the respiratory quotient for the observation-based estimate, we do not impose a particular respiratory quotient or a maximum value for the biological flux in our iteration of the observation-based results.

To complement the DIC budget, we partition the model $p\mathrm{CO}_2$ seasonal cycle into contributions from temperature, salinity, DIC, and alkalinity, following the approach of Takahashi et al. [2014] (see also Sarmiento and Gruber [2006] and Prend et al. [2022b]). This method uses the first-order terms of a Taylor expansion to relate changes in $p\mathrm{CO}_2$ to corresponding changes in temperature, salinity, DIC, and alkalinity. While this linear approximation is strictly valid only for small perturbations, we apply it to seasonal anomalies, defined as deviations from the annual mean.

3.3 Budget Framework Validation using B-SOSE

The budget framework offers a method to evaluate mixed layer tracer dynamics using standard model output, but it cannot perfectly account for all processes affecting mixed layer content. With access to B-SOSE's complete flux terms computed online during model integration, we can validate our budget framework, described in Section 3.2.3 and computed using offline output, against a fully closed budget where all sources and sinks are exactly accounted for with minimal residuals. We use monthly output from iteration 155 of B-SOSE for 2018, downloaded from `https://sose.ucsd.edu/SO6/ITER155/` (Table D.2 for complete variable list) to compute both a closed budget based on budget terms computed online during model run time, and the budget framework following the method described in Section 3.2.3.

For the closed budget, both monthly averages and monthly snapshots (instantaneous values at period boundaries) are utilized. We define the mixed layer using B-SOSE's mixed layer depth output computed online based on a density criterion. Attempting to use a mixed layer depth computed using the monthly-averaged temperature and salinity output introduced closure issues, particularly near coasts and deep convection regions like the Weddell Sea.

We determine the extensive budget terms for each tracer (DIC and O_2) : Tendency, Entrainment, Advection, Mixing, Air-sea flux, and Biology (detailed methodology in Appendix D). These represent the same processes as shown in Eq. 3.1 from the budget framework but are computed online during the model run instead of estimated from monthly output. In the closed budget, tendency and entrainment are computed using forward differences of snapshot output, while other terms derive from monthly-averaged fluxes. We aggregate each budget term within our defined zones (bounded by the Polar Front, sea ice edge, and 1000 m depth contour), and calculate the residual by subtracting the Tendency from the sum of all other terms. For comparison with the budget framework, we normalize each term by the appropriate zonal area to obtain fluxes in mol m^{-2} day^{-1}.

After computing the closed budget and framework estimate, we determine monthly absolute errors for each term (Figure 3.2 c) and calculate root mean squared errors across the seasonal cycle for each term/zone/tracer combination (Table 3.3). These values, applied as a percentage based on the magnitude of the flux in each OMIP model, provide an estimate of the error on the OMIP fluxes computed with the budget framework. While this approach represents the most robust quantification available given the constraints of our methodology, we recognize that uncertainties remain in our error assessment.

Table 3.3: Absolute error in mmol m^{-2} day^{-1} for each budget term, separated by zone and tracer. This absolute error is used to define error bars for the budget framework (Figures F.15 to F.20). The absolute errors are converted to relative error using the averaged value of each framework term for B-SOSE (see the value in parentheses, in %) and then applied to the OMIP models relative to the magnitude of their fluxes.

Tracer	Region	Tend-Ent	Advection	Mixing	Biology	Air-Sea Flux
DIC	ASZ	1.43 (16)	2.66 (103)	3.30 (36)	2.39 (22)	0.0003 (0.03)
	SIZ	2.46 (20)	2.20 (46)	12.28 (48)	12.94 (55)	0.0001 (0.004)
O_2	ASZ	1.73 (20)	1.04 (34)	7.00 (80)	3.37 (22)	0.0083 (0.03)
	SIZ	3.51 (38)	1.42 (55)	24.71 (107)	18.09 (55)	0.0014 (0.004)

units: mmol m^{-2} day^{-1} (%)

Our validation against B-SOSE's closed budget confirms the framework's ability to capture key biogeochemical processes in the Southern Ocean mixed layer, while highlighting specific limitations and uncertainties. Framework accuracy varies by term, zone, and tracer. Error analysis reveals several patterns in framework performance. Generally, errors are larger in the SIZ than in the ASZ, with mixing and biological flux estimates showing the greatest discrepancies across tracers and zones (Figure 3.2 a, c for the ASZ, and b, d for the SIZ).

The mixing flux error stems directly from our parameterization approach. Following Sauvé et al. [2023], we represent mixing using a time-invariant vertical eddy diffusivity multiplied by the vertical tracer gradient at the mixed layer base. This parameterization struggles with DIC mixing, which shows minimal sea-

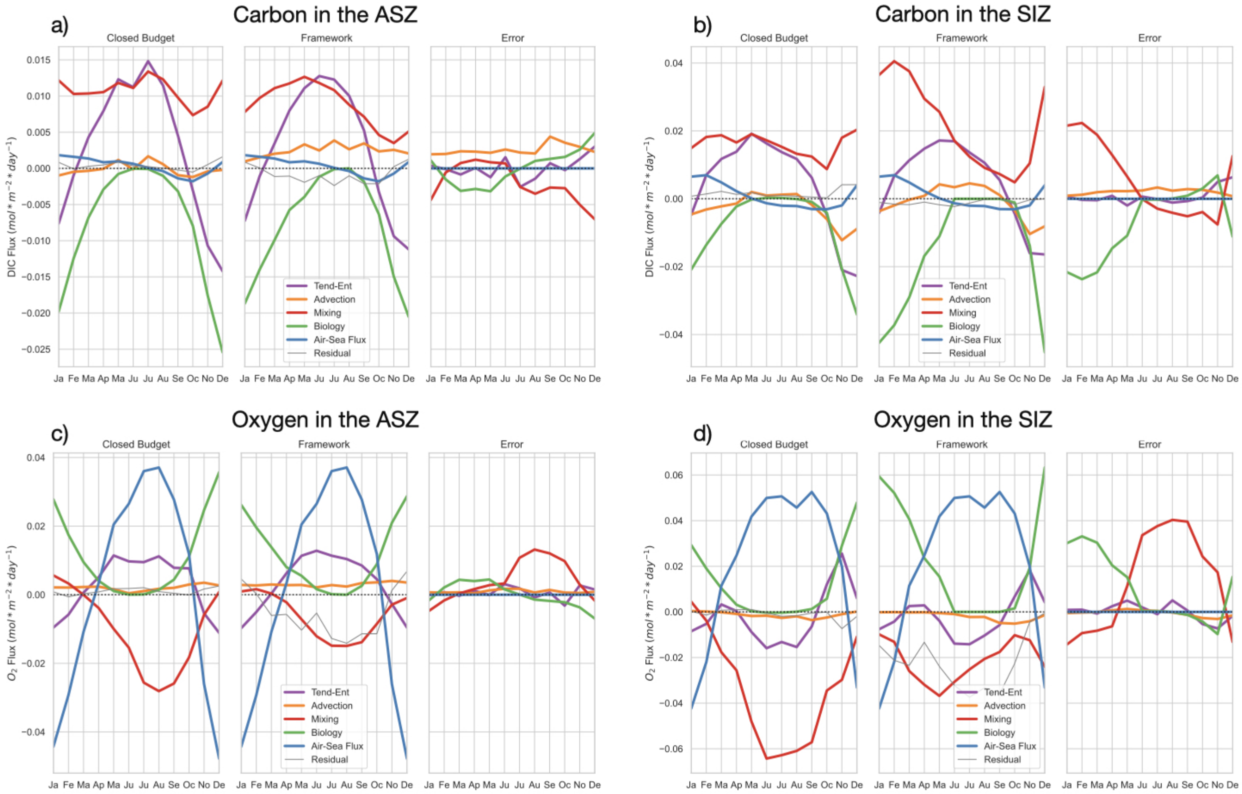

Figure 3.2: DIC (a and b) and O_2 (c and d) budget results for the closed budget (left frame), the budget framework (middle frame), and the difference between them (right frame) for the Antarctic Southern Zone (ASZ, a and c) and the Sea Ice Zone (SIZ, b and d). Tend-Ent corresponds to the tendency minus the entrainment flux. Positive fluxes indicate that DIC is added to the mixed layer.

sonal variation in the closed budget despite significant vertical gradient changes. The issue is particularly pronounced in the SIZ, where seasonal vertical gradient variations are larger. The mixing flux does vary seasonally for oxygen, but accurately capturing SIZ dynamics would require both time-varying vertical diffusivity and gradient considerations, which our parameterization lacks. This limitation affects both tracers since our optimization scheme couples oxygen and carbon budgets through the respiratory quotient. The biological flux error is also related to our optimization approach. With both vertical eddy diffusivity and biological flux as unknowns, our algorithm necessarily balances errors between these terms, introducing compensating biases in biological flux estimates.

Framework-estimated advective fluxes systematically exceed closed budget values. In the ASZ, the closed budget shows net DIC advection oscillating around zero annually, while our framework consistently estimates positive values. This discrepancy occurs despite good agreement in individual horizontal and vertical advection components (Figure F.23 a). In the SIZ, while seasonal patterns match better, the framework still overestimates net DIC advection year-round, though horizontal and vertical components are underestimated from August to October (Figure F.23 c).

In-depth investigation revealed that assuming spatially-constant time-varying mixed layer depth (as our framework does) omits important contributions to horizontal advection at the mixed layer base in the SIZ due to latitudinal mixed layer depth gradients. However, this assumption simultaneously neglects a counterbalancing vertical advection contribution from areas with deeper-than-average mixed layers, resulting in similar net advection magnitude and seasonality in the SIZ. In the ASZ, short-term variations eliminated by offline advection computation using averaged output differ between horizontal and vertical components, causing framework estimates to incorrectly represent net advective flux direction. This limitation represents a known challenge in offline estimates that depend on time-dependent fields as they can miss temporal correlations [Griffies et al., 2016].

Despite these limitations, the budget framework successfully reproduces major seasonal patterns in DIC and O_2 budgets across both zones. For DIC, both methods show that seasonal variations in mixed layer concentration (*Tend-Ent*) are primarily driven by biological processes, with mixing consistently adding DIC throughout the year. Air-sea exchange and advection have smaller magnitudes in the seasonal DIC budget. Similarly for oxygen, both methods identify that mixed layer concentration changes from the combined effects of air-sea exchange, biological processes, and mixing, with advection having less influence. Both methods also produce higher flux magnitudes in the SIZ compared to the ASZ. Our validation confirms that the budget framework successfully captures the features and driving mechanisms of Southern Ocean mixed layer biogeochemistry, providing confidence for its application to OMIP model analysis while appropriately acknowledging uncertainties.

3.4 Results

We focus on the Antarctic Southern Zone because we note more intermodel differences in this zone. All results shown will be for this zone.

3.4.1 Controls on Mixed Layer DIC Variability over the Seasonal Cycle

Models have different mean DIC_{ml} concentrations, with the OMIP1 models strictly smaller than the OMIP2 models (Figure 3.3 a). This is expected due to additional anthropogenic carbon uptake by the ocean between 2009 and 2014. However, there is still variability in the DIC_{ml} among models from a particular OMIP project. MRIo2 has the highest annually averaged DIC_{ml} concentration of OMIP2 models, and ACCo2 the lowest. We identify this difference throughout the seasonal cycle and for the whole Southern Ocean going back at least as far as the year 2000 (Figure F.3). As such, it is beyond the scope of this project to explain why this difference is present. We assume it is something intrinsic to the models or their spin-up protocol.

Of more immediate relevance to seasonal variability in mixed layer DIC is the DIC anomaly, defined as the deviation from each dataset's annual mean. Both the models and the float-based observational estimate show a broadly consistent seasonal cycle: DIC_{ml} increases in fall and winter and decreases in spring and summer (Figure 3.3 b). However, the amplitude and timing of this cycle differ across datasets. Most strikingly, the float-based estimate shows relatively higher DIC in winter and spring, and lower DIC in summer, resulting in a larger overall seasonal amplitude. In addition, observed maximum mixed layer depth and temperature are generally lower than in the models, except for B-SOSE, whose mixed layer depth closely follows the observations (Figure 3.3 c, d). Among models, there are differences in maximum mixed layer depths that correlate with their average DIC_{ml} concentrations (Figure 3.3 a, c).

The different seasonal pattern in DIC between models and observations is evident when analyzing the

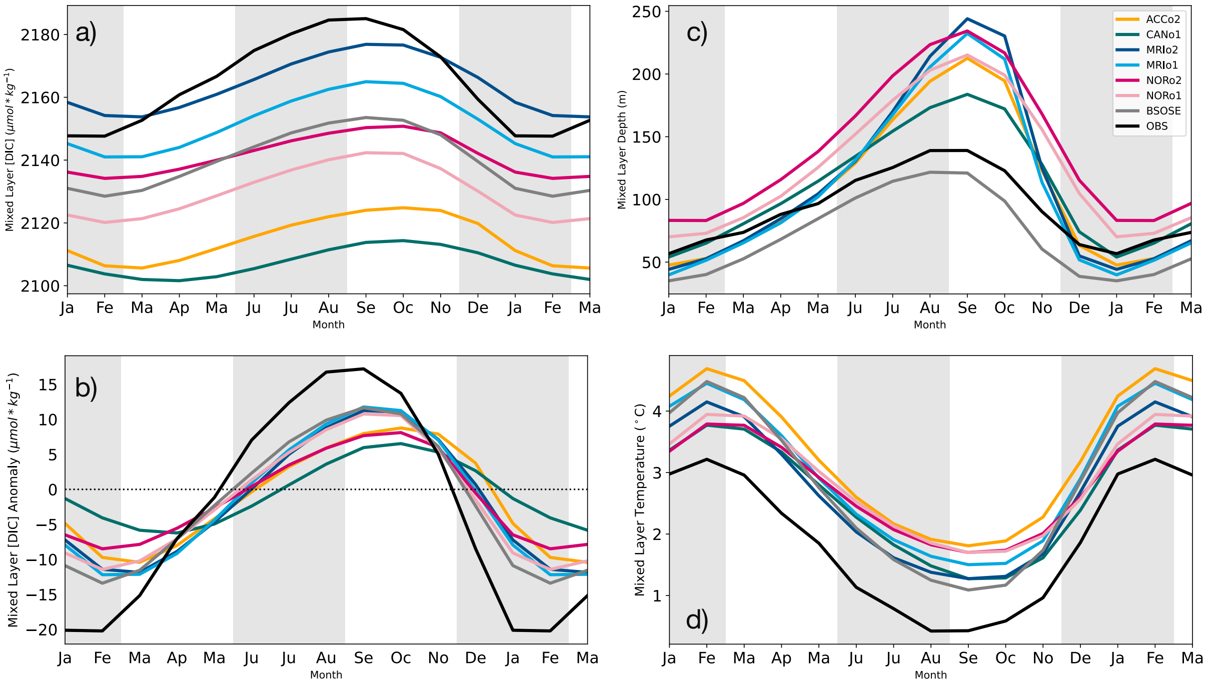

Figure 3.3: a) Seasonal cycle of the zone-averaged DIC$_{ml}$ concentration for all datasets. b) Seasonal cycle of the anomaly from the annual mean of the zone-averaged DIC$_{ml}$ concentration for all datasets. c) Seasonal cycle of the zone-averaged mixed layer depth for all datasets. d) Seasonal cycle of the zone-averaged mixed layer temperature for all datasets. (OBS: Float-based values)

tendency of DIC content minus the entrainment flux (*Tend-Ent*), which represents the rate of change of DIC_{ml} concentration scaled by mixed layer depth (Figure 3.4 a). Since mixed layer depth is always positive, positive values of *Tend-Ent* reflect increasing DIC concentrations, while negative values indicate a decrease. Across models, *Tend-Ent* shows a remarkably consistent seasonal cycle, with positive values in fall and winter and a sharp decline in spring and summer. This consistency likely reflects the models' broadly similar seasonal cycles of DIC_{ml} concentrations and mixed layer depth (Figure 3.3 b, c). The float estimate captures an earlier and steeper increase in DIC concentrations during fall and a correspondingly earlier, sharper decline in spring (Figure 3.4 a). Additionally, the magnitude of the *Tend–Ent* term is larger in the float-derived estimate, highlighting a larger amplitude to its seasonal cycle than what is simulated by the models.

Biological processes emerge as the primary driver of the seasonal transition from DIC accumulation to depletion and vice versa. In the observation-based estimate, this transition occurs when the biological flux turns negative, indicating net biological production, and intensifies rapidly (Figure 3.4 b and F.13). Although the models also show a switch to a negative biological flux between September and November, the sharp increase in biological production seen in the float-based estimate is delayed by at least one month in most models. In some cases (ACCo2, CANo1, MRIo1, MRIo2), the biological flux never undergoes rapid decline. In December, the peak biological flux from the float-based estimate not only reaches a larger negative magnitude more abruptly than in the models but also declines sharply shortly afterward. Among the models, NOR and B-SOSE capture a biological production peak that occurs at roughly the same time as in observations, while others (ACCo2, MRIo1, MRIo2) show a delayed peak, and CANo1 shows no clear seasonal maximum.

Because the biological and mixing fluxes are derived through optimization, they carry greater uncertainty and are prone to biases in both magnitude and seasonal cycle. As shown for B-SOSE (Section 3.3), the mixing flux can be distorted by the framework's fixed vertical eddy diffusivity, especially in models like MRI with large seasonal DIC concentration gradient amplitude (Figure 3.8). Errors in the mixing flux can propagate to the biological flux, since the two are linked in the optimization balance (Section 3.2.3). Therefore, the coincident peaks in biological production and DIC concentration gradient in MRI models may partly reflect methodological artifacts.

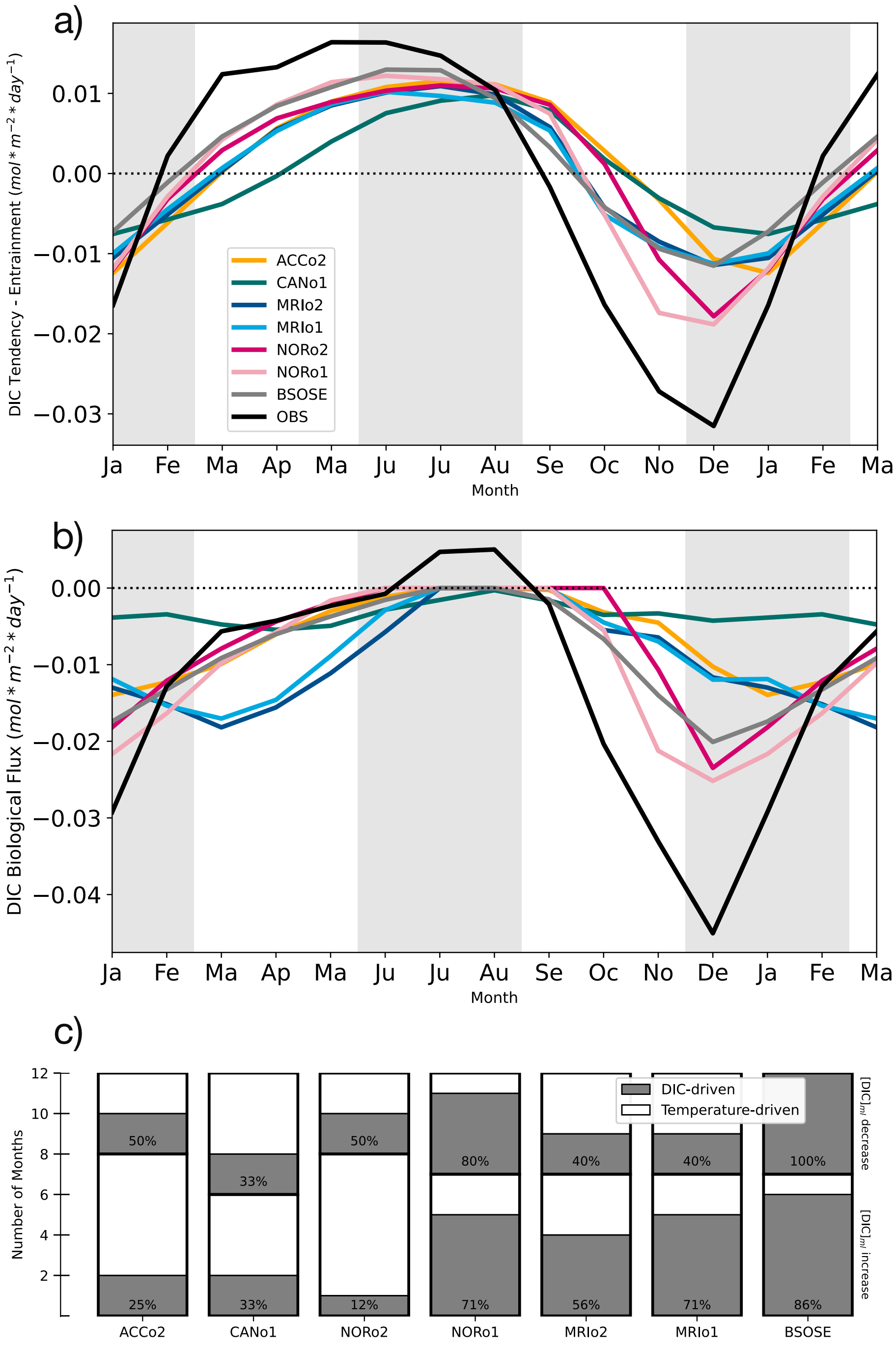

Figure 3.4: a) Seasonal cycle of the DIC Tendency minus Entrainment flux for all datasets. This budget term is equivalent to the change in the DIC$_{ml}$ concentration multiplied by the mixed layer depth. Note that we repeat January through March and that the gray shading highlights austral Summer and Winter. b) Seasonal cycle of the biological flux of DIC into the mixed layer for all datasets. Negative values indicate that the flux acts to remove DIC from the mixed layer. c) Stacked bar graph indicating the number of months in the periods of DIC$_{ml}$-increase and -decrease. The shaded parts of the bars, as well as the percentage, indicate the proportion of months which saw DIC-driven pCO$_2$ change during each period. (OBS: Float-based estimate)

While direct validation of mixing flux estimates is difficult, we examine proxies for biological flux available in the model output. We analyze zone-averaged organic carbon production by phytoplankton for all models except CANo1 (Figure F.12 a). As phytoplankton production likely dominates the seasonal cycle, we expect it to reflect biological flux variability. Models with stronger (weaker) maximum production generally show stronger (weaker) net biological flux, with both peaking in summer. An exception is the MRI models, which peak in November, suggesting aliasing effects from the optimization scheme used here. For CANo1, we assess chlorophyll concentration in the upper 100 m (Figure F.12 b), finding a distinct seasonal cycle with a May peak, consistent with its DIC biological flux and supporting the credibility of the derived biological DIC flux despite its outlier behavior.

All datasets exhibit broadly consistent seasonal patterns in DIC_{ml} concentration change, marked by increases during fall and winter and decreases during spring and summer. However, the models diverge from the float-derived estimate in both the timing and magnitude of these changes. In particular, most models show delayed biological production peaks and lack the sharp intensification of biological activity that appears critical in driving the observed seasonal shift from DIC accumulation to depletion. These discrepancies suggest that even when models reproduce the overall seasonal DIC pattern, they may misrepresent the timing and dynamics of the processes controlling it.

3.4.2 Drivers of Annual-Mean Mixed Layer DIC

Despite the apparent similarity in the models' *Tend-Ent* term (Figure 3.4 a), the underlying mechanisms driving DIC_{ml} changes over the annual cycle vary across models. Analysis of annually integrated carbon fluxes reveals that biological and mixing fluxes dominate in magnitude but oppose each other in all datasets (Figure 3.5). Mixing with DIC-rich waters at the base of the mixed layer acts as a carbon source, while net biological production serves as a carbon sink by consuming DIC. The contributions from advection, entrainment, and air-sea flux remain smaller in comparison across all datasets (note that the tendency integrates to zero over the annual cycle).

Our iteration of the observation-derived DIC budget from [Sauvé et al., 2023] reveals that all physical processes at the base of the mixed layer (mixing, entrainment, and advection) supply DIC to the mixed layer. While biological production consumes the majority of this DIC, a portion is also outgassed to the

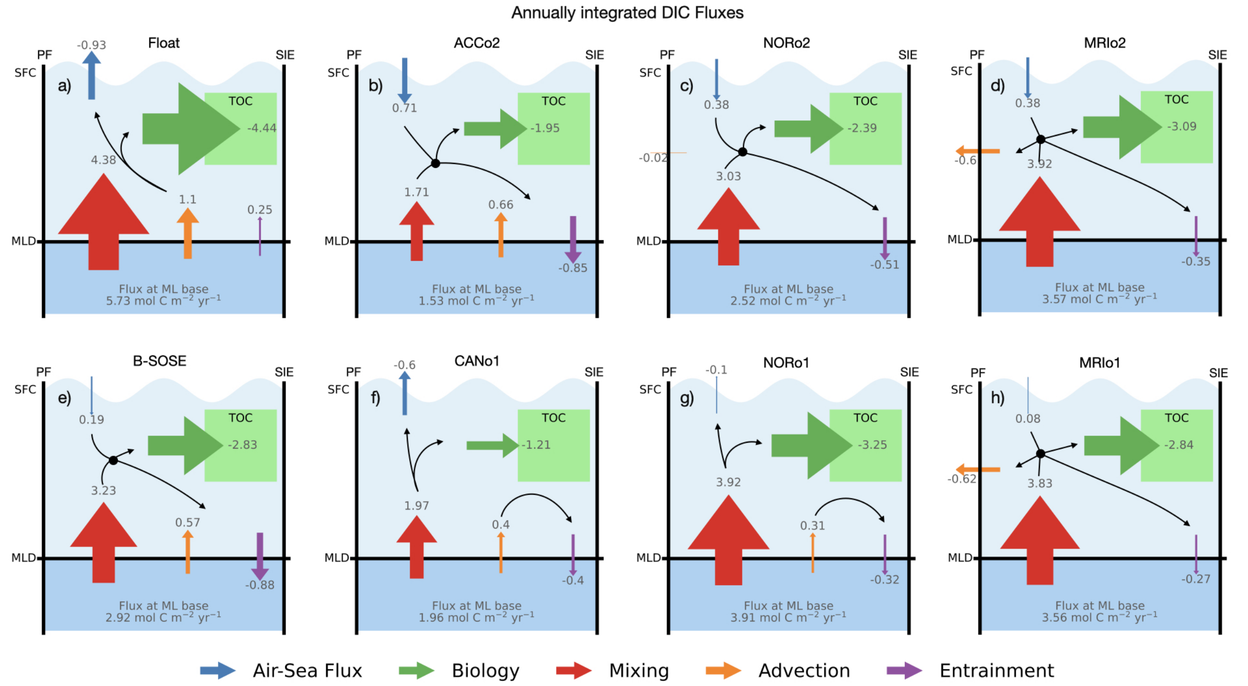

Figure 3.5: Annually integrated fluxes of DIC shown in a schematic view (Figure F.21 for a barplot) for a) the observation-based estimate, b) ACCo1, c) NORo2, d) MRIo2, e) B-SOSE, f) CANo1, g) NORo1 and h) MRIo1. Each flux is represented by a colored arrow. Black arrows are a visual aid to visualize the flow of DIC through the mixed layer. Note that the tendency integrates to 0 for the year and that positive flux values indicate DIC is added to the mixed layer. (SFC: Surface, MLD: Mixed Layer Depth, PF: Polar Front, SIE: Sea Ice Edge, TOC: Total Organic Carbon, ML: Mixed Layer)

atmosphere. Model-derived carbon budgets, however, present a contrasting picture: entrainment acts as a DIC sink rather than a source, though mixing with carbon-rich water at the mixed layer base remains the primary carbon supply mechanism (Figure 3.5).

We identify three distinct model groups based on the relative balance between entrainment and advective fluxes. Entrainment-balanced models (CANo1 and NORo1) feature negative entrainment fluxes counterbalanced by positive advective fluxes of similar magnitude. This results in carbon outgassing modulated by net biological production strength. Entrainment-dominated models (B-SOSE and ACCo2) exhibit positive advective fluxes weaker than the entrainment fluxes, driving surface carbon uptake with magnitude modulated by the strength of DIC supply at the mixed layer base: ACCo2 shows greater uptake than B-SOSE due to its weaker mixing flux. Finally, double-sink models (MRIo1, MRIo2, and NORo2) display negative fluxes for both entrainment and advection, also demonstrating ocean carbon uptake modulated by the relative contributions of the different fluxes.

We seek to understand why the entrainment flux is negative in the models but positive in the observation-based estimate. To do so, we examine the relative seasonal evolution of the two components of advection: the mixed layer depth tendency ($d(\text{MLD})/dt$) and the DIC concentration of entrained or detrained waters ($\text{DIC}_{ent/det}$) (Section 4.2.3). The normalized $d(\text{MLD})/dt$, where we subtract the annual mean and divide by the standard deviation, shows similar behavior across all datasets, with gradual deepening from late summer to late winter and rapid shoaling in spring (Figure 3.6 a). In contrast, the float-derived $\text{DIC}_{ent/det}$ is higher than in the models from March to June (when the mixed layer deepens) and lower from October to December (when it shoals rapidly) (Figure 3.6 b). This seasonal offset mirrors the differences seen in the *Tend-Ent* term between floats and models (Figure 3.4 a). The larger amplitude of the float-based $\text{DIC}_{ent/det}$ suggests that entrainment adds more DIC during deepening and detrainment removes less during shoaling. This is consistent with the pattern in annual entrainment flux since a negative entrainment flux means that detrainment removes more DIC than entrainment supplies, given our assumption of zero net storage.

To investigate this further, we average the normalized $\text{DIC}_{ent/det}$ separately over the periods of entrainment and detrainment. For the float-based estimate, the average DIC concentration of entrained waters (DIC_{ent}) is nearly identical to that of detrained waters (DIC_{det}), whereas all models show a markedly higher DIC_{det} than DIC_{ent} (Figure 3.6 c). B-SOSE, which exhibits the most negative annual entrainment flux

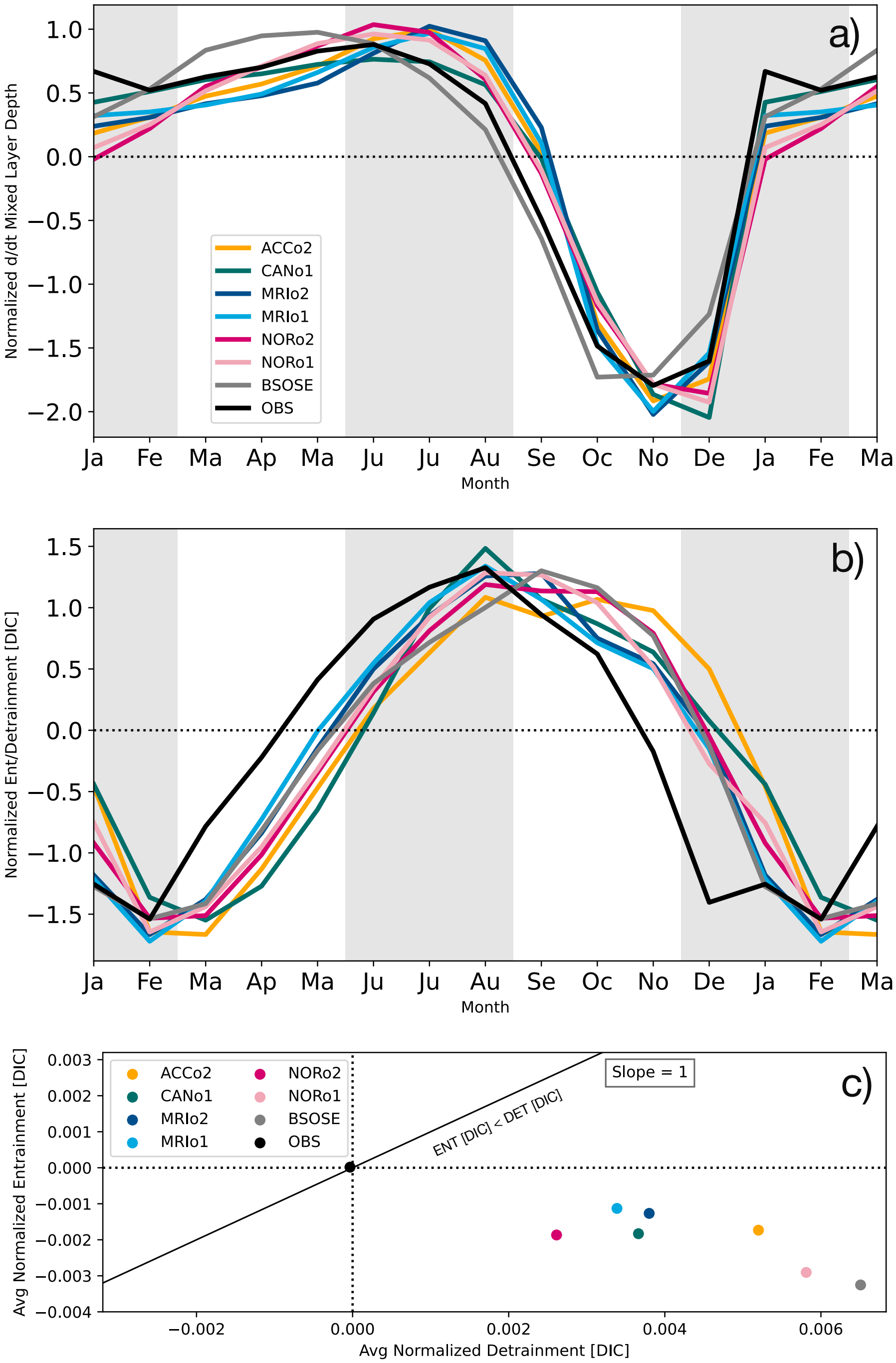

Figure 3.6: a) Normalized time derivative of the mixed layer depth for all datasets. b) Normalized DIC concentration in entrained or detrained waters ($\mathrm{DIC}_{ent/det}$) for all datasets. c) Scatter plot of the normalized $\mathrm{DIC}_{ent/det}$ averaged over periods of entrainment ($d(\mathrm{MLD})/dt$>0, determined separately for each model) against the normalized $\mathrm{DIC}_{ent/det}$ averaged over periods of detrainment for all datasets. The black 1:1 line shows where the $\mathrm{DIC}_{ent/det}$ during entrainment would be equal to the $\mathrm{DIC}_{ent/det}$ during detrainment. Note that we normalize by subtracting the time mean and dividing by the standard deviation.

(Figure 3.5 e), also shows the largest DIC$_{det}$–DIC$_{ent}$ difference (0.0098 mol m^{-3}). However, this average difference alone does not fully explain the spread in annually integrated entrainment fluxes. For example, NORo1 has the second largest DIC$_{det}$–DIC$_{ent}$ difference (0.0087 mol m^{-3}) but one of the smallest annual entrainment fluxes. Since the normalized $d(\text{MLD})/dt$ is similar across models, we infer that the spatial patterns of DIC$_{ent}$ and DIC$_{det}$ must interact with local variations in $d(\text{MLD})/dt$ in ways not captured by spatial averages. For instance, regions with higher DIC$_{det}$ coinciding with larger amplitude MLD variations, and vice versa, could amplify the negative annual entrainment flux.

3.4.3 Drivers of Mixed Layer DIC Concentration Increase and Decrease

While examining the full seasonal cycle helps reveal the overall balance of processes controlling DIC$_{ml}$, this integrated perspective can also obscure key details. All models predict a negative annual entrainment flux, driven by higher detrainment DIC compared to entrainment DIC, which implies that *Tend-Ent* during detrainment is smaller in magnitude than during entrainment. To better understand the processes responsible for the seasonal increase in DIC$_{ml}$ (when *Tend-Ent* > 0) during fall and winter, and its decrease in spring and summer (Figure 3.4 a), we integrate the DIC fluxes over these respective periods for each model (Figure 3.4 c shows the relative duration of each period by model). We find that the float-based estimate exhibits DIC$_{ml}$ changes that are, on average, 1.5 times larger than the models during the increasing period and 2.4 times larger during the decreasing period. Furthermore, there is spread among models in the drivers of surface ocean pCO$_2$ variability during each period, with some models being dominated by solubility effects (ACCo2, CANo1, NORo2) and others by DIC variability (NORo1, MRIo1, MRIo2, B-SOSE) (Figure 3.4 c).

During the period of DIC$_{ml}$ increase, all models exhibit a smaller *Tend-Ent* and a weaker DIC supply from the base of the mixed layer compared to the float-derived estimate (Figure 3.7). We also observe a correlation between more prevalent DIC-driven pCO$_2$ variability and a relatively larger DIC supply from below, suggesting that enhanced subsurface supply may be key for non-thermal processes to dominate pCO$_2$ variability. This DIC supply is primarily driven by mixing fluxes, with some models also showing a smaller contribution from advection. However, the link between mixed layer DIC supply and surface outgassing is further influenced by the magnitude of the biological flux.

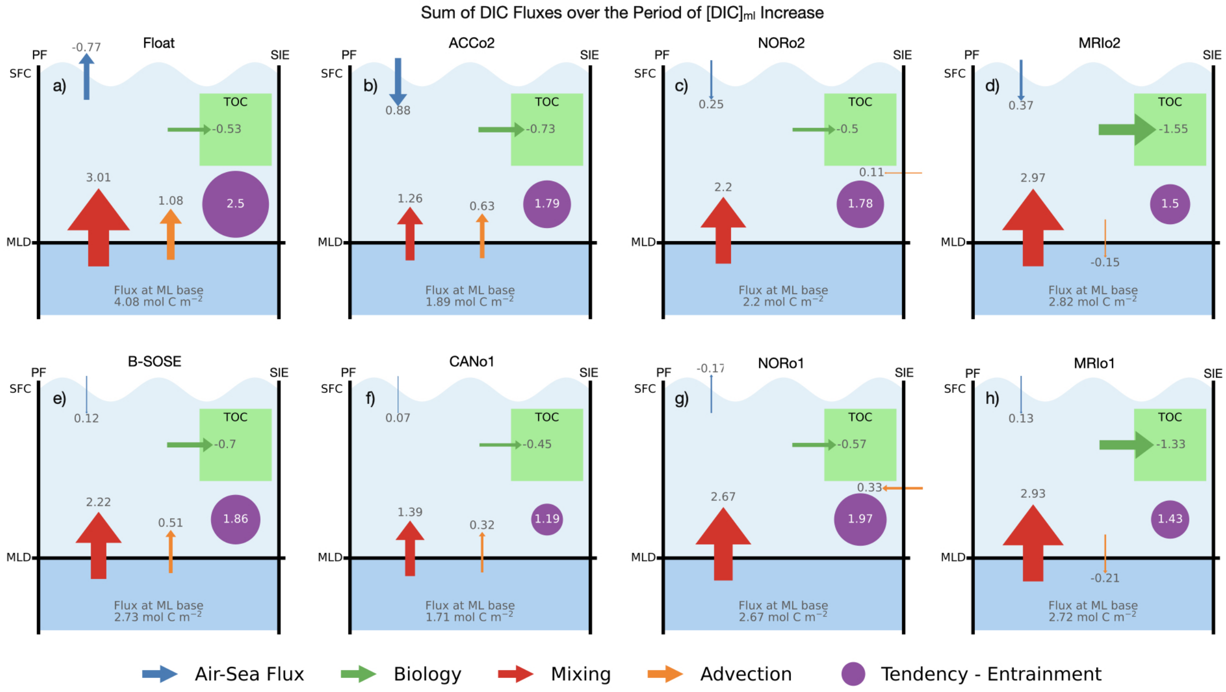

Figure 3.7: Fluxes of DIC integrated over the period of DIC_{ml}-increase as determined by *Tend-Ent* > 0 in each dataset for a) the observation-based estimate, b) ACCo1, c) NORo2, d) MRIo2, e) B-SOSE, f) CANo1, g) NORo1 and h) MRIo1. Each flux is represented by a colored arrow and positive flux values indicate DIC is added to the mixed layer. The purple circle represents the magnitude of the *Tend-Ent* and positive values indicate mixed layer DIC concentration is increasing. (SFC: Surface, MLD: Mixed Layer Depth, PF: Polar Front, SIE: Sea Ice Edge, TOC: Total Organic Carbon, ML: Mixed Layer)

In the float-derived budget, DIC enters the mixed layer primarily through mixing with DIC-rich subsurface waters, supplemented by an advective flux dominated by upwelling (Figure 3.7 a). A small portion of this DIC (8%) is consumed by net biological production, while the majority either escapes to the atmosphere through outgassing (25%) or contributes to the rise in DIC$_{ml}$ (60%). The percentages do not sum to 100% due to the framework residual, which is omitted from the schematic but shown in Figures F.13–F.20 along with estimated uncertainties for each budget term. Among all datasets, the float-derived estimate shows the strongest DIC$_{ml}$ increase (1.3 to 2.1 times larger than the models) and the largest subsurface DIC supply (1.5 to 2.4 times greater). It is also one of only two datasets to capture outgassing during this period.

We find that the reasons for reduced DIC supply at the mixed layer base vary among models, and we again identify three distinct groups, though with some differences from the previous section. In entrainment-dominated models (ACCo2, B-SOSE), the smaller DIC supply results from weaker mixing and advective fluxes compared to the float-derived estimate (Figure 3.7 b and e). B-SOSE has one of the largest total flux of DIC at the mixed layer base among models (Figure 3.7 e) and predicts a small amount of DIC-driven CO_2 uptake by the ocean. ACCo2, in contrast, has a much smaller DIC supply at the mixed layer base due to a weaker mixing flux (Figure 3.7 b), yet still ranks third among models for DIC$_{ml}$ increase because this supply is supplemented by strong CO_2 uptake from the atmosphere. CANo1 also shows reduced mixing and advection (Figure 3.7 f) but stands out as an outlier with the smallest values for nearly every term (Figure 3.7 f). Its period of DIC$_{ml}$ increase also begins several months later than in the other datasets.

Both MRI models predict a weaker DIC supply at the mixed layer base, primarily due to net downwelling (Figure 3.7 d and h). Although their mixing fluxes are similar in magnitude to the float-derived estimate, the negative advection offsets this supply. This effect is compounded by their large biological fluxes, which consume about 50% of the DIC supplied at the mixed layer base, compared to around 25% in most models and just 13% in the float-derived estimate. Consequently, both MRI models exhibit modest DIC$_{ml}$ increases (larger only than CANo1) despite ranking among the top three for total base supply, and predict weak, DIC-driven atmospheric carbon uptake.

Both NOR models predict a reduced DIC supply at the mixed layer base, primarily due to weaker mixing (Figure 3.7 c and g). However, unlike the MRI models, their negative vertical advection is smaller and offset by a positive horizontal advection, leading to an additional DIC source associated with horizontal transport convergence. Despite this, the positive advective flux remains modest, being 3 to 10 times smaller than the float-derived net advection and 2 to 5 times smaller than the upwelling-driven advection in the entrainment-dominated models. With this added advective source, NORo1 stands out among models with the largest DIC supply (excluding atmospheric fluxes), the largest DIC$_{ml}$ increase, and as the only model to predict carbon outgassing to the atmosphere. This outgassing is DIC-driven, though smaller in magnitude than for the float-based estimate. In contrast, NORo2 shows nearly balanced vertical and horizontal advection, resulting in a weaker DIC supply and a smaller DIC$_{ml}$ increase compared to NORo1. It also predicts a modest solubility-driven carbon uptake. Overall, the NOR models seem to occupy an intermediate position between entrainment-balanced and double-sink models during the DIC$_{ml}$ increase period. Nonetheless, we still observe a consistent link between a larger DIC supply at the mixed layer base and a DIC-driven air-sea carbon flux.

The 2.4-fold range in mixing fluxes across datasets arises from the combined effects of vertical DIC gradients and vertical eddy diffusivities. All datasets except CANo1 exhibit a positive mixing flux that peaks in fall and reaches a minimum in late spring (Figure 3.8 a), with the greatest divergence in magnitude occurring in fall (3x difference), coinciding with the onset of the DIC$_{ml}$ increase. The float-derived estimate maintains a larger annually integrated mixing flux, mainly because its spring decline is smaller than in the models (except NORo1, which closely follows the observations). This stronger mixing flux in the float estimate results from its pronounced vertical DIC gradient at the mixed layer base, despite having the smallest eddy diffusivity of all datasets (Figures 3.8 b and c). The MRI models generate strong mixing during the DIC$_{ml}$ increase period by having the steepest gradients (800–1000 μmol m^{-4}) early in the season, despite moderate diffusivities. In contrast, the NOR models achieve strong mixing by combining average gradients with the highest diffusivities (38–45 m^2 day^{-1}). These differences highlight that not all models generate mixing fluxes for the same reasons: some rely on steep gradients, others on high diffusivities, and some on a combination of both.

During the period of DIC$_{ml}$ decrease, *Tend-Ent* is negative across all datasets, reflecting the seasonal depletion of DIC (Figure 3.9). As with the accumulation phase, the magnitude of this depletion is larger in the observation-based estimate than in the models. However, while the float-derived estimate shows stronger depletion than accumulation (–2.72 mol C m^{-2} vs. 2.5 mol C m^{-2}), the models show the opposite pattern:

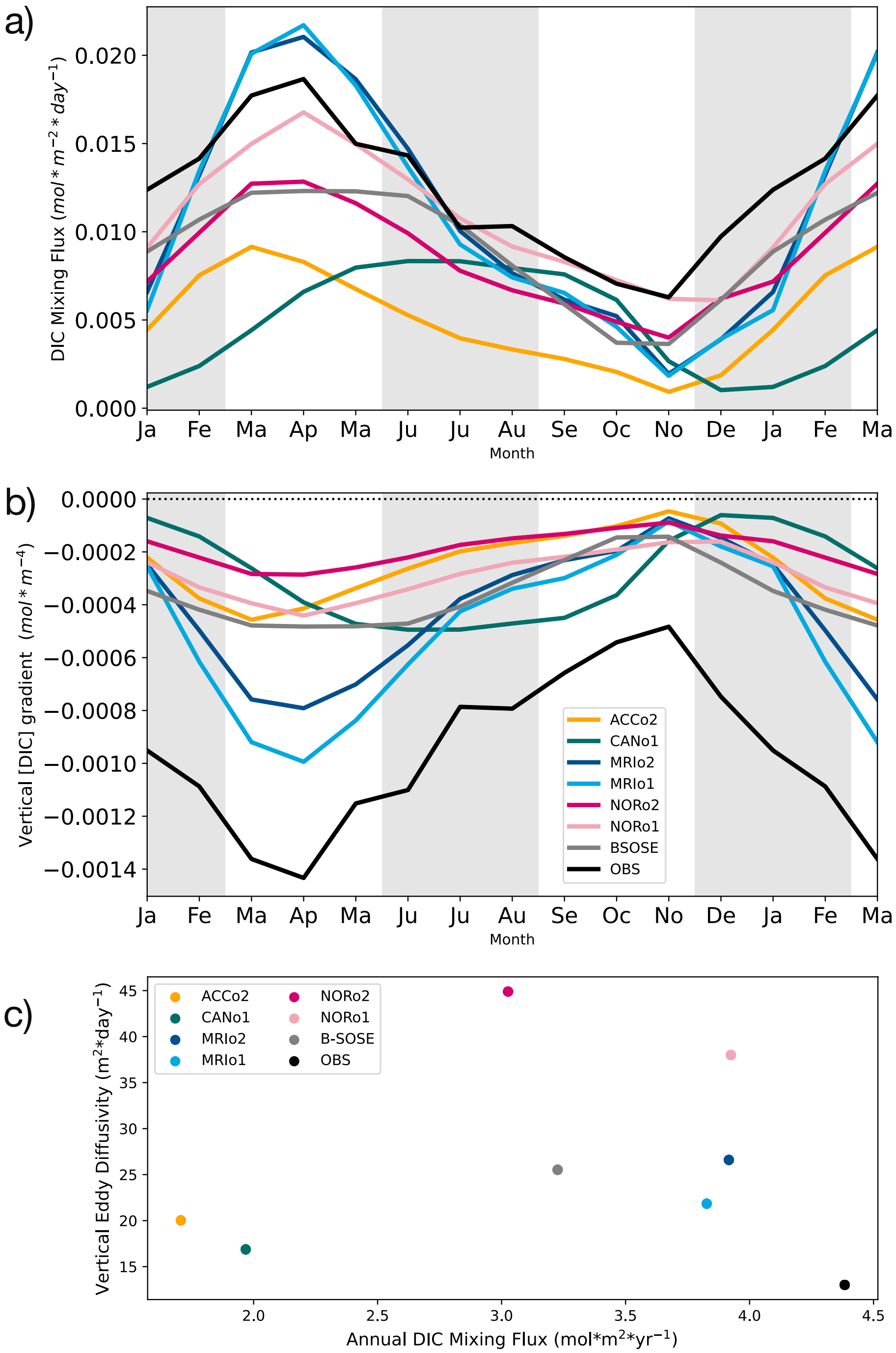

Figure 3.8: a) Seasonal cycle of the mixing flux of DIC into the mixed layer for all datasets. Positive values indicate DIC is added to the mixed layer b) Seasonal cycle of the zone-averaged vertical gradient in DIC concentration at the base of the mixed layer for all datasets. c) Scatter plot of the vertical eddy diffusivity against the annually integrated mixing flux of DIC for all datasets.

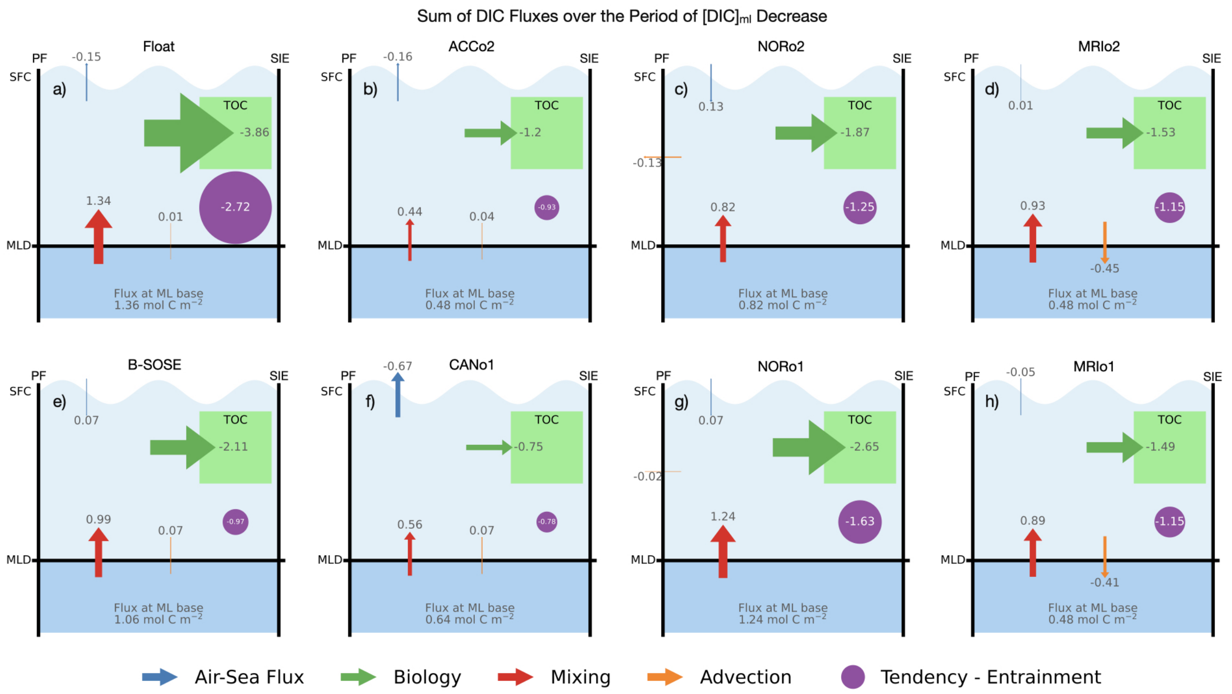

Figure 3.9: Fluxes of DIC integrated over the period of DIC_{ml}-decrease as determined by *Tend-Ent* < 0 in each datasets for a) the observation-based estimate, b) ACCo1, c) NORo2, d) MRIo2, e) B-SOSE, f) CANo1, g) NORo1 and h) MRIo1. Each flux is represented by a colored arrow and positive flux values indicate DIC is added to the mixed layer. The purple circle represents the magnitude of the *Tend-Ent* and negative values indicate mixed layer DIC concentration is decreasing.(SFC: Surface, MLD: Mixed Layer Depth, PF: Polar Front, SIE: Sea Ice Edge, TOC: Total Organic Carbon, ML: Mixed Layer)

depletion is weaker than accumulation (–1.12 mol C m^{-2} vs. 1.64 mol C m^{-2} on average across models) (Figure 3.9 and 3.7). This behavior aligns with the models' negative net entrainment flux compared to the positive flux in the float estimate. When comparing the difference in magnitude between floats and models for the two periods, we find the gap is larger during the DIC_{ml} decrease phase, suggesting that the weaker depletion in models is a key contributor to their more negative annual entrainment flux. Specifically, models show DIC_{ml} increases that are 1.3 to 2.1 times smaller than the float estimate, but decreases that are 1.7 to 3.5 times smaller.

For all datasets, the seasonal decrease in DIC_{ml} is primarily driven by strong net biological production, which dominates over all DIC sources. This biological production is weaker in models than in the float-derived estimates, consistent with the models having weaker and delayed spring biological production (Figure 3.4 b and Section 3.4.1). Although mixing with DIC-rich waters at the base of the mixed layer continues to supply carbon during this period, the role of air-sea flux and advection in either counteracting or reinforcing the biological drawdown varies across datasets.

OMIP models show large intermodel spread in carbon air-sea flux that extend beyond simple magnitude variations to include opposite flux directions and contrasting seasonal patterns (Figure 3.10). ACCo2, CANo1, MRIo1, and MRIo2 show carbon uptake by the ocean in winter and outgassing in summer while NORo1, B-SOSE and the float-derived estimate have the opposite pattern. NORo2 is unique in its pattern, peaking in winter and summer, and never outgassing. Interestingly, the absolute magnitude of the float-derived air-sea flux is greater than most of the models (MRIo1, MRIo2, NORo2, B-SOSE) except CANo1 and ACCo2 which have similar magnitude but the opposite sign (Figure 3.10). Because of this wide range of seasonal cycle shapes among models, integrating over the period of DIC$_{ml}$ decrease leads to a wide range of carbon air-sea flux contributions, including positive and negative values. In the float-derived budget, we observe net carbon outgassing, driven by significant outgassing in spring followed by uptake in summer (Figure 3.9 a and 3.10). Two models, NORo1 and B-SOSE, predict a small net carbon uptake that reflects a combination of spring outgassing and summer uptake, similar to the float estimate (Figure 3.9 e, g, and 3.10). Both MRI models show near-zero annual air-sea flux (negative for MRIo1, positive for MRIo2), but unlike NORo1 and the float estimate, this results from spring uptake offset by summer outgassing. NORo2 stands out by predicting the largest carbon uptake, as it shows sustained uptake throughout the entire period (Figure 3.9 c and 3.10). By contrast, ACCo2 and CANo1 predict continuous outgassing, with CANo1 featuring a prolonged *Tend-Ent* < 0 period extending into mid-fall (Figure 3.9 b, f, 3.10 and 3.4 a).

The observation-derived advective flux is near zero, reflecting a balance of positive and negative contributions over the period (Figure 3.9 a). Although advection is not the largest term in the budget, it significantly influences differences among models. Entrainment-dominated models (ACCo2, B-SOSE) and CANo1 exhibit a small positive advective flux, driven by net upwelling, similar to the float estimate (Figure 3.9 b, e, f). In these models, this flux acts as an additional DIC source that partially offsets the biological sink and these models have the smallest DIC$_{ml}$ decrease. In contrast, the double-sink models (MRIo1, MRIo2, NORo2) and NORo1 have negative advective fluxes that reinforce biological drawdown (Figure 3.9 c, d, g, h), resulting in the largest DIC$_{ml}$ decreases among models. The MRI models experience downwelling-dominated advection that removes about half of the DIC supplied by mixing, while the NOR

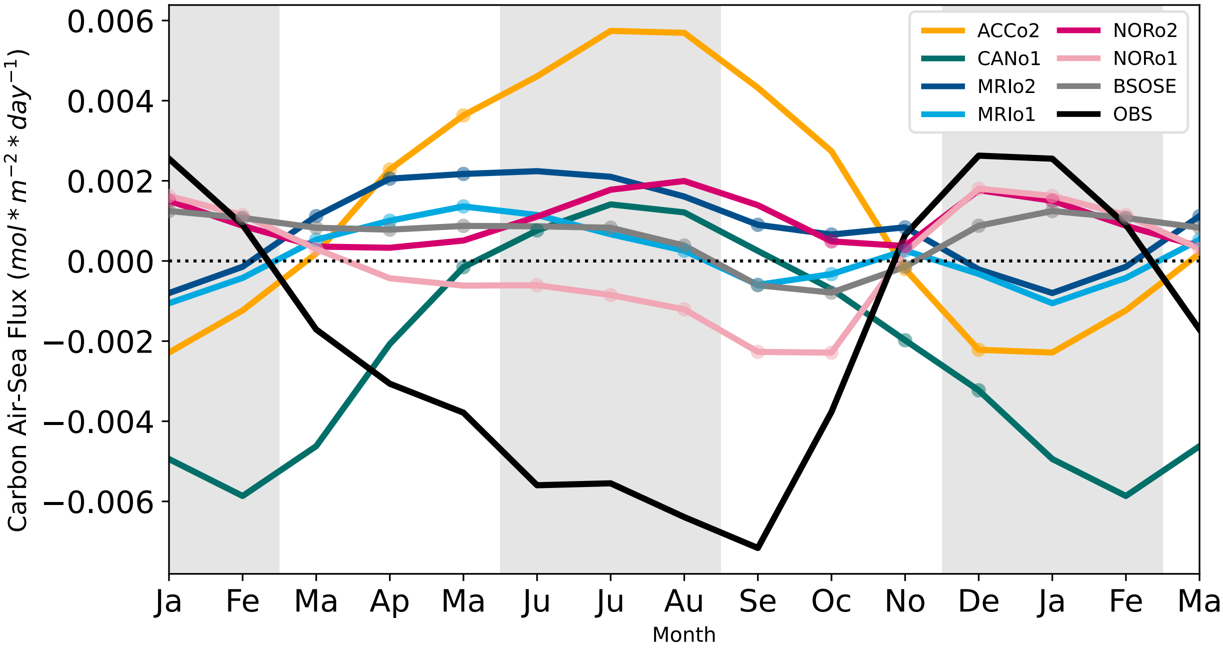

Figure 3.10: Seasonal cycle of the zone-averaged carbon air-sea flux for all datasets. Dots indicates that a month has DIC-driven $p\mathrm{CO}_2$ variations and positive values indicate ocean uptake. Note that we repeat January through March and that the gray shading highlights austral Summer and Winter.

models exhibit weaker negative advection driven by horizontal divergence. Among these, NORo1 comes closest to matching the float-derived depletion but still shows a seasonal DIC decrease more than 1.5 times smaller, largely due to its biological flux also being about 1.5 times weaker (Figure 3.9 g).

3.4.4 Drivers of Advection Differences between Models

Our results reveal distinct advection patterns across models both in the annual average and during the seasonal cycle. In the seasonally resolved DIC advection, we find that NOR and MRI models, along with the float-derived estimate, exhibit strong negative advection in spring that removes DIC from the mixed layer (Figure 3.11 a). In contrast, entrainment-dominated models (ACCo2, B-SOSE) and CANo2 show predominantly positive advection that adds DIC to the mixed layer. The observation-based estimate displays the largest seasonal range, with strong positive advection most of the year except for equally strong negative advection in October-November.

Analysis of the horizontal and vertical components of DIC advection reveals the mechanisms driving these differences (Figure 3.11 b and c). Models with strong negative spring advection (MRI and NOR) show seasonal reversals in both components: negative horizontal advection in summer/fall becomes positive in winter/spring, with an associated shift from upwelling to downwelling. Other datasets maintain consistent negative horizontal advection and positive vertical advection year-round. Notably, the observation-based estimate exhibits strong negative spring advection without the seasonal sign reversals seen in MRI and NOR models.

The budget framework setup creates an automatic coupling between positive horizontal advection and negative vertical advection (downwelling) through the mixed layer mass budget [Sauvé et al., 2023]. We verify that the downwelling signal is not a methodological artifact by examining zone-averaged vertical mass transport from available model output (Figure F.11). Both MRI and NOR models show negative vertical mass transport during winter and spring, while CANo1 and ACCo2 do not, confirming that the downwelling patterns reflect actual model behavior rather than framework limitations.

To understand the drivers of horizontal advection differences between models, we examine horizontal volume transport at each zone boundary (the Polar Front to the north and the sea ice edge to the south) (Figure 3.12). The majority of models and the observation-based estimate maintain horizontal transport

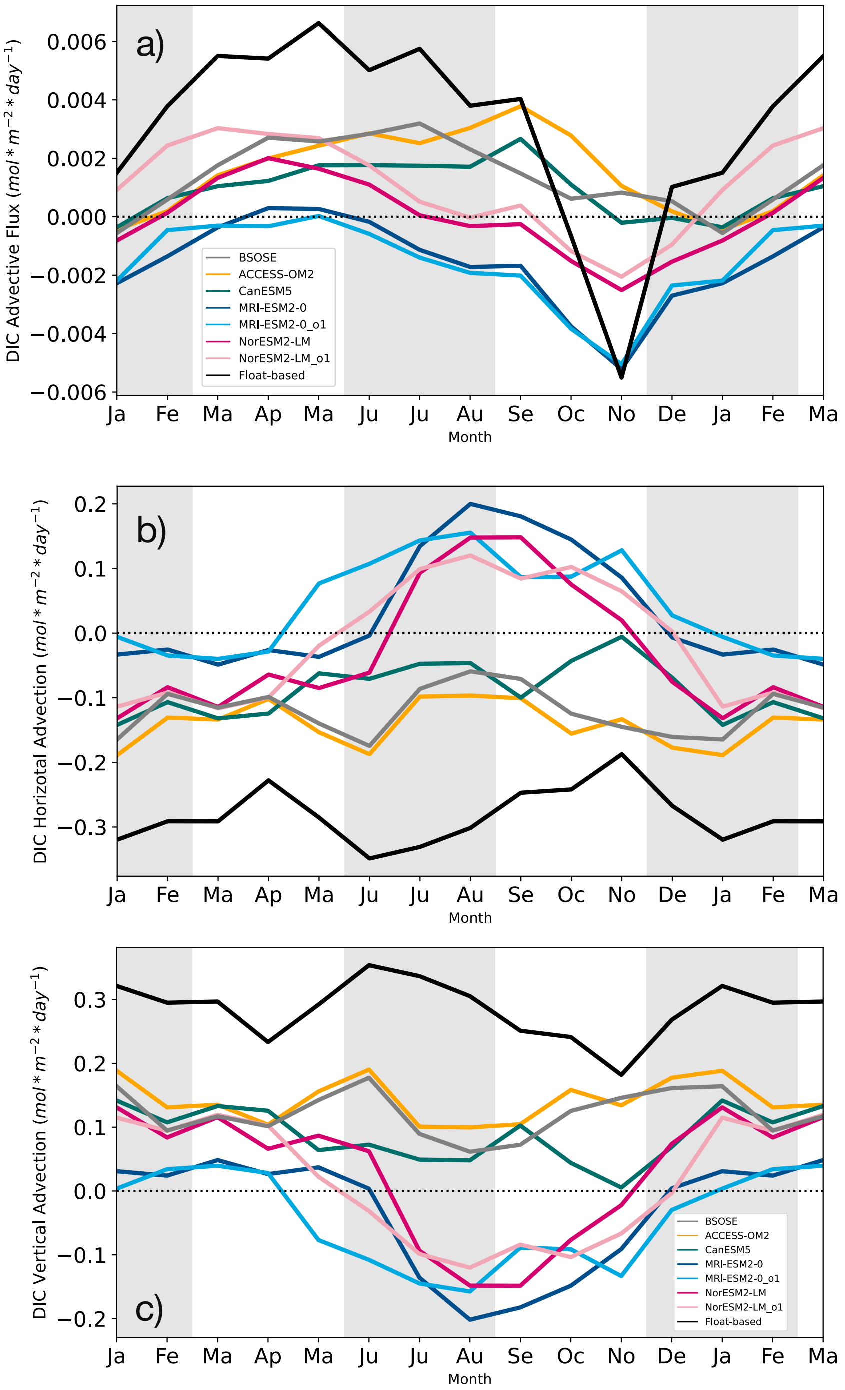

Figure 3.11: a) Seasonal cycle of the net advective flux of DIC into the mixed layer for all datasets. b) Seasonal cycle of the horizontal advection of DIC into the mixed layer for all datasets. c) Seasonal cycle of the vertical advection of DIC into the mixed layer for all datasets. Positive flux values indicate DIC is added to the mixed layer.

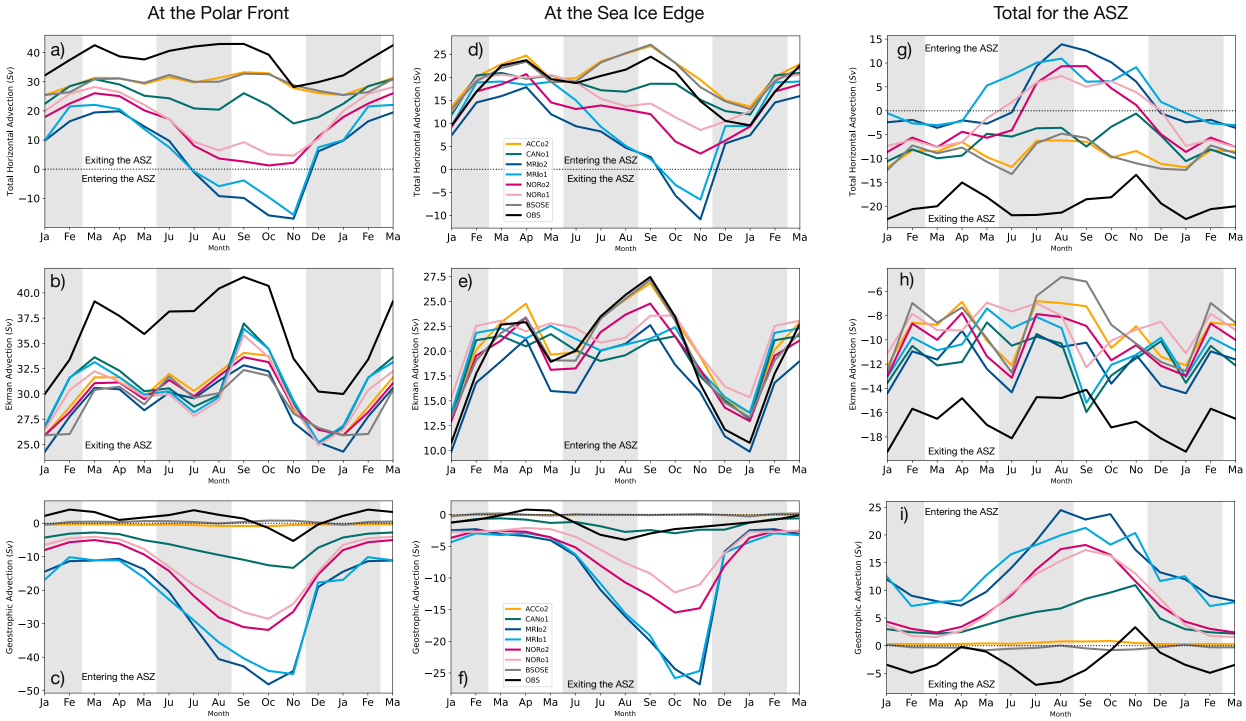

Figure 3.12: Total horizontal volume transport a) at the Polar front (PF), d) at the sea ice edge (SIE) and g) into the zone. Ekman horizontal volume transport b) at the Polar front (PF), e) at the sea ice edge (SIE) and h) into the zone. Non-Ekman horizontal volume transport c) at the Polar front (PF), f) at the sea ice edge (SIE) and i) into the zone. Note that the last column depicts the difference between the transport at the SIE and the transport at the PF (transport at the SIE - transport at the PF). At each front, positive transport is northward. For the last column, positive transport is into the ASZ. (ASZ: Antarctic Southern Zone)

divergence throughout the year, where transport out of the zone at the Polar Front exceeds transport into the zone at the sea ice edge (Figure 3.12 g). However, NOR and MRI models switch to convergence during winter and spring, creating positive total horizontal advection.

The mechanisms driving this convergence differ between model types. For NOR models, transport remains northward (positive) at both fronts throughout the year, but the convergence occurs because the relative magnitude of transport at each front changes: transport into the zone at the sea ice edge becomes larger than transport out of the zone at the Polar Front (Figure 3.12 a and d). For MRI models, the convergence results from more complex changes where the direction of transport at one or both fronts actually reverses from the typical northward pattern, creating periods when transport flows into the zone at both boundaries or when the typical transport pattern is completely reversed (Figure 3.12 a and d).

We separate transport at each boundary in Ekman and non-Ekman components using ocean wind stress (2 bottom rows of Figure 3.12). Ekman transport shows remarkable consistency across datasets in both magnitude and seasonal cycle, with all models producing similar transport out of the zone (Figure 3.12 h). The observation-based estimate has stronger Ekman transport at the Polar Front but matches model magnitudes at the sea ice edge (Figure 3.12 b and e).

The key differences emerge in non-Ekman transport, where models exhibiting horizontal convergence and downwelling also display strong non-Ekman advection that overwhelms their Ekman component (Figure 3.12 i). Specifically, MRI and NOR models show strong southward non-Ekman transport that peaks in spring at both zone boundaries, with MRI models exhibiting larger magnitudes than NOR models (Figure 3.12 c and f). While MRI and NOR are not the only models with significant non-Ekman advection, the strong magnitude of their non-Ekman transport creates positive total advection during winter and spring when it exceeds the opposing Ekman transport (Figure 3.12 g).

MRI models uniquely exhibit periods of negative horizontal advection at the fronts (Figure 3.12 a and d). Analysis of monthly zone-averaged profiles shows that both MRIo2 and NORo2 predict a section of southward total horizontal mass transport across the Polar Front during winter and spring, centered at 125 m and 25 m depth respectively, but that the section in MRIo2 makes up a larger fraction of the mixed layer than for NORo2 (Figure F.6). This negative transport occurs between layers of positive transport such that MRI's deeper mixed layer does not explain the transport differences. Model meridional transport output confirms that the southward transport across the front reflects actual transport patterns rather than methodological artifacts (Figure F.9). These non-Ekman transport differences likely reflect varying representations of mesoscale eddy activity and geostrophic circulation, contributing to intermodel differences in interior ocean-surface connections.

Finally, the observation-derived estimate shows fundamentally different non-Ekman transport mechanisms, with positive (northward) non-Ekman transport at the Polar Front, leading to non-Ekman transport divergence in all months except November, which coincides with the month of net negative DIC advection (Figure 3.12 c and i, and 3.11 a). While model non-Ekman advection is computed as *total transport - Ekman transport*, the observation-based estimate combines separate Ekman and geostrophic advection estimates, preventing direct comparison of cross-front total horizontal mass advection profiles. Investigation of cross-front geostrophic velocity profiles shows positive integrated geostrophic velocity throughout the water column, driven by strong zonal velocity crossing the Polar Front at meander locations rather than by positive meridional velocity (Figures F.7 and F.10).

Models with peak non-Ekman advection >10 Sv during winter-spring (CANo1, MRI, NOR models) fall into the double-sink or entrainment-balanced categories, while models with weak non-Ekman transport <2 Sv (ACCo2, B-SOSE) remain consistently entrainment-dominated. This eight-fold difference in non-Ekman transport directly controls whether advection acts as a carbon source or sink, with the strongest non-Ekman transport models actually reversing advection into a carbon sink.

3.5 Discussion

3.5.1 Importance of Mixing and Biological Fluxes

Comparing the monthly mean climatology of the DIC$_{ml}$ budget in the Antarctic Southern Zone across a suite of OMIP models, B-SOSE, and an observation-based estimate, we find that mixing and biological production consistently emerge as the dominant source and sink of DIC$_{ml}$, respectively. However, in all models, a delayed and weaker spring–summer biological production results in annually integrated entrainment acting as a net carbon sink, contrary to the float-based estimate. This additional sink reduces the upward supply of DIC from below the mixed layer, limiting the potential for carbon outgassing.

Our findings reinforce the role of mixing as a key process connecting the ocean interior to the surface in both models and observations. This aligns with earlier work identifying wind-driven mixing as a central driver of Southern Ocean air-sea carbon exchange [Rodgers et al., 2013] and DIC supply to the surface [Kwak et al., 2021; Dutreuil et al., 2009]. Mesoscale eddy-driven mixing also plays a crucial role in transporting iron [Uchida et al., 2019, 2020] and DIC [Dufour et al., 2013; Ellison et al., 2023] into the mixed layer, while large-scale mixing redistributes anthropogenic carbon from the surface to the interior [Groeskamp et al., 2016; Fu et al., 2022]. Within our budget framework, the mixing term reflects the aggregate, monthly, and zone-averaged effects of these small-scale processes at the base of the mixed layer. We also observe that the DIC supply by mixing is nearly balanced by a strong net biological production, consistent with previous findings in both models [Iudicone et al., 2011; Hauck et al., 2013], data-assimilating systems [Carroll et al., 2022], and direct observations [Yang et al., 2021; Williams et al., 2018]. This balance is expected, as the waters mixed into the surface not only supply DIC but are also rich in macronutrients and iron that fuel biological production.

Overall, the models tend to exhibit DIC fluxes of smaller magnitude than those estimated from observations, particularly for the mixing and biological terms. This discrepancy may stem from the differences in sampling: floats capture instantaneous, localized variability, including small-scale processes, that are not resolved in the time-averaged output of coarse-resolution models. Another contributing factor may be the relatively simple biogeochemical schemes used in the OMIP models, which generally feature only a single phytoplankton and zooplankton group [Rickard et al., 2023]. However, increasing model complexity does not guarantee better agreement with observations, as shown by Kriest [2017]. For instance, Rohr et al. [2023] demonstrated that variations in phytoplankton-specific loss rates to zooplankton grazing are a major source of intermodel differences in carbon cycle dynamics. Weaker biological production in models may also result from a reduced supply of nutrients from below. This applies both within our budget framework, where mixing and biological fluxes are linked through the optimization step, and in the simulations themselves, where coarse resolution likely limits the vertical transport of nutrients. For example, mesoscale eddies have been identified as a leading contributor to the vertical transport of iron across the base of the mixed layer [Uchida et al., 2019, 2020].

Beyond the overall weaker mixing fluxes compared to observations, we find that models differ in how the two key factors controlling mixing, vertical eddy diffusivity and the vertical DIC concentration gradient, combine to set its strength (Figure 3.8). Models with similar total mixing fluxes can rely on different balances of these factors. For example, the NOR models rely more on stronger vertical eddy diffusivity (Figure 3.8 c), while the MRI models have relatively stronger vertical DIC gradients (Figure 3.8 b); yet both produce similarly high annual mixing fluxes. These differences likely reflect how each model parameterizes unresolved small-scale processes, given their coarse resolution [Li et al., 2019]. Applying this budget framework to higher-resolution models could help clarify how explicit resolution of mixing processes affects flux estimates and offer insights for reducing intermodel spread.

Regardless of the underlying causes, the combined effect of weaker mixing and biological production leads to conistent annual negative entrainment flux in the models examined here (Figure 3.5). This represents an additional carbon sink in the models and contrasts sharply with the observation-based estimate, where entrainment acts as a small but positive source of carbon to the mixed layer. Observations have shown that entrainment is a key mechanism behind the zonal asymmetry of air–sea carbon fluxes in the Antarctic Circumpolar Current region [Prend et al., 2022a]. Episodic wind-driven entrainment events have also been linked to strong CO_2 outgassing [Nicholson et al., 2022] and elevated summer chlorophyll-a concentrations [Carranza and Gille, 2015] in the Southern Ocean. Moreover, detrainment plays a role in organic carbon export out of the mixed layer. This "mixed layer pump," a physical process analogous to the biological pump, is particularly important in regions with strong seasonal changes in mixed layer depth and can significantly contribute to organic carbon export [Lacour et al., 2019, 2023; Thompson et al., 2024]. Since entrainment and detrainment are inherently seasonal processes tied to changes in mixed layer depth, it is important to evaluate their net impact over the annual cycle. However, most existing DIC budgets have a fixed bottom boundary [Rosso et al., 2017; Jersild and Ito, 2020; Iudicone et al., 2011; Carroll et al., 2022]. Even among studies of DIC_{ml} budgets, the focus is typically on concentration changes rather than on the explicit balance of entrainment and detrainment [Bronselaer et al., 2018; Dufour et al., 2013; Williams et al., 2018; Merlivat et al., 2015; Yang et al., 2021; Munro et al., 2015]. By contrast, our results underscore that this balance is a key term in the mixed layer carbon budget and is essential for understanding model to observation discrepancies.

3.5.2 Advection as the Largest Inter-model Difference

The advective flux of DIC, though smaller in magnitude than mixing or biological fluxes, is the primary driver of intermodel differences. This agrees with the findings of Fu et al. [2022], who showed that variability in physical processes in the ocean helps explain the spread in carbon cycle representation among models. In our analysis, the largest discrepancies arise from differences in volume transport patterns. Notably, the NOR and MRI models predict unexpected periods of downwelling linked to anomalous horizontal transport convergence. In the MRI models, for some months, southward non-Ekman transport overwhelms the expected northward Ekman transport at the Polar Front or at both zonal boundaries, leading to net convergence. This behavior contradicts expectations for this region, where northward Ekman transport in the surface layer generally drives divergence and upwelling [Marshall and Speer, 2012; Rintoul and Garabato, 2013]. High-resolution models also support this prevailing upwelling at the latitudes of the Antarctic Circumpolar Current [Tamsitt et al., 2017; Yung et al., 2022]. Furthermore, a CMIP6 multi-model study (excluding MRI and NOR) found vertical transport patterns consistent with Ekman dynamics: upwelling south of approximately 50°S and downwelling farther north [Liao et al., 2025].

Importantly, we find that the unexpected downwelling in the NOR and MRI models occurs seasonally during winter and spring, which may explain why it is not apparent in annual means (Figure 3.11). Although both model families exhibit horizontal transport convergence within the Antarctic Southern Zone (ASZ), the mechanisms differ. In the NOR models, both boundaries maintain northward transport, but convergence arises when the northward transport at the sea ice edge exceeds that at the Polar Front (from July to November in OMIP2 and from June to December in OMIP1). In contrast, the MRI models show a succession of mechanisms, including reversals from northward to southward transport at one boundary between July and September, or at both boundaries in October and November.

Because all models are forced by a reanalysis atmosphere (one dataset each for OMIP1 and OMIP2), this intermodel spread in circulation patterns cannot be attributed to differences in wind strength or the position of peak wind stress, two key factors influencing Southern Ocean overturning circulation [Sijp and England, 2009; Rintoul, 2018]. Nor does it reflect differences in the time periods analyzed, as we observe consistent patterns across both OMIP1 and OMIP2 simulations for a particular model family. This suggests that the source of variability lies in the underlying model dynamics and parameterizations rather than external forcing. Future work should extend this analysis to a wider range of models from OMIP, adapting the framework to non-standard grid or deriving missing input, to determine if this anomalous circulation is a common feature of low-resolution models.

Several factors may help explain the circulation differences we observe among models. Beadling et al. [2020] reported that the CMIP6 versions of MRI and ACCo2 simulate a lower-than-average sea ice extent, and variations in sea ice melt location could influence circulation patterns. Sea ice characteristics also appear important: Mohrmann et al. [2021] showed that the CMIP6 version of MRI produces only coastal polynyas, whereas the CMIP6 Earth system version of ACCo2 has very few coastal polynyas and a large number of open-ocean polynyas (with CANo1 near the ensemble average; NOR was not included in their study). They also found that models prone to excessive open-ocean deep convection, which often leads to open-ocean polynyas, are more likely to simulate realistic Antarctic Circumpolar Current (ACC) transport, with both ACCo2 family models belonging to the group with the most realistic mixed layer depths. This is notable given that, in our analysis, MRI and NOR exhibit the deepest mixed layers (Figure 3.3 c). Another possible factor is the positioning of key frontal features. While zone boundaries are broadly similar among models, each model places the Polar Front and sea ice edge differently. Based on a temperature-defined front, we find that the Polar Front in MRI lies farther south on average than in other models (Figure F.2). Although identifying the root cause of these differences is beyond the scope of this study, previous research clearly shows that MRI, ACCo2, CANo1 and NOR differ in important aspects of sea ice, circulation, and frontal structure.

Differences in vertical and horizontal volume transports influence the net advection of DIC, but their effect is compounded by the seasonal cycle of DIC concentration in the advected waters. The impact of concentration is evident from the fact that the seasonal cycle of net mass advection does not mirror that of net DIC advection (Figures 3.11 and F.8). While net mass advection consistently removes water from the ASZ throughout the year, albeit with distinct seasonal cycles in the OMIP models compared to B-SOSE and observations, the seasonal cycle of net DIC advection is more similar across datasets. However, their annual mean values differ in sign (Figure 3.5). This suggests that the DIC concentration of waters entering and leaving the mixed layer varies across models and seasons. As a result, the small net effect of these large opposing DIC fluxes hinges on a delicate balance, making the DIC budget highly sensitive to circulation differences among models. These subtle circulation-driven differences contribute significantly to the intermodel spread in carbon cycle behavior.

3.5.3 Supply of DIC from Below and Surface $p\mathrm{CO}_2$ Variability

We find that a stronger supply of DIC at the base of the mixed layer is associated with greater DIC-driven $p\mathrm{CO}_2$ variability (Figure 3.13). However, this relationship does not extend to carbon outgassing, which shows no clear correlation with DIC supply. This apparent decoupling may reflect the compensating effect of biological fluxes in some models, though other factors such as surface alkalinity and temperature also influence the sign and magnitude of the air–sea carbon flux [Takahashi et al., 2002; Mongwe et al., 2018; Prend et al., 2022b].

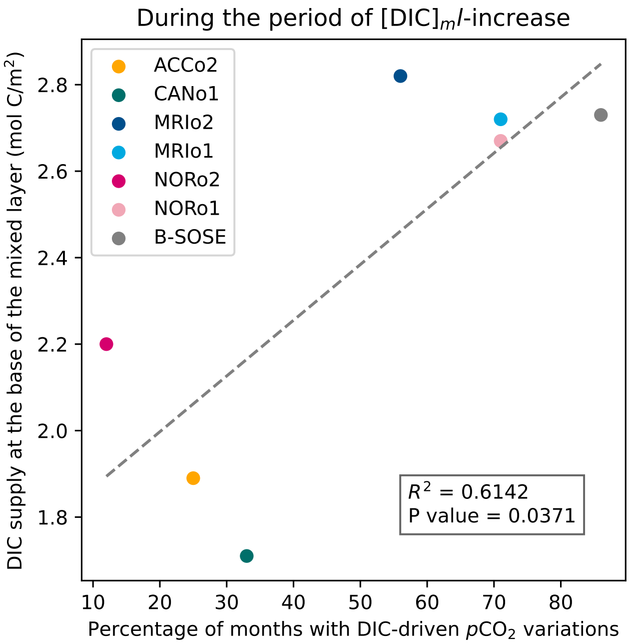

Figure 3.13: Scatter plot of the supply of DIC at the base of the mixed layer against the percentage of months with DIC-driven $p\mathrm{CO}_2$ variations for the period of DIC$_{ml}$-increase as determined by *Tend-Ent* > 0 in each datasets. The dashed line is the best fit with R^2 and P value labelled.

This link between DIC supply and surface $p\mathrm{CO}_2$ variability is particularly relevant in light of Hauck et al. [2023], who showed that thermal $p\mathrm{CO}_2$ variations in ocean-biogeochemistry models forced by atmospheric reanalysis generally agree with observations. They concluded that model-to-model differences in $p\mathrm{CO}_2$ variability mainly arise from the non-thermal component, likely controlled by near-surface DIC concentrations. Building on this, our results suggest that intermodel differences in $p\mathrm{CO}_2$ variability are driven in part by differences in DIC supply at the mixed layer base, especially during fall and winter. This reduced DIC supply results from a combination of weaker mixing, negative entrainment, and, in some models, an advective DIC sink. The lower availability of DIC in the mixed layer could allow solubility-driven variability to dominate, potentially explaining why solubility appears to control $p\mathrm{CO}_2$ variability for up to nine months of the year in some models (Figure 3.4 c). This interpretation aligns with previous findings by Dutreuil et al. [2009] and Rodgers et al. [2013], who showed that enhanced vertical mixing increases carbon outgassing or reduces uptake through increased DIC supply, and with Prend et al. [2022b], who linked the transition between solubility- and DIC-driven $p\mathrm{CO}_2$ variability with a poleward decline in the amplitude of temperature seasonality.

Finally, Hauck et al. [2023] also reported that intermodel spread in air–sea CO_2 fluxes is dominated by natural, rather than anthropogenic, carbon variability, highlighting systematic model biases in representing interior-to-surface carbon transport. Our results support this conclusion. While we identify advection as the primary source of intermodel spread, we also find that the largest model–observation discrepancy lies in the entrainment flux. Together, these findings underscore the importance of accurately capturing the net effect of three-dimensional physical processes, including vertical mixing, entrainment, and advection, in shaping air–sea carbon exchange. Our findings emphasize the need to better understand and constrain these processes, as they play a central role in shaping intermodel differences in air–sea carbon fluxes.

3.6 Conclusion

This study provides a process-based comparison of the seasonal mixed-layer dissolved inorganic carbon (DIC) budget in the Antarctic Southern Zone across a suite of Ocean Model Intercomparison Project (OMIP) models, a data-assimilating model (B-SOSE), and an observation-derived estimate [Sauvé et al., 2023]. Despite structural and parametric differences among models, several robust features emerge. Across all datasets, vertical eddy-driven mixing is consistently identified as the largest source of DIC to the mixed layer, while biological production is the largest sink. However, a key discrepancy arises in the timing and strength of biological production: all models exhibit a weaker and delayed spring/summer biological drawdown compared to the float-based estimate. This results in a negative annually-integrated entrainment flux of DIC in all models, in contrast to the positive flux inferred from float data. This model bias suggests a reduced supply of DIC from the base of the mixed layer, which could diminish the potential for the transfer of carbon from the interior ocean to the surface and impact air-sea fluxes to the atmosphere, and would thus contribute to biases seen when comparing ocean-only models and observation-based products [Friedlingstein et al., 2025]. These persistent discrepancies between models and observations appear despite generally good large-scale evaluations of the biogeochemical components in these OMIP models [Rickard et al., 2023; Séférian et al., 2020; Fu et al., 2022]. This underscores the importance of mechanistic evaluation, as models may reproduce global annual means for the wrong combination of processes.

Inter-model differences in the DIC budget are primarily driven by variations in advective fluxes. Though smaller in magnitude than mixing or biological terms, advective fluxes exhibit the greatest variability across models. These differences stem largely from the non-Ekman component of advection and can reverse the direction of vertical and horizontal transports, challenging expectations based on known regional circulation patterns. The supply of DIC at the mixed layer base, whether from mixing or advection, appears to be correlated with stronger DIC-driven $p\text{CO}_2$ variability and, potentially, with DIC-driven air-sea carbon fluxes (Figure 3.13). Yet, this relationship is strongly modulated by biological activity, which explains why greater subsurface DIC supply does not necessarily translate to increased carbon outgassing. Overall, this analysis underscores the importance of accurately representing the seasonal cycle of biogeochemical processes and physical transport mechanisms in models.

Understanding the processes that govern carbon exchange between the Southern Ocean and the atmosphere is essential for improving projections of the global carbon cycle under climate change. Given the Southern Ocean's outsized role in oceanic carbon uptake and the persistent model uncertainties in this region, improving the representation of physical and biological processes in ocean models remains a high priority. Future work should expand the analysis conducted here to models with higher resolution or more complex biogeochemical components, including multiple phytoplankton functional types and sophisticated nutrient cycling, to determine whether our results and the delayed and weaker spring bloom in particular still hold, and to identify which specific biogeochemical mechanisms are responsible for the observed biases in seasonal timing and magnitude of biological carbon fluxes. This work also underscores how regional and seasonal model assessments can reveal discrepancies which are not evident at global and annual scales. Such advances are critical to refining Earth system models and enhancing their predictive capabilities in the face of a changing climate.

Chapter 4

Zonal Asymmetry in the Physical Drivers of Southern Ocean Carbon Fluxes

Abstract

The Southern Ocean is central to the global carbon cycle, regulating carbon exchange between the atmosphere and the deep ocean. Its circulation is often studied using a zonal-mean framework, reflecting the dominant influence of the Antarctic Circumpolar Current. However, such approaches can obscure important spatial variations in carbon fluxes. This chapter directly addresses the third core research question posed in Chapter 1: What is the role of zonal asymmetries in driving mixed layer dissolved inorganic carbon (DIC) variability in the high-latitude Southern Ocean? Previous chapters explored observational and model-based perspectives on DIC variability but relied mainly on zonally averaged frameworks. Here, we extend that analysis by resolving the drivers of air-sea carbon flux at sub-circumpolar spatial scales using a closed mixed layer budget of DIC in B-SOSE, a high-resolution, data-assimilating model of the Southern Ocean. We find that carbon outgassing is concentrated at a few Indo-Pacific hotspots, closely aligned with regions of strong vertical DIC mixing. Eastward extensions of these hotspots suggest that lateral advection helps sustain elevated surface DIC downstream. While biological fluxes are zonally uniform in the model, allowing us to isolate physical drivers, entrainment contributes to localized variability and may explain smaller-scale outgassing features. By examining how vertical mixing, advection, and entrainment vary across longitudes

and ocean basins, this chapter demonstrates that zonal asymmetries in physical processes play a critical role in structuring surface carbon fluxes, insights that are not captured in traditional zonal mean diagnostics. In doing so, this chapter complements earlier work on seasonal dynamics and model spread by offering a spatially resolved understanding of carbon cycle variability in the Southern Ocean.

4.1 Introduction

The Southern Ocean is central to the global carbon cycle, regulating carbon exchange between the atmosphere and the deep ocean. However, the uncertainty of the ocean carbon sink is highest in the Southern Ocean [Friedlingstein et al., 2022; Gloege et al., 2021] and the discrepancy between models and observations is also most significant there compared to other ocean basins [Hauck et al., 2020]. Air-sea carbon fluxes depend on the gradient in the partial pressure of CO_2 ($p$$CO_2$) between the atmosphere and the ocean, with variability in surface ocean $p$$CO_2$, not atmospheric CO_2, controlling seasonal and regional flux patterns [Gruber et al., 2019]. To understand the processes behind these changes, $p$$CO_2$ can be separated into thermal and non-thermal components, the latter largely governed by surface DIC variability. Changes in temperature and changes in DIC act counter to one another and the sum of their impact sets ocean $p$$CO_2$ [Gruber et al., 2009; Prend et al., 2022b]. While sea surface temperature is adequately observed and represented in ocean models [Hauck et al., 2023], there are still several unanswered questions about the mechanisms driving mixed layer DIC variability.

Understanding the dynamics of the Southern Ocean has traditionally relied on zonally-averaged approaches, based on the assumption that the strong eastward-flowing Antarctic Circumpolar Current (ACC) rapidly homogenizes tracers along longitude. The historical lack of observations in this region, due to the presence of sea ice, frequent cloud cover, and strong winds, has also favored this approach, as sparse data available in a few locations can be assumed to accurately represent the entire region in a zonally-symmetric system. While zonal averaging provides valuable insights into large-scale processes, it obscures the complexity of regional processes. The ACC itself does not follow a zonal path and is significantly influenced by the zonally asymmetric distribution of topography in the Southern Ocean (Figure 4.1) [Marshall, 1995; Sallée, J. B., et al., 2011; Thompson and Sallée, 2012].

Further evidence suggests that the conventional zonally-averaged understanding of Southern Ocean

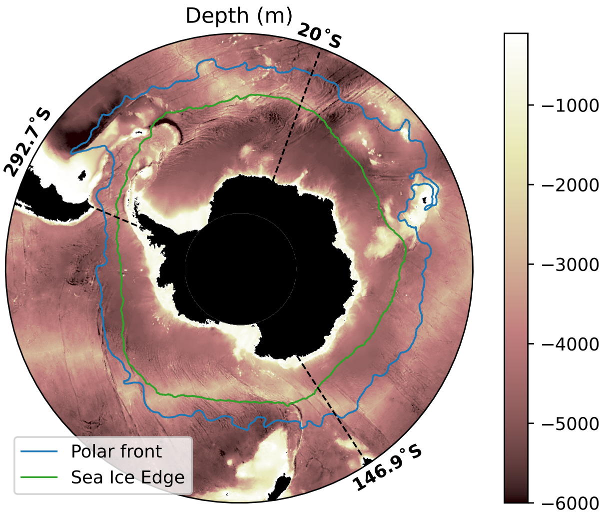

Figure 4.1: Map of the Southern Ocean south of 42°S. The background color corresponds to the elevation of the ocean floor (m). The contours correspond to the zonal boundaries of the ASZ. The northern contour is the Polar front (blue) while the southern contour is the sea ice edge (green). The Polar Front is a major front of the Antarctic Circumpolar Current and is associated with a steep southward rise in isopycnals. The boundaries between the Atlantic, Pacific and Indian Ocean basins are indicated by black dashed line and the longitude of the boundaries are labelled. (ASZ: Antarctic Southern Zone)

circulation is insufficient to fully comprehend the variability of Southern Ocean processes on seasonal to decadal timescales. Specifically, zonally asymmetric differences have been found in Southern Ocean wind [Fogt et al., 2012], sea surface temperature [de Boer et al., 2022], upper ocean heat budget [Tamsitt et al., 2016], phytoplankton biomass [Thomalla et al., 2011], mixed layer depth [Sallée et al., 2010] and sea ice [Schroeter et al., 2023]. Several studies have identified topographic features, which are distributed asymmetrically throughout the Southern Ocean (Figure 4.1), as the main guideways from the deep ocean to the interior and from the interior to the mixed layer [Rintoul, 2018; Tamsitt et al., 2017; Viglione and Thompson, 2016; Wu et al., 2011]. Furthermore, biogeochemical tracers exhibit particularly strong spatial variability, which is linked to topographic features and regional processes. Previous work found that upwelling of carbon across the 1000-meter depth contour also occurs near topographic features [Brady et al., 2021] and that the standing meanders associated with such bottom roughness are linked to enhanced ventilation of oxygen [Dove et al., 2022]. Carbon air-sea fluxes and their drivers also vary zonally across the different ocean basins [Prend et al., 2022a; MacGilchrist et al., 2019; Gregor et al., 2018] and regional differences in air-sea CO_2 flux have been identified on interannual to decadal timescales [Keppler and Landschützer, 2019].

Despite increased recognition for the role of localized processes in Southern Ocean circulation, important knowledge gaps remain regarding the impact of local dynamics on near-surface dissolved inorganic carbon (DIC) concentration and its drivers. Here, we use a closed mixed layer budget of DIC in a data assimilating model of the Southern Ocean to better understand the drivers of zonal asymmetry in mixed layer carbon fluxes.

4.2 Methods

4.2.1 Study Region

We analyzed the mixed layer DIC budget for three basins of the Antarctic Southern Zone (ASZ). The ASZ covers the southern half of the ACC, bounded by the Polar Front to the north and the September 15% sea ice area contour to the south (the sea ice edge, SIE). These zonal boundaries were used in previous studies where carbon air-sea fluxes were found to differ across observational datasets [Gray et al., 2018; Bushinsky et al., 2019]. We define the Polar Front based on the method defined in Chapter 3, which combines the Orsi et al. [1995] temperature criteria and sea surface height (SSH) gradients, as demonstrated in the work of Dufour et al. [2015] and Le Chevère et al. (under review).

We define 3 subregions of the ASZ based on oceanic basins: the Indian, Pacific and Atlantic. We separate each basin using lines of constant longitude that correspond to the edge of a model cell at 20°, 146.9197° and 292.7 333° (Figure 4.1). These boundaries are within 5° longitude of the basin boundaries used in Prend et al. [2022a].

4.2.2 The Biogeochemical Southern Ocean State Estimate

We use monthly output from iteration 155 of the Biogeochemical Southern Ocean State Estimate (B-SOSE), a 1/6° physical-biogeochemical data-assimilating model of the Southern Ocean with available output from 2013 to 2023 (Table 4.1) [Verdy and Mazloff, 2017]. B-SOSE's physical component is built on the MIT general circulation model [Marshall et al., 1997] and its biogeochemical ocean component is adapted from the BLING model of Galbraith et al. [2010]. The output was downloaded from `https://sose.ucsd.edu/SO6/ITER155/`. B-SOSE assimilates observational data and maintains closed tracer budgets through the adjoint method, minimizing weighted least-squares misfits between model solutions and observations. Data sources include biogeochemical Argo floats [Riser et al., 2016, 2018], instrumented Southern elephant seals [Charrassin et al., 2010], shipboard data, satellites and other platforms [Rosso et al., 2017] and assimilated variables include temperature, salinity, sea surface height, oxygen, nitrate, pH and more [Verdy and Mazloff, 2017].

Table 4.1: Model descriptions for B-SOSE, including grid details, biogeochemical components, and references.

Model name	**B-SOSE**
Organization	The Southern Ocean Carbon and Climate Observations and Modeling (SOCCOM) Project
Available time period	2013–2023
Grid extent	30°S – 78°S
Horizontal Grid	Mercator
Ocean-sea ice model	MITgcm and ECCO
Ocean Resolution	1/6° lon × 1/6° lat
Ocean vertical coord.	52 levels
BGC model	N-BLING (3P, 9PT)
Atmospheric forcing	6-hourly ERA5 Hersbach et al. [2020]
References	Verdy and Mazloff [2017]

4.2.3 Mixed Layer DIC Budget

We compute the budget of DIC content for each cell integrated over the mixed layer using monthly model output for the year 2018. We choose 2018 because it is the halfway point of the available years and because it is representative of the average seasonal cycle for several important variables including the carbon air-sea flux, ocean $p\mathrm{CO}_2$ and DIC concentration at the surface (Figure 4.2). It is important to note that the mixed layer budget described here is extensive (i.e. tracer amount, and not concentration, is conserved). Unlike a tracer concentration budget, an extensive tracer budget does not require a dilution term, and both entrainment and detrainment can impact DIC content. We use monthly-averaged variables for average values of the fluxes and monthly snapshots (instantaneous values at period boundaries) to determine time-derivatives (Table D.2 for a list of necessary model output).

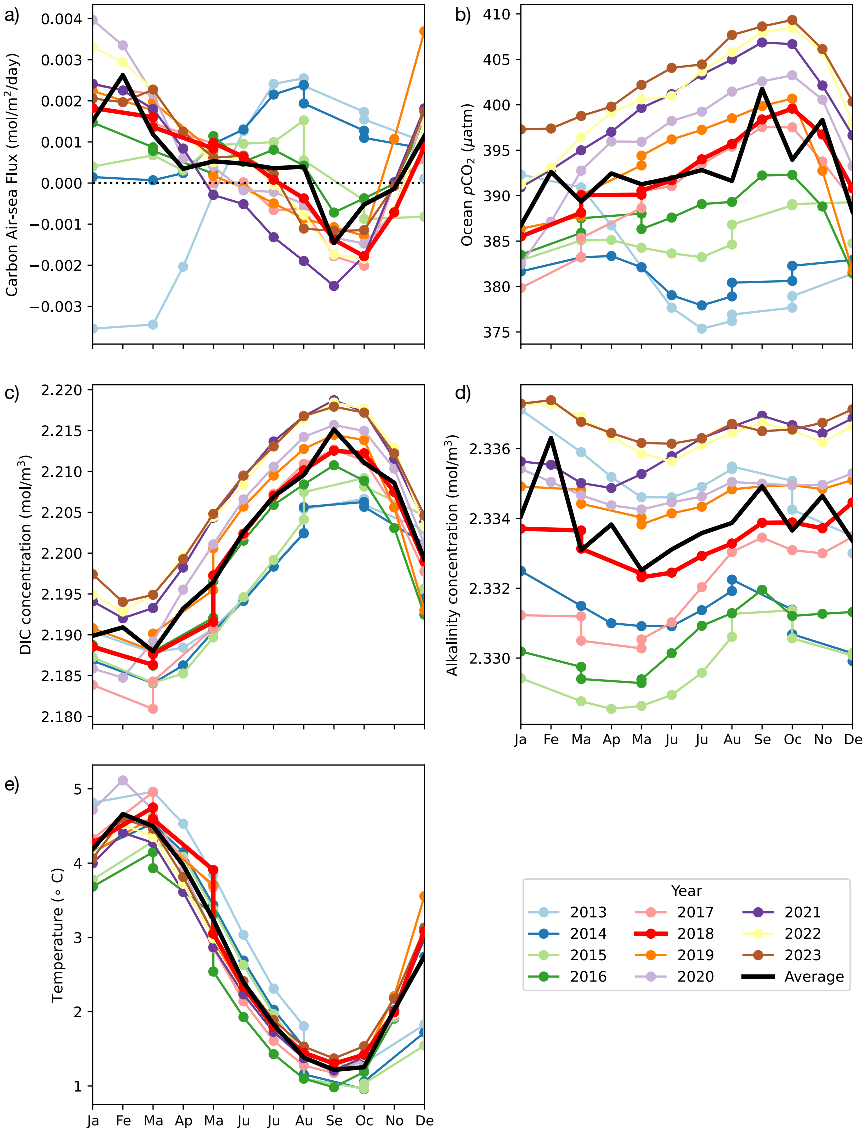

Figure 4.2: Seasonal cycle for each year from 2013 to 2023 of a) carbon air-sea flux, b) ocean pCO$_2$, c) surface DIC concentration, d) surface alkalinity concentration and e) temperature averaged for the ASZ. The red line shows the year 2018 used in this study and the black shows the average over all available years. The x-axis for all panels (ASZ: Antarctic Southern Zone)

Several methods exist to define the mixed layer depth [Holte and Talley, 2009]. We use the B-SOSE mixed layer depth output, which is computed based on a density criterion at a small-temporal scale and then averaged monthly. From the raw output, we identify the cell whose bottom is closest to the monthly averaged mixed layer depth and designate this cell as the last cell of the mixed layer. It is essential for the mixed layer depth to correspond to the bottom of a cell in order to close the budget. Using the provided depth output instead of computing the mixed layer depth from monthly-averaged fields reduced the budget residual in regions of large temporal mixed layer depth change.

The mixed layer budget equation (Eq. 4.1) is based on the three-dimensional tracer conservation equation that is solved by B-SOSE.

$$\textit{Tend} = F_{entrain} + F_{horiz-adv} + F_{vert-adv} + F_{air-sea} + F_{mixing} + F_{bio} \tag{4.1}$$

It includes the following budget terms: Tendency (*Tend*), Entrainment ($F_{entrain}$), Advection ($F_{horiz-adv} + F_{vert-adv}$), Mixing ($F_{mixing}$), Air-sea flux ($F_{air-sea}$) and Biology ($F_{bio}$).

The tendency, or time rate of change of the mixed layer DIC content, is computed based on the snapshot output of DIC concentration ($[DIC]^{snap}$, Eq. 4.2).

$$\textit{Tend} = \frac{\partial \ v[DIC]^{snap}}{\partial t} \tag{4.2}$$

We first multiply the snapshot tracer concentration (in mol m^{-3}) by the volume (v) of each cell to find the amount of tracer in each cell at the beginning and end of each time period (here, one month). We then sum the resulting tracer content (in mol) for all cells corresponding to the mixed layer. Finally, we take the mixed layer tracer content and compute the time derivative using the difference between the snapshot at the beginning and end of the time step, dividing by the length of time (mol day^{-1}).

Defining a budget with a time-varying bottom boundary like the mixed layer introduces an additional budget term. Entrainment is the process by which the mixed layer deepens and waters that were previously below the mixed layer are incorporated. Detrainment is the opposite process by which mixed layer volume decreases. While all other terms of the closed budget are defined for each cell of the 3-dimensional ocean model, the entrainment term is only relevant because we are computing a budget with a time-varying bottom boundary, and so can only be defined for the mixed layer as a whole. Since this budget term is approximated using monthly-averaged output, it is more affected than other budget terms by the loss of precision associated with closing the budget on a monthly time scale, a coarser resolution than was used when running the model. For this reason, flux due to entrainment can be very sensitive to large variations in mixed layer depth from one time step to the next. In regions where we noticed such large variations, mostly in the Weddell Sea in winter or in coastal regions, the closed budget can have a large residual. We found that using the mixed layer depth computed online and then averaged monthly (output provided by the B-SOSE modeling team) reduced the mixed layer depth's susceptibility to drastic variations and improved the residual.

The contribution of entrainment and detrainment to the budget is calculated using the concentration of DIC in entrained waters and the temporal change in the mixed layer depth (Eq. 4.3).

$$F_{entrain} = a\frac{T}{h}\frac{\partial H^{snap}}{\partial t} \tag{4.3}$$

where T is the DIC content in entrained and detrained water (mol m^{-2}), a is the surface area of each cell (m^{2}), h is the amount (m) by which the mixed layer depth has changed over one time step (here one month), and H^{snap} is the mixed layer depth snapshot (m). We first identify which cells at the bottom of the mixed layer have been entrained or detrained. We create a mask where cells within the mixed layer are set to 1 and those outside are set to 0. Then, we calculate the first-order discrete difference along the time axis. The resulting array is -1 or 1 where cells have been added or removed from the mixed layer, and 0 everywhere else. Using this mask, we identify the cells being entrained or detrained at each time step and sum the tracer amount in this water, in mol m^{-2}, representing the DIC concentration multiplied by the depth of each cell. We also determine the amount by which the mixed layer depth has changed over one time step by selecting the cell height at locations of mixed layer change and summing over depth. After identifying these quantities for each cell, we calculate the average concentration in the entrained water (T/h in mol m^{-3}). Finally, we multiply the tracer entrainment concentration by the time derivative of the mixed layer depth (in m day^{-1}), computed using the snapshot. This spatially-resolved entrainment is then multiplied by the horizontal cell area which gives the final entrainment term (mol day^{-1}). Note that the tendency and entrainment terms dominate over other fluxes, reflecting the fact that much of the mixed layer tracer content change is driven by volume changes during entrainment and detrainment. As a result, examining the difference between the tendency and entrainment terms (*Tend-Ent*), which corresponds to the time rate of change of mixed layer tracer concentration multiplied by mixed layer depth (see Sauvé et al. [2023], EQ. 7), allows for comparison on a scale comparable to other flux terms.

Both the exchange of carbon between the atmosphere and the ocean, and biological processes occurring in the mixed layer can act to modify DIC content. To compute the carbon air-sea flux at the surface, we take the B-SOSE output (**surfCO2flx**) and multiply by the cell area (a) (Eq.4.4).

$$F_{air-sea} = a \, \textbf{surfCO2flx} \tag{4.4}$$

For the biological flux of DIC, we select the mixed layer cells of the B-SOSE output (**BLGBIOC**) multiplied by the volume (v), and take the sum over depth.

$$F_{bio} = v \, \textbf{BLGBIOC} \tag{4.5}$$

B-SOSE computes the advective and mixing fluxes of each tracer (in mol s^{-1}) separately for the zonal, meridional and vertical directions. The vertical advective and mixing fluxes require boundary condition adjustments, which are required to close the budget (Eq. 4.6).

$$\begin{aligned} \text{DFrIDIC}^{sflr} &= 0 \\ \text{ADVrDIC}^{sflr} &= 0 \\ \text{ADVrDIC}^{sfc} &= a[DIC]^{sfc}\textbf{WvelMass}^{sfc} - v\textbf{ForcDIC} \end{aligned} \tag{4.6}$$

For both terms, we set the flux for the bottom cell to 0 as there is no flux through the sea floor (DFrIDIC^{sflr} and ADVrDIC^{sflr}). For the mixing flux, only the bottom flux should be modified and no correction is required at the surface. For the advection, at the surface, we need to make an adjustment for the flux of tracer due to the surface freshwater flux (ADVrDIC^{sfc}). We take the vertical mass-weighted component of velocity at the surface (**WvelMass**, m s^{-1}) and multiply it by the tracer concentration at the surface ($[DIC]^{sfc}$, mol m^{-3}) and by the area of the cell (a, m^2). From this flux, we then subtract the dilution of tracer due to freshwater flux at the surface (**ForcDIC**, mol m^{-3} s^{-1}) converted to the right units using the volume (v, m^3) of the cell.

While most budget terms are located in the center of a model grid cell, advection and mixing are located on the edges of the model cells. This introduces some challenges as the position of these fluxes on the model grid are staggered relative to the location of other terms like the air-sea flux. To get the flux due to advection or mixing for each cell from the flux at the boundaries, we need to take the 1st order discrete difference of the B-SOSE output (for example **ADVxDIC**, mol s^{-1}) along the appropriate axis (Eq. 4.7). This should take place after the boundary condition adjustments described above.

$$\begin{aligned}\text{Zonal Advection} &= \Delta_x\,\mathbf{ADVxDIC}\\ \text{Meridional Advection} &= \Delta_y\,\mathbf{ADVyDIC}\\ \text{Vertical Advection} &= \Delta_z\,\mathbf{ADVrDIC}\end{aligned} \tag{4.7}$$

As a final step, we then select the cells that are part of the mixed layer and take the sum for each component of advection and mixing. We add the zonal, meridional and vertical components to obtain the total flux due to advection and due to mixing (mol s^{-1}).

We analyze the mixed layer DIC budget for several spatial regions. To determine the budget terms for each region, we add the fluxes for each cell that is part of a region. Note that the units of the budget terms are in mol per unit time (not mol m^2 time) to ensure correct summation across cells of different surface area. For more details on calculating the budget for a particular region of interest, see the Section 3.2.3 of Chapter 3.

To complement the DIC budget, we partition the model $p\text{CO}_2$ seasonal cycle into contributions from temperature, salinity, DIC, and alkalinity, following the approach of Takahashi et al. [2014] (see also Sarmiento and Gruber [2006] and Prend et al. [2022b]). This method uses the first-order terms of a Taylor expansion to relate changes in $p\text{CO}_2$ to corresponding changes in temperature, salinity, DIC, and alkalinity. While this linear approximation is strictly valid only for small perturbations, we apply it to seasonal anomalies, defined as deviations from the annual mean.

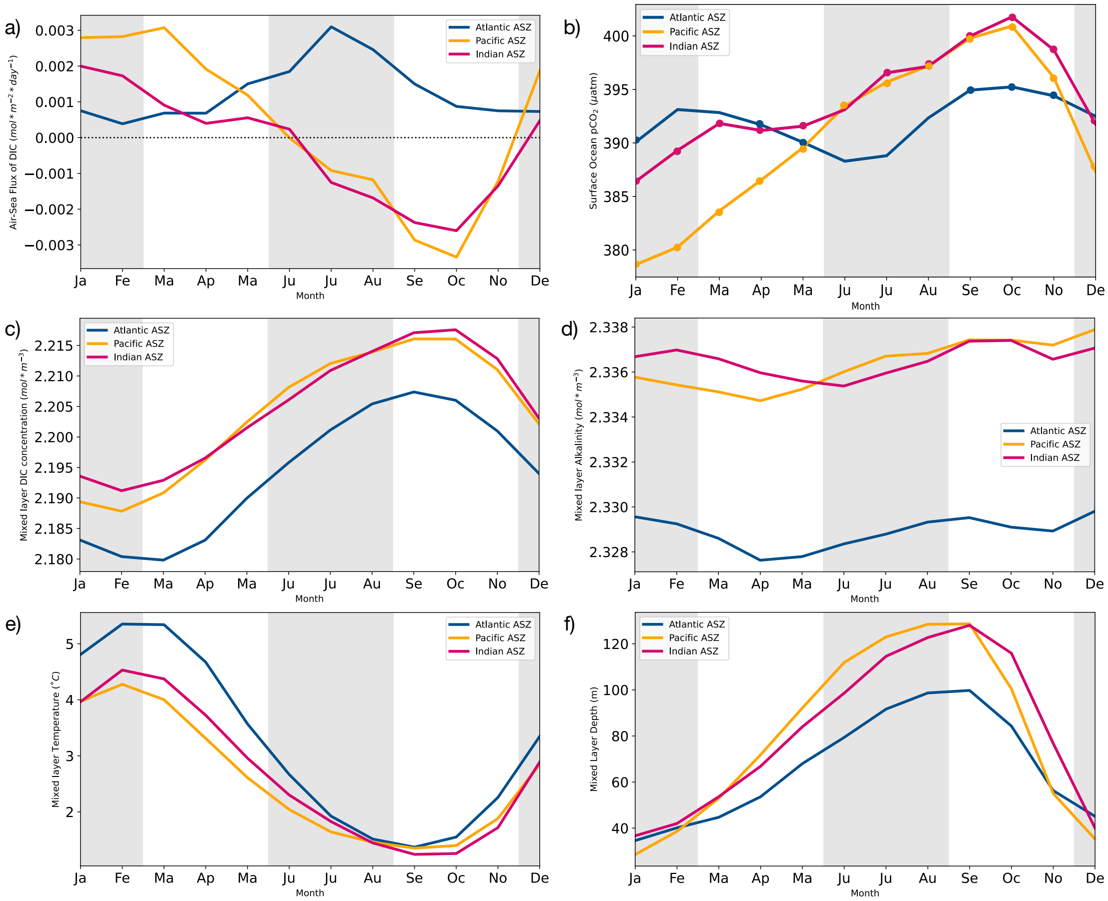

Figure 4.3: Seasonal cycle of a) carbon air-sea flux (positive values indicate uptake by the ocean), b) surface ocean $p\mathrm{CO}_2$, c) mixed layer DIC concentration, d) mixed layer alkalinity, e) mixed layer temperature and f) mixed layer depth averaged for the Atlantic, Pacific and Indian Ocean basins. The circle markers in panel b indicate that $p\mathrm{CO}_2$ variability was DIC-driven in that month. Lack of marker indicates temperature-driven $p\mathrm{CO}_2$ variability.

4.3 Results

4.3.1 Basin-scale Variability in DIC Fluxes

We observe clear basin-to-basin differences in the carbon air-sea flux across the ASZ (Figure 4.3 a). The Atlantic basin exhibits persistent carbon uptake throughout the year, while the Indian and Pacific basins show seasonal variability, taking up carbon during summer and fall and releasing it during winter and spring

.

We also find regional contrasts in the variability of surface $p\mathrm{CO}_2$ and its drivers. Our results show that while the average magnitude of $p\mathrm{CO}_2$ is similar across basins, the shape of its seasonal cycle stands out in the Atlantic compared to the Indian and Pacific, with the latter two undergoing stronger variability from summer to late winter (Figure 4.3 b). The drivers of $p\text{CO}_2$ variability also differ in the Atlantic, where temperature-driven variability dominates over DIC for half of the year (dots in Figure 4.3 b indicate DIC-driven variability, Figure G.1). This is not the case in the Indian and Pacific basins where DIC dominates for 11 and 12 months out of 12, respectively (Figure 4.3 b and Figure G.1). In addition to its unique air-sea flux and associated drivers, the Atlantic basin has strictly lower mixed layer concentrations of DIC and alkalinity compared to the Indian and Pacific basins (Figures 4.3 c and d). Basin-scale variability is of a similar order of magnitude as interannual fluctuations (Figure 4.2). Mixed layer temperature is similar among basins in winter and spring but the Atlantic is warmer in summer, which could explain why summer uptake is weaker in the Atlantic basin (Figure 4.3 e), but not why there is no outgassing in winter. Finally, winter mixed layer depths are shallower in the Atlantic basin, which could contribute to lower mixed layer DIC concentration. Overall, lower DIC concentrations are associated with reduced $p\text{CO}_2$, whereas warmer temperatures tend to elevate $p\text{CO}_2$, suggesting that both thermal and non-thermal effects contribute to the observed differences between basins.

We can use the mixed layer DIC budget, summed for each basin of the ASZ, to start exploring these differences (Figure 4.4). We find that in all basins, mixing with carbon-rich waters at the base of the mixed layer supplies DIC to the mixed layer year-round (Figure 4.4 a and f). This carbon is then largely consumed by biological production in summer and spring (Figure 4.4 a and d). All three basins undergo a period of mixed layer DIC concentration increase in winter and a period of concentration decrease in summer (Figure 4.4 a and c). The net advection of DIC and the carbon air-sea fluxes have smaller magnitudes than the other terms in all basins (Figure 4.4 a, b and e). However, as noted previously, the Atlantic basin stands out with strict carbon uptake year-round (Figure 4.4 b). We also note that the Indian and Pacific basins show a higher DIC mixing flux than the Atlantic during winter and spring, when they are outgassing carbon (Figure 4.4 f), suggesting that a larger supply of DIC from below could contribute to elevated $p\text{CO}_2$ and outgassing.

4.3.2 Small-scale Variability in DIC Fluxes

To better understand what fine-scale spatial variability may be driving basin-to-basin differences in carbon fluxes, we analyze the annually-integrated, cell-by-cell mixed layer budget of DIC (Figure 4.5). We find that

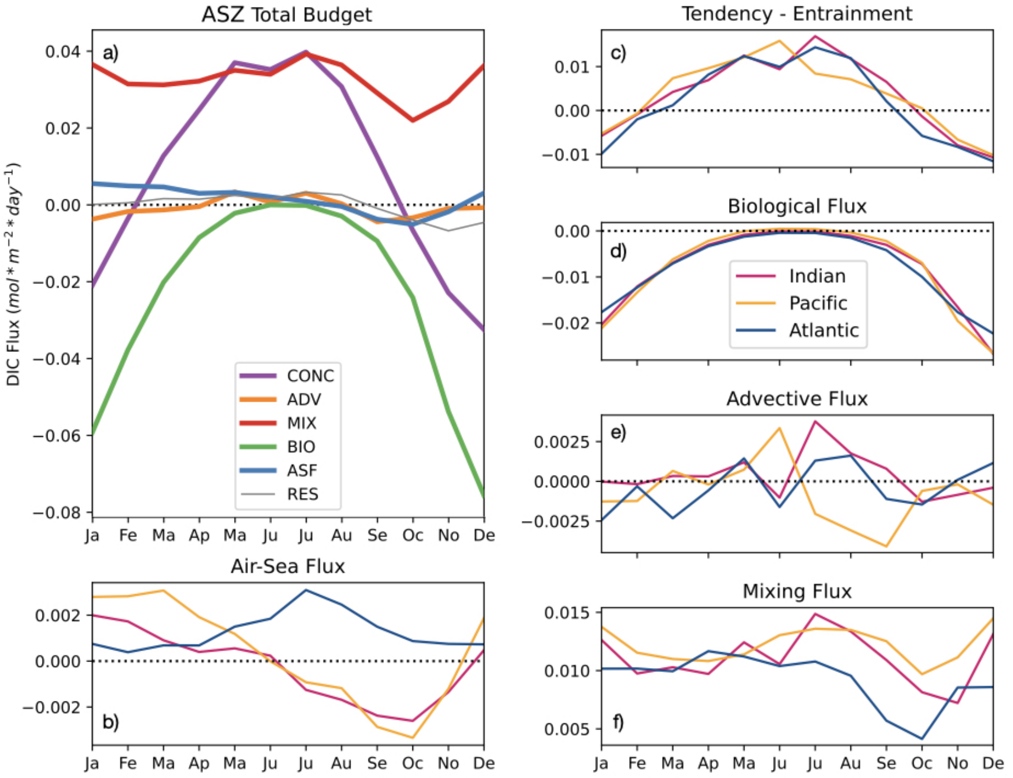

Figure 4.4: Seasonal cycle of the mixed layer DIC budget terms for a) the ASZ and separated by basin for each budget term: b) the carbon air-sea flux, c) tendency of DIC in the mixed layer minus the entrainment flux (*Tend-Ent*), d) the biological flux of DIC, e) the advective flux of DIC and f) the mixing flux of DIC. Note that *Tend-Ent* is equivalent to the temporal change in mixed layer DIC concentration multiplied by the mixed layer depth. Positive flux values indicate that DIC is added to the mixed layer. (ASZ: Antarctic Southern Zone, CONC: *Tend-Ent*, ADV: Advection, MIX: Mixing, BIO: Biology, ASF: Air-sea flux, RES: residual)

DIC fluxes are not spatially uniform and significant sub-basin scale variability is evident. Specifically, we identify three distinct outgassing hotspots within the ASZ: at the boundary between the Atlantic and Indian Oceans (around 20° longitude), in the central Indian Ocean (around 80° longitude), and near the western boundary of the Pacific Ocean (around 150° longitude) (Figure 4.5 a). Each of these hotspots is followed eastward by a trailing region of continued, though weaker, outgassing. Given the strength and direction of the ACC, this pattern suggests that favorable conditions for outgassing at each hotspot, potentially linked to strong local DIC supply, may be advected downstream, sustaining outgassing east of each core region.

Next, we examine the annually integrated biological flux of DIC from the mixed layer (Figure 4.5 b). In contrast to the air-sea flux, this term displays minimal zonal variability across the ASZ. The biological flux consistently removes DIC from the mixed layer throughout the region, without clearly identifiable hotspots or gradients in the ASZ, though that is not the case for the Southern Ocean as a whole. While this spatial uniformity may reflect limitations of the model rather than real-world biological variability, it allows us to isolate the influence of physical drivers on zonal variability in the air-sea carbon flux.

Turning to the mixing flux of DIC (Figure 4.5 c), we find clear hotspots of vertical DIC input into the mixed layer that coincide approximately with the locations of outgassing maxima. Since mixing is the dominant physical source of DIC to the mixed layer in this region (as seen in the ASZ-integrated budget, Figure 4.4 a), this spatial correlation supports the idea that enhanced vertical supply of DIC may trigger or sustain localized outgassing.

We then consider the advective flux of DIC (Figure 4.5 d). This term exhibits strong spatial heterogeneity in both sign and magnitude across the ASZ, with many small-scale features indicating strong but localized sources and sinks. While advection is generally weaker than mixing in the ASZ-wide budget, these patterns suggest it could still contribute to local DIC variability and possibly to the formation or modulation of outgassing hotspots.

Finally, we examine the entrainment flux (Figure 4.5 e), another potential source of DIC to the mixed layer. South of 42°S, the entrainment field shows a dipole-like structure, characterized by alternating patches of strong positive and negative values. These patchy features are roughly aligned with the Polar Front and are present across all three basins, though their intensity varies regionally. Interestingly, this patchiness disappears when we examine the difference between the DIC concentration tendency and the entrainment

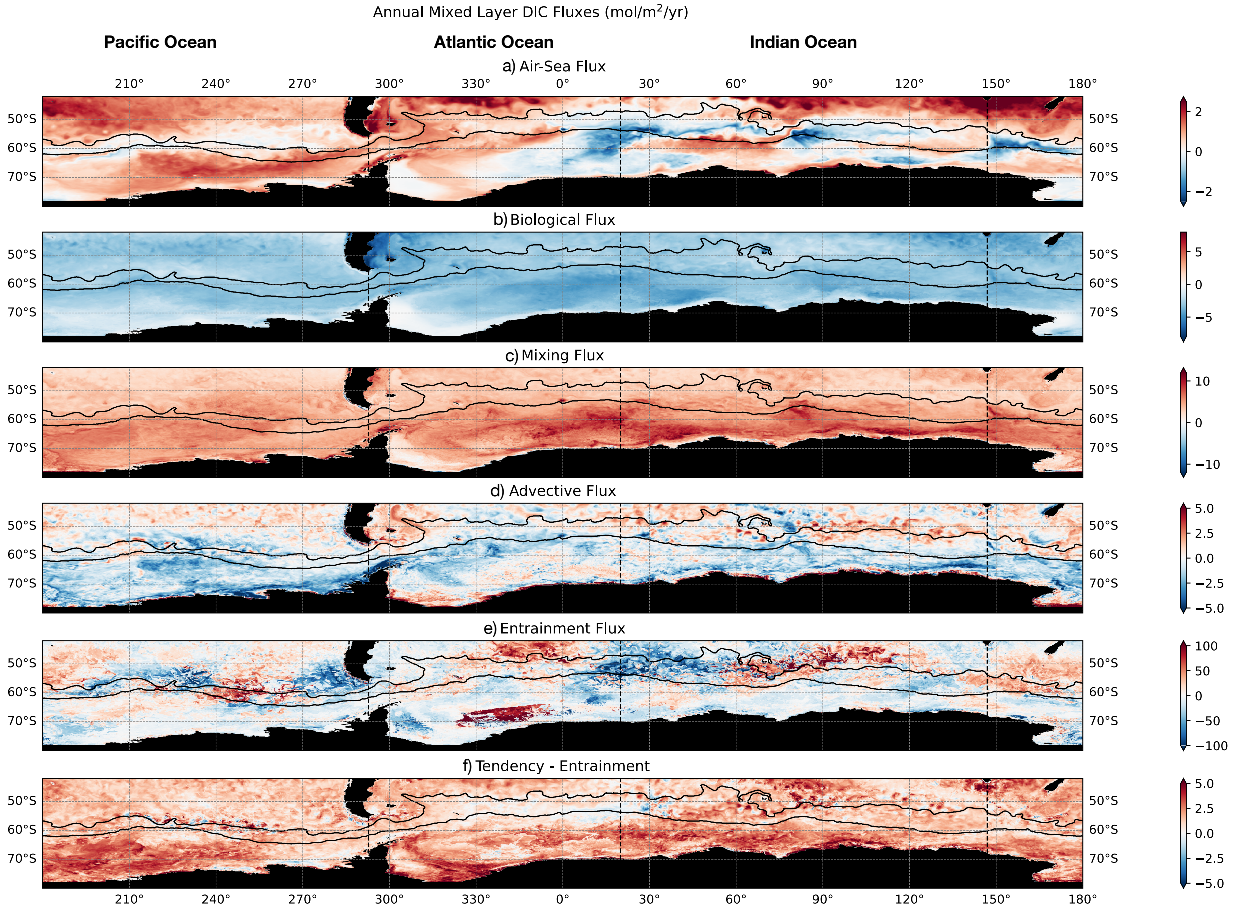

Figure 4.5: Map of the annually integrated cell-by-cell mixed layer DIC a) air-sea flux, b) biological flux, c) mixing flux, d) advective flux, e) the entrainment flux, and f) the tendency minus entrainment flux, all in mol m^{-2} yr^{-1}. The black contours shown are the Polar Front (northern contour) and the Sea Ice Edge (southern contour), and they define the ASZ (Figure 4.1). Dashed black lines separate the different basins. Positive (negative) values, shown in red (blue) color indicates the the flux is adding (removing) DIC to (from) the mixed layer. (ASZ: Antarctic Southern Zone)

flux (*Tend–Ent*, Figure 4.5 f and G.5). This quantity, defined as the rate of change in mixed layer DIC concentration multiplied by the mixed layer depth (Section 4.2.3), reflects net DIC accumulation in the mixed layer after accounting for entrainment. Across most of the study region, *Tend–Ent* is positive, with the strongest values located south of the sea ice edge. This indicates that, overall, the mixed layer DIC concentration increased in 2018.

In summary, we find that sub-basin scale outgassing hotspots in the ASZ align with regions of enhanced vertical mixing of DIC, while biological drawdown appears spatially uniform. Advection and entrainment contribute additional fine-scale variability but do not show the same clear spatial correspondence with outgassing. These results suggest that vertical mixing is a key driver of the zonally asymmetric structure of air-sea carbon flux in the ASZ.

4.3.3 Circumpolar Variability within the ASZ

We collapse each budget term over the latitudes of the ASZ to further investigate zonal variability (Figure 4.6). The zonal distribution of the air-sea carbon flux reveals four prominent outgassing bands, three of which correspond to the previously identified hotspots in the Indian and Pacific basins: from 359.25° to 50.08° (Atlantic–Indian boundary), from 79.08° to 122.58° (central Indian Ocean), from 147.58° to 179.08° (western Pacific), from 216.92° to 224.58° (central Pacific, not clearly visible in map view) (Figure 4.6 a and Figure 4.5 a).

Each of the larger outgassing regions (Atlantic–Indian boundary, central Indian Ocean and western Pacific) is immediately preceded to the west by a sharp peak in the DIC mixing flux (Figure 4.6 b). This spatial relationship supports the idea that intense vertical supply of DIC can elevate surface ocean $p\text{CO}_2$, prompting outgassing. However, not all peaks in vertical mixing are associated with outgassing. For instance, in the Atlantic between 292° and 300°, and in the eastern Pacific, we observe large mixing fluxes without corresponding outgassing. Furthermore the small outgassing region in the central Pacific lacks a preceding peak in mixing altogether.

The biological flux of DIC, when integrated over latitude (Figure 4.6 d), shows only modest zonal variation (±0.75 mol m^{-2} yr^{-1}). These variations are small relative to those in the mixing and advective fluxes, and they do not appear to align with the longitudinal structure of air-sea carbon flux. This reinforces earlier

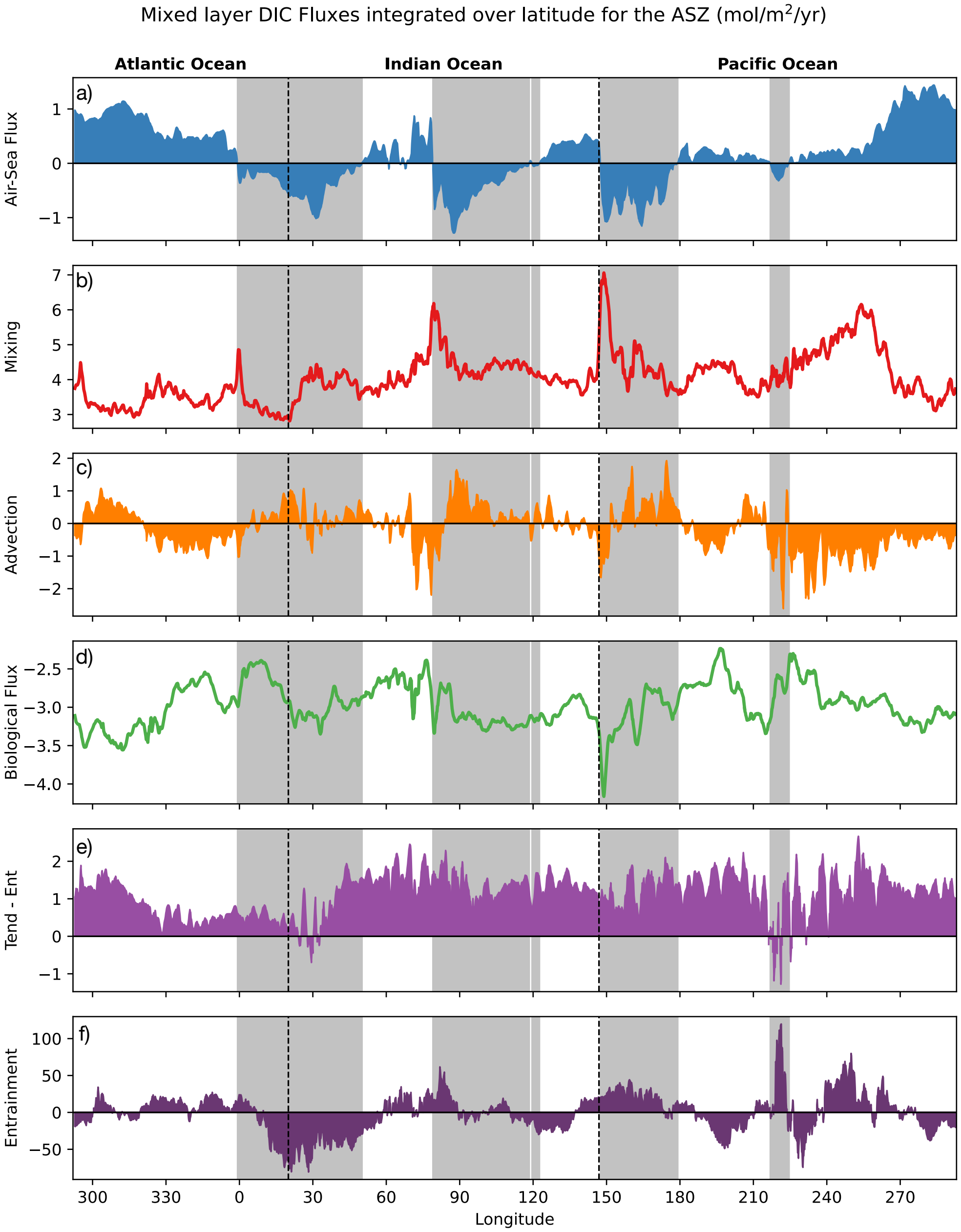

Figure 4.6: Mixed layer DIC fluxes integrated over the latitudes of the ASZ and plotted against longitude, eastward from Drake Passage: a) the carbon air-sea flux, b) the mixing flux, c) the advective flux, d) the biological flux, e) tendency minus the entrainment (*Tend-Ent*), and f) the entrainment flux. Note that *Tend-Ent* is equivalent to the temporal change in mixed layer DIC concentration multiplied by the mixed layer depth. Fluxes are in mol m^{-2} yr^{-1}. Positive values indicate that the flux is adding DIC to the mixed layer. Note that the direction of the dominant current in this region (the ACC) is eastward or from left to right. (ASZ: Antarctic Southern Zone)

findings that biological drawdown, while important in magnitude, is relatively uniform across longitudes, and not the primary driver of localized outgassing in B-SOSE.

By contrast, the zonal distribution of the advective flux (Figure 4.6 c) mirrors the structure of outgassing more closely. The three widest outgassing regions (Atlantic–Indian boundary, central Indian Ocean and western Pacific) coincide with areas of positive net advection (the smaller net sum of large contributions from horizontal and vertical advection), and the transition to negative advection coincides with a shift from outgassing to uptake. This suggests that advection helps transport DIC supplied by vertical mixing downstream, supporting outgassing along the eastward "tails" observed in Figure 4.5 a. In the eastern Pacific, while the mixing flux is strong, the advective flux is negative, likely counteracting the DIC supply from below and reducing the potential for outgassing. This highlights the importance of both vertical and lateral supply pathways in sustaining surface DIC levels.

However, this explanation does not account for the Atlantic mixing hotspot near Drake Passage (between 292° and 300°), which is associated with positive advection but no outgassing. To understand this discrepancy, we examine zonally-resolved ocean $p\text{CO}_2$, surface DIC concentration and surface temperature (Figure G.7). In this region, ocean $p\text{CO}_2$ is more than 10 μatm lower than at the Atlantic–Indian boundary, despite a comparable peak in mixing. However, surface temperatures are lower, which would act to decrease $p\text{CO}_2$ and could suppress air-sea carbon exchange. We also found that the Atlantic basin, which includes this region, displays more temperature-driven $p\text{CO}_2$ variability and exhibits a larger seasonal temperature amplitude. This suggests that supply of DIC by mixing alone is not sufficient to elevate ocean $p\text{CO}_2$ above atmospheric levels in this region, and that the thermal component of $p\text{CO}_2$ variability dominates over DIC. This interpretation aligns with the findings of Prend et al. [2022b], who showed that the transition between temperature- and DIC-driven $p\text{CO}_2$ variability in the South Pacific was associated with a meridional decline in the seasonal amplitude of temperature.

The outgassing band in the central Pacific, the smallest and most enigmatic outgassing region, is not associated with strong vertical mixing or positive advection. Instead, it coincides with the strongest net positive entrainment flux in the ASZ (Figure 4.5 e). This location lies where the Polar Front is topographically steered through a narrow zonal valley (Figure 4.1), leading to a constriction of the ASZ and likely enhancing current speeds. Annually integrated, a positive entrainment flux indicates that either DIC entrainment exceeds detrainment over the year, or that the mixed layer deepens over the course of this particular year (2018), or both. While the change in mixed layer depth here is among the largest in the ASZ, it is not anomalously large (Figure G.6). This implies that the seasonal timing and carbon content of entrained vs. detrained waters must align in such a way that net entrainment introduces more DIC to the mixed layer than it removes. This additional source could be sufficient to elevate surface $p\mathrm{CO}_2$ and drive the localized outgassing seen in this region.

In summary, outgassing in the ASZ is not zonally uniform but concentrated at a few distinct hotspots, primarily in the Indo-Pacific sector. These hotspots are preceded by sharp peaks in vertical mixing, which appear to inject DIC into the mixed layer. However, the full spatial extent of outgassing, particularly the downstream tails, suggests that mixing alone is not the full story. While the current analysis does not provide definitive proof, it suggests that advection is linked to these outgassing tails. Zonal advection appears to transport excess DIC from the mixing regions, sustaining outgassing until the lateral supply is interrupted or depleted. In areas where this advective support is absent or opposing, such as in parts of the Pacific and Atlantic, strong mixing may not be sufficient to trigger outgassing. Finally, isolated outgassing can also occur in regions where entrainment is particularly strong, likely due to a favorable seasonal interplay between mixed layer depth evolution and the DIC content of waters below the mixed layer. These findings highlight the complex interplay between vertical and horizontal processes in shaping the zonal asymmetry of carbon flux in the ASZ.

4.3.4 Vertical Structure of Mixing Hotspots

To investigate why strong DIC mixing fluxes occur in specific regions, we examine the vertical structure of DIC across longitude. The net DIC mixing flux is dominated by vertical mixing, while horizontal mixing is approximately two orders of magnitude smaller on average (Figure G.2). Since the vertical mixing flux is typically parameterized as the product of a vertical concentration gradient and a vertical eddy diffusivity, we investigate the vertical DIC gradient in the top 500 m of the water column (Figure 4.7 b). We find that regions where the mixing flux increases sharply with longitude, particularly at the Atlantic–Indian boundary and in the central Indian Ocean, coincide with enhanced vertical DIC gradients beneath the mixed layer. The strongest gradient values are found approximately 20–50 m below the base of the annual averaged

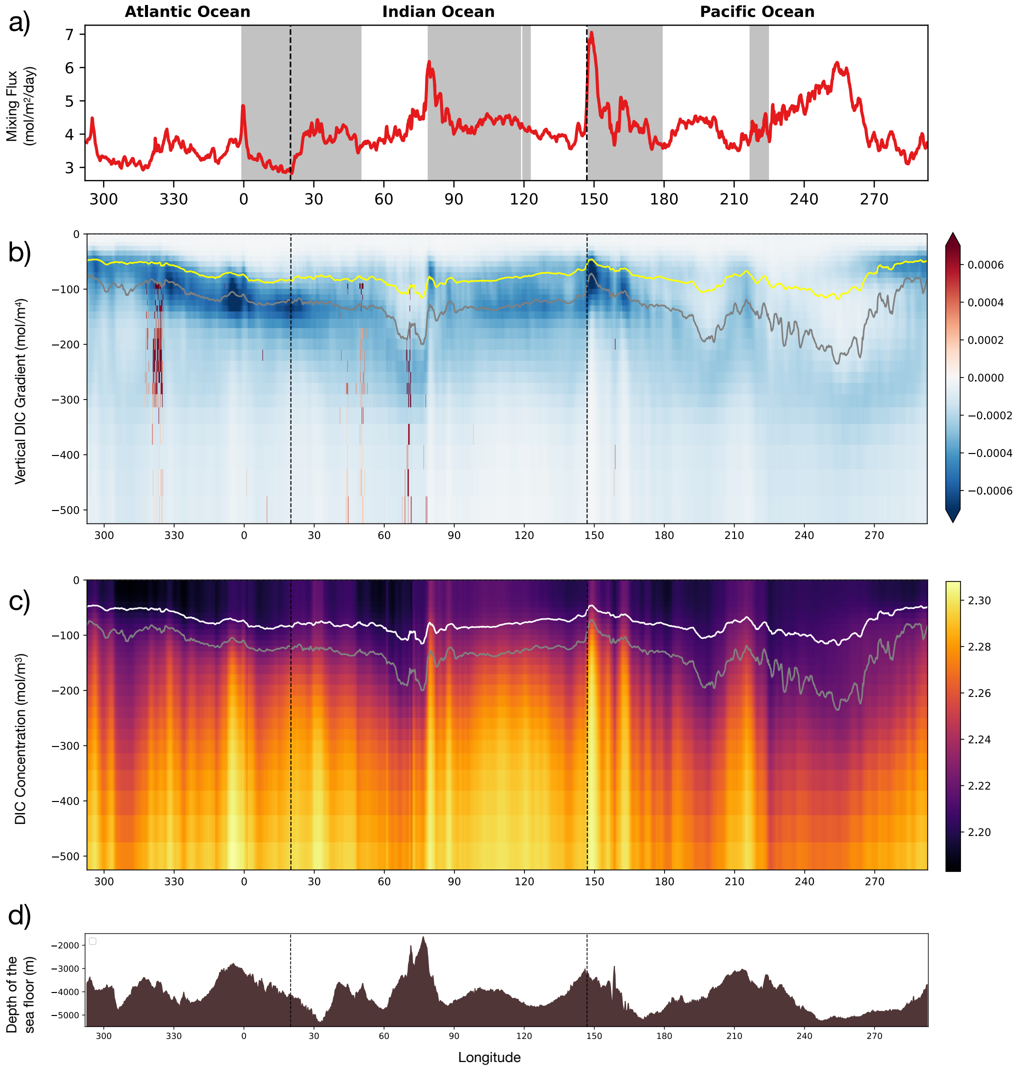

Figure 4.7: Latitudinally and annually integrated a) DIC mixing flux, b) vertical gradient of DIC concentration, c) DIC profile and d) elevation of the sea foor. The yellow (white) line in panel b (c) corresponds to the mixed layer depth and the gray line corresponds to the maximum mixed layer depth. (ASZ: Antarctic Southern Zone)

mixed layer, but at the depth of the maximum mixed layer depth, suggesting a strong potential for vertical exchange. In the central Indian Ocean, the gradient decreases slightly west of the mixing hotspot but still exhibits a localized peak, although this peak lies within the annual mean mixed layer rather than below it. The longitudes of the mixing peaks in the three larger outgassing bands are also preceded by a shoaling of the mixed layer, which may further enhance the vertical gradient at the base. Together, these patterns suggest that enhanced vertical DIC gradients are closely tied to the observed peaks in the mixing flux. Supporting this, vertical sections of DIC concentration (Figure 4.7 c) show clear intrusions of DIC-rich waters extending upward from below at the longitudes of the mixing hotspots. Elevated DIC values span the full water column at these locations and often reach into the mixed layer, suggesting intensified vertical exchange throughout the water column, not just at the base of the mixed layer.

Notably, all sharp peaks in mixing are located downstream of major topographic features, where seafloor depth shallows significantly, reaching less than 3000 m in all cases, and less than 2000 m in the central Indian Ocean (Figure 4.7 d). This suggests outgassing is linked to the enhanced upwelling and mixing associated with topography, providing an explanation for why these outgassing regions are visible in the annually integrated air-sea flux despite overall seasonal variability in the zone-averaged air-sea flux.

4.3.5 Drivers of the Net Advective Flux of DIC

Since longitudinal transitions in the carbon air-sea flux often align with changes in the sign of net advection, we examine the components of the DIC advection term to better understand the drivers behind these shifts. Although both horizontal and vertical advection remain highly variable, even when integrated over the latitudes of the ASZ (Figure G.4 b and c), their cumulative sum over longitude reveals a clearer signal (Figure 4.8 b). From this cumulative sum, we observe that, over broad longitudinal bands, horizontal advection consistently acts to remove DIC from the mixed layer, while vertical advection supplies DIC to the mixed layer. However, this does not imply that horizontal advection is uniformly negative.

To explore local dynamics, we classify each grid cell in the ASZ based on whether horizontal or vertical advection determines the sign of the net advection (Figure 4.8 d). At all longitudes, all four scenarios are present: positive net advection driven by horizontal advection, positive net advection driven by vertical advection, negative net advection driven by horizontal advection, and negative net advection driven by

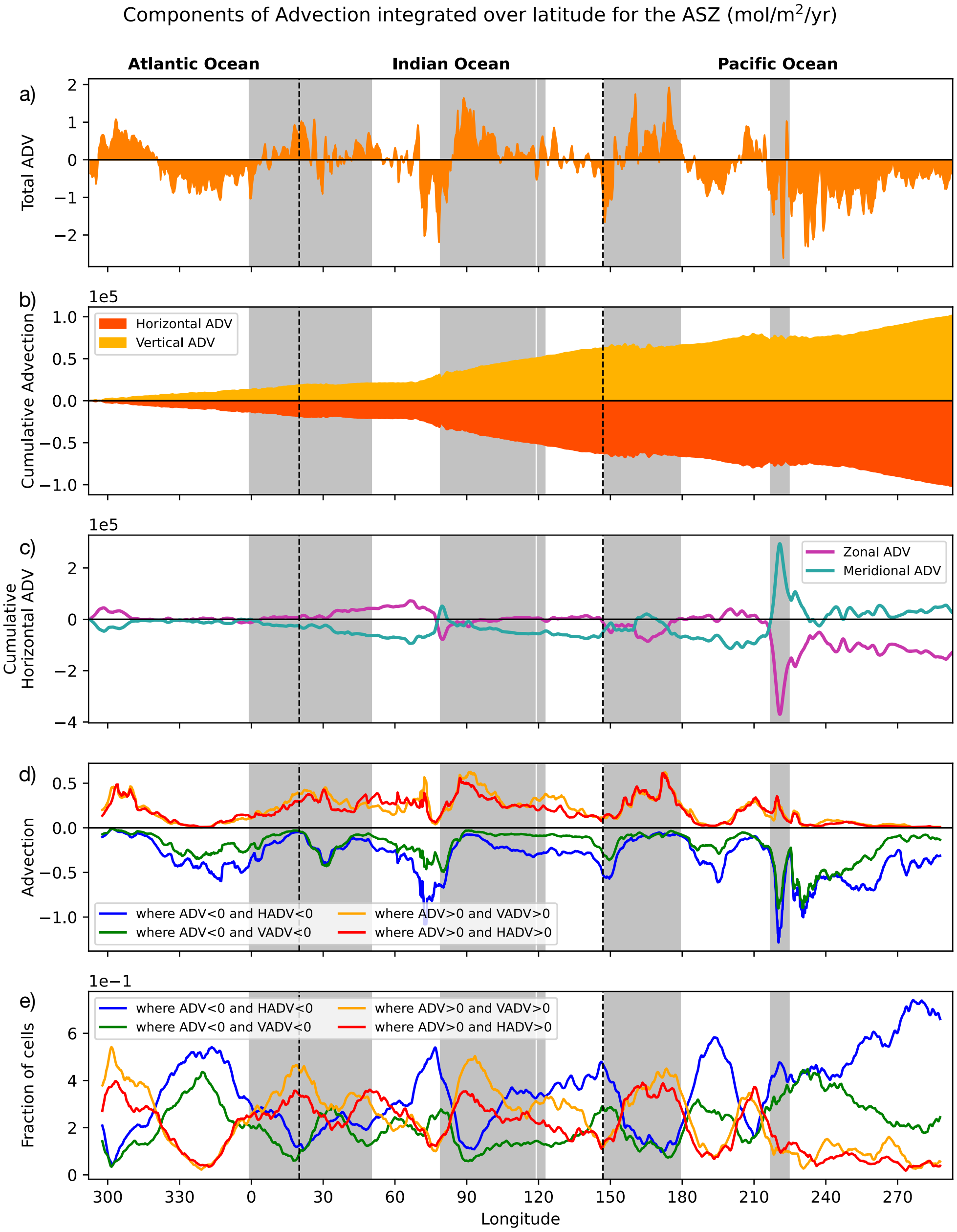

Figure 4.8: Latitudinally and annually integrated a) DIC advective flux, b) cumulative sum along longitude and starting at Drake Passage of the horizontal and vertical advective flux of DIC, c) cumulative sum along longitude and starting at Drake Passage of the zonal and meridional advective flux of DIC, and d) advection of DIC summed over cells of 4 different types: where net advection is positive and horizontal advection is positive (red), where net advection is positive and vertical advection is positive (orange), where net advection is negative and vertical advection is negative (green), and where net advection is negative and horizontal advection is negative (blue). Panels a to d are in mol m^{-2} yr^{-1} and positive values indicate the flux is adding DIC to the mixed layer. e) Same as d except fraction of model cells in the ASZ where each criteria is met. (ASZ: Antarctic Southern Zone)

vertical advection. Overall, cells where negative horizontal advection or positive vertical advection drive the net signal are more prevalent. In areas where the net advective flux transitions between positive and negative values, we observe a shift in the dominant driver—i.e., the relative fractions of these four cell types change over a short distance (Figure 4.8 e). These transition zones are typically characterized by a redistribution of cell types, with the largest change often seen in cells dominated by negative horizontal or positive vertical advection.

When we sum the advective DIC flux across these classified cells, we find that in regions where the net advection is negative, horizontal advection contributes more to the total flux than vertical advection, consistent with the cumulative horizontal flux being negative overall. However, in several longitudinal bands, horizontal and vertical contributions to negative net advection are comparable. This is even more evident for regions with positive net advection, where either component may dominate depending on longitude.

To further dissect horizontal advection, we decompose it into its zonal and meridional components (Figure 4.8 c). Across most longitudes, cumulative meridional advection is the primary driver of negative horizontal advection. Yet this pattern breaks down at the outgassing band in the eastern Pacific: a strong positive meridional advection, linked to a local peak in the entrainment flux, reverses the sign of the cumulative meridional contribution. Interestingly, this positive meridional advection is nearly balanced by negative zonal advection of similar magnitude but opposite sign, indicating compensating flow structures.

Similar dynamics are found in the central Indian Ocean outgassing region and in the two regions to the east. Just upstream of each outgassing region, the net advective flux is negative, primarily due to negative horizontal advection—driven, in turn, by zonal divergence, meaning more DIC is being exported eastward than imported from the south by meridional convergence. As the advection reaches the outgassing regions themselves, the zonal component of horizontal advection transitions from negative to positive. This indicates a shift from zonal divergence to convergence, with DIC now being advected in from the west. Despite this convergence, the net advection may still be negative because of concurrent meridional divergence. In other words, as the zonal convergence increases, meridional outflow becomes the dominant mechanism removing DIC, maintaining a negative net advective flux in the western part of each outgassing region, before the transition to net positive advection.

The region at the Atlantic–Indian boundary differs from this pattern. Unlike the other outgassing zones, this hotspot appears to be the downstream tail of a broader outgassing band located south of the sea ice edge (Figure 4.5 a). It is possible that elevated DIC concentrations in this region are being sustained by lateral advection from the Weddell Gyre, which could act as a remote source of carbon-rich water to the ASZ. This may explain why the structure of advection diverges from that of the other Indian and Pacific hotspots, which are more strongly tied to local vertical mixing and zonal transport processes. This interpretation is consistent with the findings of Sauvé et al. [2023], who showed that Ekman transport of DIC from the sea ice zone into the ASZ played a key role in supporting carbon outgassing.

4.4 Discussion

Our study reveals that carbon outgassing in the ASZ is concentrated in a few discrete hotspots, primarily in the Indian and Pacific basins, while the Atlantic basin exhibits persistent carbon uptake throughout the year. These outgassing hotspots closely align with regions of enhanced vertical mixing of DIC, suggesting that the upward supply of carbon-rich waters is a key driver of the zonally asymmetric air-sea carbon flux structure in the ASZ. Notably, all sharp peaks in vertical mixing occur downstream of major topographic features where seafloor depth shoals significantly. This spatial correspondence points to topographically driven upwelling and mixing as the underlying mechanism sustaining localized outgassing.

These findings are consistent with previous studies that emphasize the role of bathymetry in connecting the deep ocean to the surface via enhanced upwelling and eddy activity in models [Viglione and Thompson, 2016; Tamsitt et al., 2017; Cai et al., 2022; Yung et al., 2022] and observations [Watson et al., 2013; Stappard et al., 2025]. In particular, topographic features are known to intensify eddies and promote vertical transport between the interior and mixed layer. Using Lagrangian particle tracking in a high-resolution model, Brady et al. [2021] found that 71% of DIC-rich water upwelling across 1000 m, and 63% across 200 m, occurs near such features, showing that the impact of topography extends to the upper ocean. Similarly, Dove et al. [2022] identified enhanced ventilation downstream of standing meanders in the ACC, further implicating topography as a control on surface-ocean tracer pathways. Our results build on this understanding by linking topographically driven vertical mixing into the mixed layer to hotspots of carbon outgassing. Prior studies also highlight the role of both background [Ellison et al., 2023] and eddy-driven mixing [Song et al., 2016] in modulating surface $p\mathrm{CO}_2$ variability, supporting the mechanism we identify here. Future work should investigate the potential for targeted process studies using observations from profiling floats or gliders in these regions to validate the proposed mechanisms and further constrain the role of topographically driven mixing in driving carbon outgassing.

However, vertical mixing alone does not fully explain the zonal pattern of carbon flux. Many of the outgassing hotspots display downstream “tails” of elevated flux, aligned with pathways of DIC transport by lateral advection. These features suggest that horizontal advection also plays a crucial role in sustaining outgassing beyond the regions of intense mixing. This is consistent with the well-established ability of the ACC to transport tracer signals zonally, which underpins the widespread use of zonal averaging in Southern Ocean studies [Marshall and Speer, 2012; Rintoul, 2018]. In particular, within the core of the ACC jets, the strong flow carries tracers downstream so quickly that eddies have little chance to mix them across the current [Ferrari and Nikurashin, 2010; Naveira Garabato et al., 2011], resulting in elongated zonal structures with limited meridional spread, just as we observe in the downstream tails. The presence of these downstream plumes also reflects the fact that carbon introduced into the mixed layer from below does not equilibrate with the atmosphere instantaneously. Instead, air-sea equilibration occurs over a timescale of weeks to months [Jones et al., 2014], allowing carbon-rich waters to be advected downstream before being fully outgassed. Future work should explore this downstream transport more explicitly by adopting along-stream coordinate frameworks, which would allow for a clearer assessment of whether the ACC is advecting DIC supplied from below [Marshall and Radko, 2003; Foppert et al., 2025]. Such an approach could also help identify the processes responsible for the termination of these outgassing tails, particularly where lateral advection weakens or reverses, and carbon uptake once again dominates.

It is important to acknowledge that our results are based on a single model, B-SOSE, which exhibits known biases relative to observations [Verdy and Mazloff, 2017; Mazloff et al., 2023]. For instance, we find little zonal asymmetry in biologically driven DIC flux in the mixed layer, whereas Thomalla et al. [2011] identified zonal differences in the phytoplankton seasonal cycle and its sensitivity to physical variability using satellite chlorophyll data. Furthermore, our interbasin flux patterns are partially consistent with those reported by Prend et al. [2022a], who used biogeochemical float data from 2014 to 2020 to estimate air-sea carbon fluxes across both the ASZ and the adjacent Polar Frontal Zone (PFZ). While both studies agree that climatological outgassing is concentrated in the Indo-Pacific, Prend et al. [2022a] also found evidence of outgassing in the Atlantic ASZ, in contrast to our results showing persistent uptake. Prend et al. [2022a] further suggested that entrainment was the primary cause of inter-basin differences, whereas here we are finding that mixing seems to be the dominant factor. Despite these discrepancies with observations, the model provides a valuable framework for constructing a mixed layer DIC budget and investigating the physical drivers of carbon fluxes. While its relatively zonally uniform biological response likely diverges from the real ocean, it facilitates the isolation of physical mechanisms that shape zonal asymmetries in carbon exchange. Although using observations to reconstruct mixed layer DIC budgets at the spatial resolution required to detect these localized hotspots is challenging, validating the relationships identified here using other models, with higher resolution, alternative physical parameterizations, or differing biogeochemical schemes, would provide valuable insight and help assess the robustness of our findings.

Given that the dominant mode of variability in both surface ocean $p\mathrm{CO}_2$ and air-sea carbon flux is seasonal [Gruber et al., 2019], it is essential to examine the seasonal evolution of the DIC budget. This is particularly important considering the inherently seasonal nature of entrainment, which has been shown to drive outgassing in regions such as the central Pacific. A key question is whether outgassing hotspots and their underlying drivers persist year-round, including during summer, when uncertainty in the drivers of the Southern Ocean carbon sink is greatest, and winter, when model–observation discrepancies are largest [Hauck et al., 2023]. While the influence of topographic features on mixing is not expected to vary strongly with season, other processes that affect $p\mathrm{CO}_2$, such as biological drawdown and entrainment, do exhibit strong seasonality and may either amplify or mask the effects of mixing. Extending this analysis to explicitly resolve the seasonal cycle could provide deeper insight into the interplay of these processes and help constrain the mechanisms driving temporal variability in carbon fluxes.

A major advantage of using a model like B-SOSE is the ability to investigate interannual variability, an essential consideration given that the patterns identified in this study may not represent the long-term mean state of the ocean. Such analysis could also shed light on regional discrepancies, such as the area east of Drake Passage, where strong vertical mixing and positive lateral advection are present, yet no clear outgassing signal is observed. Previous studies have documented both interannual and decadal variability in the Southern Ocean carbon sink [Seferian et al., 2013; Resplandy et al., 2015; Gruber et al., 2019]. For example, Landschützer et al. [2015] found that this variability is zonally asymmetric, with thermally and non-thermally driven trends often offsetting each other across basins. Similarly, Gregor et al. [2018] showed that interannual variability is primarily driven by summer processes, whereas winter variability contributes more to decadal trends. While the present study focuses on a single year, it highlights the value of a DIC budget approach for diagnosing carbon flux dynamics in this region. Future work should extend this framework to multiple years to better understand how DIC fluxes and their drivers evolve across seasonal to interannual timescales.

The ASZ exhibits a distinct biogeochemical and physical regime, shaped by its position between two contrasting regions. To the north, the Polar Front acts as a dynamic barrier to meridional exchange, while to the south, the subpolar regime is characterized by weakly sheared circulations and strong sea ice influence [Orsi et al., 1995; Rintoul, 2018]. While the Polar Front represents a dynamical boundary, the southern limit defined by the sea ice edge is seasonal and less effective as a barrier to exchange. Although the ASZ encompasses the primary outgassing regions of interest, it does not evolve in isolation. Interpreting our results therefore requires situating them within the broader Southern Ocean system. For example, the outgassing hotspot near the Atlantic–Indian sector boundary appears to be connected to a larger region of outgassing in the Weddell Gyre, just south of the sea ice edge. This linkage is supported by previous work showing that carbon transport from the Weddell Sea can fuel outgassing in the ASZ [Brown et al., 2015; Sauvé et al., 2023]. Future research could extend this budget framework to the seasonally ice-covered regions to assess broader connectivity. The use of B-SOSE facilitates such analysis by offering detailed, three-dimensional information about adjacent water masses and their interactions.

4.5 Conclusion

The Southern Ocean plays a pivotal role in the global carbon cycle, mediating the exchange of carbon between the atmosphere and the deep ocean. Traditionally, its circulation and biogeochemistry have been understood through a zonally-averaged framework, underpinned by the strong eastward ACC. However, emerging evidence suggests that this zonal-mean view is insufficient to capture the full spatial and temporal variability of Southern Ocean carbon processes, particularly those influencing air-sea carbon flux on seasonal to decadal timescales.

In this study, we address an important gap in understanding how localized physical processes shape the near-surface distribution of dissolved inorganic carbon (DIC) and drive zonal asymmetry in air-sea carbon fluxes. Using a closed mixed layer DIC budget based on monthly output from the high-resolution, data-assimilating B-SOSE model for the year 2018, we investigate sub-basin-scale variations in the ASZ.

We find that carbon outgassing in the ASZ is concentrated at a few discrete hotspots, primarily in the Indian and Pacific basins, while the Atlantic basin is dominated by carbon uptake year-round. The outgassing hotspots align closely with peaks in vertical DIC mixing, who are themselves located just downstream of prominent topographic features, implicating topography-driven enhanced upward supply of carbon-rich waters as a key driver. However, the spatial extent of outgassing, particularly downstream "tails" extending from these hotspots, suggests that lateral advection of DIC also plays a critical role in sustaining outgassing downstream. Entrainment contributes to DIC variability at finer scales, and in isolated cases may initiate localized outgassing. Taken together, our results reveal that zonal asymmetry in carbon fluxes in the ASZ can arise from a complex interplay between vertical and horizontal physical processes, and not only from basin-scale differences in biological activity. These findings support a growing body of work emphasizing the importance of regional and localized dynamics in shaping large-scale carbon fluxes.

Future research should extend this analysis across multiple years and models to assess the robustness of these patterns. The role of biology should also be investigated using approaches capable of resolving finer-scale variability. Moreover, understanding how small-scale features, such as mesoscale eddies and storm-driven mixing, interact with the large-scale circulation to modulate carbon flux is essential. Increasing evidence suggests that regional and event-scale processes can have outsized impacts on global carbon cycling [Gray, 2024]. To improve projections of ocean–atmosphere carbon exchange in a changing climate, we must continue refining our understanding of these regional dynamics and their connections to basin-wide and global processes.

Chapter 5

Conclusion

In view of the importance of the Southern Ocean in the global carbon cycle, it is essential to understand what drives Southern Ocean air-sea exchanges of carbon in order to make predictions about future states of the climate system. This thesis aims to further our process-based understanding of the surface ocean DIC variability which is essential to explain variability in ocean surface $p\mathrm{CO}_2$ and thus carbon air-sea fluxes. A circumpolar DIC budget framework is developed and applied to both observations and global ocean biogeochemistry models in order to quantify the relative importance of different processes in driving the total variability in mixed layer DIC. A closed mixed layer budget in a high resolution data-assimilating model of the Southern Ocean is used to deepen our understanding of variability at smaller spatial scales, thus furthering our understanding of the dominant drivers of the high latitude Southern Ocean carbon cycle.

Chapter 2 presents the first observation-based monthly mixed layer carbon budget for the circumpolar Southern Ocean, constructed using six years of autonomous under-ice capable biogeochemical float data. Focusing on two distinct regions, the Sea Ice Zone (SIZ) and the Antarctic Southern Zone (ASZ), the analysis reveals that seasonal changes in mixed layer DIC concentration are primarily driven by biological fluxes, with a significant contribution from northward Ekman transport, particularly out of the SIZ. On annual timescales, vertical mixing with carbon-rich waters supplies DIC to the mixed layer in both regions, but the fate of this carbon differs between the zones. In the ASZ, this DIC is either utilized by biological production or outgassed to the atmosphere, while in the SIZ, limited by ice cover and light availability, much of the excess DIC is exported northward to the ASZ via Ekman transport. This wind-driven redistribution of DIC highlights an important, previously underappreciated mechanism contributing to carbon outgassing in the southern Antarctic Circumpolar Current. The findings have implications for understanding how the Southern Ocean carbon cycle may respond to future climate change, particularly as diminishing ice cover could shift the location and magnitude of carbon outgassing. These results offer a valuable benchmark for assessing and improving the performance of climate models, which often struggle to capture carbon dynamics in this region.

Chapter 3 adapts the budget framework from Chapter 2 to conduct a process-based analysis of the seasonal variability in mixed-layer DIC in the ASZ, comparing outputs from multiple OMIP models, the data-assimilating B-SOSE model, and an updated observation-based estimate based on Chapter 2. Across all datasets, vertical mixing emerges as the dominant source of DIC to the mixed layer, while biological production is the primary sink. However, models consistently underestimate and delay the spring/summer biological drawdown relative to observations, resulting in a negative annually integrated entrainment flux, opposite in sign to float-based estimates. Advective fluxes, though smaller in magnitude, show the greatest variability across models, largely due to differences in non-Ekman circulation, which, in some cases, reverses expected transport patterns. These discrepancies persist despite models performing well in global-scale evaluations, highlighting the value of seasonal, process-based diagnostics. The findings underscore the importance of accurately capturing both physical and biogeochemical processes, especially biological timing and transport pathways, to improve model fidelity and reduce uncertainty in future projections of the Southern Ocean's role in the global carbon cycle.

Chapter 4 demonstrates that zonal asymmetries in the physical drivers of carbon flux are fundamental to understanding spatial variability in Southern Ocean air-sea CO_2 exchange. Using a closed mixed layer DIC budget derived from the B-SOSE data-assimilating model, we identify three prominent carbon outgassing hotspots in the Indo-Pacific sector of the ASZ, along with a smaller feature in the eastern Pacific. These hotspots are closely associated with enhanced vertical mixing of carbon-rich waters from below the mixed layer, highlighting vertical mixing as the dominant physical mechanism supplying DIC to the surface. Downstream of these mixing maxima, zonal advection transports DIC eastward, sustaining continued outgassing along the path of the Antarctic Circumpolar Current. In some regions, particularly where entrainment fluxes are strong, vertical supply of DIC from changes in mixed layer depth also contributes to localized outgassing. The structure of the net advective flux is shaped by complex interactions between meridional and zonal flow, with changes in the sign of net advection often coinciding with transitions in air-sea CO_2 flux. Critically, all significant DIC mixing hotspots occur downstream of major topographic features, reinforcing the role of bathymetry in modulating vertical exchange. Taken together, these findings illustrate that zonal variability in mixing, advection, and entrainment drives substantial spatial heterogeneity in carbon fluxes within the ASZ, underscoring the limitations of zonally averaged frameworks and the importance of resolving regional processes in understanding and modeling the Southern Ocean carbon sink.

At the heart of this work is an effort to understand the processes that govern the carbon cycle in the Southern Ocean, not just identifying what is happening, but uncovering why it happens. This emphasis on underlying mechanisms has underscored the importance of both physical and biological drivers in shaping the non-thermal component of surface ocean $p\mathrm{CO}_2$, which is often attributed solely to biological processes. In Chapter 2, we showed that seasonal variability in mixed layer DIC is influenced by both biological fluxes and advective transport. This dual influence is echoed in Chapter 3, where both models and observations indicate that biology acts as the dominant sink of DIC, while vertical mixing serves as the largest source. Moreover, Chapter 3 highlighted the interconnectedness of physical and biological processes, showing how a delayed and weakened biological response can lead to a negative entrainment flux, and how limited exchanges between the mixed layer and the interior ocean through mixing may in turn constrain biological activity. Chapter 4 further reveals that even when biological fluxes are relatively uniform across longitudes, regional outgassing is still driven by different physical mechanisms in different areas. For example, vertical mixing may dominate in one sector while lateral advection or entrainment prevails in another. Together, these findings reinforce the need to view carbon fluxes as the product of tightly coupled physical-biogeochemical interactions.

Another central theme of this work is the importance of examining variability beyond global or annual scales. Focusing only on broad averages risks overlooking key regional and seasonal dynamics that are critical to understanding the carbon cycle. A consistent finding throughout this thesis is that the supply of DIC to the mixed layer varies significantly across both space and time, and that this variability is closely linked to patterns of air-sea CO_2 flux. In Chapter 2, we found that advective DIC supply to both the ASZ and SIZ varied seasonally, with a marked decrease in supply from the SIZ during the summer period of carbon uptake. Chapter 3 further emphasized the importance of seasonal resolution, revealing that the magnitude of DIC supply during periods of mixed layer DIC accumulation was correlated with stronger DIC-driven variability in surface ocean $p\text{CO}_2$. Moreover, while the annual mean fluxes appeared comparable across models, resolving their seasonal behavior was key to understanding differences between models and with observations. For instance, only by examining the seasonal evolution of biological fluxes could we explain the emergence of a negative entrainment flux, and the seasonal evolution of the advective flux revealed fundamental circulation difference between models. In Chapter 4, we found that vertical supply of DIC to the mixed layer exhibited strong zonal asymmetry, with localized hotspots initiating outgassing that was then sustained downstream through advection. Together, these findings highlight the limitations of generalizing from a single location or season and demonstrate that capturing the full spatial and temporal complexity of the system is essential for robust predictions of carbon dynamics in the Southern Ocean.

Looking ahead, both the observation-based budget framework and the model-based closed budget can be extended along several key dimensions. The observational framework could be expanded to encompass the full Southern Ocean by leveraging additional Argo float data available since 2020 and adapting the methodology to include more northerly zones that are segmented by continental boundaries. This would broaden the spatial scope of the observational baseline that proved essential for model evaluation in Chapter 3. Expanding the model evaluation itself to include a wider range of models, from high-resolution ocean biogeochemistry models to fully coupled Earth system models with dynamic atmospheres, would strengthen our process-level understanding and help identify common model limitations. Extending the closed budget analysis to seasonal timescales or applying it in along-stream coordinates would further clarify the mechanisms that initiate or terminate carbon outgassing in specific regions. Future work should also project this analysis into the coming decades to assess how mixed layer DIC fluxes evolve under climate change. CMIP model output, from Phases 5 and 6 as well as from future phases of CMIP, offers a valuable opportunity to evaluate whether future trends are robust across models and to uncover the drivers behind intermodel divergence. Such insights are critical for improving the representation of carbon dynamics in models and for enhancing our ability to project how the ocean will respond to climate change. In turn, more reliable projections can support evidence-based climate policymaking, contributing to a just transition toward a low-carbon economy and more effective adaptation strategies.

Bibliography

C. Amante and B.W. Eakins. 2009. ETOPO1 1 Arc-Minute Global Relief Model: Procedures, Data Sources and Analysis. Technical report, National Geophysical Data Center, NOAA.

A Anav, P Friedlingstein, M Kidston, L Bopp, P Ciais, P Cox, C Jones, M Jung, R Myneni, and Z Zhu. 2013. Evaluating the Land and Ocean Components of the Global Carbon Cycle in the CMIP5 Earth System Models. *Journal of Climate*, 26(18):6801–6843. Publisher: American Meteorological Society Place: Boston MA, USA.

Laurence A Anderson and Jorge L Sarmiento. 1994. Redfield ratios of remineralization determined by nutrient data analysis. *Global Biogeochemical Cycles*, 8(1):65–80.

Argo. 2021. Argo float data and metadata from global data assembly centre (argo gdac).

Lionel A Arteaga, Markus Pahlow, Seth M Bushinsky, and Jorge L Sarmiento. 2019. Nutrient Controls on Export Production in the Southern Ocean. *Global Biogeochemical Cycles*, 33(8):942–956.

William M Balch, Nicholas R Bates, Phoebe J Lam, Benjamin S Twining, Sarah Z Rosengard, Bruce C Bowler, Dave T Drapeau, Rebecca Garley, Laura C Lubelczyk, Catherine Mitchell, and Sara Rauschenberg. 2016. Factors regulating the Great Calcite Belt in the Southern Ocean and its biogeochemical significance. *Global Biogeochemical Cycles*, 30(8):1124–1144.

R L Beadling, J L Russell, R J Stouffer, M Mazloff, L D Talley, P J Goodman, J B Sallée, H T Hewitt, P Hyder, and Amarjiit Pandde. 2020. Representation of Southern Ocean Properties across Coupled Model Intercomparison Project Generations: CMIP3 to CMIP6. *Journal of Climate*, 33(15):6555–6581. Publisher: American Meteorological Society Place: Boston MA, USA.

Agatha M de Boer, David K Hutchinson, Fabien Roquet, Louise C Sime, Natalie J Burls, and Céline Heuzé. 2022. The Impact of Southern Ocean Topographic Barriers on the Ocean Circulation and the Overlying Atmosphere. *Journal of Climate*, 35(18):5805–5821. Publisher: American Meteorological Society Place: Boston MA, USA.

L Bopp, M Lévy, L Resplandy, and J B Sallée. 2015. Pathways of anthropogenic carbon subduction in the global ocean. *Geophysical Research Letters*, 42(15):6416–6423.

Mark A Bourassa, Sarah T Gille, Cecilia Bitz, David Carlson, Ivana Cerovecki, Carol Anne Clayson, Meghan F Cronin, Will M Drennan, Chris W Fairall, Ross N Hoffman, Gudrun Magnusdottir, Rachel T Pinker, Ian A Renfrew, Mark Serreze, Kevin Speer, Lynne D Talley, and Gary A Wick. 2013. High-Latitude Ocean and Sea Ice Surface Fluxes: Challenges for Climate Research. *Bulletin of the American Meteorological Society*, 94(3):403–423. Publisher: American Meteorological Society Place: Boston MA, USA.

Riley X Brady, Mathew E Maltrud, Phillip J Wolfram, Henri F Drake, and Nicole S Lovenduski. 2021. The Influence of Ocean Topography on the Upwelling of Carbon in the Southern Ocean. *GEOPHYSICAL RESEARCH LETTERS*, 48(19). Publisher: AMER GEOPHYSICAL UNION Place: 2000 FLORIDA AVE NW, WASHINGTON, DC 20009 USA.

Mary Ann Branch, Thomas F Coleman, and Yuying Li. 1999. A Subspace, Interior, and Conjugate Gradient Method for Large-Scale Bound-Constrained Minimization Problems. *SIAM Journal on Scientific Computing*, 21(1):1–23.

Ellen M Briggs, Todd R Martz, Lynne D Talley, Matthew R Mazloff, and Kenneth S Johnson. 2018. Physical and Biological Drivers of Biogeochemical Tracers Within the Seasonal Sea Ice Zone of the Southern Ocean From Profiling Floats. *Journal of Geophysical Research: Oceans*, 123(2):746–758.

Ben Bronselaer, Laure Zanna, David R Munday, and Jason Lowe. 2018. Southern Ocean carbon-wind stress feedback. *Climate Dynamics*, 51(7):2743–2757.

Peter J Brown, Loïc Jullion, Peter Landschützer, Dorothee C E Bakker, Alberto C Naveira Garabato, Michael P Meredith, Sinhue Torres-Valdés, Andrew J Watson, Mario Hoppema, Brice Loose, Elizabeth M

Jones, Maciej Telszewski, Steve D Jones, and Rik Wanninkhof. 2015. Carbon dynamics of the Weddell Gyre, Southern Ocean. *Global Biogeochemical Cycles*, 29(3):288–306.

Seth M Bushinsky and Ivana Cerovečki. 2023. Subantarctic Mode Water Biogeochemical Formation Properties and Interannual Variability. *AGU Advances*, 4(2):e2022AV000722.

Seth M Bushinsky, Alison R Gray, Kenneth S Johnson, and Jorge L Sarmiento. 2017. Oxygen in the Southern Ocean From Argo Floats: Determination of Processes Driving Air-Sea Fluxes. *Journal of Geophysical Research: Oceans*, 122(11):8661–8682.

Seth M Bushinsky, Peter Landschützer, Christian Rödenbeck, Alison R Gray, David Baker, Matthew R Mazloff, Laure Resplandy, Kenneth S Johnson, and Jorge L Sarmiento. 2019. Reassessing Southern Ocean Air-Sea CO2 Flux Estimates With the Addition of Biogeochemical Float Observations. *Global Biogeochemical Cycles*, 33(11):1370–1388.

Brian J Butterworth and Scott D Miller. 2016. Air-sea exchange of carbon dioxide in the Southern Ocean and Antarctic marginal ice zone. *Geophysical Research Letters*, 43(13):7223–7230.

Richard H. Byrd, Peihuang Lu, Jorge Nocedal, and Ciyou Zhu. 1995. A Limited Memory Algorithm for Bound Constrained Optimization. *SIAM Journal on Scientific Computing*, 16(5):1190–1208. _eprint: https://doi.org/10.1137/0916069.

Yongqing Cai, Dake Chen, Matthew R. Mazloff, Tao Lian, and Xiaohui Liu. 2022. Topographic Modulation of the Wind Stress Impact on Eddy Activity in the Southern Ocean. *Geophysical Research Letters*, 49(13):e2022GL097859. _eprint: https://agupubs.onlinelibrary.wiley.com/doi/pdf/10.1029/2022GL097859.

Magdalena M. Carranza and Sarah T. Gille. 2015. Southern Ocean wind-driven entrainment enhances satellite chlorophyll-a through the summer. *Journal of Geophysical Research: Oceans*, 120(1):304–323. _eprint: https://agupubs.onlinelibrary.wiley.com/doi/pdf/10.1002/2014JC010203.

Dustin Carroll, Dimitris Menemenlis, Stephanie Dutkiewicz, Jonathan M Lauderdale, Jess F Adkins, Kevin W Bowman, Holger Brix, Ian Fenty, Michelle M Gierach, Chris Hill, Oliver Jahn, Peter Landschützer, Manfredi Manizza, Matt R Mazloff, Charles E Miller, David S Schimel, Ariane Verdy, Daniel B

Whitt, and Hong Zhang. 2022. Attribution of Space-Time Variability in Global-Ocean Dissolved Inorganic Carbon. *Global Biogeochemical Cycles*, 36(3):e2021GB007162.

B R Carter, R A Feely, N L Williams, A G Dickson, M B Fong, and Y Takeshita. 2018. Updated methods for global locally interpolated estimation of alkalinity, pH, and nitrate. *Limnology and Oceanography: Methods*, 16(2):119–131.

Sandra L Castro, Gary A Wick, and Michael Steele. 2016. Validation of satellite sea surface temperature analyses in the Beaufort Sea using UpTempO buoys. *Remote Sensing of Environment*, 187:458–475.

J. B. Charrassin, F. Roquet, Y. H. Park, F. Bailleul, C. Guinet, M. Meredith, K. Nicholls, S. Thorpe, Y. Tremblay, D. Costa, Miriam Göbel, M. Muelbert, M. N. Bester, Joachim Plötz, Horst Bornemann, Ralph Timmermann, M. Hindell, A. Meijers, R. C. Coleman, I. C. Field, C. McMahon, S. Rintoul, S. Sokolov, M. Fedak, P. Lovell, M. Biuw, K. Kovacs, and C. Lydersen. 2010. New insights into Southern Ocean physical and biological processes revealed by instrumented elephant seals. *Proceedings of OceanObs 09: Sustained Ocean Observations and Information for Society (Vol. 2), Venice, Italy, 21-25 September 2009, Hall, J., Harrison D.E. & Stammer, D., Eds., ESA Publication WPP-306.*

P. Ciais, C. Sabine, G. Bala, L. Bopp, V. Brovkin, J. Canadell, A. Chhabra, R. DeFries, J. Galloway, M. Heimann, C.Jones, C. Le Quéré, R.B. Myneni, S. Piao, and P. Thornton. 2013. Carbon and Other Biogeochemical Cycles. In T.F. Stocker, D. Qin, G.-K. Plattner, M. Tignor, S.K. Allen, J. Boschung, A. Nauels, Y. Xia, V. Bex, and P.M. Midgley, editors, *Climate Change 2013: The Physical Science Basis. Contribution of Working Group I to the Fifth Assessment Report of the Intergovernmental Panel on Climate Change*. Cambridge, United Kingdom and New York, NY, USA.

Aimee Coggins, Andrew J Watson, Ute Schuster, Neill Mackay, Brian King, Elaine McDonagh, and Alex J Poulton. 2023. Surface ocean carbon budget in the 2017 south Georgia diatom bloom: Observations and validation of profiling biogeochemical argo floats. *Deep Sea Research Part II: Topical Studies in Oceanography*, 209:105275.

Climate Data Store Copernicus Climate Change Service. 2021. Oras5 global ocean reanalysis monthly data from 1958 to present.

Meghan F Cronin, Noel A Pelland, Steven R Emerson, and William R Crawford. 2015. Estimating diffusivity from the mixed layer heat and salt balances in the North Pacific. *Journal of Geophysical Research: Oceans*, 120(11):7346–7362.

Clément de Boyer Montégut, Gurvan Madec, Albert S Fischer, Alban Lazar, and Daniele Iudicone. 2004. Mixed layer depth over the global ocean: An examination of profile data and a profile-based climatology. *Journal of Geophysical Research: Oceans*, 109(C12).

Tim DeVries. 2014. The oceanic anthropogenic CO2 sink: Storage, air-sea fluxes, and transports over the industrial era. *Global Biogeochemical Cycles*, 28(7):631–647. Publisher: AMER GEOPHYSICAL UNION Place: 2000 FLORIDA AVE NW, WASHINGTON, DC 20009 USA.

Tim DeVries and Curtis Deutsch. 2014. Large-scale variations in the stoichiometry of marine organic matter respiration. *Nature Geoscience*, 7(12):890–894.

Tim DeVries, Corinne Le Quéré, Oliver Andrews, Sarah Berthet, Judith Hauck, Tatiana Ilyina, Peter Landschützer, Andrew Lenton, Ivan D Lima, Michael Nowicki, Jörg Schwinger, and Roland Séférian. 2019. Decadal trends in the ocean carbon sink. *Proceedings of the National Academy of Sciences*, 116(24):11646–11651.

Tim DeVries, Kana Yamamoto, Rik Wanninkhof, Nicolas Gruber, Judith Hauck, Jens Daniel Müller, Laurent Bopp, Dustin Carroll, Brendan Carter, Thi-Tuyet-Trang Chau, Scott C. Doney, Marion Gehlen, Lucas Gloege, Luke Gregor, Stephanie Henson, Ji Hyun Kim, Yosuke Iida, Tatiana Ilyina, Peter Landschützer, Corinne Le Quéré, David Munro, Cara Nissen, Lavinia Patara, Fiz F. Pérez, Laure Resplandy, Keith B. Rodgers, Jörg Schwinger, Roland Séférian, Valentina Sicardi, Jens Terhaar, Joaquin Triñanes, Hiroyuki Tsujino, Andrew Watson, Sayaka Yasunaka, and Jiye Zeng. 2023. Magnitude, Trends, and Variability of the Global Ocean Carbon Sink From 1985 to 2018. *Global Biogeochemical Cycles*, 37(10):e2023GB007780. _eprint: https://agupubs.onlinelibrary.wiley.com/doi/pdf/10.1029/2023GB007780.

Andrew G Dickson. 1990. Standard potential of the reaction: AgCl(s) + 12H2(g) = Ag(s) + HCl(aq), and

and the standard acidity constant of the ion HSO4 in synthetic sea water from 273.15 to 318.15 K. *The Journal of Chemical Thermodynamics*, 22(2):113–127.

Lilian A Dove, Dhruv Balwada, Andrew F Thompson, and Alison R Gray. 2022. Enhanced Ventilation in Energetic Regions of the Antarctic Circumpolar Current. *Geophysical Research Letters*, 49(13):e2021GL097574.

Carolina O. Dufour, Stephen M. Griffies, Gregory F. de Souza, Ivy Frenger, Adele K. Morrison, Jaime B. Palter, Jorge L. Sarmiento, Eric D. Galbraith, John P. Dunne, Whit G. Anderson, and Richard D. Slater. 2015. Role of mesoscale eddies in cross-frontal transport of heat and biogeochemical tracers in the Southern Ocean. *Journal of Physical Oceanography*, 45(12):3057–3081.

Carolina O Dufour, Julien Le Sommer, Marion Gehlen, James C Orr, Jean-Marc Molines, Jennifer Simeon, and Bernard Barnier. 2013. Eddy compensation and controls of the enhanced sea-to-air CO2 flux during positive phases of the Southern Annular Mode. *Global Biogeochemical Cycles*, 27(3):950–961.

S. Dutreuil, L. Bopp, and A. Tagliabue. 2009. Impact of enhanced vertical mixing on marine biogeochemistry: lessons for geo-engineering and natural variability. *Biogeosciences*, 6(5):901–912.

E. Ellison, A. Mashayek, and M. Mazloff. 2023. The Sensitivity of Southern Ocean Air-Sea Carbon Fluxes to Background Turbulent Diapycnal Mixing Variability. *Journal of Geophysical Research: Oceans*.

V Eyring, S Bony, G A Meehl, C A Senior, B Stevens, R J Stouffer, and K E Taylor. 2016. Overview of the Coupled Model Intercomparison Project Phase 6 (CMIP6) experimental design and organization. *Geoscientific Model Development*, 9(5):1937–1958.

A R Fay and G A McKinley. 2021. Observed Regional Fluxes to Constrain Modeled Estimates of the Ocean Carbon Sink. *Geophysical Research Letters*, 48(20):e2021GL095325.

Amanda R Fay, Luke Gregor, Peter Landschützer, Galen A McKinley, Nicolas Gruber, Marion Gehlen, Yosuke Iida, Goulven Gildas Laruelle, Christian Rödenbeck, and Jiye Zeng. 2021. Harmonization of global surface ocean pCO2 mapped products and their flux calculations; an improved estimate of the ocean carbon sink. *Earth System Science Data Discussions*, pages 1–32.

Raffaele Ferrari and Maxim Nikurashin. 2010. Suppression of Eddy Diffusivity across Jets in the Southern Ocean. *Journal of Physical Oceanography*, 40(7):1501 – 1519. Place: Boston MA, USA Publisher: American Meteorological Society.

B J Fisher, A J Poulton, M P Meredith, K Baldry, O Schofield, and S F Henley. 2023. Biogeochemistry of climate driven shifts in Southern Ocean primary producers. *Biogeosciences Discussions*, 2023:1–29.

Ryan L. Fogt, Julie M. Jones, and James Renwick. 2012. Seasonal Zonal Asymmetries in the Southern Annular Mode and Their Impact on Regional Temperature Anomalies. *Journal of Climate*, 25(18):6253 – 6270. Place: Boston MA, USA Publisher: American Meteorological Society.

Annie Foppert, Stephen R. Rintoul, and Helen E. Phillips. 2025. Absolute Velocity, Transport and Stability of the Polar Front Downstream of the Southeast Indian Ridge. *Journal of Geophysical Research: Oceans*, 130(6):e2024JC021853. _eprint: https://agupubs.onlinelibrary.wiley.com/doi/pdf/10.1029/2024JC021853.

P Friedlingstein, M W Jones, M O'Sullivan, R M Andrew, D C E Bakker, J Hauck, C Le Quéré, G P Peters, W Peters, J Pongratz, S Sitch, J G Canadell, P Ciais, R B Jackson, S R Alin, P Anthoni, N R Bates, M Becker, N Bellouin, L Bopp, T T T Chau, F Chevallier, L P Chini, M Cronin, K I Currie, B Decharme, L M Djeutchouang, X Dou, W Evans, R A Feely, L Feng, T Gasser, D Gilfillan, T Gkritzalis, G Grassi, L Gregor, N Gruber, Ö Gürses, I Harris, R A Houghton, G C Hurtt, Y Iida, T Ilyina, I T Luijkx, A Jain, S D Jones, E Kato, D Kennedy, K Klein Goldewijk, J Knauer, J I Korsbakken, A Körtzinger, P Landschützer, S K Lauvset, N Lefèvre, S Lienert, J Liu, G Marland, P C McGuire, J R Melton, D R Munro, J E M S Nabel, S.-I. Nakaoka, Y Niwa, T Ono, D Pierrot, B Poulter, G Rehder, L Resplandy, E Robertson, C Rödenbeck, T M Rosan, J Schwinger, C Schwingshackl, R Séférian, A J Sutton, C Sweeney, T Tanhua, P P Tans, H Tian, B Tilbrook, F Tubiello, G R van der Werf, N Vuichard, C Wada, R Wanninkhof, A J Watson, D Willis, A J Wiltshire, W Yuan, C Yue, X Yue, S Zaehle, and J Zeng. 2022. Global Carbon Budget 2021. *Earth System Science Data*, 14(4):1917–2005.

P. Friedlingstein, M. O'Sullivan, M. W. Jones, R. M. Andrew, J. Hauck, P. Landschützer, C. Le Quéré, H. Li, I. T. Luijkx, A. Olsen, G. P. Peters, W. Peters, J. Pongratz, C. Schwingshackl, S. Sitch, J. G. Canadell, P. Ciais, R. B. Jackson, S. R. Alin, A. Arneth, V. Arora, N. R. Bates, M. Becker, N. Bellouin, C. F.

Berghoff, H. C. Bittig, L. Bopp, P. Cadule, K. Campbell, M. A. Chamberlain, N. Chandra, F. Chevallier, L. P. Chini, T. Colligan, J. Decayeux, L. M. Djeutchouang, X. Dou, C. Duran Rojas, K. Enyo, W. Evans, A. R. Fay, R. A. Feely, D. J. Ford, A. Foster, T. Gasser, M. Gehlen, T. Gkritzalis, G. Grassi, L. Gregor, N. Gruber, Ö. Gürses, I. Harris, M. Hefner, J. Heinke, G. C. Hurtt, Y. Iida, T. Ilyina, A. R. Jacobson, A. K. Jain, T. Jarníková, A. Jersild, F. Jiang, Z. Jin, E. Kato, R. F. Keeling, K. Klein Goldewijk, J. Knauer, J. I. Korsbakken, X. Lan, S. K. Lauvset, N. Lefèvre, Z. Liu, J. Liu, L. Ma, S. Maksyutov, G. Marland, N. Mayot, P. C. McGuire, N. Metzl, N. M. Monacci, E. J. Morgan, S.-I. Nakaoka, C. Neill, Y. Niwa, T. Nützel, L. Olivier, T. Ono, P. I. Palmer, D. Pierrot, Z. Qin, L. Resplandy, A. Roobaert, T. M. Rosan, C. Rödenbeck, J. Schwinger, T. L. Smallman, S. M. Smith, R. Sospedra-Alfonso, T. Steinhoff, Q. Sun, A. J. Sutton, R. Séférian, S. Takao, H. Tatebe, H. Tian, B. Tilbrook, O. Torres, E. Tourigny, H. Tsujino, F. Tubiello, G. van der Werf, R. Wanninkhof, X. Wang, D. Yang, X. Yang, Z. Yu, W. Yuan, X. Yue, S. Zaehle, N. Zeng, and J. Zeng. 2025. Global Carbon Budget 2024. *Earth System Science Data*, 17(3):965–1039.

Weiwei Fu, J. Keith Moore, Francois Primeau, Nathan Collier, Oluwaseun O. Ogunro, Forrest M. Hoffman, and James T. Randerson. 2022. Evaluation of Ocean Biogeochemistry and Carbon Cycling in CMIP Earth System Models With the International Ocean Model Benchmarking (IOMB) Software System. *Journal of Geophysical Research: Oceans*, 127(10):e2022JC018965. _eprint: https://agupubs.onlinelibrary.wiley.com/doi/pdf/10.1029/2022JC018965.

E. D. Galbraith, A. Gnanadesikan, J. P. Dunne, and M. R. Hiscock. 2010. Regional impacts of iron-light colimitation in a global biogeochemical model. *Biogeosciences*, 7(3):1043–1064.

Lucas Gloege, Galen A McKinley, Peter Landschützer, Amanda R Fay, Thomas L Frölicher, John C Fyfe, Tatiana Ilyina, Steve Jones, Nicole S Lovenduski, Keith B Rodgers, Sarah Schlunegger, and Yohei Takano. 2021. Quantifying Errors in Observationally Based Estimates of Ocean Carbon Sink Variability. *Global Biogeochemical Cycles*, 35(4):e2020GB006788.

Alison R. Gray. 2024. The Four-Dimensional Carbon Cycle of the Southern Ocean. *Annual Review of Marine Science*, 16(Volume 16, 2024):163–190. Publisher: Annual Reviews Type: Journal Article.

Alison R. Gray, Kenneth S. Johnson, Seth M. Bushinsky, Stephen C. Riser, Joellen L. Russell, Lynne D.

Talley, Rik Wanninkhof, Nancy L. Williams, and Jorge L. Sarmiento. 2018. Autonomous Biogeochemical Floats Detect Significant Carbon Dioxide Outgassing in the High-Latitude Southern Ocean. *Geophysical Research Letters*, 45(17):9049–9057.

Alison R Gray and Stephen C Riser. 2014. A Global Analysis of Sverdrup Balance Using Absolute Geostrophic Velocities from Argo. *Journal of Physical Oceanography*, 44(4):1213–1229.

L Gregor, S Kok, and P M S Monteiro. 2018. Interannual drivers of the seasonal cycle of CO$_{2}$ in the Southern Ocean. *Biogeosciences*, 15(8):2361–2378.

Luke Gregor and Amanda Fay. 2021. SeaFlux: harmonised sea-air CO2 fluxes from surface pCO2 data products using a standardised approach.

S. M. Griffies, G. Danabasoglu, P. J. Durack, A. J. Adcroft, V. Balaji, C. W. Böning, E. P. Chassignet, E. Curchitser, J. Deshayes, H. Drange, B. Fox-Kemper, P. J. Gleckler, J. M. Gregory, H. Haak, R. W. Hallberg, P. Heimbach, H. T. Hewitt, D. M. Holland, T. Ilyina, J. H. Jungclaus, Y. Komuro, J. P. Krasting, W. G. Large, S. J. Marsland, S. Masina, T. J. McDougall, A. J. G. Nurser, J. C. Orr, A. Pirani, F. Qiao, R. J. Stouffer, K. E. Taylor, A. M. Treguier, H. Tsujino, P. Uotila, M. Valdivieso, Q. Wang, M. Winton, and S. G. Yeager. 2016. OMIP contribution to CMIP6: experimental and diagnostic protocol for the physical component of the Ocean Model Intercomparison Project. *Geoscientific Model Development*, 9(9):3231–3296.

Sjoerd Groeskamp, Andrew Lenton, Richard Matear, Bernadette M. Sloyan, and Clothilde Langlais. 2016. Anthropogenic carbon in the ocean—Surface to interior connections. *Global Biogeochemical Cycles*, 30(11):1682–1698. _eprint: https://agupubs.onlinelibrary.wiley.com/doi/pdf/10.1002/2016GB005476.

Nicolas Gruber, Dorothee C E Bakker, Tim DeVries, Luke Gregor, Judith Hauck, Peter Landschützer, Galen A McKinley, and Jens Daniel Müller. 2023. Trends and variability in the ocean carbon sink. *Nature Reviews Earth & Environment*.

Nicolas Gruber, Manuel Gloor, Sara E Mikaloff Fletcher, Scott C Doney, Stephanie Dutkiewicz, Michael J Follows, Markus Gerber, Andrew R Jacobson, Fortunat Joos, Keith Lindsay, Dimitris Menemenlis, Anne

Mouchet, Simon A Müller, Jorge L Sarmiento, and Taro Takahashi. 2009. Oceanic sources, sinks, and transport of atmospheric CO2. *Global Biogeochemical Cycles*, 23(1).

Nicolas Gruber, Peter Landschützer, and Nicole S Lovenduski. 2019. The Variable Southern Ocean Carbon Sink. *Annual Review of Marine Science*, 11(1):159–186.

Mukund Gupta, Michael J Follows, and Jonathan Maitland Lauderdale. 2020. The Effect of Antarctic Sea Ice on Southern Ocean Carbon Outgassing: Capping versus Light Attenuation. *Global Biogeochemical Cycles*, n/a(n/a):e2019GB006489.

Robert Hallberg and Anand Gnanadesikan. 2006. The role of eddies in determining the structure and response of the wind-driven southern hemisphere overturning: Results from the Modeling Eddies in the Southern Ocean (MESO) project. *Journal of physical oceanography*, 36(12):2232–2252.

J Hauck, C Völker, T Wang, M Hoppema, M Losch, and D A Wolf-Gladrow. 2013. Seasonally different carbon flux changes in the Southern Ocean in response to the southern annular mode. *Global Biogeochemical Cycles*, 27(4):1236–1245.

Judith Hauck, Luke Gregor, Cara Nissen, Lavinia Patara, Mark Hague, Precious Mongwe, Seth Bushinsky, Scott C. Doney, Nicolas Gruber, Corinne Le Quéré, Manfredi Manizza, Matthew Mazloff, Pedro M. S. Monteiro, and Jens Terhaar. 2023. The Southern Ocean Carbon Cycle 1985–2018: Mean, Seasonal Cycle, Trends, and Storage. *Global Biogeochemical Cycles*, 37(11):e2023GB007848. _eprint: https://onlinelibrary.wiley.com/doi/pdf/10.1029/2023GB007848.

Judith Hauck, Moritz Zeising, Corinne Le Quéré, Nicolas Gruber, Dorothee C E Bakker, Laurent Bopp, Thi Tuyet Trang Chau, Özgür Gürses, Tatiana Ilyina, Peter Landschützer, Andrew Lenton, Laure Resplandy, Christian Rödenbeck, Jörg Schwinger, and Roland Séférian. 2020. Consistency and Challenges in the Ocean Carbon Sink Estimate for the Global Carbon Budget. *Frontiers in Marine Science*, 7.

H Hersbach, B Bell, P Berrisford, G Biavati, A Horányi, J Muñoz Sabater, J Nicolas, C Peubey, R Radu, I Rozum, D Schepers, A Simmons, C Soci, D Dee, and J-N Thépaut. 2021. Era5 monthly averaged data on single levels from 1940 to present.

Hans Hersbach, Bill Bell, Paul Berrisford, Shoji Hirahara, András Horányi, Joaquín Muñoz-Sabater, Julien Nicolas, Carole Peubey, Raluca Radu, Dinand Schepers, Adrian Simmons, Cornel Soci, Saleh Abdalla, Xavier Abellan, Gianpaolo Balsamo, Peter Bechtold, Gionata Biavati, Jean Bidlot, Massimo Bonavita, Giovanna De Chiara, Per Dahlgren, Dick Dee, Michail Diamantakis, Rossana Dragani, Johannes Flemming, Richard Forbes, Manuel Fuentes, Alan Geer, Leo Haimberger, Sean Healy, Robin J Hogan, Elías Hólm, Marta Janisková, Sarah Keeley, Patrick Laloyaux, Philippe Lopez, Cristina Lupu, Gabor Radnoti, Patricia de Rosnay, Iryna Rozum, Freja Vamborg, Sebastien Villaume, and Jean-Noël Thépaut. 2020. The ERA5 global reanalysis. *Quarterly Journal of the Royal Meteorological Society*, 146(730):1999–2049.

James Holte and Lynne Talley. 2009. A New Algorithm for Finding Mixed Layer Depths with Applications to Argo Data and Subantarctic Mode Water Formation. *Journal of Atmospheric and Oceanic Technology*, 26(9):1920–1939.

Yibin Huang, Andrea J Fassbender, and Seth M Bushinsky. 2023. Biogenic carbon pool production maintains the Southern Ocean carbon sink. *Proceedings of the National Academy of Sciences*, 120(18):e2217909120.

M. P. Humphreys, A. J. Schiller, D. E. Sandborn, L. Gregor, D. Pierrot, S. M. A. C. van Heuven, E. R. Lewis, and D. W. R. Wallace. 2021. PyCO2SYS: marine carbonate system calculations in Python.

T Ito, M Woloszyn, and M Mazloff. 2010. Anthropogenic carbon dioxide transport in the Southern Ocean driven by Ekman flow. *Nature*, 463(7277):80–83.

D Iudicone, K B Rodgers, I Stendardo, O Aumont, G Madec, L Bopp, O Mangoni, and M Ribera d'Alcala'. 2011. Water masses as a unifying framework for understanding the Southern Ocean Carbon Cycle. *Biogeosciences*, 8(5):1031–1052.

Annika Jersild and Takamitsu Ito. 2020. Physical and Biological Controls of the Drake Passage pCO2 Variability. *Global Biogeochemical Cycles*, 34(9):e2020GB006644.

Kenneth S Johnson, Joshua N Plant, Luke J Coletti, Hans W Jannasch, Carole M Sakamoto, Stephen C Riser, Dana D Swift, Nancy L Williams, Emmanuel Boss, Nils Haëntjens, Lynne D Talley, and Jorge L

Sarmiento. 2017a. Biogeochemical sensor performance in the SOCCOM profiling float array. *Journal of Geophysical Research: Oceans*, 122(8):6416–6436.

Kenneth S Johnson, Joshua N Plant, John P Dunne, Lynne D Talley, and Jorge L Sarmiento. 2017b. Annual nitrate drawdown observed by SOCCOM profiling floats and the relationship to annual net community production. *Journal of Geophysical Research: Oceans*, 122(8):6668–6683.

Daniel C. Jones, Takamitsu Ito, Yohei Takano, and Wei-Ching Hsu. 2014. Spatial and seasonal variability of the air-sea equilibration timescale of carbon dioxide. *Global Biogeochemical Cycles*, 28(11):1163–1178. _eprint: https://agupubs.onlinelibrary.wiley.com/doi/pdf/10.1002/2014GB004813.

Marie Paule Jouandet, Stephane Blain, Nicolas Metzl, Christian Brunet, Thomas W Trull, and Ingrid Obernosterer. 2008. A seasonal carbon budget for a naturally iron-fertilized bloom over the Kerguelen Plateau in the Southern Ocean. *Deep Sea Research Part II: Topical Studies in Oceanography*, 55(5):856–867.

Lydia Keppler and Peter Landschützer. 2019. Regional Wind Variability Modulates the Southern Ocean Carbon Sink. *Scientific Reports*, 9(1):7384.

Stefan Kern and Gunnar Spreen. 2015. Uncertainties in Antarctic sea-ice thickness retrieval from ICESat. *Annals of Glaciology*, 56(69):107–119.

A. E. Kiss, A. McC. Hogg, N. Hannah, F. Boeira Dias, G. B. Brassington, M. A. Chamberlain, C. Chapman, P. Dobrohotoff, C. M. Domingues, E. R. Duran, M. H. England, R. Fiedler, S. M. Griffies, A. Heerdegen, P. Heil, R. M. Holmes, A. Klocker, S. J. Marsland, A. K. Morrison, J. Munroe, M. Nikurashin, P. R. Oke, G. S. Pilo, O. Richet, A. Savita, P. Spence, K. D. Stewart, M. L. Ward, F. Wu, and X. Zhang. 2020. ACCESS-OM2 v1.0: a global ocean–sea ice model at three resolutions. *Geoscientific Model Development*, 13(2):401–442.

I. Kriest. 2017. Calibration of a simple and a complex model of global marine biogeochemistry. *Biogeosciences*, 14:4965–4984.

K M Krumhardt, M C Long, K Lindsay, and M N Levy. 2020. Southern Ocean Calcification Controls the Global Distribution of Alkalinity. *Global Biogeochemical Cycles*, 34(12):e2020GB006727.

Kyungmin Kwak, Hajoon Song, John Marshall, Hyodae Seo, and Dennis J McGillicuddy Jr. 2021. Suppressed pCO2 in the Southern Ocean Due to the Interaction Between Current and Wind. *Journal of Geophysical Research: Oceans*, 126(12):e2021JC017884.

L. Lacour, N. Briggs, H. Claustre, M. Ardyna, and G. Dall'Olmo. 2019. The Intraseasonal Dynamics of the Mixed Layer Pump in the Subpolar North Atlantic Ocean: A Biogeochemical-Argo Float Approach. *Global Biogeochemical Cycles*, 33(3):266–281. _eprint: https://agupubs.onlinelibrary.wiley.com/doi/pdf/10.1029/2018GB005997 Citaiton Key: Lacour2019.

L. Lacour, Joan Llort, N. Briggs, P. Strutton, and P. Boyd. 2023. Seasonality of downward carbon export in the Pacific Southern Ocean revealed by multi-year robotic observations. *Nature Communications*, 14.

P Landschützer, N Gruber, D C E Bakker, and U Schuster. 2014. Recent variability of the global ocean carbon sink. *Global Biogeochemical Cycles*, 28(9):927–949.

Peter Landschützer, Nicolas Gruber, and Dorothee C E Bakker. 2016. Decadal variations and trends of the global ocean carbon sink. *Global Biogeochemical Cycles*, 30(10):1396–1417.

Peter Landschützer, Nicolas Gruber, F Alexander Haumann, Christian Rödenbeck, Dorothee C E Bakker, Steven van Heuven, Mario Hoppema, Nicolas Metzl, Colm Sweeney, Taro Takahashi, Bronte Tilbrook, and Rik Wanninkhof. 2015. The reinvigoration of the Southern Ocean carbon sink. *Science*, 349(6253):1221–1224.

W. G. Large and S. G. Yeager. 2009. The global climatology of an interannually varying air–sea flux data set. *Climate Dynamics*, 33(2):341–364.

C S Law, E R Abraham, A J Watson, and M I Liddicoat. 2003. Vertical eddy diffusion and nutrient supply to the surface mixed layer of the Antarctic Circumpolar Current. *JOURNAL OF GEOPHYSICAL RESEARCH-OCEANS*, 108(C8). Publisher: AMER GEOPHYSICAL UNION Place: 2000 FLORIDA AVE NW, WASHINGTON, DC 20009 USA.

Kitack Lee, Tae-Wook Kim, Robert H Byrne, Frank J Millero, Richard A Feely, and Yong-Ming Liu. 2010. The universal ratio of boron to chlorinity for the North Pacific and North Atlantic oceans. *Geochimica et Cosmochimica Acta*, 74(6):1801–1811.

Paul Lerner, Anastasia Romanou, Maxwell Kelley, Joy Romanski, Reto Ruedy, and Gary Russell. 2021. Drivers of Air-Sea CO2 Flux Seasonality and its Long-Term Changes in the NASA-GISS Model CMIP6 Submission. *Journal of Advances in Modeling Earth Systems*, 13(2):1–33.

M Levy, L Bopp, P Karleskind, L Resplandy, C Ethe, and F Pinsard. 2013. Physical pathways for carbon transfers between the surface mixed layer and the ocean interior. *Global Biogeochemical Cycles*, 27(4):1001–1012. Publisher: AMER GEOPHYSICAL UNION Place: 2000 FLORIDA AVE NW, WASHINGTON, DC 20009 USA.

Changyu Li, Jianping Huang, Lei Ding, Yu Ren, Linli An, Xiaoyue Liu, and Jiping Huang. 2022. The Variability of Air-sea O2 Flux in CMIP6: Implications for Estimating Terrestrial and Oceanic Carbon Sinks. *Advances in Atmospheric Sciences*, 39(8):1271–1284.

Huan Li, Hongjie Xie, Stefan Kern, Wei Wan, Burcu Ozsoy, Stephan Ackley, and Yang Hong. 2018. Spatio-temporal variability of Antarctic sea-ice thickness and volume obtained from ICESat data using an innovative algorithm. *Remote Sensing of Environment*, 219:44–61.

Qing Li, Brandon G. Reichl, Baylor Fox-Kemper, Alistair J. Adcroft, Stephen E. Belcher, Gokhan Danabasoglu, Alan L. M. Grant, Stephen M. Griffies, Robert Hallberg, Tetsu Hara, Ramsey R. Harcourt, Tobias Kukulka, William G. Large, James C. McWilliams, Brodie Pearson, Peter P. Sullivan, Luke Van Roekel, Peng Wang, and Zhihua Zheng. 2019. Comparing Ocean Surface Boundary Vertical Mixing Schemes Including Langmuir Turbulence. *Journal of Advances in Modeling Earth Systems*, 11(11):3545–3592. _eprint: https://agupubs.onlinelibrary.wiley.com/doi/pdf/10.1029/2019MS001810.

Fanglou Liao, Kunde Yang, Yaping Wang, Guandong Gao, Peng Zhan, Daquan Guo, Zipeng Li, and Ibrahim Hoteit. 2025. A Study on the Southern Ocean Upwelling Over the 21st Century Under a High-Emission Scenario. *Journal of Geophysical Research: Oceans*, 130(4):e2023JC020765. _eprint: https://agupubs.onlinelibrary.wiley.com/doi/pdf/10.1029/2023JC020765.

Matthew C Long, Britton B Stephens, Kathryn McKain, Colm Sweeney, Ralph F Keeling, Eric A Kort, Eric J Morgan, Jonathan D Bent, Naveen Chandra, Frederic Chevallier, Róisín Commane, Bruce C Daube, Paul B Krummel, Zoë Loh, Ingrid T Luijkx, David Munro, Prabir Patra, Wouter Peters, Michel Ramonet, Christian Rödenbeck, Ann Stavert, Pieter Tans, and Steven C Wofsy. 2021. Strong Southern Ocean carbon uptake evident in airborne observations. *Science*, 374(6572):1275–1280.

Timothy J Lueker, Andrew G Dickson, and Charles D Keeling. 2000. Ocean pCO2 calculated from dissolved inorganic carbon, alkalinity, and equations for K1 and K2: validation based on laboratory measurements of CO2 in gas and seawater at equilibrium. *Marine Chemistry*, 70(1):105–119.

Graeme A. MacGilchrist, Alberto C. Naveira Garabato, Peter J. Brown, Loïc Jullion, Sheldon Bacon, Dorothee C.E. Bakker, Mario Hoppema, Michael P. Meredith, and Sinhué Torres-Valdés. 2019. Reframing the carbon cycle of the subpolar Southern Ocean. *Science Advances*, 5(8):1–8.

Neill Mackay and Andrew Watson. 2021. Winter Air-Sea CO2 Fluxes Constructed From Summer Observations of the Polar Southern Ocean Suggest Weak Outgassing. *Journal of Geophysical Research: Oceans*, 126(5):e2020JC016600.

David Marshall. 1995. Topographic Steering of the Antarctic Circumpolar Current. *Journal of Physical Oceanography*, 25(7):1636 – 1650. Place: Boston MA, USA Publisher: American Meteorological Society.

J Marshall and T Radko. 2003. Residual-mean solutions for the Antarctic Circumpolar Current and its associated overturning circulation. *JOURNAL OF PHYSICAL OCEANOGRAPHY*, 33(11):2341–2354.

John Marshall, Alistair Adcroft, Chris Hill, Lev Perelman, and Curt Heisey. 1997. A finite-volume, incompressible Navier Stokes model for studies of the ocean on parallel computers. *Journal of Geophysical Research: Oceans*, 102(C3):5753–5766. _eprint: https://agupubs.onlinelibrary.wiley.com/doi/pdf/10.1029/96JC02775.

John Marshall and Kevin Speer. 2012. Closure of the meridional overturning circulation through Southern Ocean upwelling. *Nature Geoscience*, 5(3):171–180.

Tanya L Maurer, Joshua N Plant, and Kenneth S Johnson. 2021. Delayed-Mode Quality Control of Oxygen, Nitrate, and pH Data on SOCCOM Biogeochemical Profiling Floats. *Frontiers in Marine Science*, 8:1118.

Matthew R. Mazloff, Ariane Verdy, Sarah T. Gille, Kenneth S. Johnson, Bruce D. Cornuelle, and Jorge Sarmiento. 2023. Southern Ocean Acidification Revealed by Biogeochemical-Argo Floats. *Journal of Geophysical Research: Oceans*, 128(5):e2022JC019530. _eprint: https://agupubs.onlinelibrary.wiley.com/doi/pdf/10.1029/2022JC019530.

T.J. McDougall and P.M. Barker. 2011. *Getting started with TEOS-10 and the Gibbs Seawater (GSW) Oceanographic Toolbox,*. SCOR/IAPSO WG127.

B I McNeil and B Tilbrook. 2009. A seasonal carbon budget for the sub-Antarctic Ocean, South of Australia. *Marine Chemistry*, 115(3):196–210.

L Merlivat, J Boutin, and D Antoine. 2015. Roles of biological and physical processes in driving seasonal air–sea CO2 flux in the Southern Ocean: New insights from CARIOCA pCO2. *Journal of Marine Systems*, 147:9–20.

M. Mohrmann, C. Heuzé, and S. Swart. 2021. Southern Ocean polynyas in CMIP6 models. *The Cryosphere*, 15(9):4281–4313.

N P Mongwe, M Vichi, and P M S Monteiro. 2018. The seasonal cycle of pCO$_{2}$ and CO$_{2}$ fluxes in the Southern Ocean: diagnosing anomalies in CMIP5 Earth system models. *Biogeosciences*, 15(9):2851–2872.

Allison R. Moreno, Catherine A. Garcia, Alyse A. Larkin, Jenna A. Lee, Wei Lei Wang, J. Keith Moore, Francois W. Primeau, and Adam C. Martiny. 2020. Latitudinal gradient in the respiration quotient and the implications for ocean oxygen availability. *Proceedings of the National Academy of Sciences of the United States of America*, 117(37):22866–22872.

David R Munro, Nicole S Lovenduski, Britton B Stephens, Timothy Newberger, Kevin R Arrigo, Taro Takahashi, Paul D Quay, Janet Sprintall, Natalie M Freeman, and Colm Sweeney. 2015. Estimates of net community production in the Southern Ocean determined from time series observations (2002–2011) of nutrients, dissolved inorganic carbon, and surface ocean pCO2 in Drake Passage. *Deep Sea Research Part II: Topical Studies in Oceanography*, 114:49–63.

A. C. Naveira Garabato, R. Ferrari, and K. L. Polzin. 2011. Eddy stirring in the Southern Ocean. *Journal of Geophysical Research: Oceans*, 116(C9). _eprint: https://agupubs.onlinelibrary.wiley.com/doi/pdf/10.1029/2010JC006818.

Louise Newman, Petra Heil, Rowan Trebilco, Katsuro Katsumata, Andrew Constable, Esmee van Wijk, Karen Assmann, Joana Beja, Phillippa Bricher, Richard Coleman, Daniel Costa, Steve Diggs, Riccardo Farneti, Sarah Fawcett, Sarah T Gille, Katharine R Hendry, Sian Henley, Eileen Hofmann, Ted Maksym, Matthew Mazloff, Andrew Meijers, Michael M Meredith, Sebastien Moreau, Burcu Ozsoy, Robin Robertson, Irene Schloss, Oscar Schofield, Jiuxin Shi, Elisabeth Sikes, Inga J Smith, Sebastiaan Swart, Anna Wahlin, Guy Williams, Michael J M Williams, Laura Herraiz-Borreguero, Stefan Kern, Jan Lieser, Robert A Massom, Jessica Melbourne-Thomas, Patricia Miloslavich, and Gunnar Spreen. 2019. Delivering Sustained, Coordinated, and Integrated Observations of the Southern Ocean for Global Impact. *Frontiers in Marine Science*, 6.

Sarah-Anne Nicholson, Daniel B. Whitt, Ilker Fer, Marcel D. du Plessis, Alice D. Lebéhot, Sebastiaan Swart, Adrienne J. Sutton, and Pedro M. S. Monteiro. 2022. Storms drive outgassing of CO2 in the subpolar Southern Ocean. *Nature Communications*, 13(1):158.

Cara Nissen, Nicolas Gruber, Matthias Münnich, and Meike Vogt. 2021. Southern Ocean Phytoplankton Community Structure as a Gatekeeper for Global Nutrient Biogeochemistry. *Global Biogeochemical Cycles*, 35(8):e2021GB006991.

NOAA National Geophysical Data Center. 2009. Etopo1 1 arc-minute global relief model.

J. C. Orr, R. G. Najjar, O. Aumont, L. Bopp, J. L. Bullister, G. Danabasoglu, S. C. Doney, J. P. Dunne, J.-C. Dutay, H. Graven, S. M. Griffies, J. G. John, F. Joos, I. Levin, K. Lindsay, R. J. Matear, G. A. McKinley, A. Mouchet, A. Oschlies, A. Romanou, R. Schlitzer, A. Tagliabue, T. Tanhua, and A. Yool. 2017. Biogeochemical protocols and diagnostics for the CMIP6 Ocean Model Intercomparison Project (OMIP). *Geoscientific Model Development*, 10(6):2169–2199.

Alejandro H Orsi, Thomas Whitworth, and Worth D Nowlin. 1995. On the meridional extent and fronts of the Antarctic Circumpolar Current. *Deep Sea Research Part I: Oceanographic Research Papers*, 42(5):641–673.

A. Paulmier, I. Kriest, and A. Oschlies. 2009. Stoichiometries of remineralisation and denitrification in global biogeochemical ocean models. *Biogeosciences*, 6(5):923–935.

Fiz F Perez and F Fraga. 1987. Association constant of fluoride and hydrogen ions in seawater. *Marine Chemistry*, 21(2):161–168.

Channing J Prend, Alison R Gray, Lynne D Talley, Sarah T Gille, F Alexander Haumann, Kenneth S Johnson, Stephen C Riser, Isabella Rosso, Jade Sauvé, and Jorge L Sarmiento. 2022a. Indo-Pacific Sector Dominates Southern Ocean Carbon Outgassing. *Global Biogeochemical Cycles*, 36(7):e2021GB007226.

Channing J Prend, Jess M Hunt, Matthew R Mazloff, Sarah T Gille, and Lynne D Talley. 2022b. Controls on the Boundary Between Thermally and Non-Thermally Driven pCO2 Regimes in the South Pacific. *Geophysical Research Letters*, 49(9):e2021GL095797.

Baoxiao Qu, Jinming Song, Xuegang Li, Huamao Yuan, Kun Zhang, and Suqing Xu. 2022. Global air-sea CO2 exchange flux since 1980s: results from CMIP6 Earth System Models. *Journal of Oceanology and Limnology*, 40(4):1417–1436.

L. Resplandy, R. Seferian, and L. Bopp. 2015. Natural variability of CO2 and O2 fluxes: What can we learn from centuries-long climate models simulations? *JOURNAL OF GEOPHYSICAL RESEARCH-OCEANS*, 120(1):384–404.

Graham J Rickard, Erik Behrens, Angela A Bahamondes Dominguez, and Matt H Pinkerton. 2023. An Assessment of the Oceanic Physical and Biogeochemical Components of CMIP5 and CMIP6 Models for the Ross Sea Region. *Journal of Geophysical Research: Oceans*, 128(3):e2022JC018880.

Stephen R. Rintoul. 2018. The global influence of localized dynamics in the Southern Ocean. *Nature*, 558(7709):209–218.

Stephen R. Rintoul and Alberto C. Naveira Garabato. 2013. Chapter 18 - Dynamics of the Southern Ocean Circulation. In Gerold Siedler, Stephen M. Griffies, John Gould, and John A. Church, editors, *Ocean Cir-*

culation and Climate, volume 103 of *International Geophysics*, pages 471–492. Academic Press. ISSN: 0074-6142.

Stephen C. Riser, Howard J. Freeland, Dean Roemmich, Susan Wijffels, Ariel Troisi, Mathieu Belbéoch, Denis Gilbert, Jianping Xu, Sylvie Pouliquen, Ann Thresher, Pierre-Yves Le Traon, Guillaume Maze, Birgit Klein, M. Ravichandran, Fiona Grant, Pierre-Marie Poulain, Toshio Suga, Byunghwan Lim, Andreas Sterl, Philip Sutton, Kjell-Arne Mork, Pedro Joaquín Vélez-Belchí, Isabelle Ansorge, Brian King, Jon Turton, Molly Baringer, and Steven R. Jayne. 2016. Fifteen years of ocean observations with the global Argo array. *Nature Climate Change*, 6(2):145–153.

Stephen C Riser, Dana Swift, and Robert Drucker. 2018. Profiling Floats in SOCCOM: Technical Capabilities for Studying the Southern Ocean. *Journal of Geophysical Research: Oceans*, 123(6):4055–4073.

R Ritter, P Landschützer, N Gruber, A R Fay, Y Iida, S Jones, S Nakaoka, G.-H. Park, P Peylin, C Rödenbeck, K B Rodgers, J D Shutler, and J Zeng. 2017. Observation-Based Trends of the Southern Ocean Carbon Sink. *Geophysical Research Letters*, 44(24):12,312–339,348.

Carol Robinson. 2019. Microbial Respiration, the Engine of Ocean Deoxygenation. *Frontiers in Marine Science*, 5:533.

K. Rodgers, O. Aumont, S. M. Fletcher, Y. Plancherel, L. Bopp, C. D. B. Montégut, D. Iudicone, R. Keeling, G. Madec, and R. Wanninkhof. 2013. Strong sensitivity of Southern Ocean carbon uptake and nutrient cycling to wind stirring. *Biogeosciences*, 11:4077–4098.

Dean Roemmich and John Gilson. 2009. The 2004–2008 mean and annual cycle of temperature, salinity, and steric height in the global ocean from the Argo Program. *Progress in Oceanography*, 82(2):81–100.

Tyler Rohr, Anthony J. Richardson, Andrew Lenton, Matthew A. Chamberlain, and Elizabeth H. Shadwick. 2023. Zooplankton grazing is the largest source of uncertainty for marine carbon cycling in CMIP6 models. *Communications Earth & Environment*, 4(1):212.

Isabella Rosso, Matthew R Mazloff, Ariane Verdy, and Lynne D Talley. 2017. Space and time variability of the Southern Ocean carbon budget. *Journal of Geophysical Research: Oceans*, 122(9):7407–7432.

J B Sallée, K G Speer, and S R Rintoul. 2010. Zonally asymmetric response of the Southern Ocean mixed-layer depth to the Southern Annular Mode. *Nature Geoscience*, 3(4):273–279.

Sallée, J. B.,, Speer, K., and Rintoul, S. R. 2011. Mean-flow and topographic control on surface eddy-mixing in the Southern Ocean. *Journal of Marine Research*, 69(4).

Jorge Louis Sarmiento and Nicolas Gruber. 2006. Ocean biogeochemical dynamics. ISBN: 9780691017075 Place: Princeton Publication Title: Ocean biogeochemical dynamics.

Jade Sauvé, Alison R. Gray, Channing J. Prend, Seth M. Bushinsky, and Stephen C. Riser. 2023. Carbon Outgassing in the Antarctic Circumpolar Current Is Supported by Ekman Transport From the Sea Ice Zone in an Observation-Based Seasonal Mixed-Layer Budget. *Journal of Geophysical Research: Oceans*, 128(11):e2023JC019815. _eprint: https://agupubs.onlinelibrary.wiley.com/doi/pdf/10.1029/2023JC019815.

S. Schroeter, T. J. O'Kane, and P. A. Sandery. 2023. Antarctic sea ice regime shift associated with decreasing zonal symmetry in the Southern Annular Mode. *The Cryosphere*, 17(2):701–717.

R. Seferian, L. Bopp, D. Swingedouw, and J. Servonnat. 2013. Dynamical and biogeochemical control on the decadal variability of ocean carbon fluxes. *EARTH SYSTEM DYNAMICS*, 4(1):109–127. Seferian2013.

Ø. Seland, M. Bentsen, D. Olivié, T. Toniazzo, A. Gjermundsen, L. S. Graff, J. B. Debernard, A. K. Gupta, Y.-C. He, A. Kirkevåg, J. Schwinger, J. Tjiputra, K. S. Aas, I. Bethke, Y. Fan, J. Griesfeller, A. Grini, C. Guo, M. Ilicak, I. H. H. Karset, O. Landgren, J. Liakka, K. O. Moseid, A. Nummelin, C. Spensberger, H. Tang, Z. Zhang, C. Heinze, T. Iversen, and M. Schulz. 2020. Overview of the Norwegian Earth System Model (NorESM2) and key climate response of CMIP6 DECK, historical, and scenario simulations. *Geoscientific Model Development*, 13(12):6165–6200.

E H Shadwick, O A De Meo, S Schroeter, M C Arroyo, D G Martinson, and H Ducklow. 2021. Sea Ice Suppression of CO2 Outgassing in the West Antarctic Peninsula: Implications For The Evolving Southern Ocean Carbon Sink. *Geophysical Research Letters*, 48(11):e2020GL091835.

E H Shadwick, T W Trull, B Tilbrook, A J Sutton, E Schulz, T W Trull, B Tilbrook, A J Sutton, E Schulz, and C L Sabine. 2015. Seasonality of biological and physical controls on surface ocean CO 2 from hourly observations at the Southern Ocean Time Series site south of Australia. *Global biogeochemical cycles.*, 29(2):223–238. Publisher: American Geophysical Union Place: Washington, DC :.

W. Sijp and M. England. 2009. Southern Hemisphere Westerly Wind Control over the Ocean's Thermohaline Circulation. *Journal of Climate*, 22:1277–1286.

Hajoon Song, John Marshall, David R. Munro, Stephanie Dutkiewicz, Colm Sweeney, D. J. McGillicuddy Jr., and Ute Hausmann. 2016. Mesoscale modulation of air-sea CO2 flux in Drake Passage. *Journal of Geophysical Research: Oceans*, 121(9):6635–6649. _eprint: https://agupubs.onlinelibrary.wiley.com/doi/pdf/10.1002/2016JC011714.

Southern Ocean Carbon and Climate Observations and Modeling Project. 2021. Entire SOCCOM/UW MBARI float data set.

D. Stappard, B. Fernández Castro, A. Naveira Garabato, and T. Tyrrell. 2025. Identification of Southern Ocean Upwelling From Biogeochemical-Argo Floats. *Journal of Geophysical Research: Oceans*, 130(6):e2023JC020597. _eprint: https://agupubs.onlinelibrary.wiley.com/doi/pdf/10.1029/2023JC020597.

N. C. Swart, J. N. S. Cole, V. V. Kharin, M. Lazare, J. F. Scinocca, N. P. Gillett, J. Anstey, V. Arora, J. R. Christian, S. Hanna, Y. Jiao, W. G. Lee, F. Majaess, O. A. Saenko, C. Seiler, C. Seinen, A. Shao, M. Sigmond, L. Solheim, K. von Salzen, D. Yang, and B. Winter. 2019. The Canadian Earth System Model version 5 (CanESM5.0.3). *Geoscientific Model Development*, 12(11):4823–4873.

Roland Séférian, Sarah Berthet, Andrew Yool, Julien Palmiéri, Laurent Bopp, Alessandro Tagliabue, Lester Kwiatkowski, Olivier Aumont, James Christian, John Dunne, Marion Gehlen, Tatiana Ilyina, Jasmin G John, Hongmei Li, Matthew C Long, Jessica Y Luo, Hideyuki Nakano, Anastasia Romanou, Jörg Schwinger, Charles Stock, Yeray Santana-Falcón, Yohei Takano, Jerry Tjiputra, Hiroyuki Tsujino, Michio Watanabe, Tongwen Wu, Fanghua Wu, and Akitomo Yamamoto. 2020. Tracking Improvement in

Simulated Marine Biogeochemistry Between CMIP5 and CMIP6. *Current Climate Change Reports*, 6(3):95–119.

Taro Takahashi, Richard A Feely, Ray F Weiss, Rik H Wanninkhof, David W Chipman, Stewart C Sutherland, and Timothy T Takahashi. 1997. Global air-sea flux of CO2: An estimate based on measurements of sea–air pCO2 difference. *Proceedings of the National Academy of Sciences*, 94(16):8292–8299.

Taro Takahashi, Jon Olafsson, John G Goddard, David W Chipman, and S C Sutherland. 1993. Seasonal variation of CO2 and nutrients in the high-latitude surface oceans: A comparative study. *Global Biogeochemical Cycles*, 7(4):843–878.

Taro Takahashi, S.C. Sutherland, D.W. Chipman, J.G. Goddard, Cheng Ho, Timothy Newberger, Colm Sweeney, and D.R. Munro. 2014. Climatological distributions of pH, pCO2, total CO2, alkalinity, and CaCO3 saturation in the global surface ocean, and temporal changes at selected locations. *Marine chemistry*, 164:95–125. Place: Amsterdam Publisher: Elsevier B.V.

Taro Takahashi, Stewart C Sutherland, Colm Sweeney, Alain Poisson, Nicolas Metzl, Bronte Tilbrook, Nicolas Bates, Rik Wanninkhof, Richard A Feely, Christopher Sabine, Jon Olafsson, and Yukihiro Nojiri. 2002. Global sea–air CO2 flux based on climatological surface ocean pCO2, and seasonal biological and temperature effects. *Deep Sea Research Part II: Topical Studies in Oceanography*, 49(9):1601–1622.

Taro Takahashi, Stewart C Sutherland, Rik Wanninkhof, Colm Sweeney, Richard A Feely, David W Chipman, Burke Hales, Gernot Friederich, Francisco Chavez, Christopher Sabine, Andrew Watson, Dorothee C E Bakker, Ute Schuster, Nicolas Metzl, Hisayuki Yoshikawa-Inoue, Masao Ishii, Takashi Midorikawa, Yukihiro Nojiri, Arne Körtzinger, Tobias Steinhoff, Mario Hoppema, Jon Olafsson, Thorarinn S Arnarson, Bronte Tilbrook, Truls Johannessen, Are Olsen, Richard Bellerby, C S Wong, Bruno Delille, N R Bates, and Hein J W de Baar. 2009. Climatological mean and decadal change in surface ocean pCO2, and net sea–air CO2 flux over the global oceans. *Deep Sea Research Part II: Topical Studies in Oceanography*, 56(8):554–577.

Veronica Tamsitt, Henri F Drake, Adele K Morrison, Lynne D Talley, Carolina O Dufour, Alison R Gray, Stephen M Griffies, Matthew R Mazloff, Jorge L Sarmiento, Jinbo Wang, and Wilbert Weijer. 2017.

Spiraling pathways of global deep waters to the surface of the Southern Ocean. *Nature Communications*, 8(1):172.

Veronica Tamsitt, Lynne D Talley, Matthew R Mazloff, and Ivana Cerovečki. 2016. Zonal Variations in the Southern Ocean Heat Budget. *Journal of Climate*, 29(18):6563–6579. Publisher: American Meteorological Society Place: Boston MA, USA.

Jens Terhaar, Thomas L. Frölicher, and Fortunat Joos. 2021. Southern Ocean anthropogenic carbon sink constrained by sea surface salinity. *Science Advances*, 7(18):eabd5964. _eprint: https://www.science.org/doi/pdf/10.1126/sciadv.abd5964.

S J Thomalla, N Fauchereau, S Swart, and P M S Monteiro. 2011. Regional scale characteristics of the seasonal cycle of chlorophyll in the Southern Ocean. *Biogeosciences*, 8(10):2849–2866.

Andrew F. Thompson, L. Dove, Ellie Flint, L. Lacour, and P. Boyd. 2024. Interactions Between Multiple Physical Particle Injection Pumps in the Southern Ocean. *Global Biogeochemical Cycles*, 38. Citaiton Key: Thompson2024.

Andrew F. Thompson and Jean-Baptiste Sallée. 2012. Jets and Topography: Jet Transitions and the Impact on Transport in the Antarctic Circumpolar Current. *Journal of Physical Oceanography*, 42(6):956 – 972. Place: Boston MA, USA Publisher: American Meteorological Society.

J F Tjiputra, J Schwinger, M Bentsen, A L Morée, S Gao, I Bethke, C Heinze, N Goris, A Gupta, Y.-C. He, D Olivié, Ø Seland, and M Schulz. 2020. Ocean biogeochemistry in the Norwegian Earth System Model version 2 (NorESM2). *Geoscientific Model Development*, 13(5):2393–2431.

Hiroyuki Tsujino, L. Shogo Urakawa, Stephen M. Griffies, Gokhan Danabasoglu, Alistair J. Adcroft, Arthur E. Amaral, Thomas Arsouze, Mats Bentsen, Raffaele Bernardello, Claus W. Böning, Alexandra Bozec, Eric P. Chassignet, Sergey Danilov, Raphael Dussin, Eleftheria Exarchou, Pier Giuseppe Fogli, Baylor Fox-Kemper, Chuncheng Guo, Mehmet Ilicak, Doroteaciro Iovino, Who M. Kim, Nikolay Koldunov, Vladimir Lapin, Yiwen Li, Pengfei Lin, Keith Lindsay, Hailong Liu, Matthew C. Long, Yoshiki Komuro, Simon J. Marsland, Simona Masina, Aleksi Nummelin, Jan Klaus Rieck, Yohan Ruprich-Robert, Markus Scheinert, Valentina Sicardi, Dmitry Sidorenko, Tatsuo Suzuki, Hiroaki Tatebe, Qiang Wang, Stephen G. Yeager, and Zipeng Yu. 2020. Evaluation of global ocean–sea-ice model simulations based on the experimental protocols of the Ocean Model Intercomparison Project phase 2 (OMIP-2). *Geoscientific Model Development*, 13(8):3643–3708.

Takaya Uchida, Dhruv Balwada, Ryan Abernathey, Galen McKinley, Shafer Smith, and Marina Lévy. 2019. The Contribution of Submesoscale over Mesoscale Eddy Iron Transport in the Open Southern Ocean. *Journal of Advances in Modeling Earth Systems*, 11(12):3934–3958. _eprint: https://agupubs.onlinelibrary.wiley.com/doi/pdf/10.1029/2019MS001805.

Takaya Uchida, Dhruv Balwada, Ryan P. Abernathey, Galen A. McKinley, Shafer K. Smith, and Marina Lévy. 2020. Vertical eddy iron fluxes support primary production in the open Southern Ocean. *Nature Communications*, 11(1):1125.

A. Verdy and M. R. Mazloff. 2017. A data assimilating model for estimating Southern Ocean biogeochemistry. *Journal of Geophysical Research: Oceans*, 122(9).

Giuliana A Viglione and Andrew F Thompson. 2016. Lagrangian pathways of upwelling in the Southern Ocean. *Journal of Geophysical Research: Oceans*, 121(8):6295–6309.

Timo Vihma and Jari Haapala. 2009. Geophysics of sea ice in the Baltic Sea: A review. *Progress in Oceanography*, 80(3):129–148.

R. Wanninkhof, K. Johnson, N. Williams, J. Sarmiento, S. Riser, E. Briggs, S. Bushinsky, B. Carter, A. Dickson, R. Feely, A. Gray, L. Juranek, R. Key, L. Talley, J. Russel, and A. Verdy. 2016. An evaluation of pH and NO3 sensor data from SOCCOM floats and their utilization to develop ocean inorganic carbon products. Technical report.

Rik Wanninkhof. 2014. Relationship between wind speed and gas exchange over the ocean revisited. *Limnology and Oceanography: Methods*, 12(6):351–362.

Andrew J Watson, James R Ledwell, Marie-José Messias, Brian A King, Neill Mackay, Michael P Meredith, Benjamin Mills, and Alberto C Naveira Garabato. 2013. Rapid cross-density ocean mixing at mid-depths in the Drake Passage measured by tracer release. *Nature*, 501(7467):408–411.

N. L. Williams, L. W. Juranek, R. A. Feely, J. L. Russell, K. S. Johnson, and B. Hales. 2018. Assessment of the Carbonate Chemistry Seasonal Cycles in the Southern Ocean From Persistent Observational Platforms. *Journal of Geophysical Research: Oceans*, 123(7):4833–4852.

Annie P S Wong, Susan E Wijffels, Stephen C Riser, Sylvie Pouliquen, Shigeki Hosoda, Dean Roemmich, John Gilson, Gregory C Johnson, Kim Martini, David J Murphy, Megan Scanderbeg, T V S Udaya Bhaskar, Justin J H Buck, Frederic Merceur, Thierry Carval, Guillaume Maze, Cécile Cabanes, Xavier André, Noé Poffa, Igor Yashayaev, Paul M Barker, Stéphanie Guinehut, Mathieu Belbéoch, Mark Ignaszewski, Molly O'Neil Baringer, Claudia Schmid, John M Lyman, Kristene E McTaggart, Sarah G Purkey, Nathalie Zilberman, Matthew B Alkire, Dana Swift, W Brechner Owens, Steven R Jayne, Cora Hersh, Pelle Robbins, Deb West-Mack, Frank Bahr, Sachiko Yoshida, Philip J H Sutton, Romain Cancouët, Christine Coatanoan, Delphine Dobbler, Andrea Garcia Juan, Jerôme Gourrion, Nicolas Kolodziejczyk, Vincent Bernard, Bernard Bourlès, Hervé Claustre, Fabrizio D'Ortenzio, Serge Le Reste, Pierre-Yve Le Traon, Jean-Philippe Rannou, Carole Saout-Grit, Sabrina Speich, Virginie Thierry, Nathalie Verbrugge, Ingrid M Angel-Benavides, Birgit Klein, Giulio Notarstefano, Pierre-Marie Poulain, Pedro Vélez-Belchí, Toshio Suga, Kentaro Ando, Naoto Iwasaska, Taiyo Kobayashi, Shuhei Masuda, Eitarou Oka, Kanako Sato, Tomoaki Nakamura, Katsunari Sato, Yasushi Takatsuki, Takashi Yoshida, Rebecca Cowley, Jenny L Lovell, Peter R Oke, Esmee M van Wijk, Fiona Carse, Matthew Donnelly, W John Gould, Katie Gowers, Brian A King, Stephen G Loch, Mary Mowat, Jon Turton, E Pattabhi Rama Rao, M Ravichandran, Howard J Freeland, Isabelle Gaboury, Denis Gilbert, Blair J W Greenan, Mathieu Ouellet, Tetjana Ross, Anh Tran, Mingmei Dong, Zenghong Liu, Jianping Xu, KiRyong Kang, HyeongJun Jo, Sung-Dae Kim, and Hyuk-Min Park. 2020. Argo Data 1999–2019: Two Million Temperature-Salinity Profiles and Subsurface Velocity Observations From a Global Array of Profiling Floats. *Frontiers in Marine Science*, 7:700.

Lixin Wu, Zhao Jing, Steve Riser, and Martin Visbeck. 2011. Seasonal and spatial variations of Southern Ocean diapycnal mixing from Argo profiling floats. *Nature Geoscience*, 4(6):363–366.

Yingxu Wu, Dorothee C E Bakker, Eric P Achterberg, Amavi N Silva, Daisy D Pickup, Xiang Li, Sue Hartman, David Stappard, Di Qi, and Toby Tyrrell. 2022. Integrated analysis of carbon dioxide and oxygen concentrations as a quality control of ocean float data. *Communications Earth & Environment*, 3(1):92.

Yingxu Wu and Di Qi. 2022. Inconsistency between ship- and Argo float-based pCO2 at the intense upwelling region of the Drake Passage, Southern Ocean. *Frontiers in Marine Science*, 9.

Bo Yang, Elizabeth H Shadwick, Cristina Schultz, and Scott C Doney. 2021. Annual Mixed Layer Carbon Budget for the West Antarctic Peninsula Continental Shelf: Insights From Year-Round Mooring Measurements. *Journal of Geophysical Research: Oceans*, 126(4):e2020JC016920.

A Yool, J Palmiéri, C G Jones, L de Mora, T Kuhlbrodt, E E Popova, A J G Nurser, J Hirschi, A T Blaker, A C Coward, E W Blockley, and A A Sellar. 2021. Evaluating the physical and biogeochemical state of the global ocean component of UKESM1 in CMIP6 historical simulations. *Geoscientific Model Development*, 14(6):3437–3472.

Seiji YUKIMOTO, Hideaki KAWAI, Tsuyoshi KOSHIRO, Naga OSHIMA, Kohei YOSHIDA, Shogo URAKAWA, Hiroyuki TSUJINO, Makoto DEUSHI, Taichu TANAKA, Masahiro HOSAKA, Shokichi YABU, Hiromasa YOSHIMURA, Eiki SHINDO, Ryo MIZUTA, Atsushi OBATA, Yukimasa ADACHI, and Masayoshi ISHII. 2019. The Meteorological Research Institute Earth System Model Version 2.0, MRI-ESM2.0: Description and Basic Evaluation of the Physical Component. *Journal of the Meteorological Society of Japan. Ser. II*, 97(5):931–965.

Claire K. Yung, Adele K. Morrison, and Andrew McC. Hogg. 2022. Topographic Hotspots of Southern Ocean Eddy Upwelling. *Frontiers in Marine Science*, Volume 9 - 2022.

Richard E. Zeebe and Dieter Wolf-Gladrow. 2001. *CO2 in seawater: Equilibrium, kinetics, isotopes*. Elsevier.

N. V. Zilberman, M. Scanderbeg, A. R. Gray, and P. R. Oke. 2023. Scripps Argo Trajectory-Based Velocity Product: Global Estimates of Absolute Velocity Derived from Core, Biogeochemical, and Deep Argo Float Trajectories at Parking Depth. *Journal of Atmospheric and Oceanic Technology*, 40(3):361 – 374. Place: Boston MA, USA Publisher: American Meteorological Society.

Hao Zuo, Magdalena Alonso Balmaseda, Steffen Tietsche, Kristian Mogensen, and Michael Mayer. 2019. The ECMWF operational ensemble reanalysis-analysis system for ocean and sea ice: A description of the system and assessment. *Ocean Science*, 15(3):779–808.

Chapter A

Appendix: Additional Method Information for Chapter 2

A.1 Horizontal Mass Transport

The monthly averaged Ekman mass transport is northward at the SIE and PF which is as expected due to the presence of strong westerly winds at those latitudes (Figure C.4). The monthly Ekman transport averages to 20.2 Sv at the SIE and 36.5 Sv at the PF, which is consistent with previous modeling studies that found a zonally integrated Ekman transport along 60°S (50°S) of 25 Sv (55 Sv) [Hallberg and Gnanadesikan, 2006]. There is about twice as much transport (varying from 1.5x to 2.8x) across the PF than the SIE, which is not surprising as wind driven transport can be inhibited by the presence of sea ice.

Monthly averaged mixed layer geostrophic transport is southward for the SIE and the PF, and it is one order of magnitude smaller than the monthly averaged Ekman transport, with an average of -2.4 Sv (panel b) of Figure C.4). We present mixed layer geographic transport separately for each zonal regions on either side of one boundary due to our choice of depth of integration. In the Ekman transport calculation, we assume that the Ekman depth is shallower than the mixed layer depth, an assumption which is likely true for most months but may break down in summer or fall depending on the eddy viscosity (not shown). This assumption allows us to consider the full depth of the Ekman layer and removes the need to choose a depth of integration. For the geostrophic transport calculation, we integrate the geostrophic velocity down to the mixed layer depth of the region under consideration.

We do not consider the eddy component of the horizontal advection in this region as it has been shown to be more than 50% smaller than the time mean component in the Ekman layer [Dufour et al., 2015].

A.2 Mass Budget and Vertical Velocity

The seasonal cycle of the monthly averaged mixed layer mass fluxes differs between the ASZ and the SIZ (Figure C.6). However, we observe that there is a balance between the surface fluxes of mass and the advective mass flux in both zonal regions while the term representing the difference between the tendency and the entrainment (TEND$-F_{entrain}$) is negligible. In the ASZ, the fluxes of mass do not vary strongly from month to month. Surface fluxes of mass, including precipitation, evaporation and a small contribution from sea ice melt and freeze, lead to water accumulating in the region's mixed layer. This is balanced by a mass advection out of the ASZ. The sign of the advective flux is set by a balance between the negative Ekman advection and the positive vertical advection. The geostrophic advection is at least one order of magnitude smaller. In the SIZ, the sea ice melt and freeze cycle creates strong seasonal variations in the monthly averaged surface flux which leads to seasonal variations of similar magnitude but opposite sign in the advective flux. As such, we see a positive advective flux of mass (driven by vertical advection) during ice formation and a negative advective mass flux (driven by Ekman advection) during sea ice melt. On annual time scales, mass fluxes in the SIZ and the ASZ are similar with a positive surface flux opposed by a negative advective flux driven by a dominance of Ekman transport out of the zone over vertical mass advection into the mixed layer (Figure C.7).

Using the mixed layer mass budget, we solve for the vertical velocity at the base of the mixed layer (w$_{-h}$) which is shown in Figure C.3. We find an average w$_{-h}$ of $1.19 \times 10^{-6} m/s$ ($1.07 \times 10^{-6} m/s$) in the ASZ (SIZ). This vertical velocity is of the expected scale and sign for these two zonal regions where upwelling is expected [Gruber et al., 2019]. Because we have used a mass budget to estimate w$_{-h}$, our estimate includes both the effect of Ekman upwelling and other processes such as topography-driven or storm-driven upwelling.

A.3 Estimated Parameters

We solve a non-linear system composed of the different monthly averaged budget equations for DIC and O_2 to find the missing parameters: the eddy diffusivity (κ_z), the respiration quotient (R_{O_2}) and the monthly biological flux of DIC (F_{bio}). We find an eddy diffusivity of $(6.83 \pm 5.8) \times 10^{-5}$ m^2 s^{-1} ($(2.95 \pm 2.5) \times 10^{-5}$ m^2 s^{-1}) for the ASZ (SIZ) (see Sections 2.3.5 and 2.5 for more information). We find a respiratory quotient of -0.65 ± 0.16 (-1.59 ± 0.26) for the ASZ (SIZ). The canonical value for the oxygen to carbon ratio is -1.45 [Anderson and Sarmiento, 1994]. However, DeVries and Deutsch [2014] found important latitudinal variations in the amount of oxygen consumed by unit of phosphate released during respiration ($R_{O_2/P}$). In the high-latitude Southern Ocean in particular, they find that $R_{O_2/P}$ increases from about 50 to 200 between 47°S and 70°S. When we convert $R_{O_2/P}$ to the respiratory quotient ($R_{O_2/C}$) using 106C:P, we find that we see a latitudinal variation of similar magnitude from the ASZ to the SIZ. The magnitude of the monthly averaged biological flux of DIC obtained from the optimization scheme and its clear seasonal cycle are as expected with a strong uptake of carbon during the spring bloom, stronger in the ASZ than in the SIZ (Figure C.5). The positive flux of carbon in winter, indicating dominance of respiration over photosynthesis, can be explained by the severe light and micro-nutrient limitations in the high-latitude Southern Ocean.

A.4 Error and Correlation of each Variable used in Monte Carlo Simulation

We record the error and correlation of each variable used in the Monte Carlo simulation in Table A.1.

Table A.1: Error and Correlation of each Variable used in Monte Carlo Simulation

Variable	Error	Unit	Correlation	Source
T	0.002	$^\circ$C	uncorrelated	Wong et al. [2020]
S	0.01	PSU	uncorrelated	Wong et al. [2020]
P	2.4	dbar	uncorrelated	Wong et al. [2020]
O_2	3	$\mu\mathrm{mol/kg}$	uncorrelated	Johnson et al. [2017a]
TA	8.74*	$\mu\mathrm{mol/kg}$	uncorrelated	Carter et al. [2018]
pH	0.007	total	uncorrelated	Johnson et al. [2017a]
N	0.5	$\mu\mathrm{mol/kg}$	uncorrelated	Johnson et al. [2017a]
ΔSIC_{SIZ}	3.45×10^8*	$\mathrm{m^2/day}$	uncorrelated	Hersbach et al. [2020]
ΔSIC_{ASZ}	4.23×10^7*	$\mathrm{m^2/day}$	uncorrelated	Hersbach et al. [2020]
SIT	20%	N/A	uncorrelated	Li et al. [2018]
SI transport	20%	$\mathrm{m^3/day}$	uncorrelated	
SIh	20%	m	uncorrelated	
(Precip. - Evap.)	1.24×10^{-7}*	$\mathrm{kg/m^2/s}$	uncorrelated	Hersbach et al. [2020]
$(\tau_x/\rho f)_{inter}$	0.00246*	$\mathrm{m^2/s}$	uncorrelated	Hersbach et al. [2020]
$(\tau_y/\rho f)_{inter}$	0.00167*	$\mathrm{m^2/s}$	uncorrelated	Hersbach et al. [2020]
$\vec{u}_{geo-inter}$	20%	N/A	uncorrelated	Gray and Riser [2014]
$F_{air-sea-C}$	0.506*	$\mathrm{mol/m^2/yr}$	correlated in time	Gray et al. [2018]
$F_{air-sea-O_2}$	20%	N/A	correlated in time	Bushinsky et al. [2017]

[a] *average error from field of individual errors

Chapter B

Appendix: Derivation of Budget Equation

To obtain the TEND and the F_{entrain}, we use the following equality to expand the first term of Eq. 2.1.

$$\frac{\partial}{\partial t}\int_{-h(t)}^{0}\gamma dz = \int_{-h(t)}^{0}\frac{\partial(\gamma)}{\partial t}dz + \frac{dh}{dt}\gamma_{-h} \tag{B.1}$$

We obtain

$$\int_A \left[\frac{\partial}{\partial t}\int_{-h(t)}^{0}\rho[X]dz - \frac{dh}{dt}(\rho[X])_{-h}\right] dA \tag{B.2}$$

Integrating over depth

$$\int_A \left[\frac{\partial(\rho[X](0+h))}{\partial t} - \frac{dh}{dt}(\rho[X])_{-h}\right] dA \tag{B.3}$$

Simplifying and integrating over the area

$$A\frac{\partial(\rho[X]h)}{\partial t} - A(\rho[X])_{-h}\frac{dh}{dt} \tag{B.4}$$

where

$$F_{entrain} = \rho_{-h}[X]_{-h}\frac{dh}{dt} \quad if\ \frac{dh}{dt} > 0 \tag{B.5}$$

$$F_{entrain} = \rho[X]\frac{dh}{dt} \quad if\ \frac{dh}{dt} < 0 \tag{B.6}$$

The advective flux terms originate from the second term of Eq. 2.1. We separate the horizontal and vertical advections by expanding the dot product.

$$\int_A \int_{-h(t)}^{0} \left(u\frac{\partial(\rho[X])}{\partial x} + v\frac{\partial(\rho[X])}{\partial y} \right) dzdA + \int_A \int_{-h(t)}^{0} w\partial(\rho[X])dA \tag{B.7}$$

where (u,v,w) is the velocity vector in the (x,y,z) direction. We can ignore the zonal advection term (v) due to the shape of the zone which is approximately zonally symmetric. We assume that the meridional gradient of the molar concentration of tracer (ρ[X]) doesn't vary with depth in the mixed layer.

$$\int_A \frac{\partial(\rho[X])}{\partial y} \int_{-h(t)}^{0} vdzdA + \int_A w\rho[X]\big|_{-h(t)}^{0} dA \tag{B.8}$$

In the Southern Ocean, meridional advection at the surface is mostly due to Ekman transport with additional contribution from geostrophic transport. We assume that the Ekman depth is smaller than the mixed layer depth.

$$\int_A \frac{\partial(\rho[X])}{\partial y} \int_{-h(t)}^{0} (v_{ek} + v_{geo})dzdA + \int_A \left[w\rho[X]\big|_0 - w\rho[X]\big|_{-h} \right] dA \tag{B.9}$$

Since vertical velocity (w) is 0 at the surface and using the following Coriolis equation,

$$\int_{-h(t)}^{0} \rho v_{ek} dz = -\frac{\tau_x}{f} \tag{B.10}$$

we obtain the following equation, having further assumed that the meridional gradient of the molar concentration of tracer ($\rho[X]$) doesn't vary zonally.

$$\int_y \frac{\partial(\rho[X])}{\partial y} \int_x \left[\frac{-\tau_x}{f\rho} + \int_{-h(t)}^{0} v_{geo}dz \right] dxdy - A(w\rho[X])\big|_{-h} \tag{B.11}$$

We simplify further and set the boundaries of the meridional integration as the Northern (N) and Southern (S) frontal boundaries.

$$\int_S^N \partial(\rho[X]) \int_x \left[\frac{-\tau_x}{f\rho} + \int_{-h(t)}^{0} v_{geo}dz \right] dx - A(w\rho[X])\big|_{-h} \tag{B.12}$$

We define V$_{ek}$ and V$_{geo}$, the Ekman and geostrophic mass transports,

$$\int_S^N V_{ek}\partial(\rho[X]) + \int_S^N V_{geo}\partial(\rho[X]) - A(w\rho[X])\big|_{-h} \tag{B.13}$$

and divide through by the ocean surface area to obtain the final form of the horizontal advection equation, as consistent with Eq. 2.3.

$$F_{horiz-adv} = -\frac{1}{A}\left[(\rho[X]V_{ek})\big|_N - (\rho[X]V_{ek})\big|_S + (\rho[X]V_{geo})\big|_N - (\rho[X]V_{geo})\big|_S\right] \tag{B.14}$$

$\rho[X]\big|_N$ ($\rho[X]\big|_S$) corresponds to the tracer molar concentration of the source water of the horizontal advection at the northern (southern) boundary.

The vertical advection at the base of the mixed layer depends on the vertical velocity at the base of the mixed layer (w$_{-h}$) as well as on the molar concentration of tracer ($\rho[X]\big|_{-h}$) in the downwelled or upwelled waters depending on the sign of w$_{-h}$.

$$F_{vert-adv} = (w\rho[X])\big|_{-h} \tag{B.15}$$

The mixing flux term corresponds to the last term of Eq. 2.1, which can be expressed as

$$\int_A \kappa_z \frac{\partial(\rho[X])}{\partial z}\bigg|_{-h}^{0} dA \tag{B.16}$$

Since the vertical gradient of the molar concentration is 0 at the surface and integrating over the ocean surface area, we are left with

$$-A\kappa_z \frac{\partial(\rho[X])}{\partial z}\bigg|_{-h} \tag{B.17}$$

Dividing by the area for consistency with Eq. 2.3, we obtain

$$F_{mixing} = -\kappa_z \frac{\partial(\rho[X])}{\partial z}\bigg|_{-h} \tag{B.18}$$

Chapter C

Appendix: Additional Figures for Chapter 2

This appendix contains additional figures which may be useful for readers interested in reproducing the method.

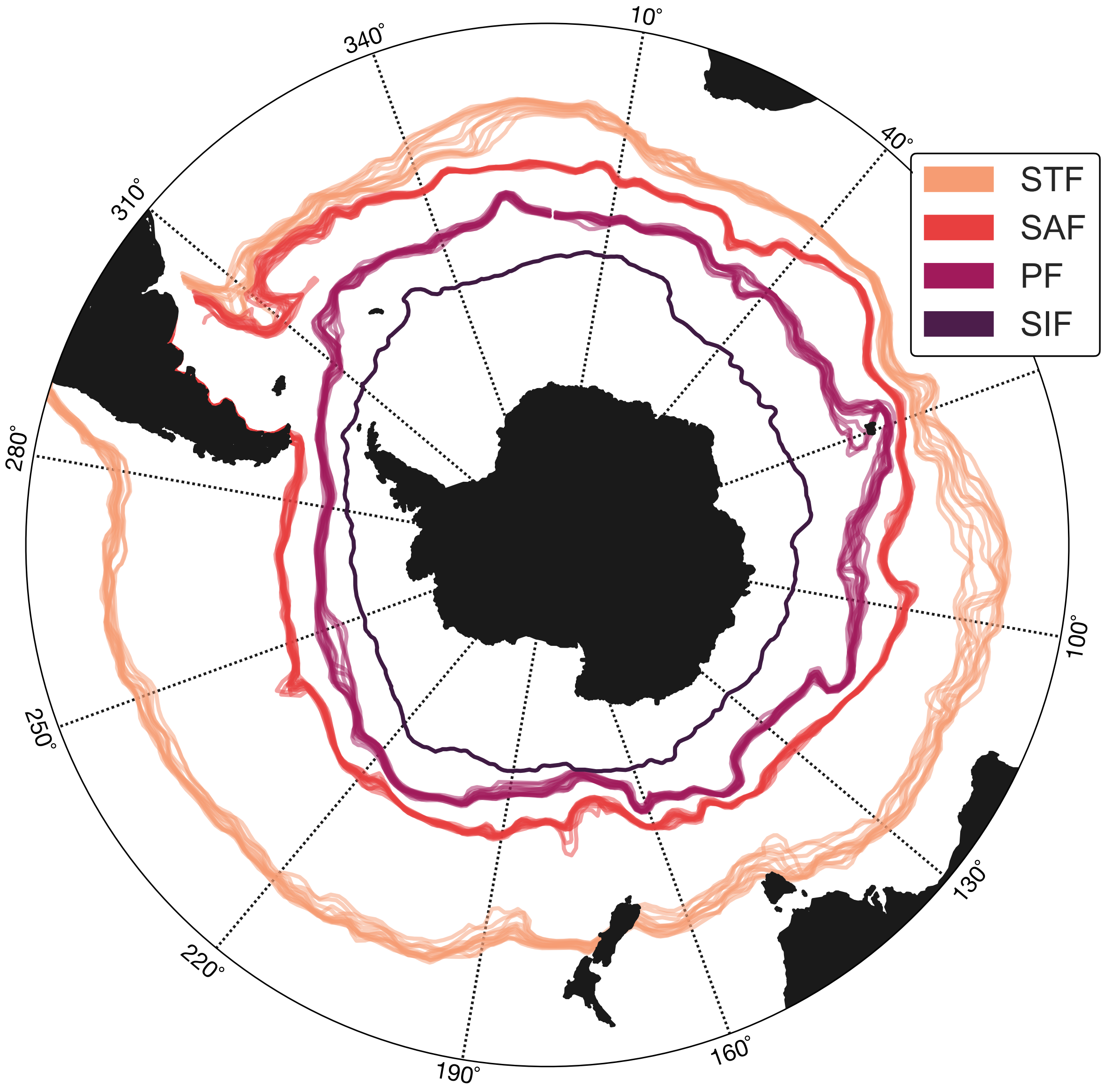

Figure C.1: Monthly position of the fronts used to define the zonal regions. (STF: Subtropical Front, SAF: Sub-Antarctic Front, PF: Polar Front, SIF: Sea Ice Front).

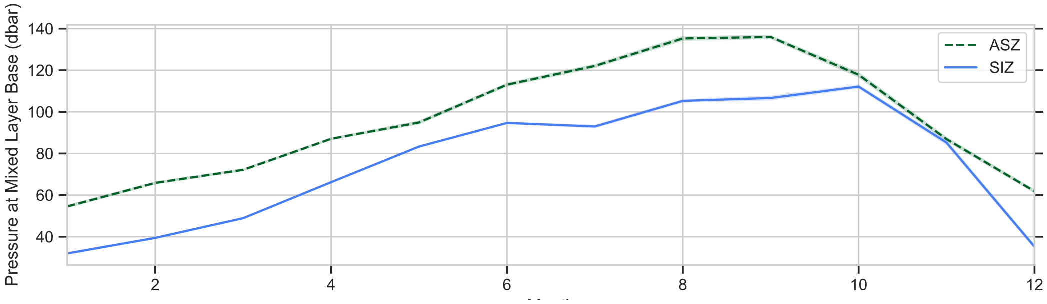

Figure C.2: Monthly pressure at the base of the mixed layer for the ASZ and the SIZ.

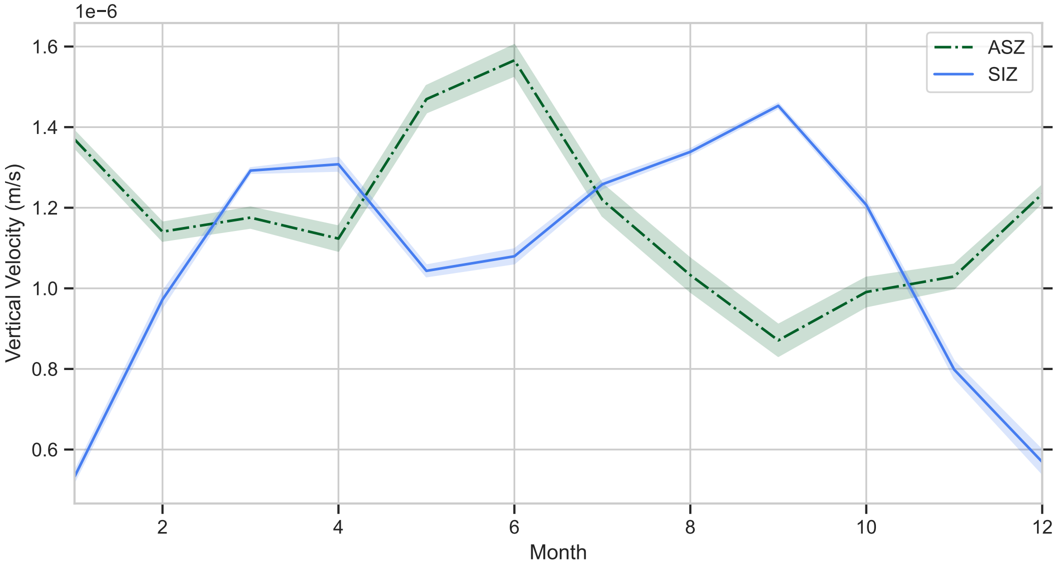

Figure C.3: Vertical Velocity at the base of the mixed layer estimated using the mixed layer mass budget. (ASZ: Antarctic Southern Zone, SIZ: Sea Ice Zone)

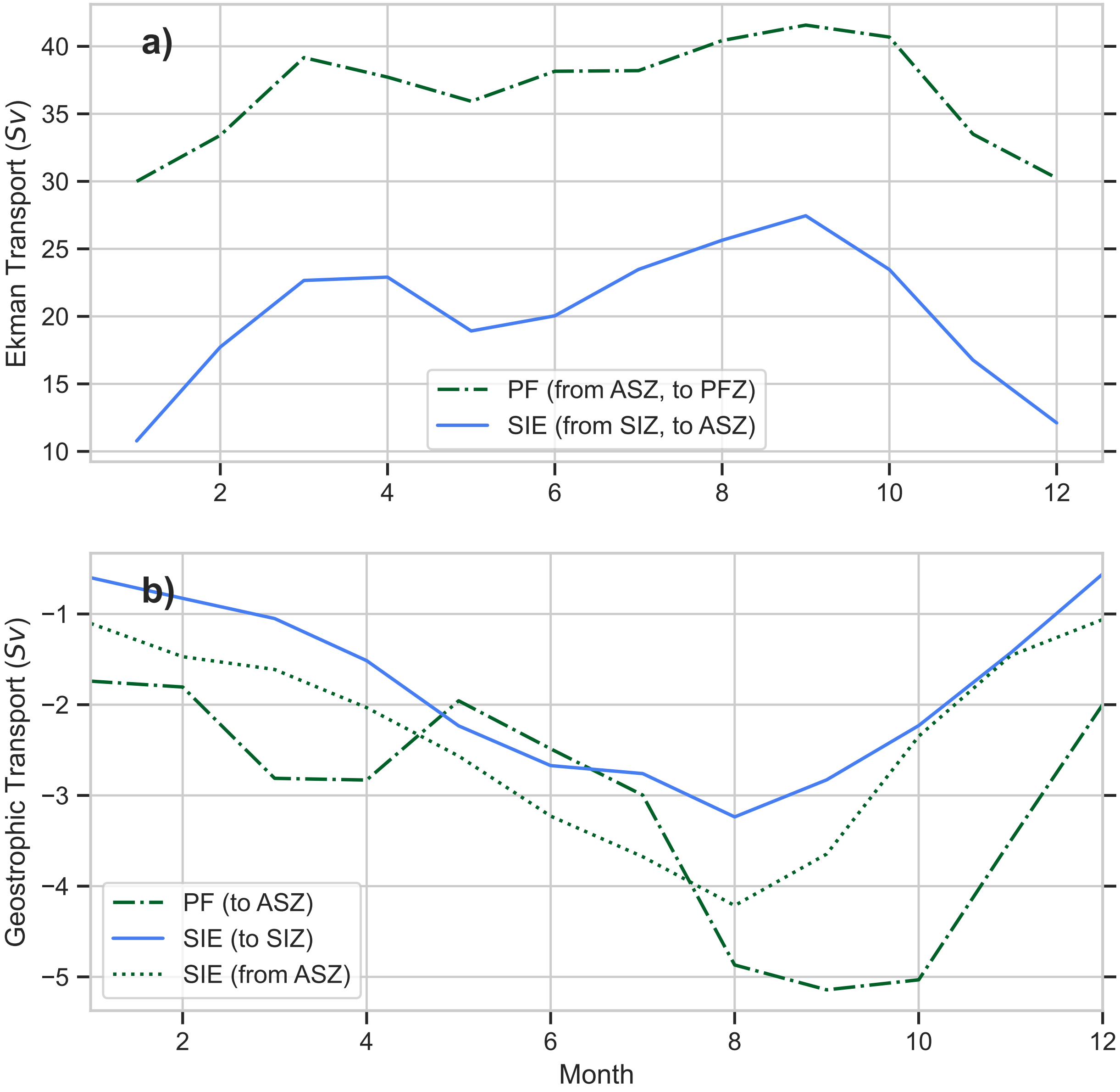

Figure C.4: Monthly mass transport of water due to a) Ekman and b) geostrophic transport. Geostrophic transport across a particular front varies by zonal region due to the choice of depth of integration, the mixed layer depth of the zone under consideration. (PF: Polar Front, SIE: Sea Ice Edge, ASZ: Antarctic Southern Zone, SIZ: Sea Ice Zone)

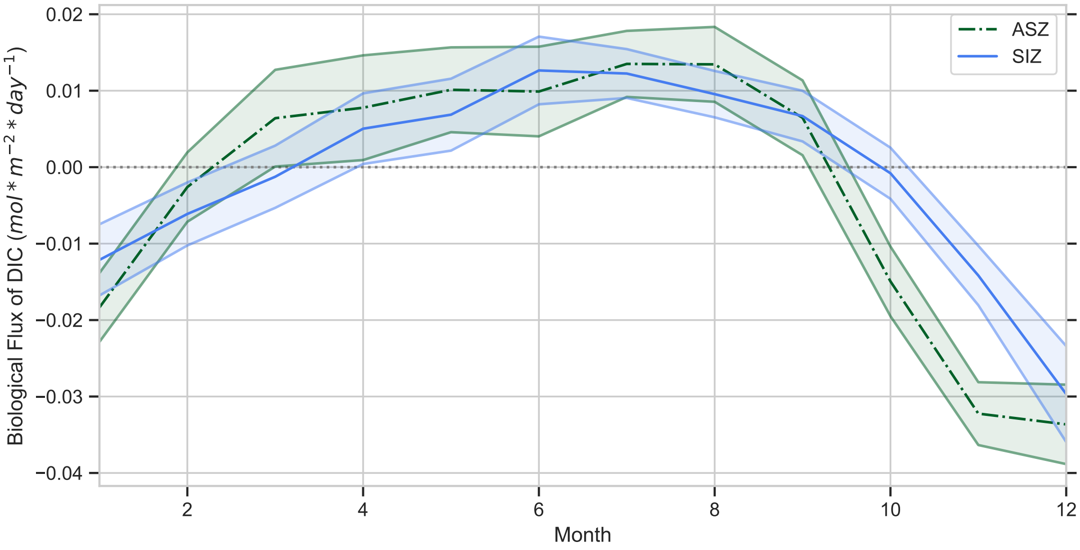

Figure C.5: Monthly biological flux of carbon estimated using the optimization scheme for the ASZ and the SIZ. The shading corresponds to one standard deviation of the Monte Carlo simulation.

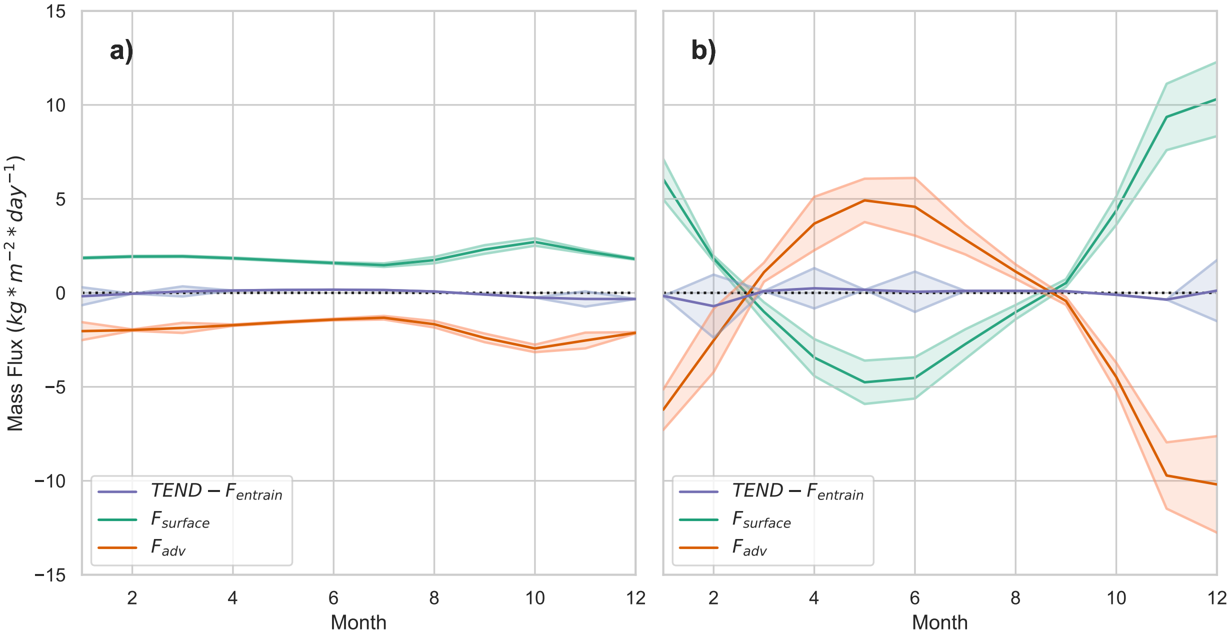

Figure C.6: Monthly averaged mixed layer mass fluxes for a) the ASZ and b) the SIZ. (TEND: Tendency, $F_{entrain}$: Entrainment flux, $F_{surface}$: Surface flux, F_{adv}: Advective flux)

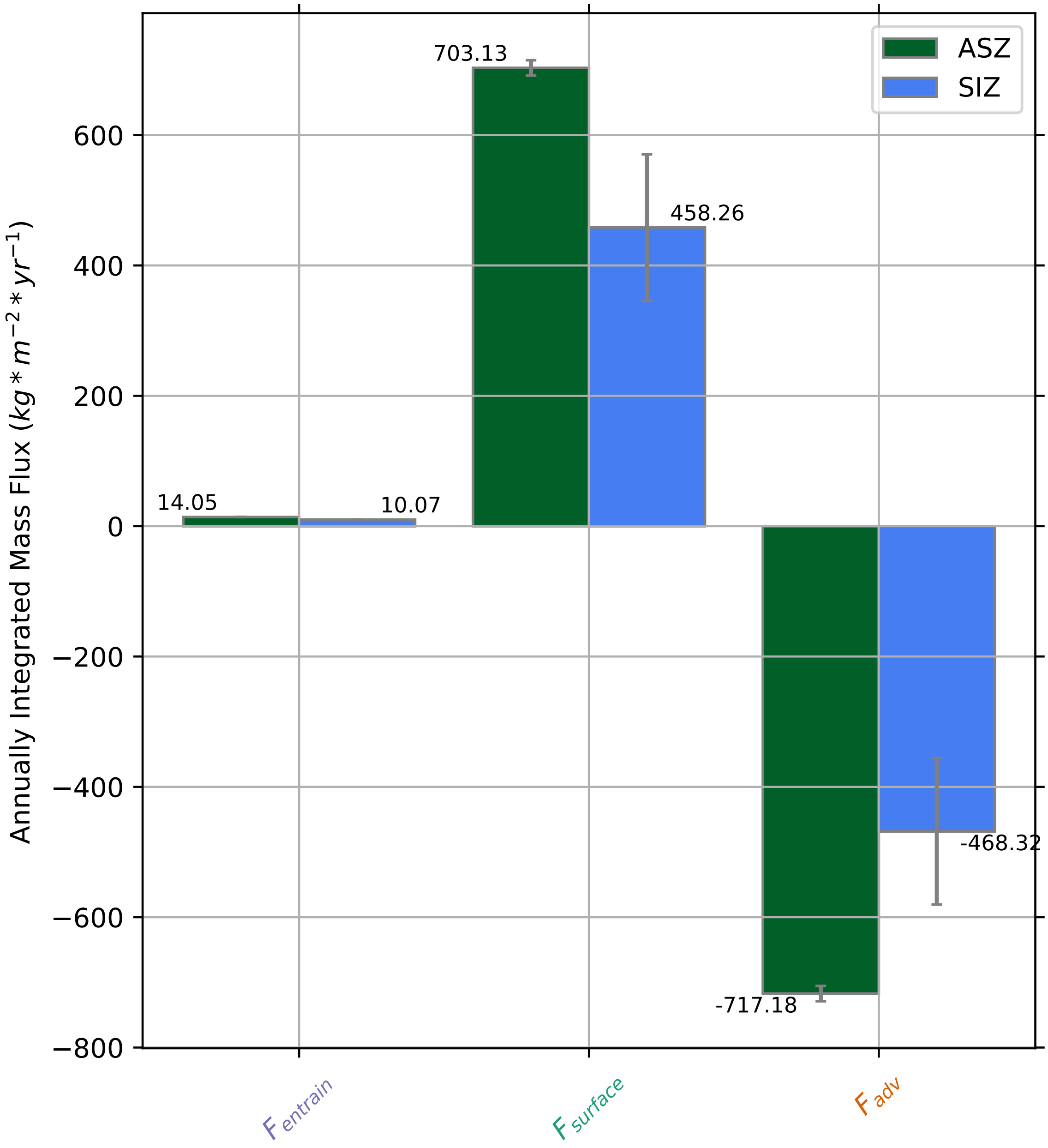

Figure C.7: Annually integrated advective fluxes of mass for the ASZ and the SIZ. ($F_{entrain}$: Entrainment flux, $F_{surface}$: Surface flux, F_{adv}: Advective flux)

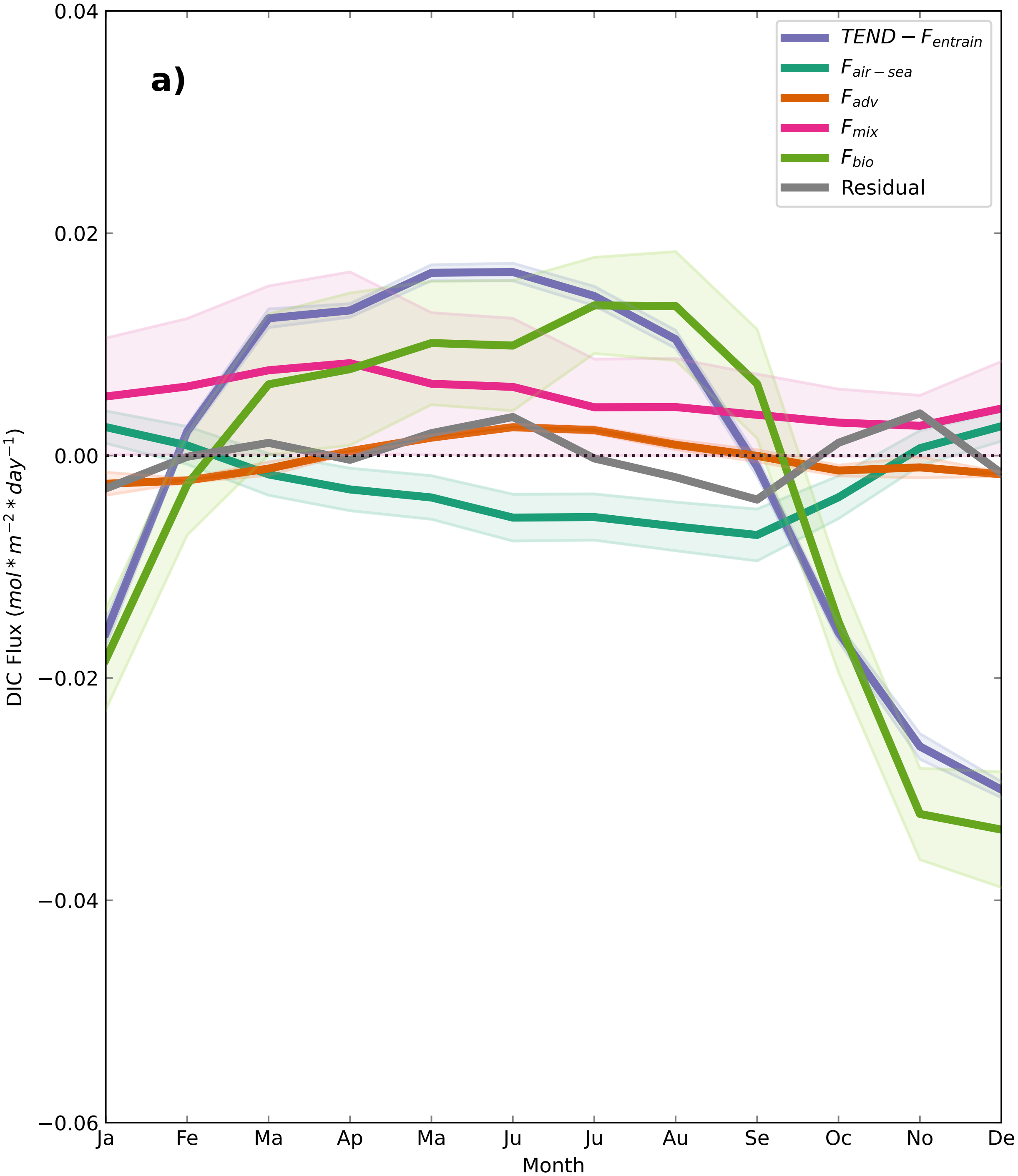

Figure C.8: Monthly averaged fluxes of DIC to and from the ASZ mixed layer as well as the budget residual in gray. Fluxes are presented with an uncertainty of one standard deviation. Negative (positive) fluxes remove (add) carbon from (to) the mixed layer. (TEND: Tendency, $F_{entrain}$: Entrainment flux, $F_{air-sea}$: Air-sea flux, F_{adv}: Advective flux, F_{mix}: Mixing flux, F_{bio}: Biological flux)

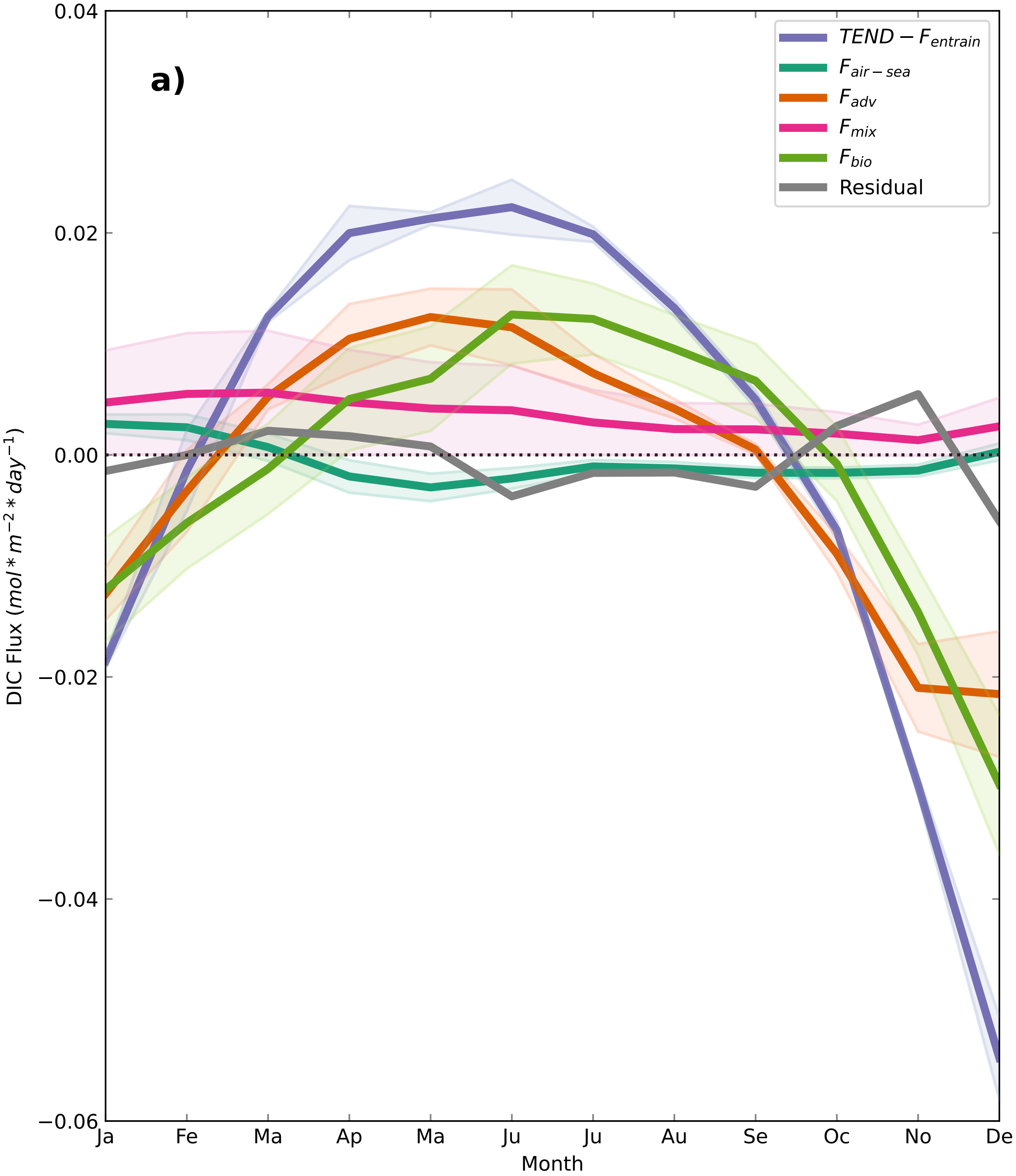

Figure C.9: Monthly averaged fluxes of DIC to and from the SIZ mixed layer as well as the budget residual in gray. Fluxes are presented with an uncertainty of one standard deviation. Negative (positive) fluxes remove (add) carbon from (to) the mixed layer. (TEND: Tendency, $F_{entrain}$: Entrainment flux, $F_{air-sea}$: Air-sea flux, F_{adv}: Advective flux, F_{mix}: Mixing flux, F_{bio}: Biological flux)

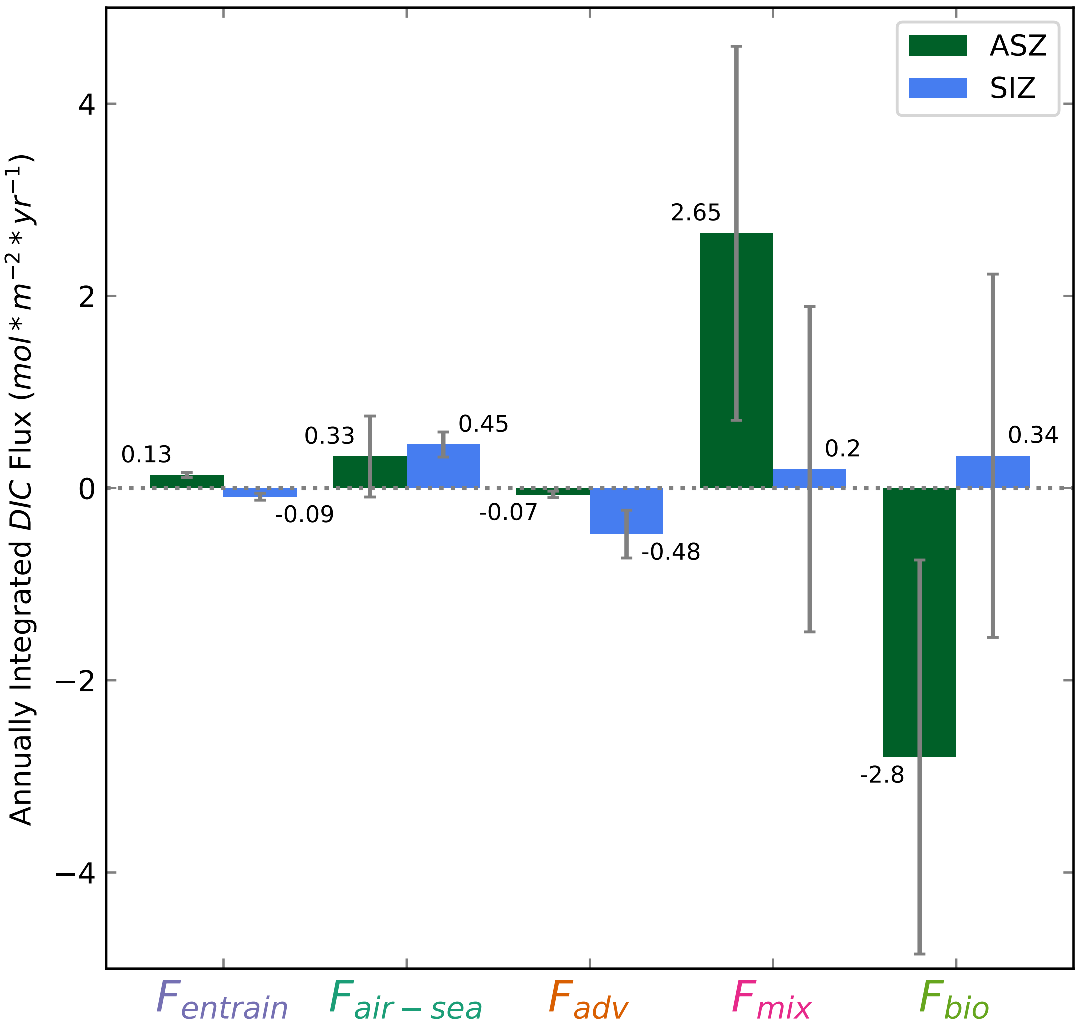

Figure C.10: Annually integrated fluxes of carbon using the SeaFlux-based air-sea flux product. ($F_{entrain}$: Entrainment flux, $F_{air-sea}$: Air-sea flux, F_{adv}: Advective flux, F_{mix}: Mixing flux, F_{bio}: Biological flux

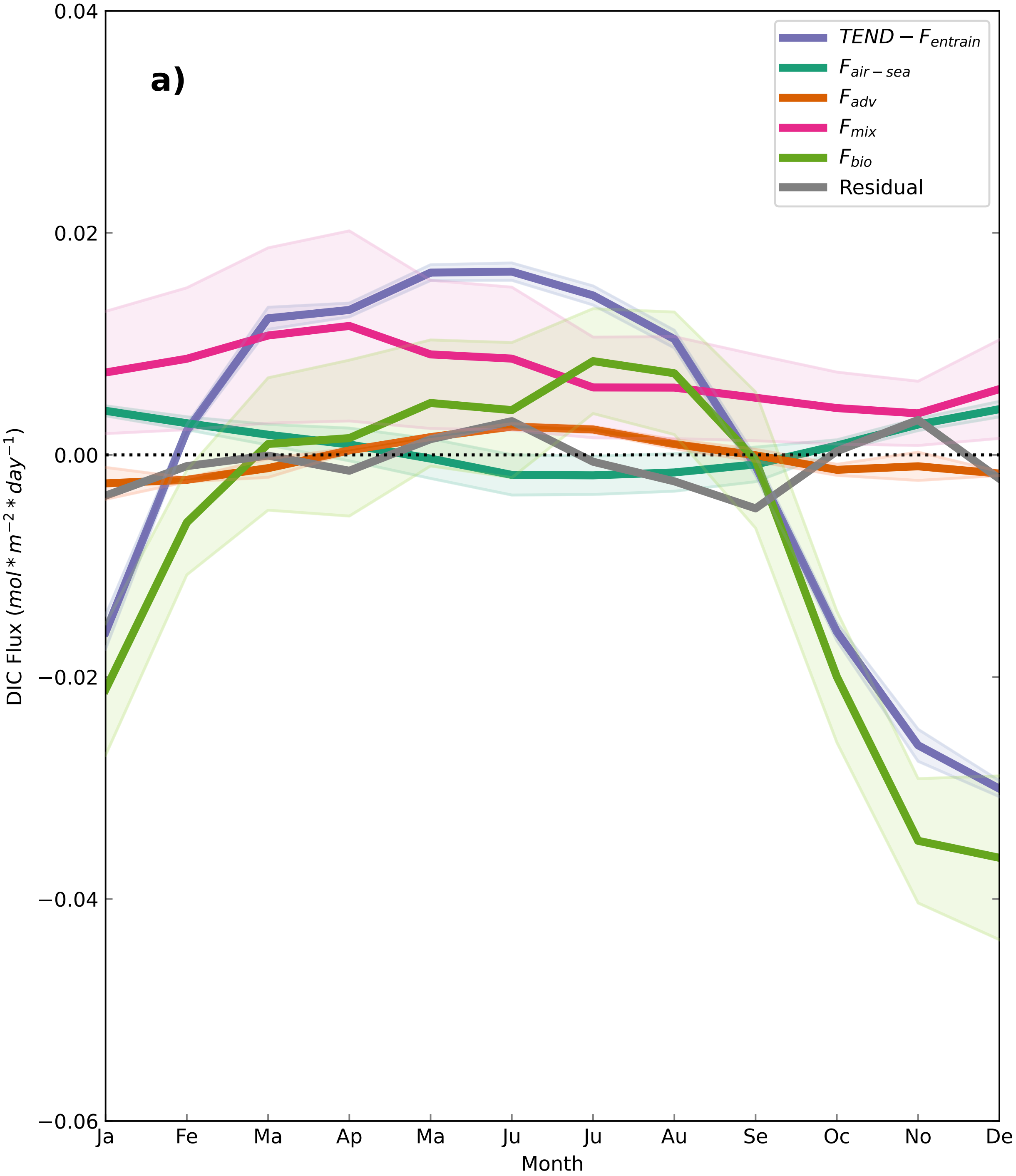

Figure C.11: Monthly averaged fluxes of DIC to and from the ASZ mixed layer using the SeaFlux-based air-sea flux product. Fluxes are presented with an uncertainty of one standard deviation. Negative (positive) fluxes remove (add) carbon from (to) the mixed layer.(TEND: Tendency, $F_{entrain}$: Entrainment flux, $F_{air-sea}$: Air-sea flux, F_{adv}: Advective flux, F_{mix}: Mixing flux, F_{bio}: Biological flux)

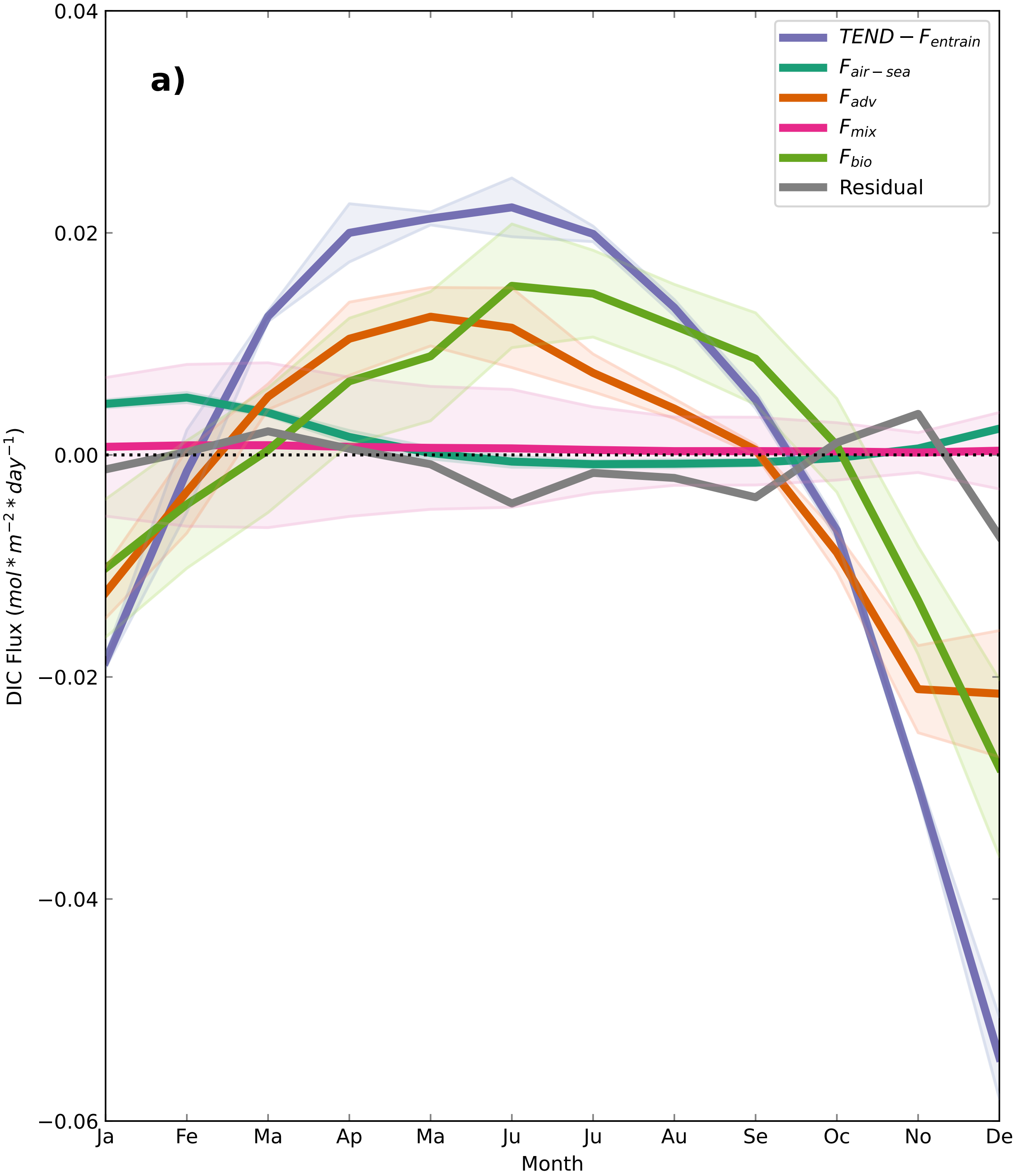

Figure C.12: Monthly averaged fluxes of DIC to and from the SIZ mixed layer using the SeaFlux-based air-sea flux product. Fluxes are presented with an uncertainty of one standard deviation. Negative (positive) fluxes remove (add) carbon from (to) the mixed layer. (TEND: Tendency, $F_{entrain}$: Entrainment flux, $F_{air-sea}$: Air-sea flux, F_{adv}: Advective flux, F_{mix}: Mixing flux, F_{bio}: Biological flux)

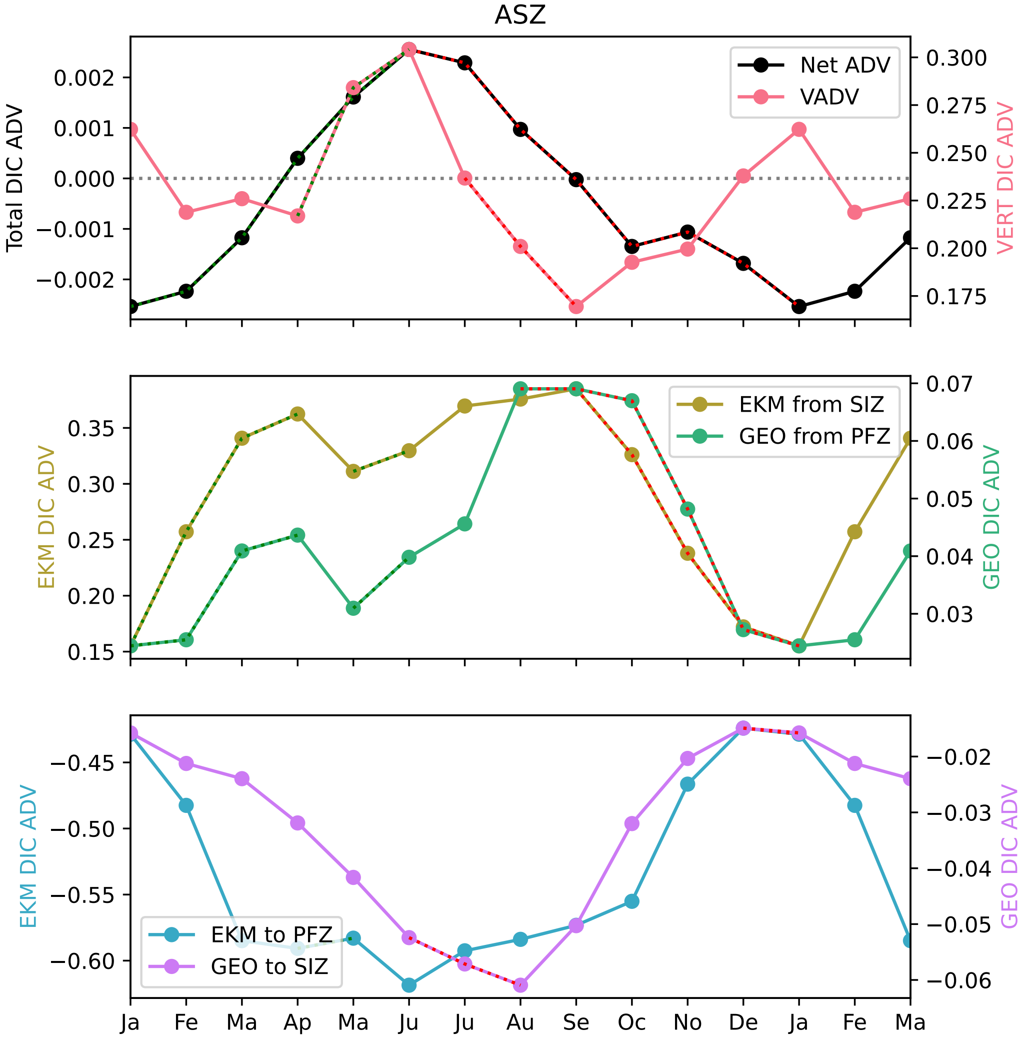

Figure C.13: Monthly averaged net advective flux of DIC and its components in the ASZ (mol C $*m^{-2}*day^{-1}$). a) Net advective flux of DIC (Net ADV) and vertical advective flux of DIC (VADV). b) Ekman advective flux of DIC from the SIZ (EKM from SIZ) and geostrophic advective flux of DIC from the PFZ (GEO from PFZ). c) Ekman advective flux of DIC to the PFZ (EKM to PFZ) and geostrophic advective flux of DIC to the SIZ (GEO to SIZ). Overlaid dotted red and green lines indicate periods where the slope of the advection component matches the sign of the slope of the total advection.

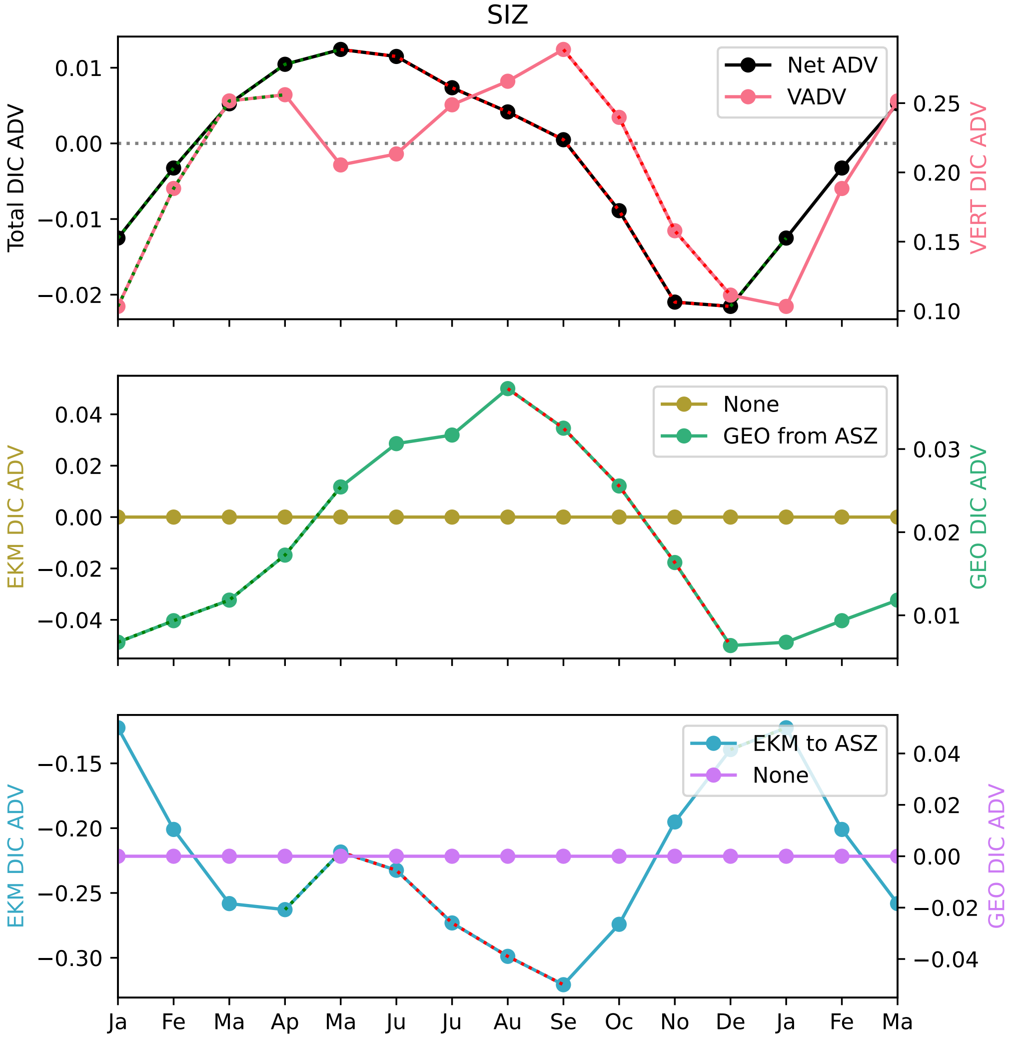

Figure C.14: Monthly averaged net advective flux of DIC and its components in the SIZ (mol C $*m^{-2}*day^{-1}$). a) Net advective flux of DIC (Net ADV) and vertical advective flux of DIC (VADV). b) Geostrophic advective flux of DIC from the ASZ (GEO from ASZ). There is no Ekman flux of mass into the SIZ. c) Ekman advective flux of DIC to the ASZ (EKM to ASZ). There is no geostrophic advective flux of DIC out the SIZ. Overlaid dotted red and green lines indicate periods where the slope of the advection component matches the sign of the slope of the total advection.

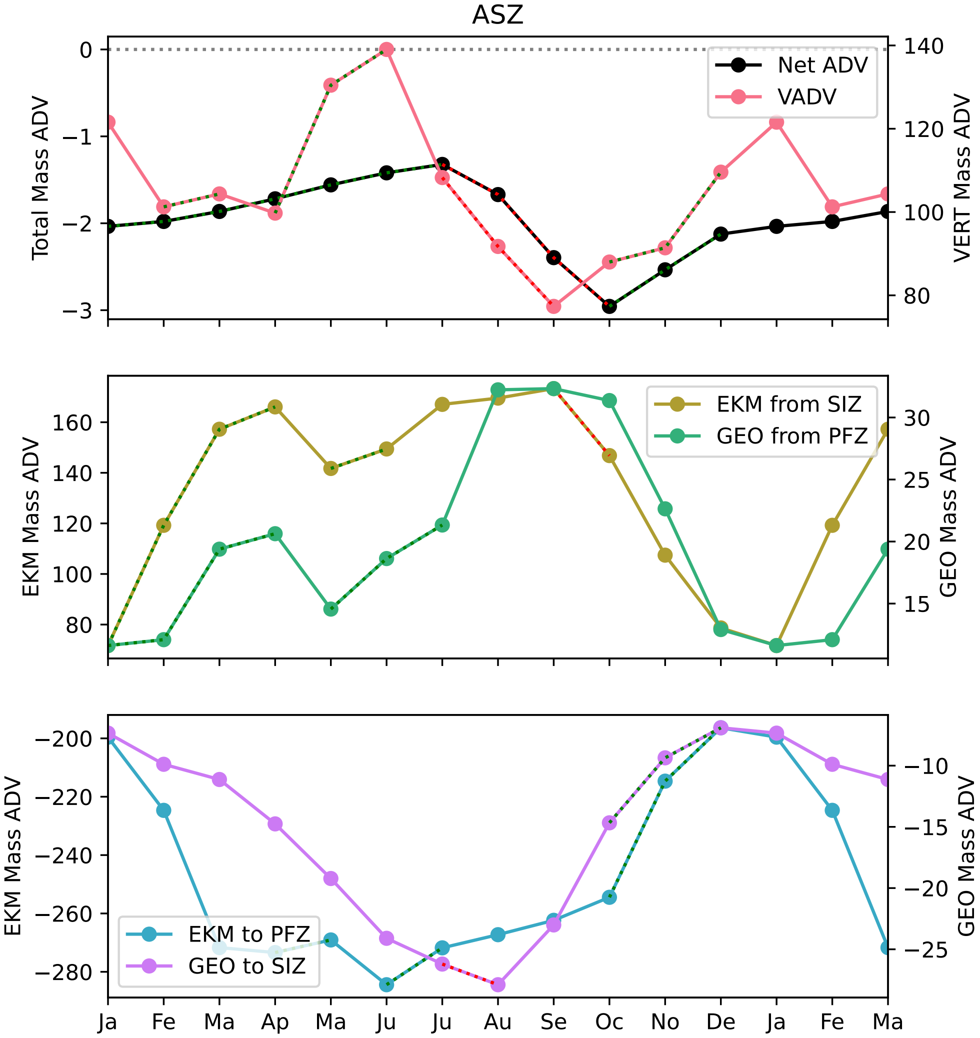

Figure C.15: Monthly averaged net advective flux of mass and its components in the ASZ (kg*m^{-2}*day^{-1}). a) Net advective flux of mass (Net ADV) and vertical advective flux of mass (VADV). b) Ekman advective flux of mass from the SIZ (EKM from SIZ) and geostrophic advective flux of mass from the PFZ (GEO from PFZ). c) Ekman advective flux of mass to the PFZ (EKM to PFZ) and geostrophic advective flux of mass to the SIZ (GEO to SIZ). Overlaid dotted red and green lines indicate periods where the slope of the advection component matches the sign of the slope of the total advection.

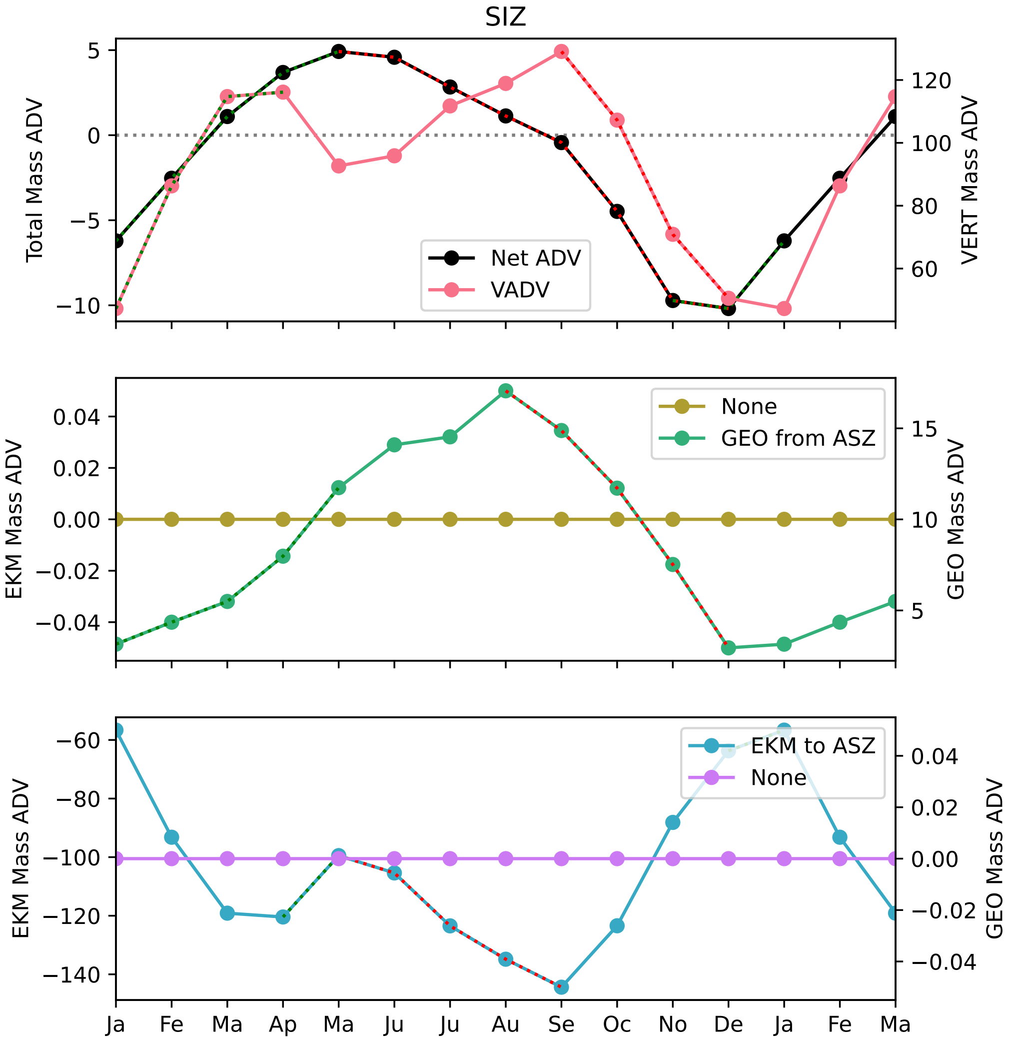

Figure C.16: Monthly averaged net advective flux of mass and its components in the SIZ (kg*m^{-2}*day^{-1}). a) Net advective flux of mass (Net ADV) and vertical advective flux of mass (VADV). b) Geostrophic advective flux of mass from the ASZ (GEO from ASZ). There is no Ekman flux of mass into the SIZ. c) Ekman advective flux of mass to the ASZ (EKM to ASZ). There is no geostrophic advective flux of mass out of the SIZ. Overlaid dotted red and green lines indicate periods where the slope of the advection component matches the sign of the slope of the total advection.

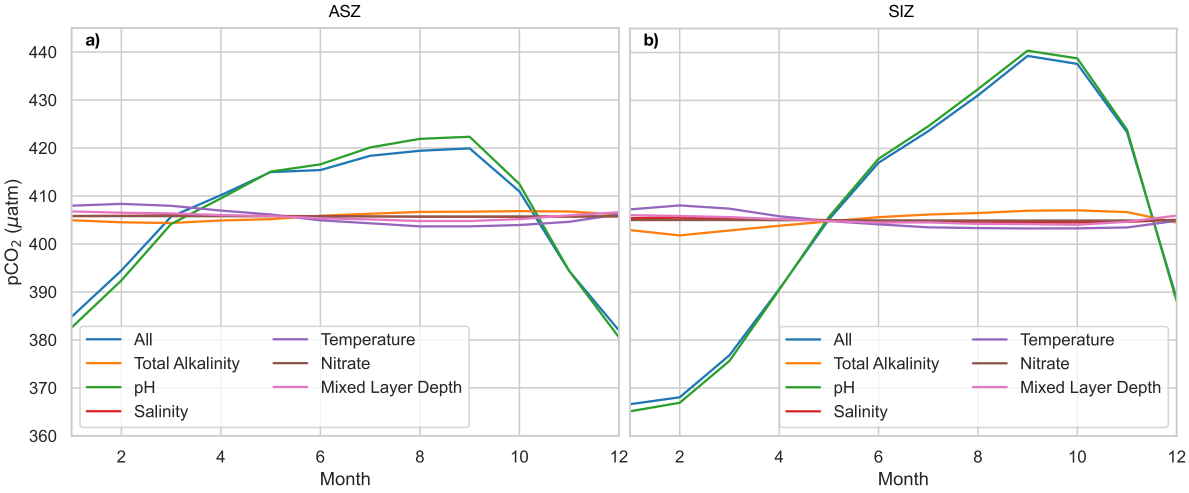

Figure C.17: Contribution to seasonal variability from each variable necessary to compute $p\mathrm{CO}_2$ using CO2SYS for a) the ASZ and b) the SIZ. (All: we vary all variables, pH: we vary pH and set all other variables to their annual average, etc.)

Chapter D

Appendix: Budget Variables for Chapter 3

This appendix contains the names of the model output used to compute the OMIP budget framework and the B-SOSE closed budget.

Table D.1: OMIP Budget Framework Variables used in this study, including the variable name, long name, units, and a brief description of their use.

Variable	Long name	Units	Used for
areacello	Grid-Cell Area for Ocean Variables	m^2	Various
deptho	Sea Floor Depth Below Geoid	mol m^{-3}	Identifying the 1000m isobath
thetao	Sea Water Potential Temperature	°C	Computing density, identifying the Polar Front
so	Sea Water Salinity	psu	Computing density
dissic	Dissolved Inorganic Carbon Concentration	mol m^{-3}	Various
o2	Dissolved Oxygen Concentration	mol m^{-3}	Various
mlotst	Ocean Mixed Layer Thickness Defined by Sigma T	m	Identifying the mixed layer depth
siconc	Sea-Ice Area Percentage (Ocean Grid)	%	Identifying the sea ice edge
zos	Sea Surface Height Above Geoid	m	Identifying the Polar Front
fgco2	Surface Downward Mass Flux of Carbon as CO_2	kg C m^{-2} s^{-1}	Air-Sea flux of carbon
fgo2	Surface Downward Flux of O_2	mol m^{-2} s^{-1}	Air-Sea flux of oxygen
wfo	Water Flux into Sea Water	kg m^{-2} s^{-1}	Air-Sea flux of mass
umo, vmo	Ocean Mass X, Y Transport	kg s^{-1}	Mass transport at zonal boundaries
tauuo, tauvo	Sea Water Surface Downward X, Y Stress	N m^{-2}	Ekman transport at zonal boundaries

Table D.2: B-SOSE closed budget variables used in this study, including the variable name, long name, units, and a brief description of their use.

Variable	**Long name**	**Units**	**Used for**
MLD	Diagnosed mixed layer depth	m	Identifying the mixed layer depth
BLGBIOC	Tendency of DIC due to biology	mol m^{-3} s^{-1}	Biology
surfCO2flx	Flux of CO_2 due to air-sea exchange	mol m^{-2} s^{-1}	Air-Sea Flux
DIC	Dissolved Inorganic Carbon concentration	mol m^{-3}	Entrainment, Advection
O_2	Dissolved oxygen concentration	mol m^{-3}	Entrainment
ForcDIC	DIC forcing tendency due to freshwater flux	mol m^{-3} s^{-1}	Advection
ForcO2	O_2 forcing tendency due to freshwater flux	mol m^{-3} s^{-1}	Advection
DIC snapshot	Dissolved Inorganic Carbon concentration	mol m^{-3}	Tendency
O2 snapshot	Dissolved oxygen concentration	mol m^{-3}	Tendency
ADVxDIC, ADVyDIC, ADVrDIC	Zonal, meridional, and vertical Advective Flux of DIC	mol m^{-3} s^{-1}	Advection
ADVxO2, ADVyO2, ADVrO2	Zonal, meridional, and vertical Advective Flux of O_2	mol m^{-3} s^{-1}	Advection
WvelMass	Vertical Mass-Weighted Component of Velocity	m s^{-1}	Advection
DFxEDIC, DFyEDIC, DFrIDIC	Zonal, meridional, and vertical Diffusive Flux of DIC	mol m^{-3} s^{-1}	Mixing
DFxEO2, DFyEO2, DFrIO2	Zonal, meridional, and vertical Diffusive Flux of O_2	mol m^{-3} s^{-1}	Mixing
Theta	Potential temperature	°C	Identifying the polar front
SeaIceArea	SEAICE fractional ice-covered area [0 to 1]	m^2 m^{-2}	Identifying the sea ice edge
ETAN	Surface Height Anomaly	m	Identifying the polar front

Chapter E

Appendix: B-SOSE Closed Budget Methodology

In this section, we give more practical details on how to close the DIC and O_2 budgets for B-SOSE using Python.

The mixed layer closed budget includes the same budget terms as the budget framework: Tendency, Entrainment, Advection, Mixing, Air-sea flux and Biology. These terms are related by the three-dimensional tracer conservation equation which is solved by B-SOSE. It can be summarized by Equation 3.1 in the main text. It is important to note that the mixed layer budget described here is extensive (ie tracer content, and not concentration, is conserved).

Utilizing the mixed layer depth output from the model, we identify the cell whose bottom is closest to the mixed layer depth and define all cells up to and including this one as the mixed layer.

Just like in the budget framework, the tendency for the closed budget is the time rate of change of tracer content in the mixed layer of each zone. To quantify it, we first multiply the snapshot tracer concentration (in $mol * m^{-3}$) by the volume of each cell to find the amount of tracer in each cell at the beginning and end of each time period (here, one month). We then sum the resulting tracer content (in mol) for all cells corresponding to the mixed layer of each zone under study (ASZ and SIZ). Finally, we take the total tracer content and we compute the time derivative using the difference between the snapshot at the beginning and end of the time step, dividing by the length of time (mol/day).

Entrainment is the process by which the mixed layer deepens and waters which were previously below the mixed layer are now part of it. Detrainment is the opposite process by which mixed layer volume decreases. While all other terms of the closed budget are defined for each cell of the 3D ocean model, the entrainment term is only relevant because we are computing a budget with a time varying bottom boundary: the mixed layer. As such, loss of precision in the closed budget that arise from using output on a coarser time step than the one used by the original model affects this term more than the others. For this reason, flux due to entrainment can be very sensitive to large variations in mixed layer depth from one time step to the next. In regions where we noticed such large variations, mostly in the Weddell Sea in winter or in coastal regions, the closed budget can have a large residual. We found that using the mixed layer depth computed online and then averaged monthly (output provided by the B-SOSE modeling team) made the mixed layer depth less subject to such drastic variations and improved the residual.

$$\text{Ent} = \frac{T}{h}\frac{dH}{dt} \tag{E.1}$$

T: tracer content in entrained water (mol) h: effective depth over which entrainment/detrainment is occurring (m) H: mixed layer depth (m)

To estimate the contribution to the closed budget from entrainment and detrainment, we first identify which cells, at the bottom of the mixed layer, have been entrained or detrained. To do so, we make a mask where the cells within the mixed layer are equal to 1 and the cells without are equal to 0. We then calculate the 1st order discrete difference along the time axis. The resulting array will be equal to -1 or 1 where cells have been added or removed from the mixed layer, and 0 everywhere else. Using this new mask, we identify the cells which are being entrained or detrained at each time step and sum the amount of tracer in this water. We also identify the vertical extent of the detrained/entrained waters using the height of each cell in the model. Once we have identified these two quantities for each cell, we can find the average concentration of the detrained/entrained water (in mol/m) for each cell by dividing the sum by the vertical extent. Finally, we take the tracer entrainment concentration and multiply it by the time derivative of the mixed layer depth (in m/day), computed using the snapshot, as above for the tendency term. The resulting spatially resolved entrainment is then summed over each zone.

The tendency of tracer due to air-sea flux is expressed in $mol/m^2/s$. We multiply the tendency by the area of the surface cells and sum the results for each zone.

Additionally, we multiply the tendency of tracer due to biology ($mol/m^3/s$) by the volume of the cells, and then sum for all cells within the mixed layer of each zone.

The advective flux of tracer is made up of contributions from the zonal, meridional and vertical advection. B-SOSE computes the advective flux of each tracer online (in mol/s) in the x,y and z direction.

The position of the advection fluxes on the model grid are staggered compared to the location of other terms like the tendency due to biology. While most budget terms are located in the center of a model grid cell, advection (and diffusion, see below) are located on the edges of the model cells. To get the flux due to advection for each cell in a way that will be consistent with the other fluxes, we first need to take the 1st order discrete difference along the appropriate axis. For example, for the advective flux in the x direction, we take the difference between neighboring cells along the x coordinate of the model. Imagining each model cell as a box, taking this difference between the values at the cell edges (the advection entering and exiting the box along the zonal direction) gives us the net zonal advection for the cell center (the net zonal advection for the box as a whole). We repeat this step for all 3 components of the advection.

The vertical advective flux requires adjustments to handle boundary conditions. First, we set the flux for the bottom cell to 0 as there is no flux through the sea floor. At the surface, we need to make an adjustment for the flux of tracer due to the surface freshwater flux. We take the vertical mass-weighted component of velocity (WvelMass in m/s) at the surface and multiply it by the tracer concentration at the surface (mol/m3) and by the area of the cell (m2). From this flux (in mol/s), we then subtract the tendency of the tracer due to freshwater converted to the right units using the volume of the cell. The resulting quantity should be set as the vertical advective flux at Z=0. Finally, note that these adjustments to the vertical advective flux should be made before taking the discrete difference described above.

$$\text{sfcflx} = a * \text{WvelMass}_{z=0} + [T]_{z=0} - D * V_{z=0} \tag{E.2}$$

$[T]$: tracer concentration (mol/m^3)

WvelMass: vertical mass-weighted component of velocity (m/s)

a: area of the cell (m^2)

D: tendency due to freshwater flux i.e. dilution ($mol/m^3/s$)

V: volume of the cell (m^3)

To ensure consistence between the components of the advection, we multiply the horizontal advective flux by -1. We then select the cells which are part of one zone's mixed layer depth and take the sum of each component of advection for these cells. We add the zonal, meridional and vertical components of advection to obtain the total advective flux.

The method for finding the mixing term is similar to the method for advection. We utilize the diffusive flux in the zonal, meridional, and vertical directions for each tracer (in mol/s). We also calculate the difference between adjacent values of the diffusive flux along the appropriate coordinates. For the vertical diffusive flux, we set the bottom flux to 0 (no correction is required at the surface) and sum the cells for the mixed layer of each zone.

Chapter F

Appendix: Additional Figures for Chapter 3

This Appendix contains additional figures for Chapter 3.

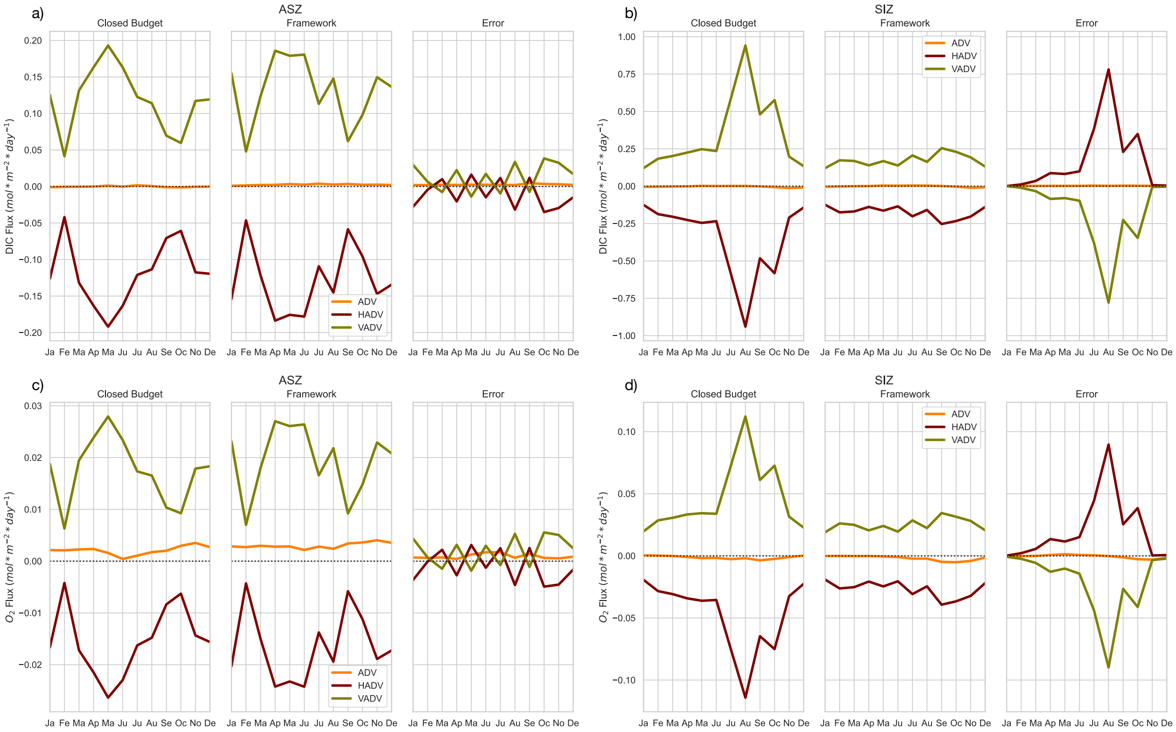

Figure F.1: Advection Components for the B-SOSE Closed Budget (leftmost panel), Budget Framework (middle panel) and the difference between them (rightmost panel) for a) the ASZ DIC budget, b) the SIZ DIC budget, c) the ASZ O_2 budget, b) the SIZ O_2 budget. The output presented is for the year 2018 and the purpose is for method validation. ADV: Total tracer advection; HADV: Horizontal tracer advection; VADV: Vertical tracer advection.

Figure F.2: Location of the Polar front (top panel) and the sea ice edge (bottom panel) for all models used in this analysis

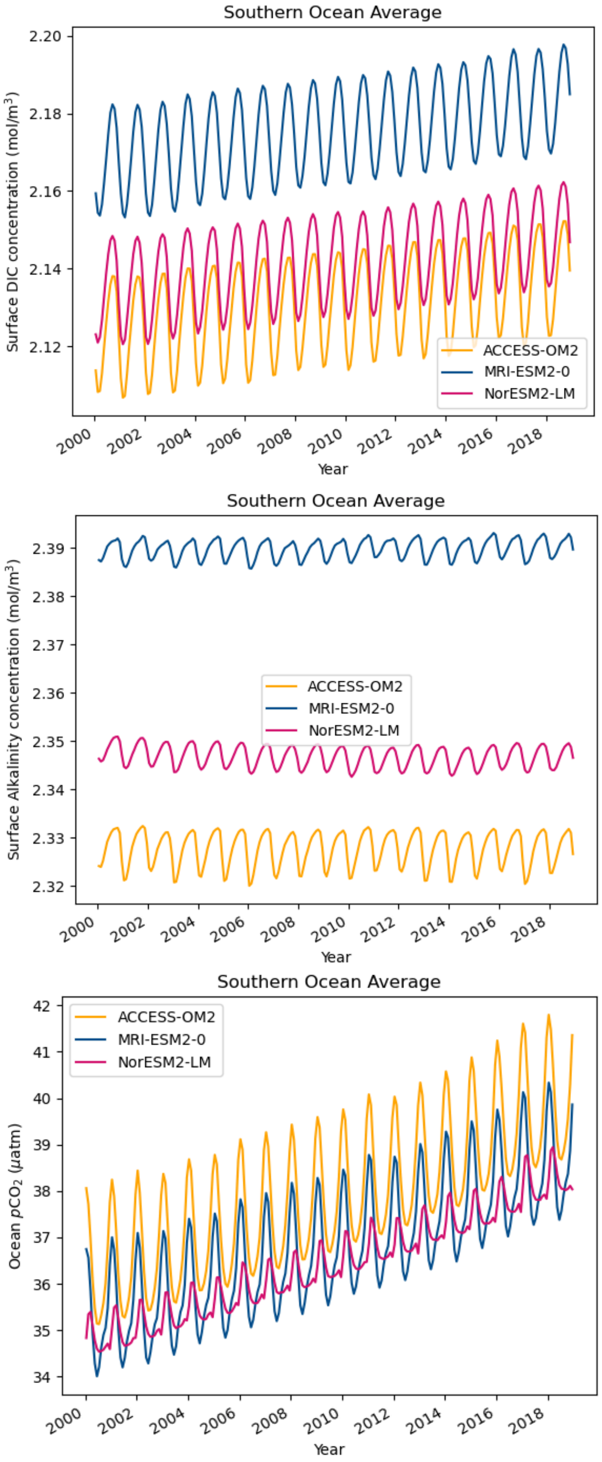

Figure F.3: Time Series of Surface Dissolved Inorganic Carbon Concentration (top panel), surface alkalinity concentration (middle panel) and ocean $p\text{CO}_2$ (bottom panel) averaged south of 30° S. for the 3 OMIP2 models

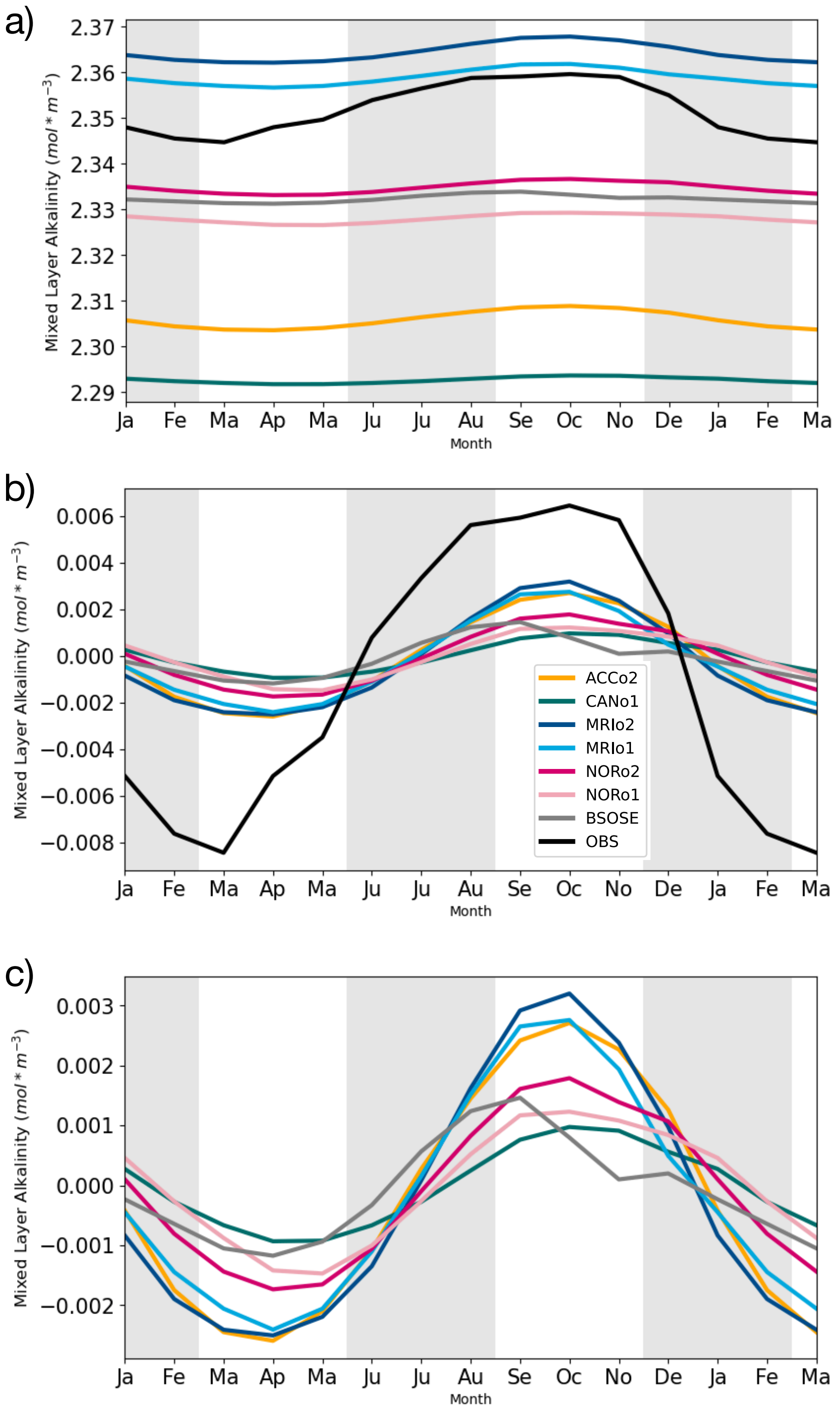

Figure F.4: a) Seasonal cycle of mixed layer alkalinity for all datasets. b) Seasonal cycle of normalized mixed layer alkalinity for all datasets. We normalize by subtracting the time-team for each dataset. c) Seasonal cycle of normalized mixed layer alkalinity for models only.

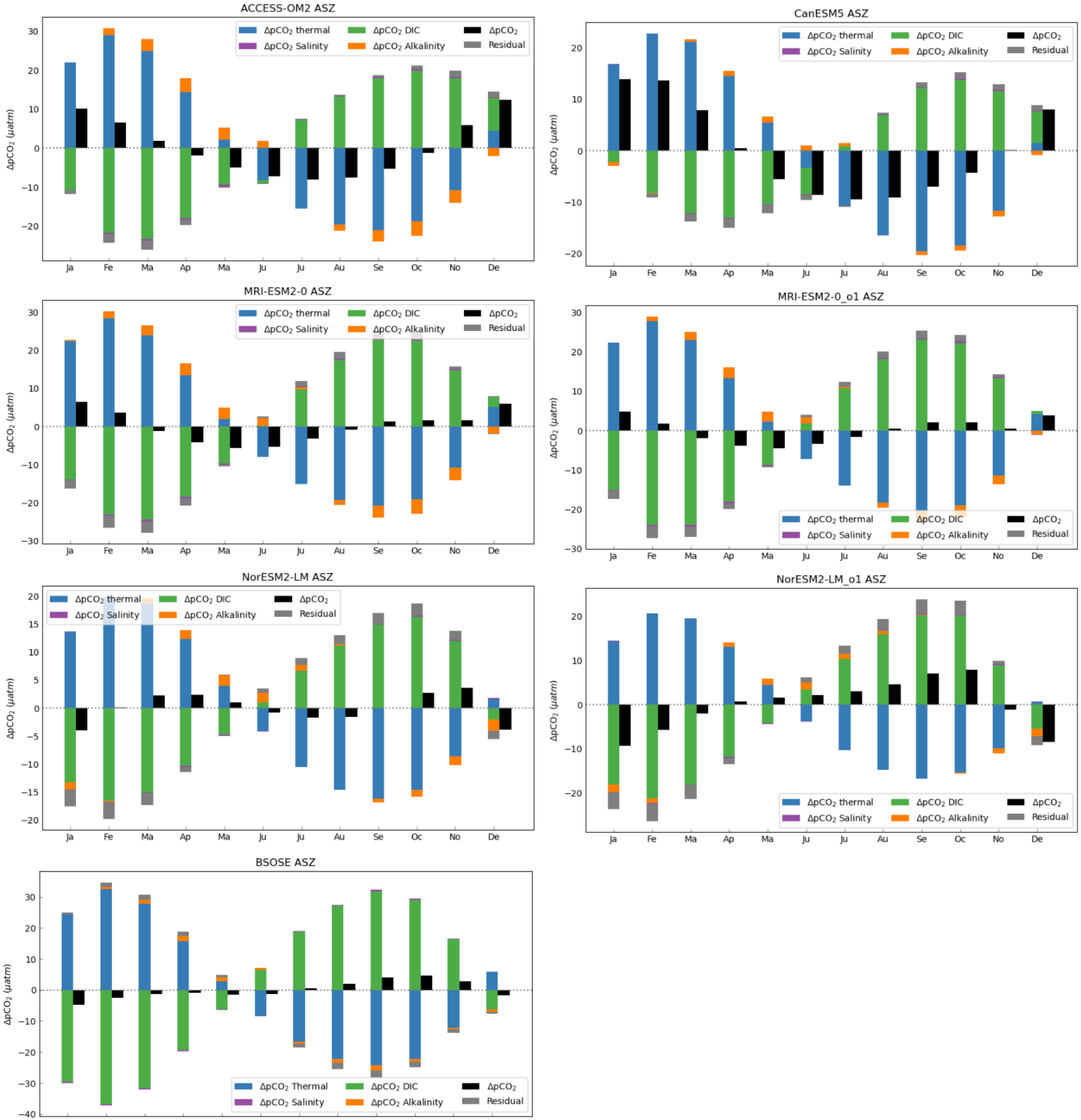

Figure F.5: Takahashi Decomposition of the seasonal variability of $p\mathrm{CO}_2$ between the Temperature, Salinity, Dissolved Inorganic Carbon, and Alkalinity components for all models.

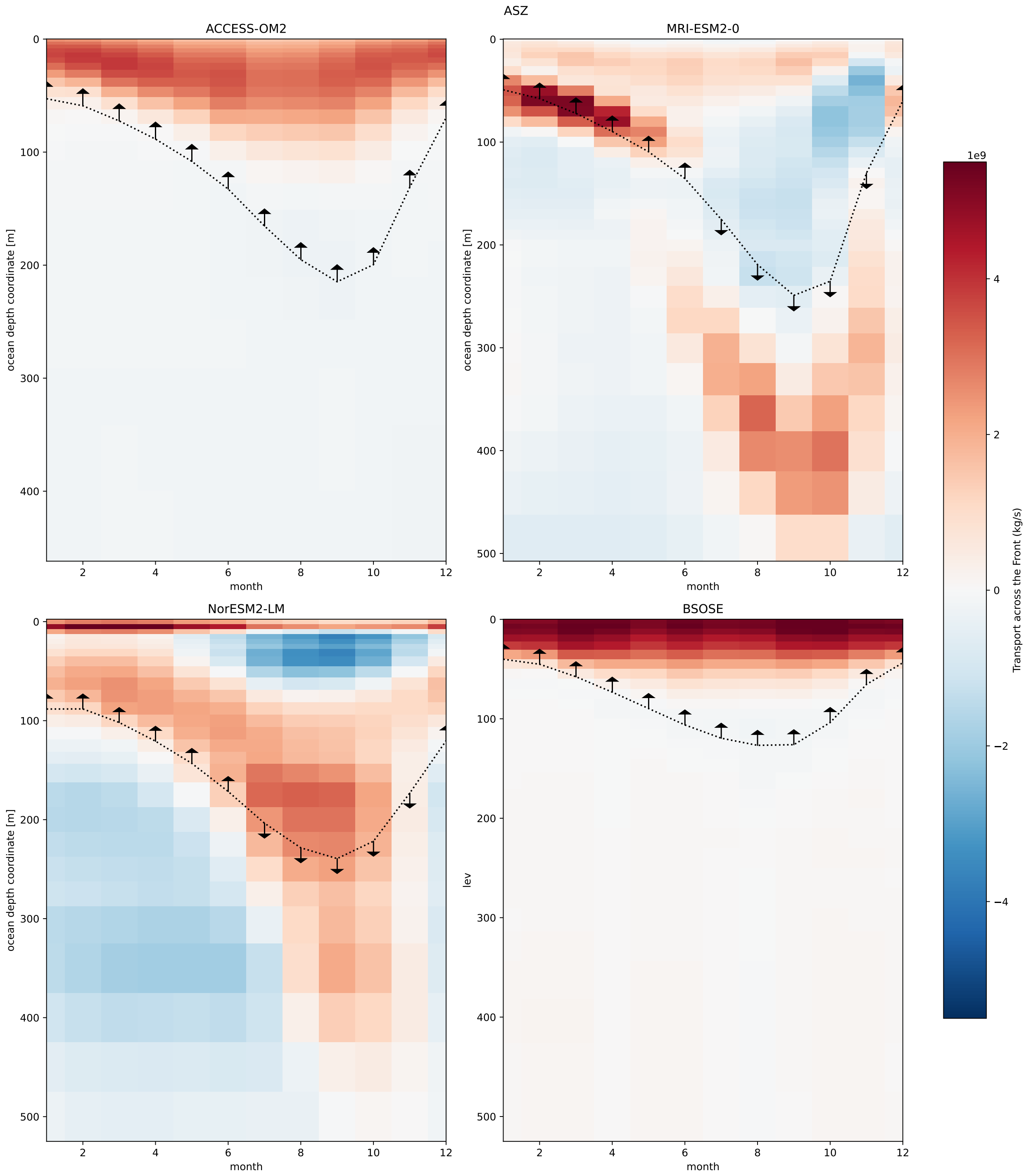

Figure F.6: Profile of the total transport of DIC across the Polar front for the OMIP2 models. Positive values indicate that the transport is exiting the zone which is located south of the front. Note that the transport shown here is the sum of meridional and zonal transport across the front. The zonal component exists because the front does not follow a parallel of constant latitude. The dashed line indicates the spatially averaged mixed layer depth. The black arrows indicate the sign of the vertical velocity.

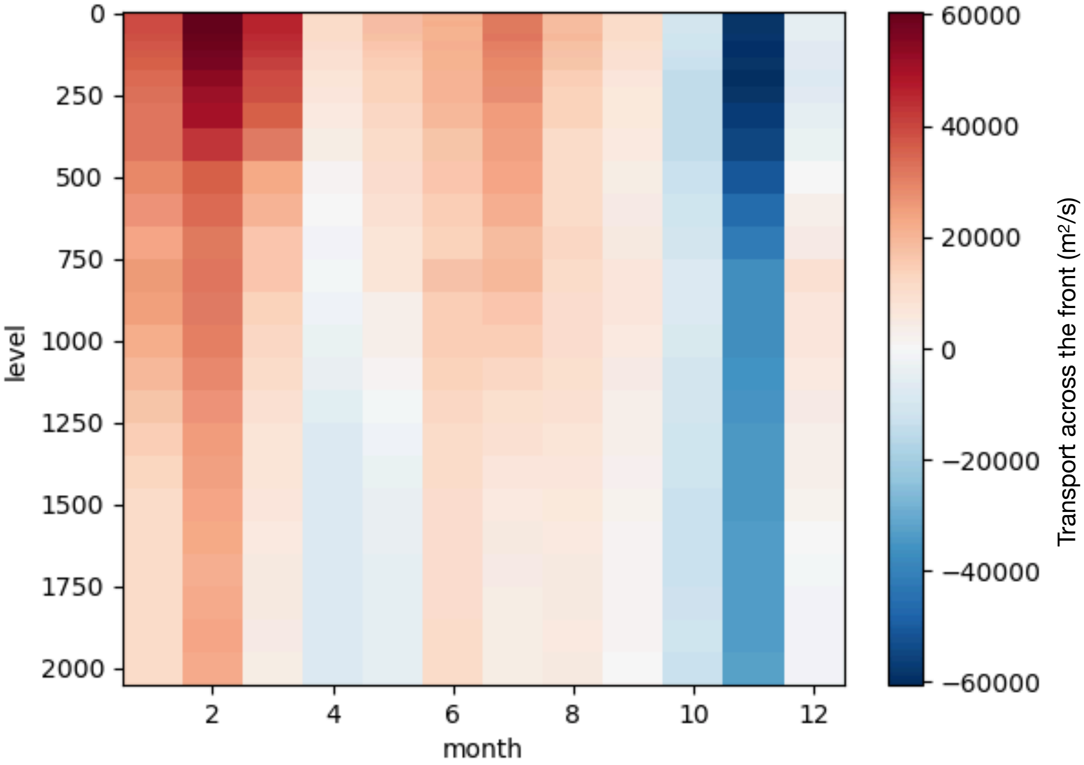

Figure F.7: Profile of the total geostrophic velocity across the Polar front integrated along the front computed from observational products. Positive values indicate that water is exiting the zone which is located south of the front. Note that the integrated velocity shown here is the sum of meridional and zonal geostrophic velocity across the front. The zonal component exists because the front does not follow a parallel of constant latitude. Note that this geostrophic component of the total advection will be added to a northward Ekman component which is not defined in depth.

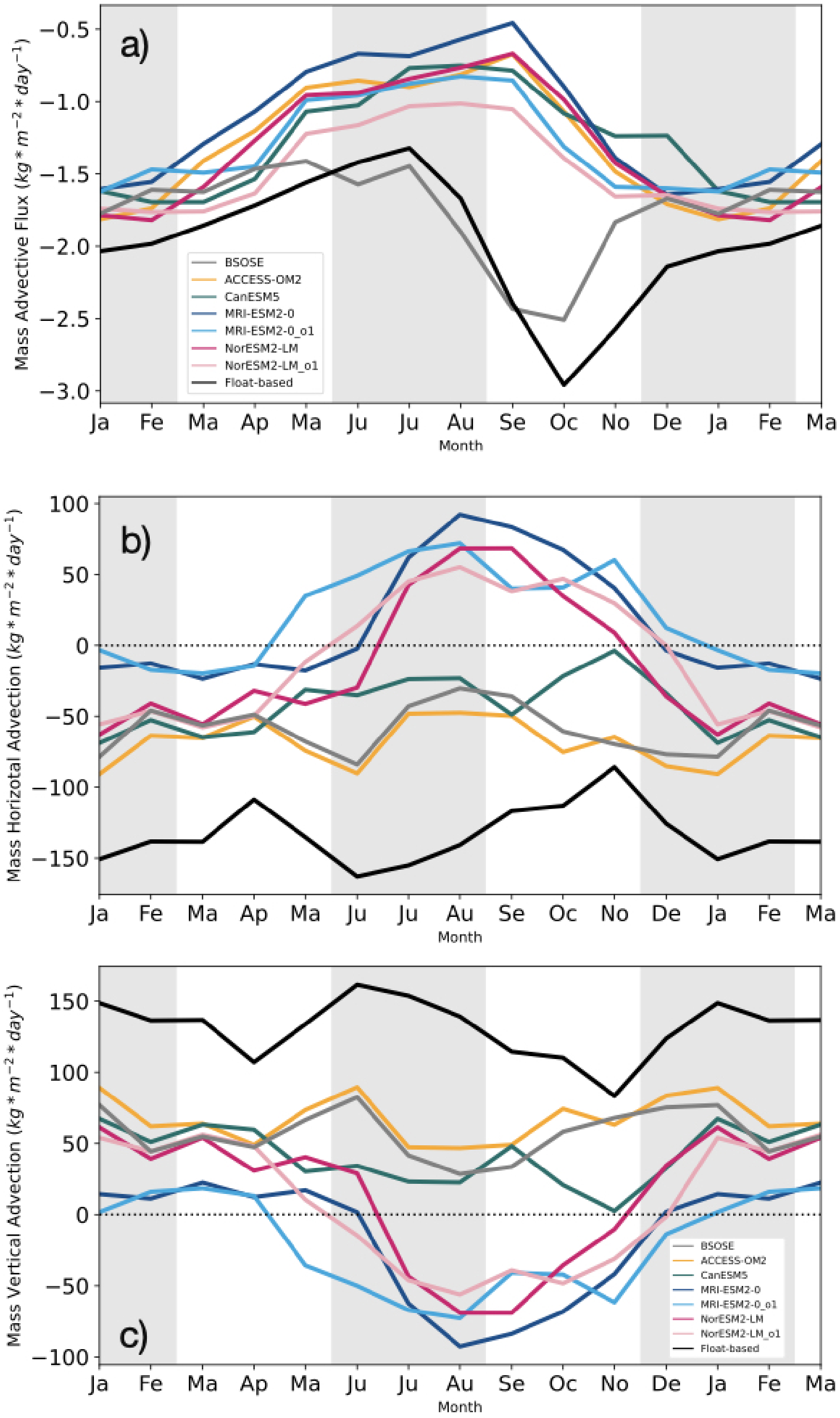

Figure F.8: a) Total, b) horizontal and c) vertical mass advection for the ASZ for each dataset. (ASZ: Antarctic Southern Zone)

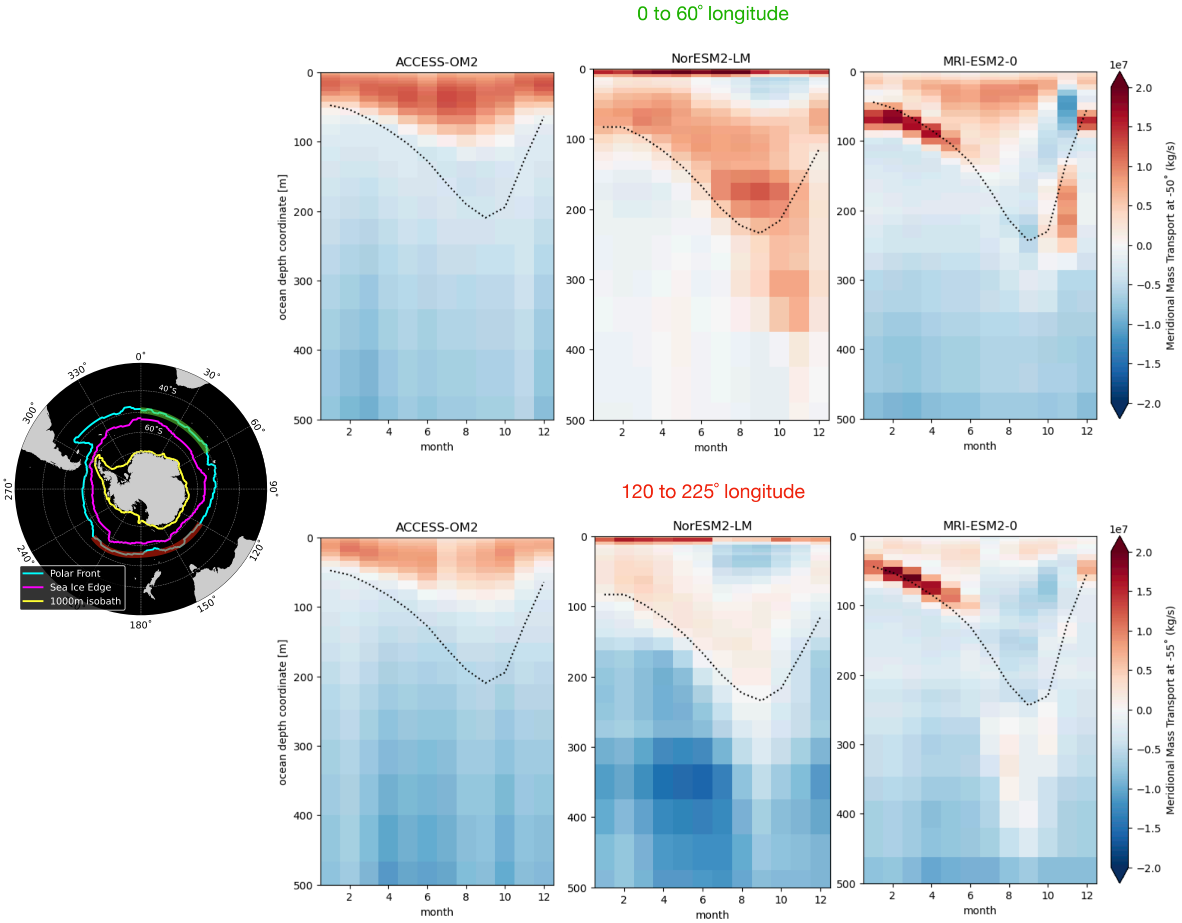

Figure F.9: Profile of the meridional mass transport for the OMIP2 models at at latitudes and longitudes chosen for their proximity to the Polar front. The top row is averaged from 0 to 60 ° longitude at 50 ° latitude and corresponds to the green highlighted portion of the map. The bottom row is averaged from 120 to 225 ° longitude at 55 ° latitude and corresponds to the red highlighted portion of the map. Positive values indicate northward transport. The dashed line indicates the spatially averaged mixed layer depth.

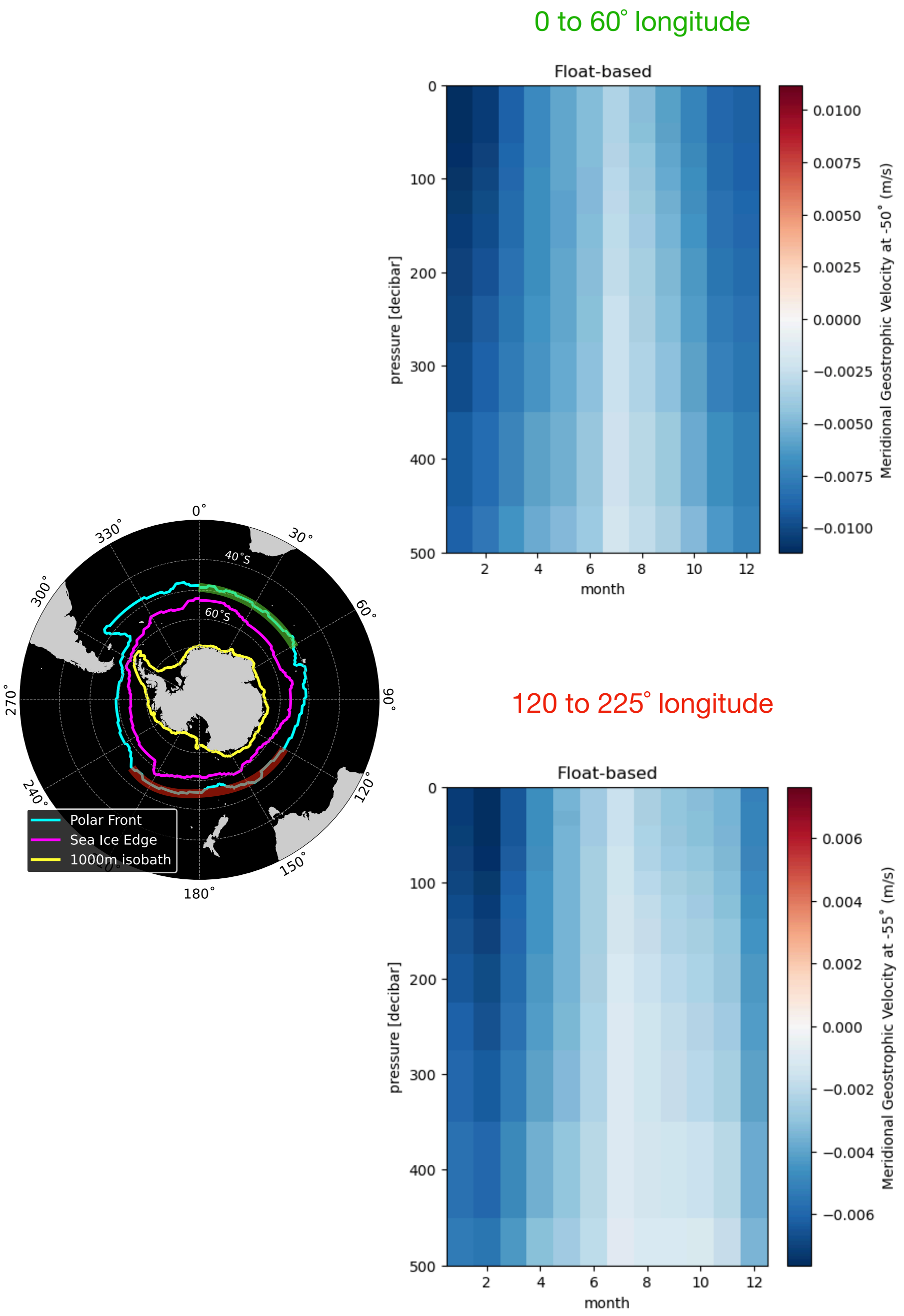

Figure F.10: Profile of the meridional geostrophic velocity based on observational products at latitudes and longitudes chosen for their proximity to the Polar front. The top row is averaged from 0 to 60 ° longitude at 50 ° latitude and corresponds to the green highlighted portion of the map. The bottom row is averaged from 120 to 225 ° longitude at 55 ° latitude and corresponds to the red highlighted portion of the map.

a) Using spatially varying mixed layer depth

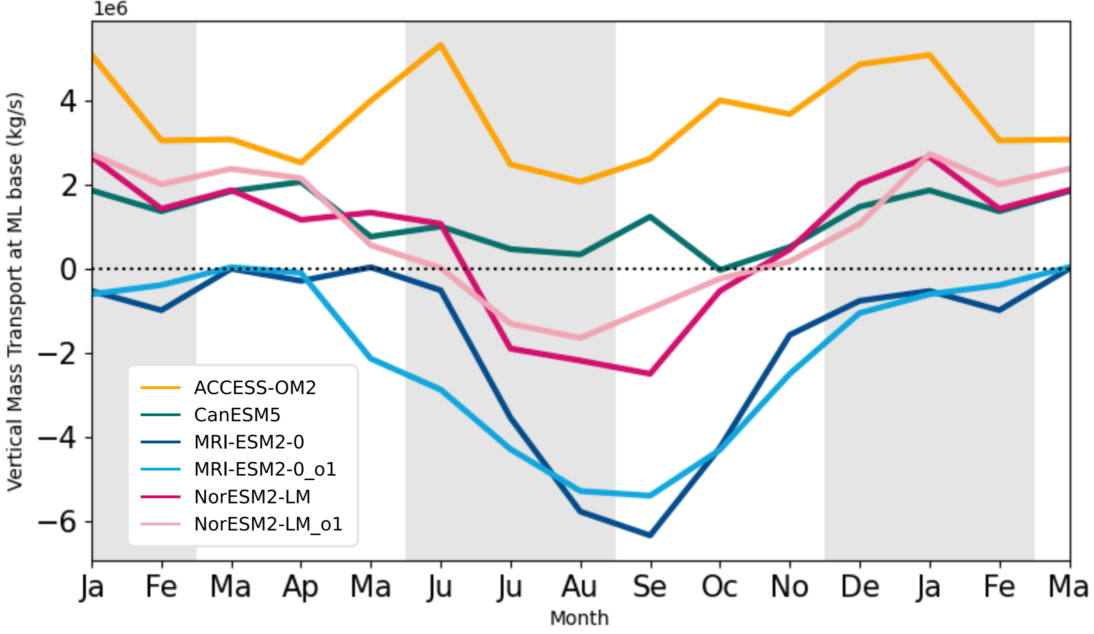

b) Using spatially averaged mixed layer depth

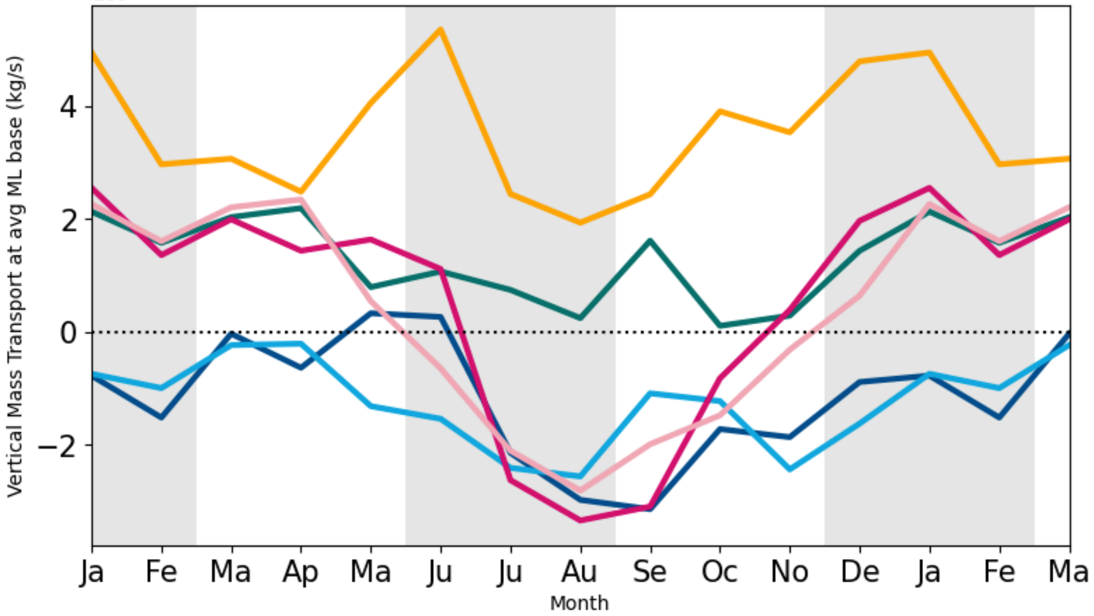

Figure F.11: Zone-averaged vertical mass transport for OMIP models computed directly from model output using a) a spatially-varying mixed layer depth and b) a zone-averaged mixed layer depth. Positive values indicate upwelling.

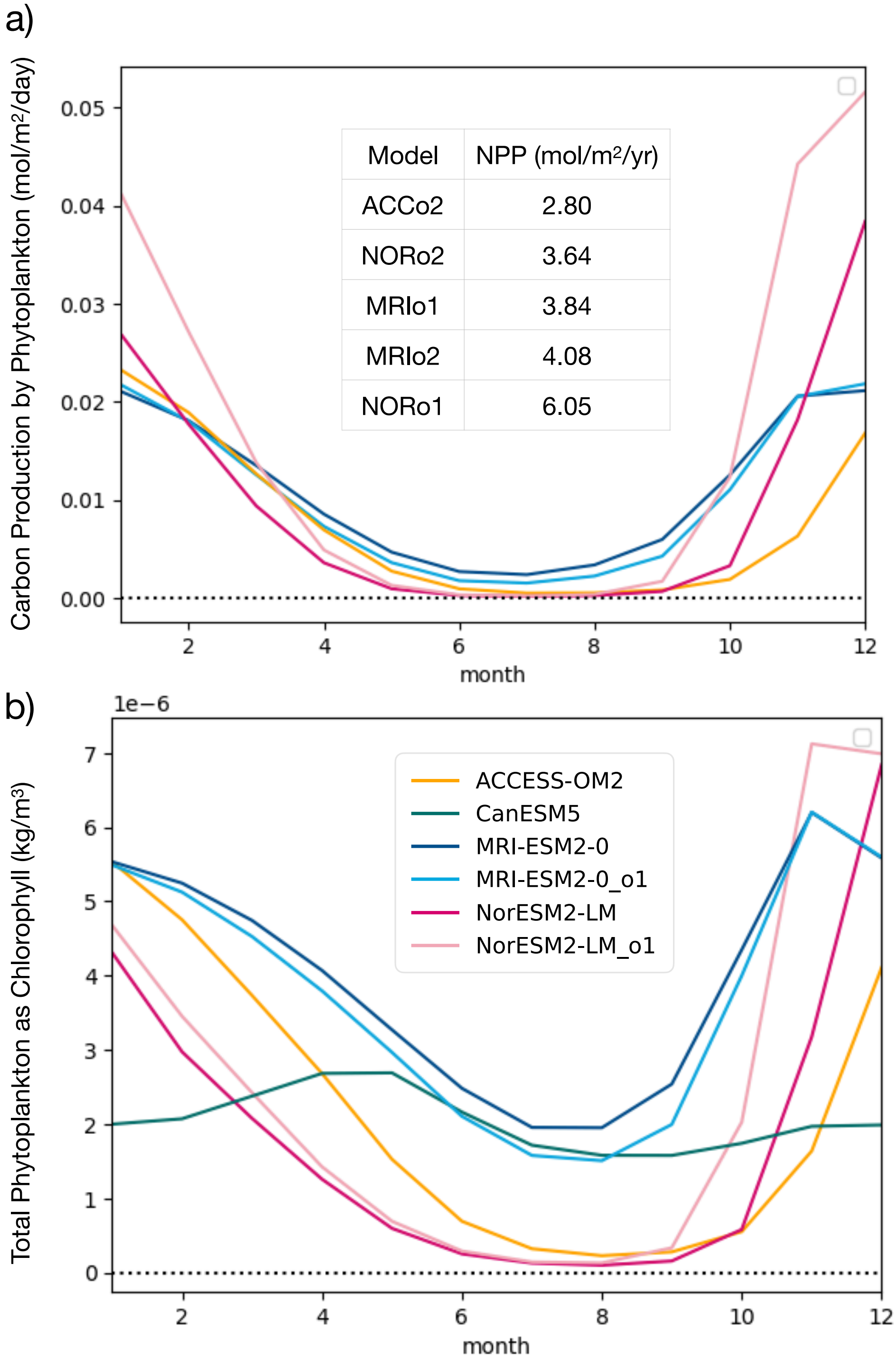

Model	NPP (mol/m²/yr)
ACCo2	2.80
NORo2	3.64
MRIo1	3.84
MRIo2	4.08
NORo1	6.05

Figure F.12: a) Zone-averaged primary organic carbon production by all types of phytoplankton for OMIP models except CanESM5 (output does not exist). b) Mass concentration of total phytoplankton expressed as chlorophyll in sea water integrated over the top 100m and zone-averaged.

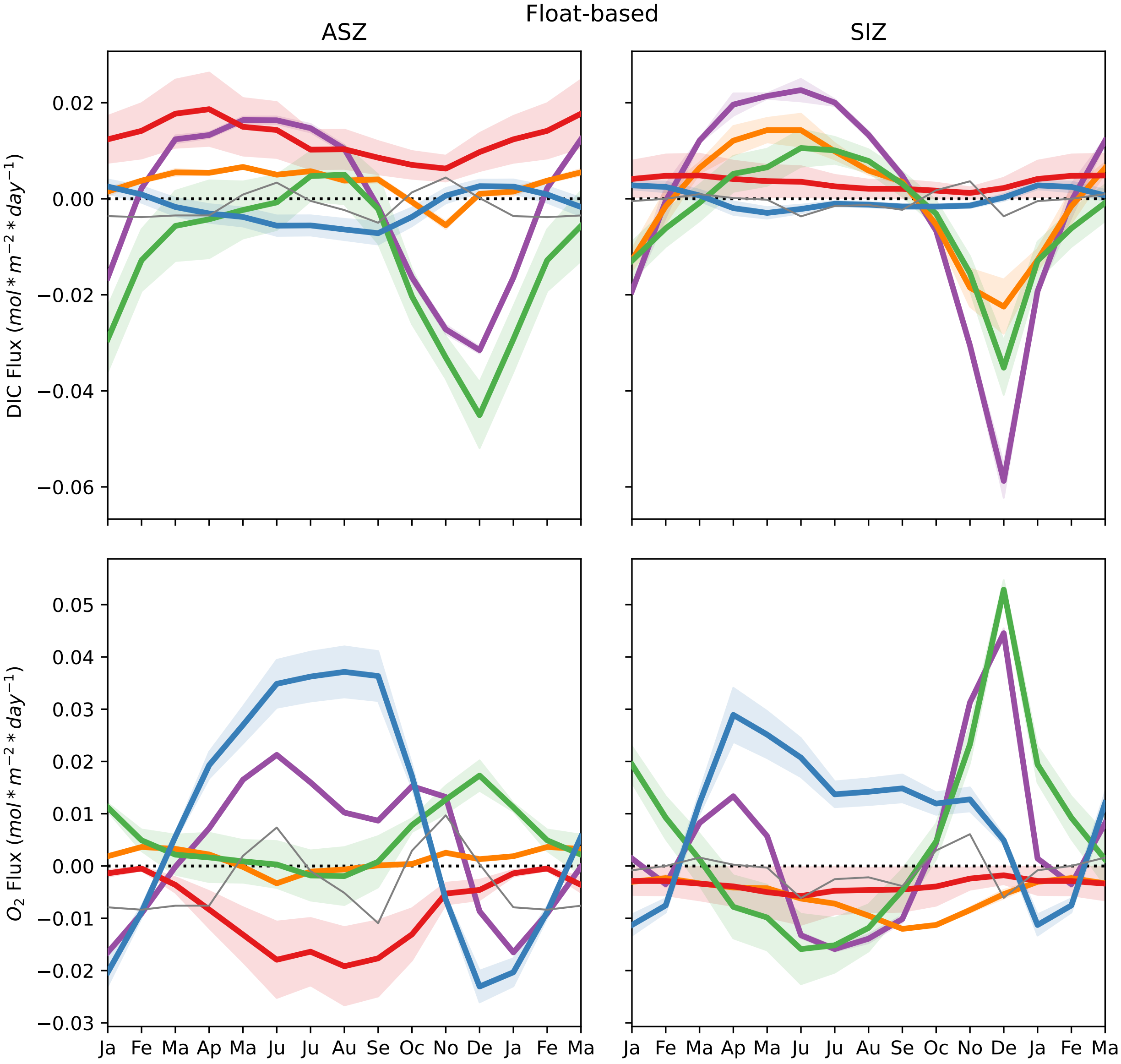

Figure F.13: Budget framework results for the observation-based estimate for the years 2014-2020. The top row is for the dissolved inorganic carbon budget and the bottom row for the dissolved oxygen budget. The left column is for the ASZ and the right column for the SIZ. The error bars are from a Monte Carlo simulation. (ASZ: Antarctic Southern Zone; SIZ: Sea ice Zone, CONC: Tendency - Entrainment; ADV: Advection flux; MIX: Mixing flux; BIO: Biological flux; ASF: Air-sea flux; RES: residual of the budget framework)

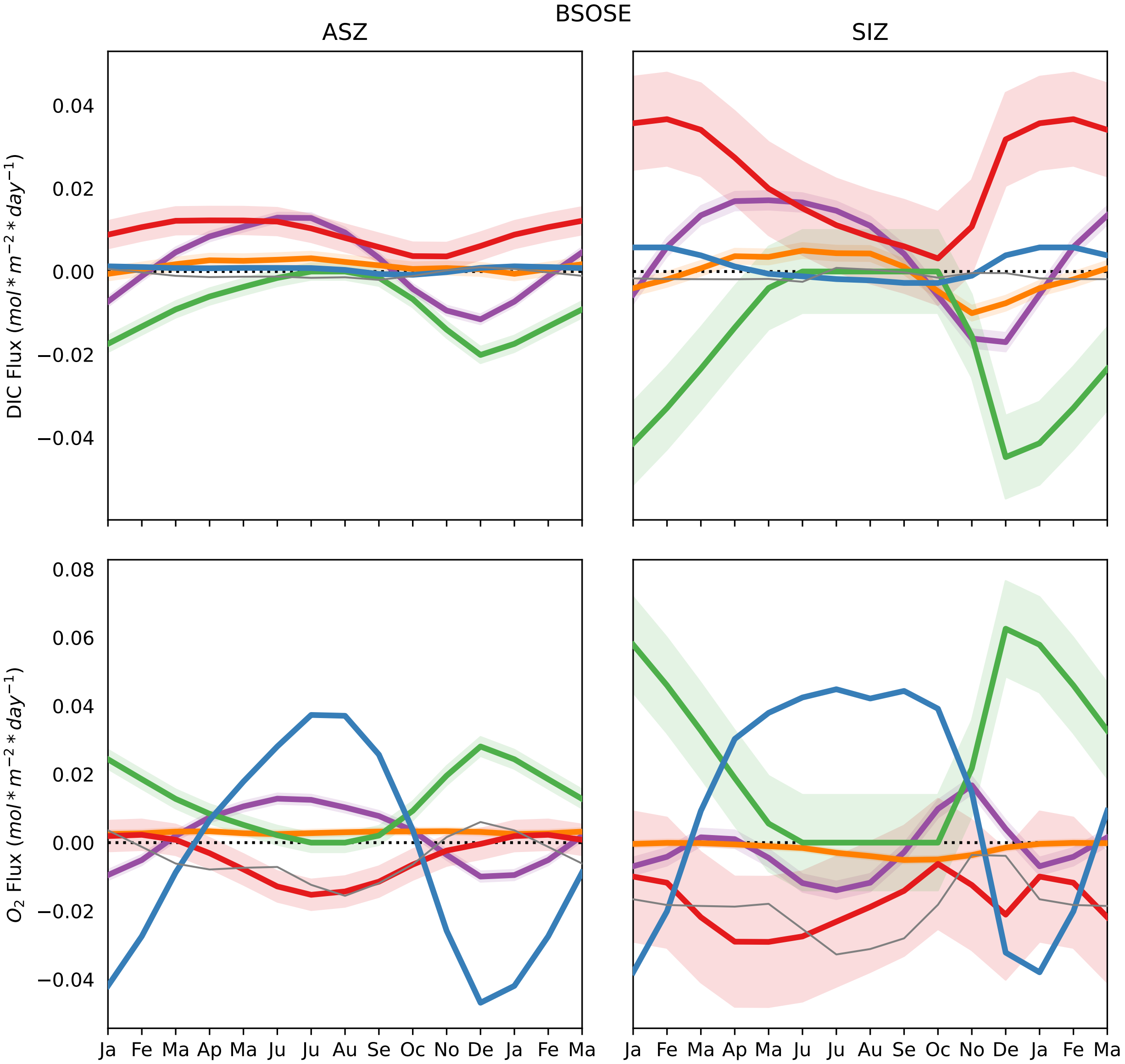

Figure F.14: Budget framework results for B-SOSE for the years 2014-2018. The top row is for the dissolved inorganic carbon budget and the bottom row for the dissolved oxygen budget. The left column is for the ASZ and the right column for the SIZ. The error bars are the difference between the closed budget and the framework budget from the method validation of B-SOSE, taken as a percentage and multiplied by the average magnitude of each flux. (ASZ: Antarctic Southern Zone; SIZ: Sea ice Zone, CONC: Tendency - Entrainment; ADV: Advection flux; MIX: Mixing flux; BIO: Biological flux; ASF: Air-sea flux; RES: residual of the budget framework)

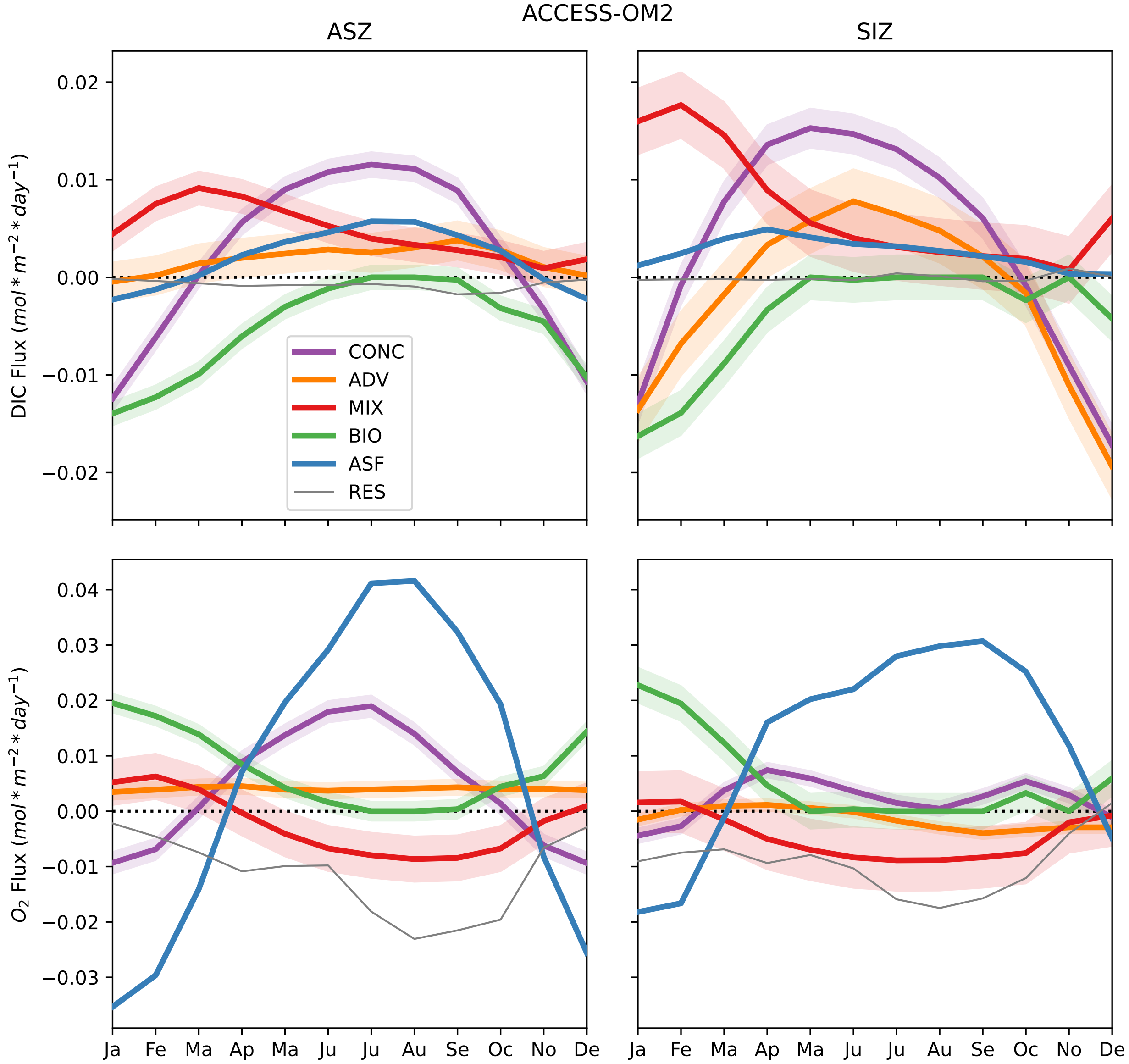

Figure F.15: Budget framework results for OMIP2 ACCESS-OM2. The top row is for the dissolved inorganic carbon budget and the bottom row for the dissolved oxygen budget. The left column is for the ASZ and the right column for the SIZ. The error bars are the difference between the closed budget and the framework budget from the method validation of B-SOSE, taken as a percentage and multiplied by the average magnitude of each flux. (ASZ: Antarctic Southern Zone; SIZ: Sea ice Zone, CONC: Tendency - Entrainment; ADV: Advection flux; MIX: Mixing flux; BIO: Biological flux; ASF: Air-sea flux; RES: residual of the budget framework)

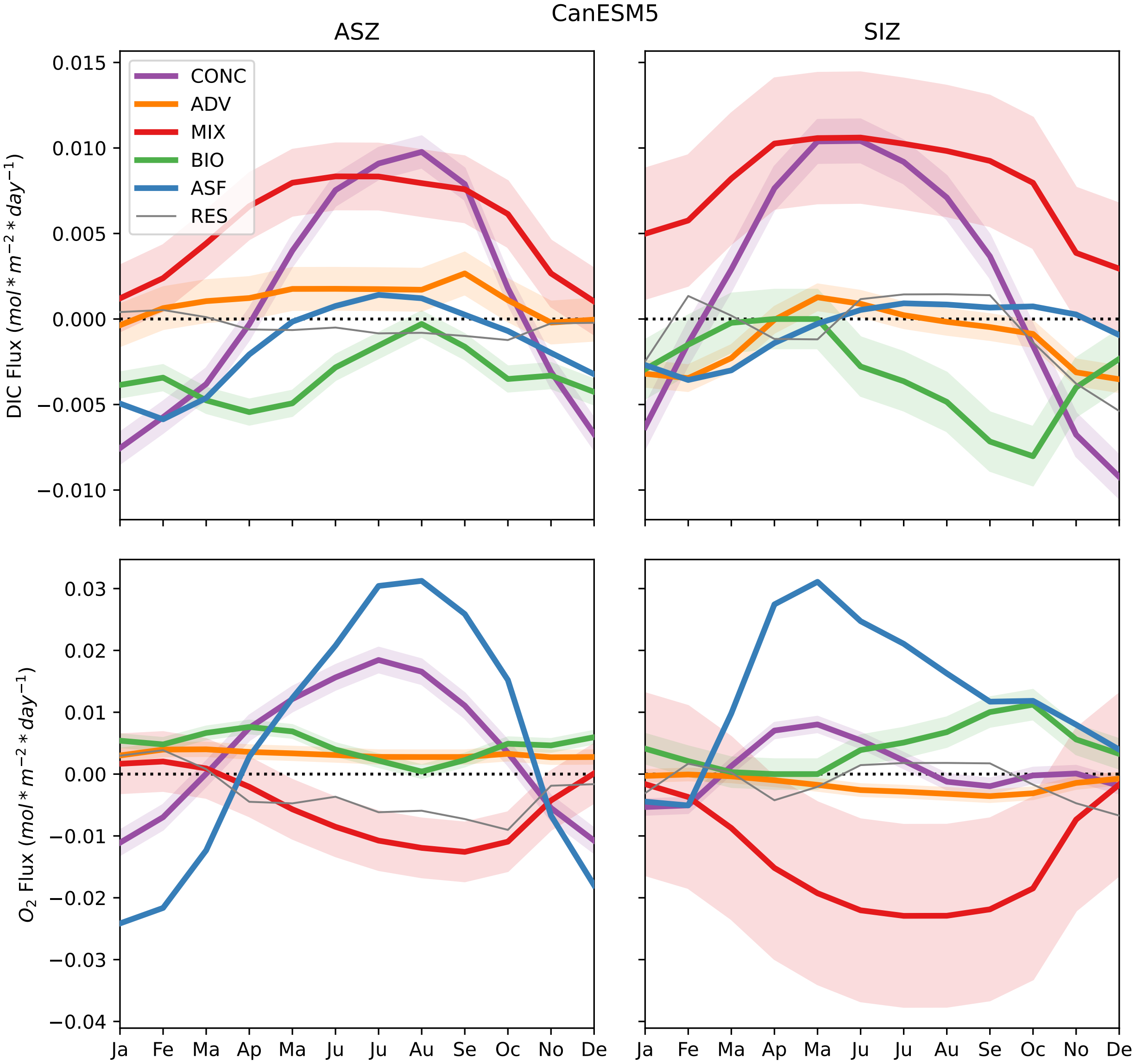

Figure F.16: Budget framework results for OMIP1 CanESM5. The top row is for the dissolved inorganic carbon budget and the bottom row for the dissolved oxygen budget. The left column is for the ASZ and the right column for the SIZ. The error bars are the difference between the closed budget and the framework budget from the method validation of B-SOSE, taken as a percentage and multiplied by the average magnitude of each flux. (ASZ: Antarctic Southern Zone; SIZ: Sea ice Zone, CONC: Tendency - Entrainment; ADV: Advection flux; MIX: Mixing flux; BIO: Biological flux; ASF: Air-sea flux; RES: residual of the budget framework)

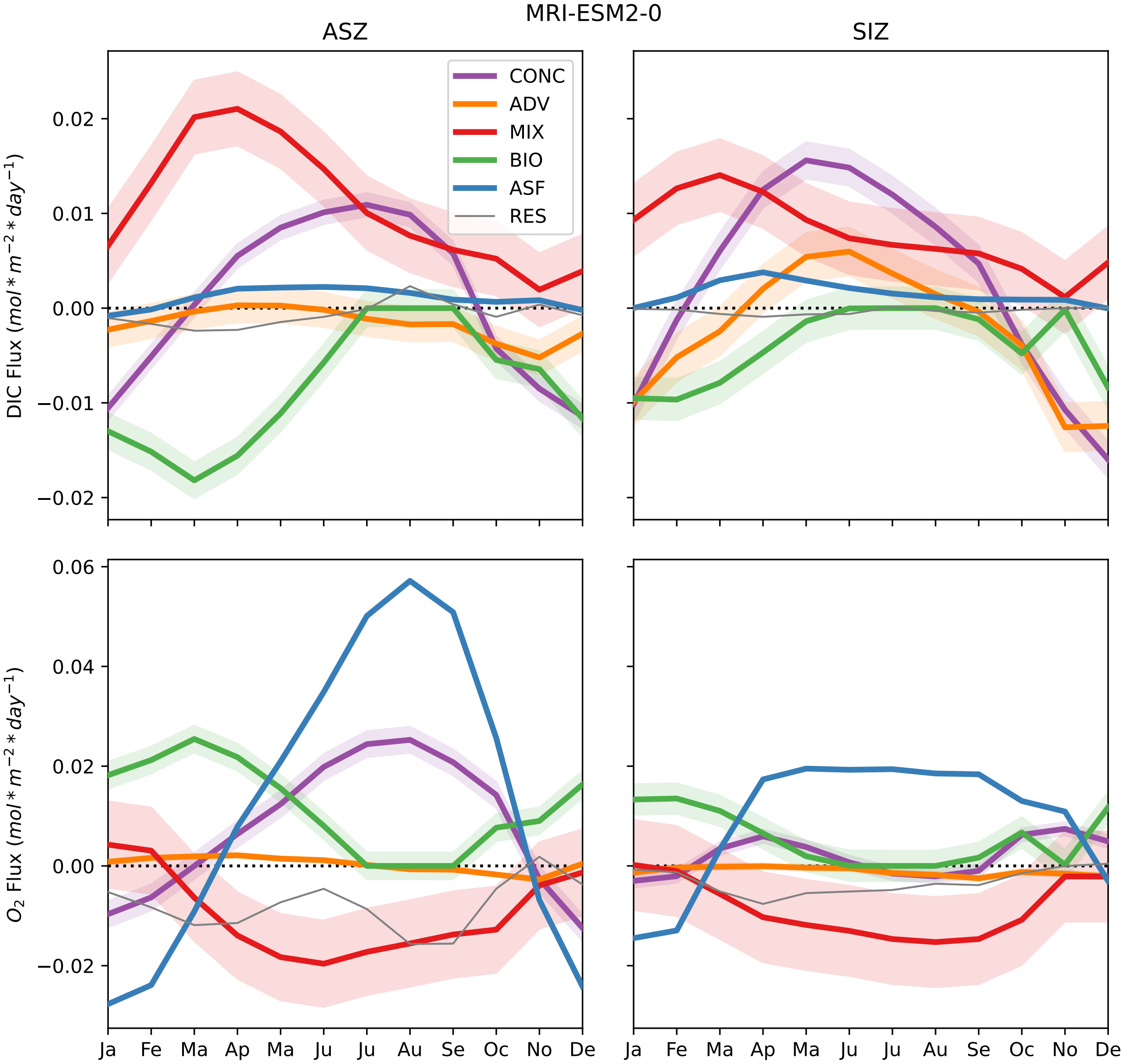

Figure F.17: Budget framework results for OMIP2 MRI-ESM2-0. The top row is for the dissolved inorganic carbon budget and the bottom row for the dissolved oxygen budget. The left column is for the ASZ and the right column for the SIZ. The error bars are the difference between the closed budget and the framework budget from the method validation of B-SOSE, taken as a percentage and multiplied by the average magnitude of each flux. (ASZ: Antarctic Southern Zone; SIZ: Sea ice Zone, CONC: Tendency - Entrainment; ADV: Advection flux; MIX: Mixing flux; BIO: Biological flux; ASF: Air-sea flux; RES: residual of the budget framework)

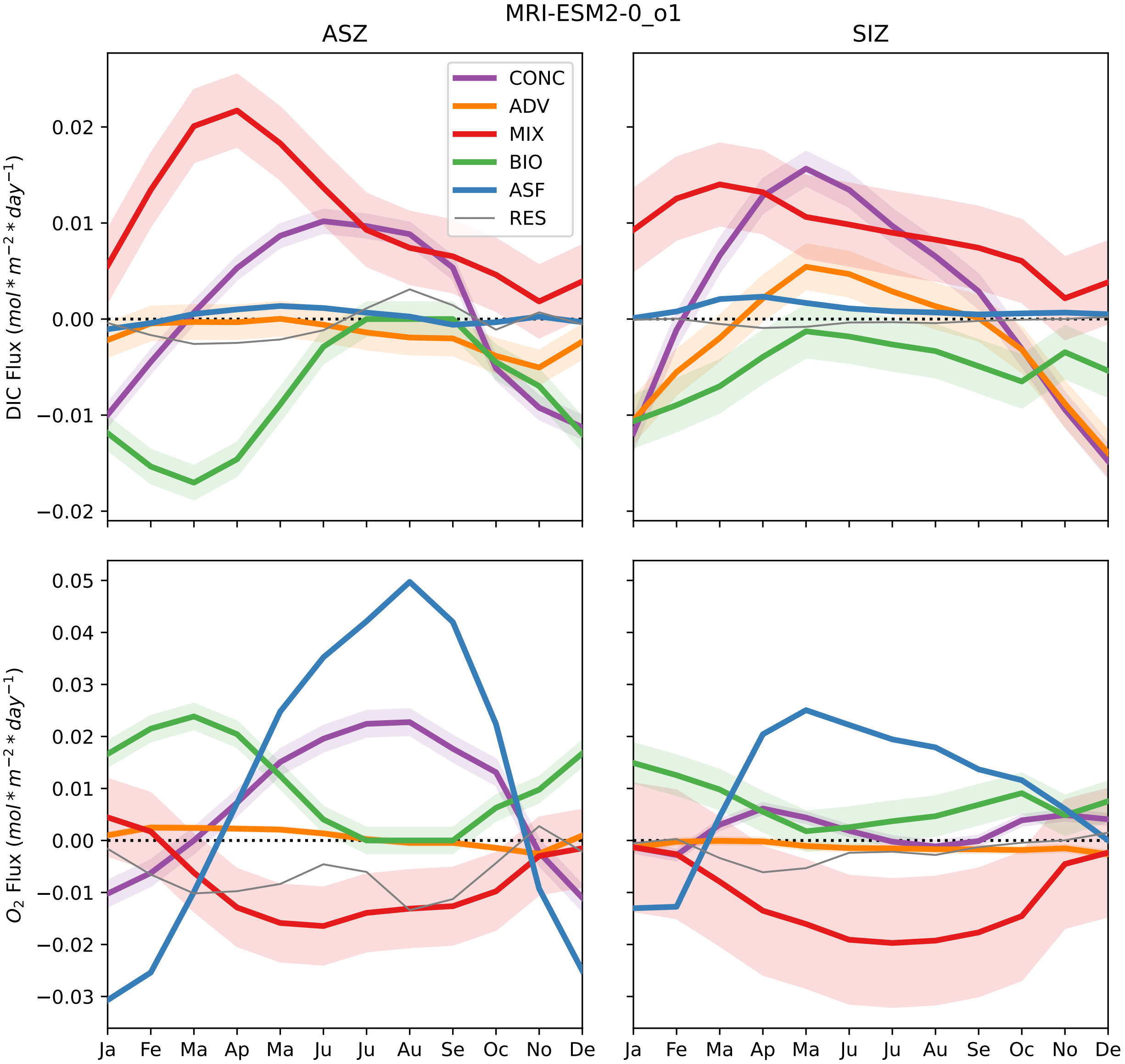

Figure F.18: Budget framework results for OMIP1 MRI-ESM2-0. The top row is for the dissolved inorganic carbon budget and the bottom row for the dissolved oxygen budget. The left column is for the ASZ and the right column for the SIZ. The error bars are the difference between the closed budget and the framework budget from the method validation of B-SOSE, taken as a percentage and multiplied by the average magnitude of each flux. (ASZ: Antarctic Southern Zone; SIZ: Sea ice Zone, CONC: Tendency - Entrainment; ADV: Advection flux; MIX: Mixing flux; BIO: Biological flux; ASF: Air-sea flux; RES: residual of the budget framework)

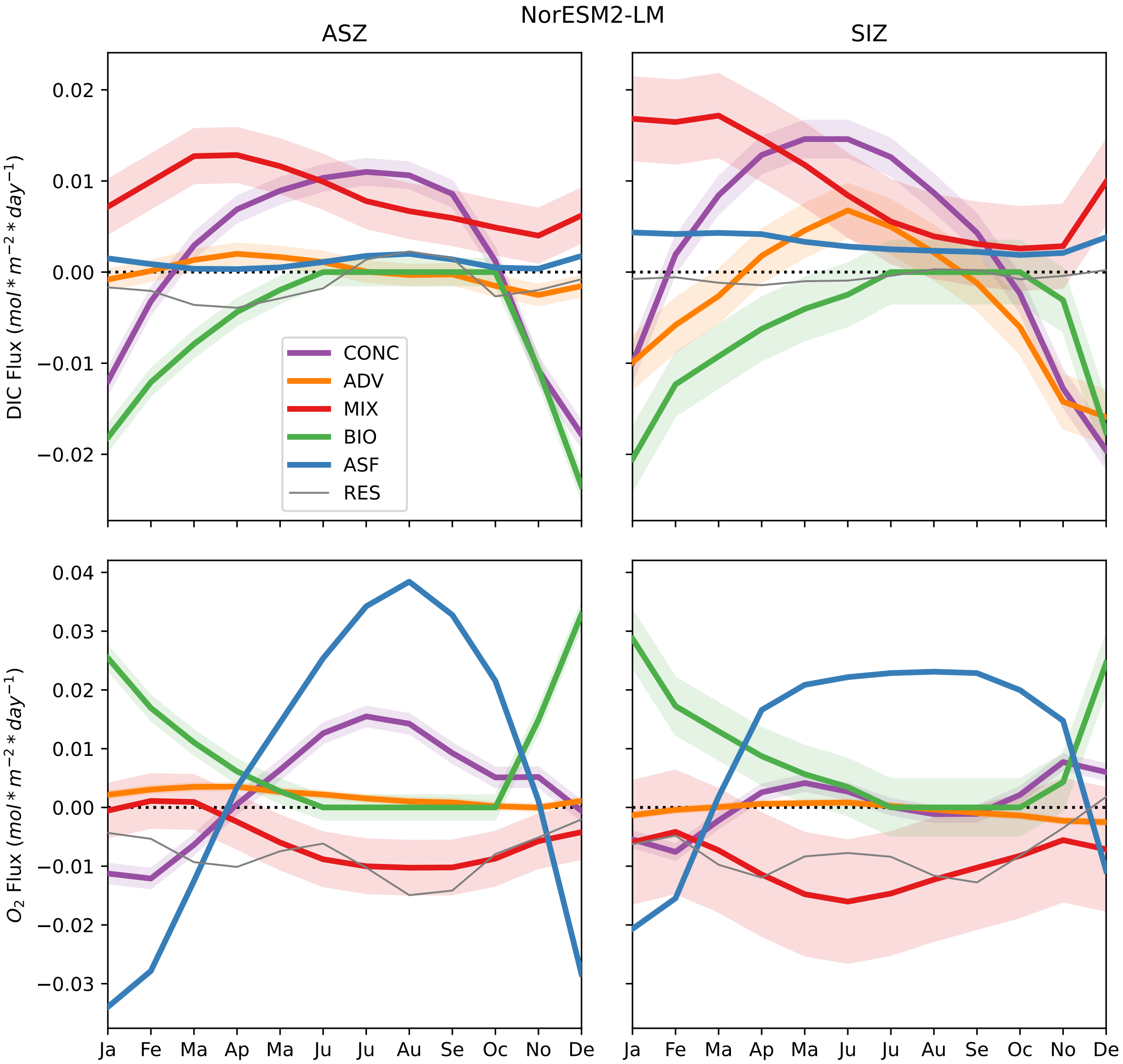

Figure F.19: Budget framework results for OMIP2 NorESM2-LM. The top row is for the dissolved inorganic carbon budget and the bottom row for the dissolved oxygen budget. The left column is for the ASZ and the right column for the SIZ. The error bars are the difference between the closed budget and the framework budget from the method validation of B-SOSE, taken as a percentage and multiplied by the average magnitude of each flux. (ASZ: Antarctic Southern Zone; SIZ: Sea ice Zone, CONC: Tendency - Entrainment; ADV: Advection flux; MIX: Mixing flux; BIO: Biological flux; ASF: Air-sea flux; RES: residual of the budget framework)

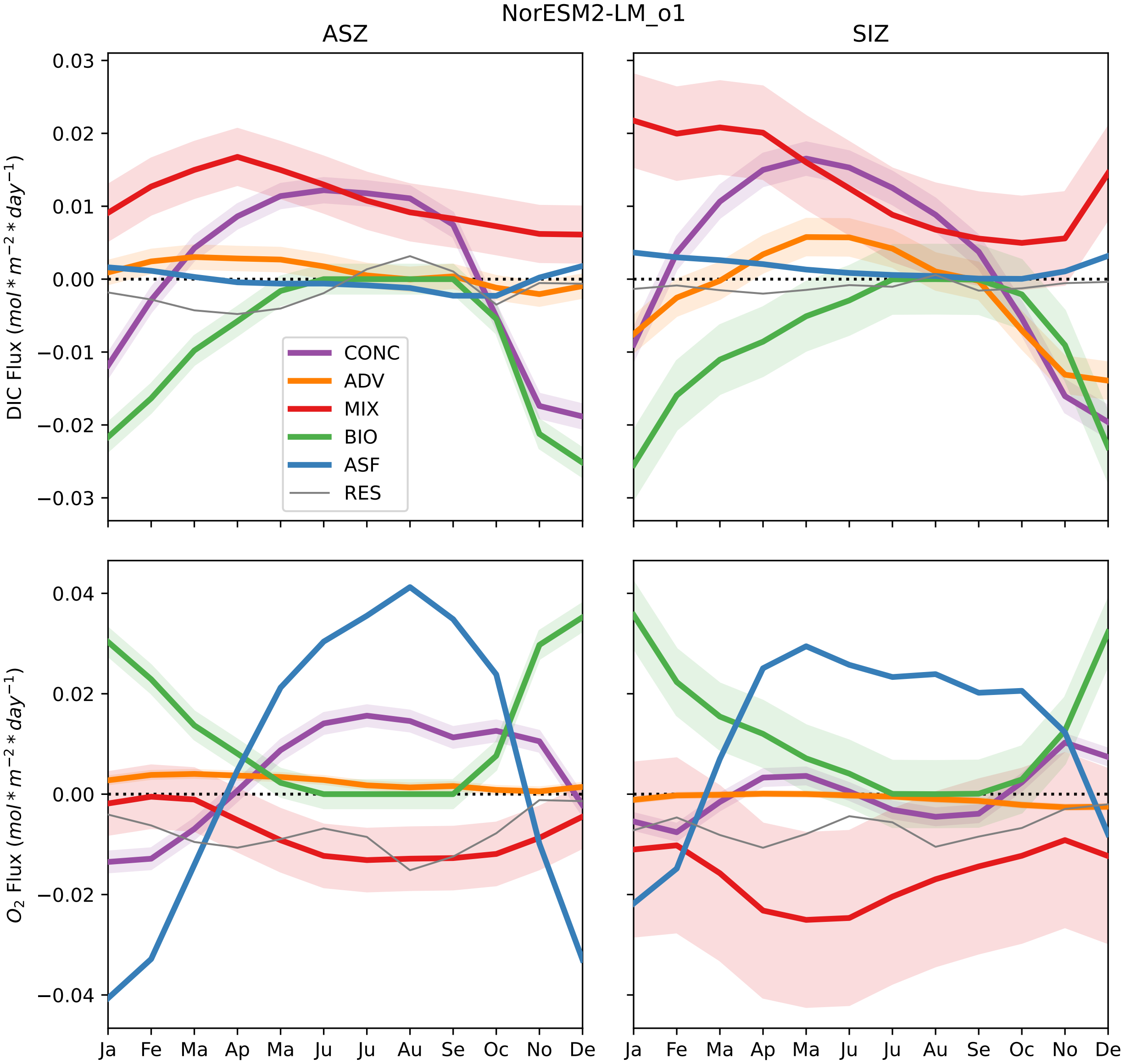

Figure F.20: Budget framework results for OMIP1 NorESM2-LM. The top row is for the dissolved inorganic carbon budget and the bottom row for the dissolved oxygen budget. The left column is for the ASZ and the right column for the SIZ. The error bars are the difference between the closed budget and the framework budget from the method validation of B-SOSE, taken as a percentage and multiplied by the average magnitude of each flux. (ASZ: Antarctic Southern Zone; SIZ: Sea ice Zone, CONC: Tendency - Entrainment; ADV: Advection flux; MIX: Mixing flux; BIO: Biological flux; ASF: Air-sea flux; RES: residual of the budget framework)

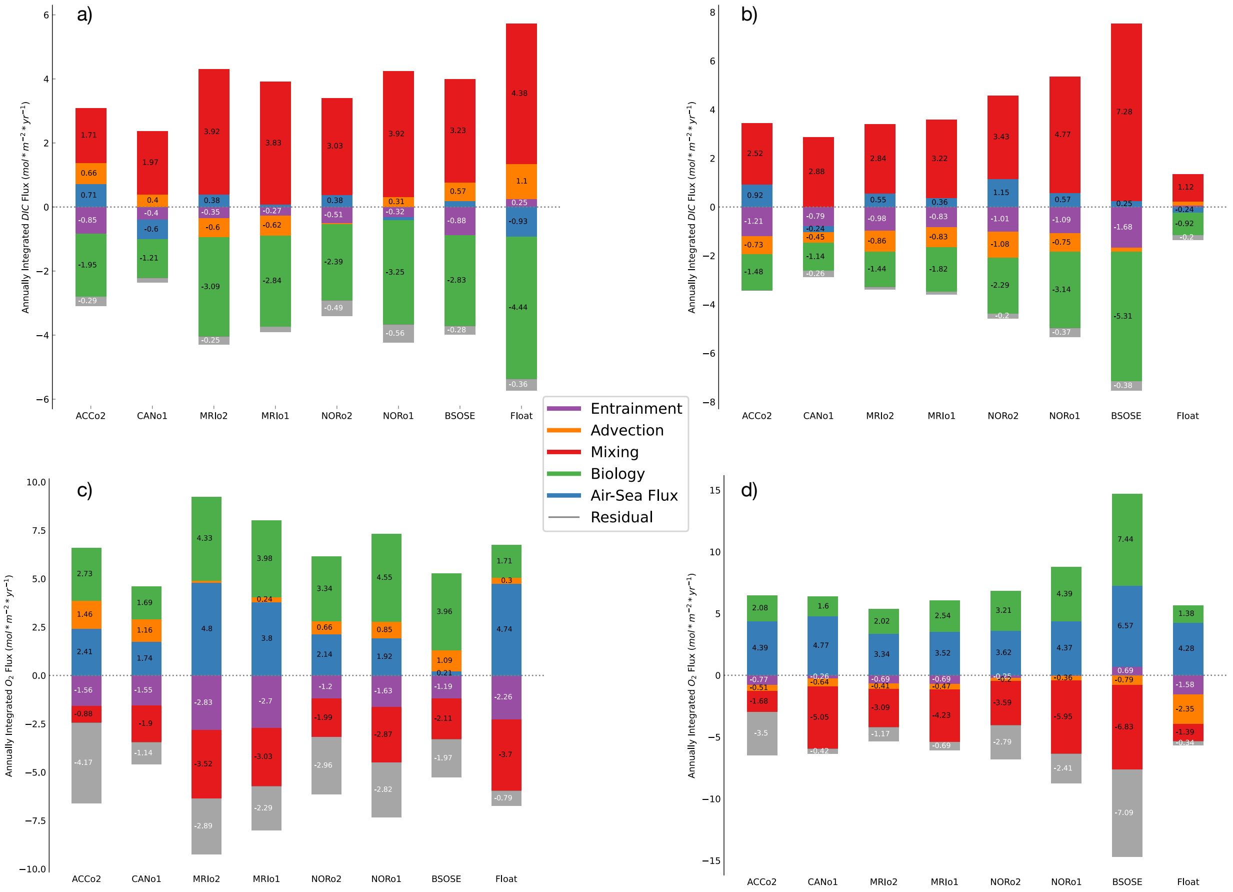

Figure F.21: Annually Integrated Fluxes of DIC (a and b) and O_2 (c and d) for the ASZ (a and c) and SIZ (b and d). (ASZ: Antarctic Southern Zone, SIZ: Sea Ice Zone)

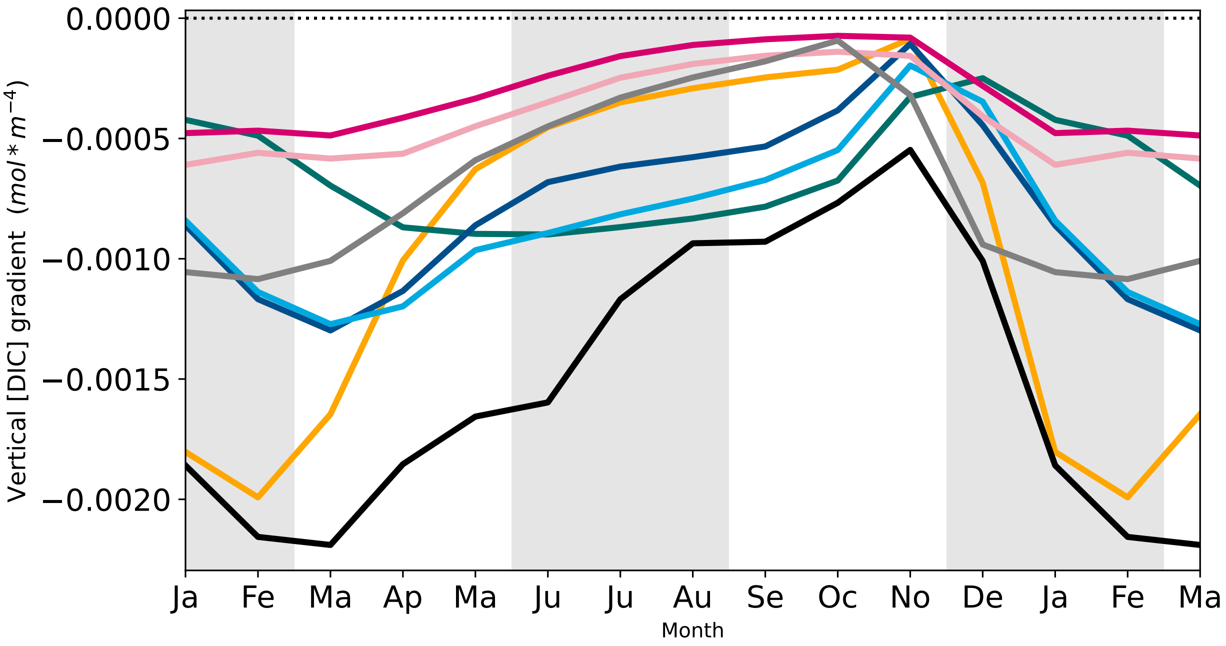

Figure F.22: Vertical gradient in DIC concentration at the base of the mixed layer for the SIZ. (SIZ: Sea Ice Zone)

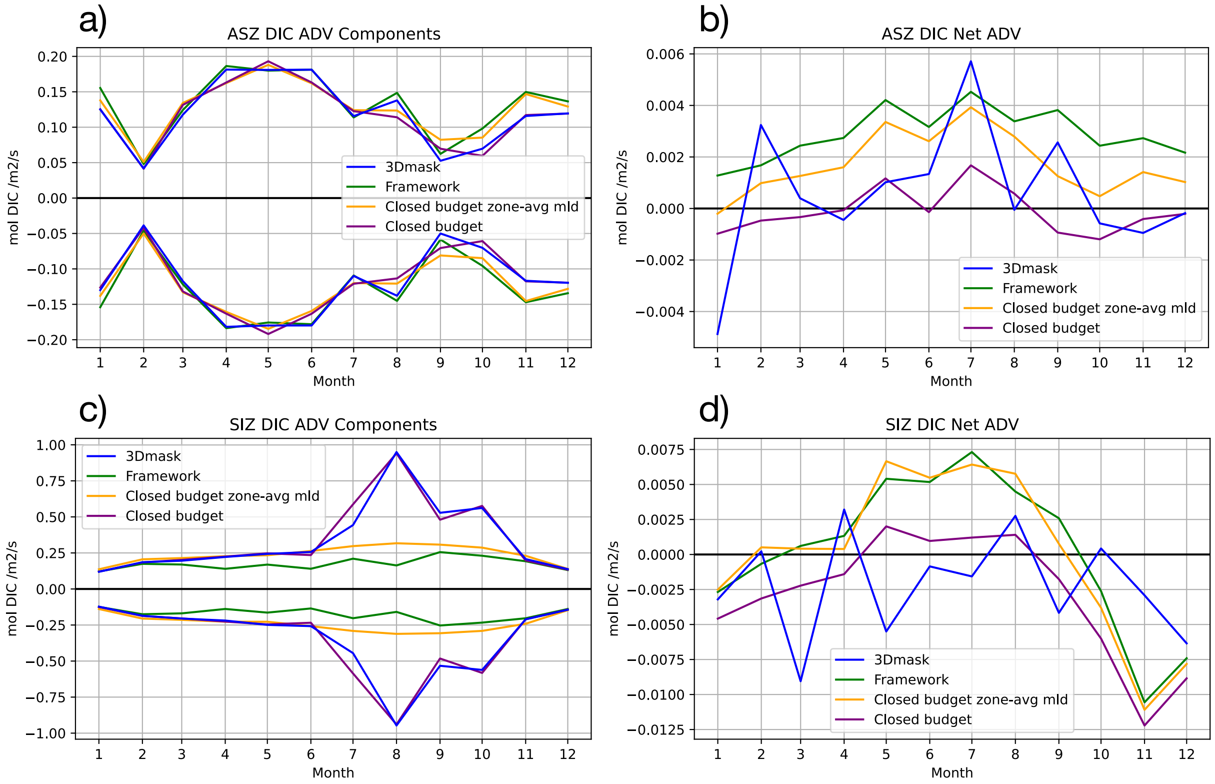

Figure F.23: Horizontal and Vertical advection of DIC computed using different methods for a) the ASZ and c) the SIZ. Net DIC advection (horizontal + vertical) computed using different methods for b) the ASZ and d) the SIZ. “Closed budget”: uses the DIC advection output computed online during model run, summed over all cells part of the mixed layer of the zone. “Closed budget zone-averaged mld”: same as for the “Closed budget” but we set the mixed layer depth of all cells to be equal to the averaged mixed layer depth (no spatial variation in mixed layer depth). “Framework”: total volume transport at the horizontal zone boundaries (PF and SIE) is multiplied by the DIC concentration averaged at the front. “3Dmask”: volume transport at each cellwise boundary between the mixed layer of the zone and the rest of the domain is multiplied by the cellwise concentration of DIC. We then take the sum. (ASZ: Antarctic Southern Zone, SIZ: Sea Ice Zone, SIE: Sea Ice Edge, PF: Polar front)

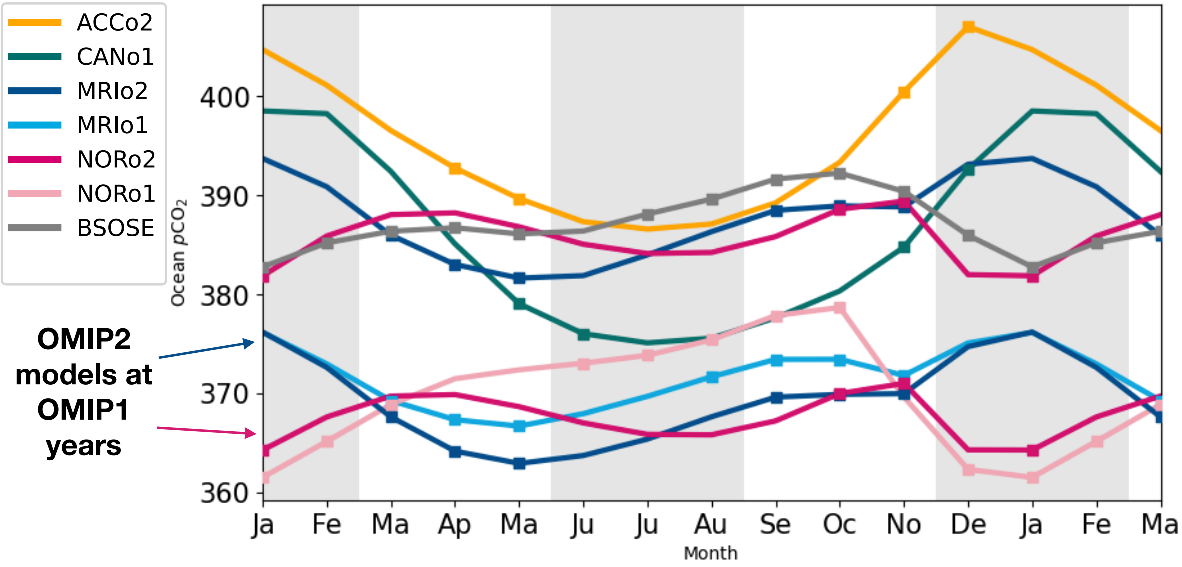

Figure F.24: Seasonal cycle in Ocean $p\text{CO}_2$ for all models and also for OMIP2 MRI and NOR models at the OMIP1 years (2005-2009).

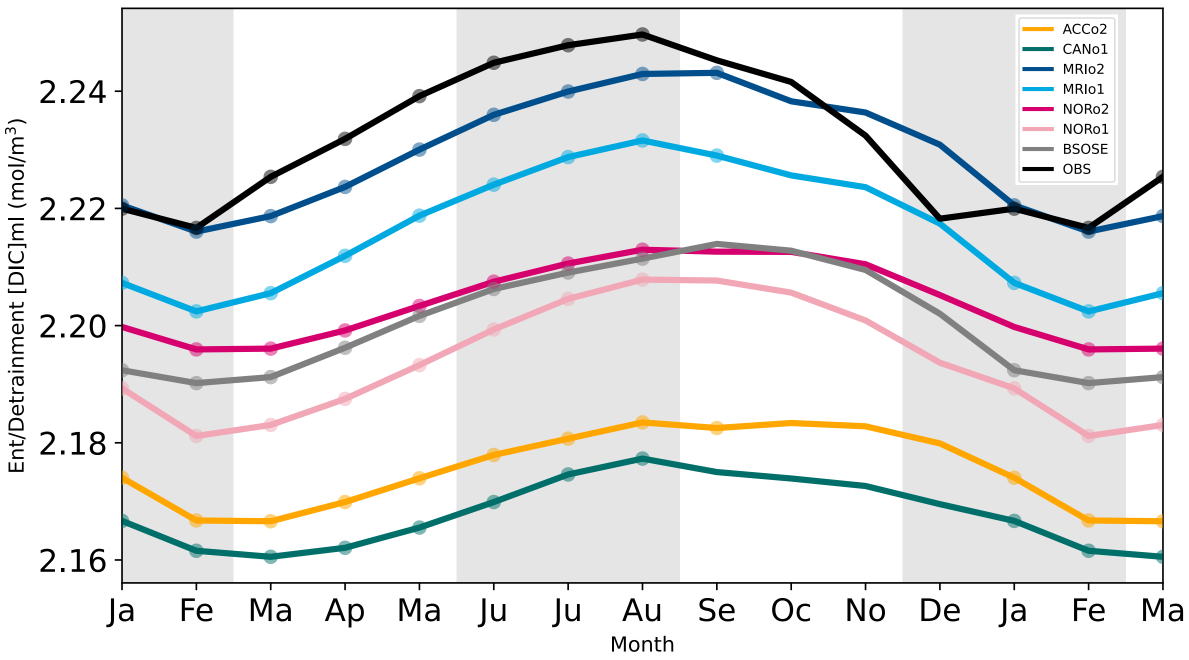

Figure F.25: Concentration of DIC in waters entrained or detrained for all datasets. Dots indicate a month of entrainment ($d\text{MLD}/dt > 0$).

Chapter G

Appendix: Additional Figures for Chapter 4

This Appendix contains additional figures for Chapter 4.

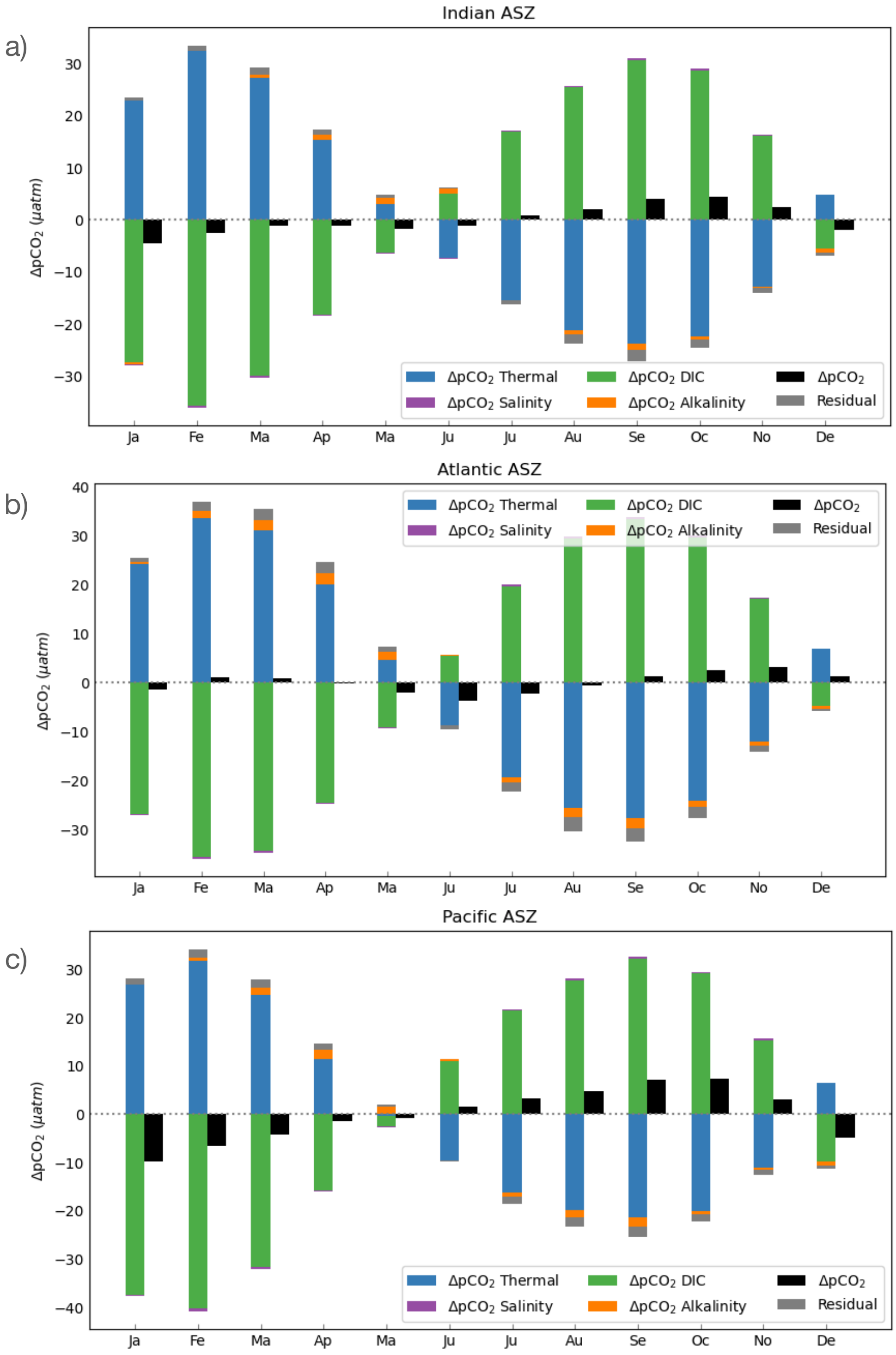

Figure G.1: Drivers of $p\mathrm{CO}_2$ variability in the a) Indian, b) Atlantic and c) Pacific basin of the ASZ over the seasonal cycle. (ASZ: Antarctic Southern Zone)

Annual Mixed Layer Mixing DIC Fluxes ($mol/m^2/yr$)

a) Mixing Flux

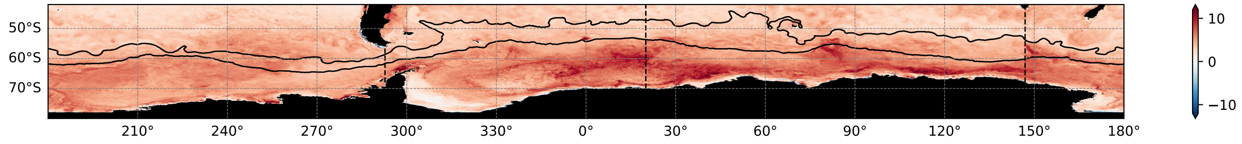

b) Horizontal Mixing Flux

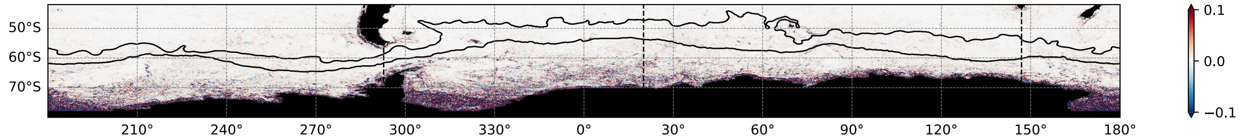

c) Vertical Mixing Flux

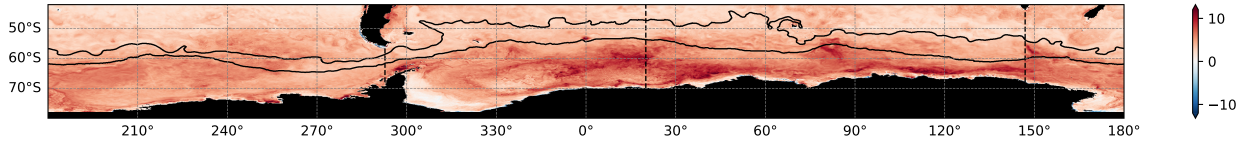

Figure G.2: Annually integrated mixed layer DIC a) net mixing, b) horizontal mixing and c) vertical mixing. The contours plotted represent the Polar front (northern contour) and the sea ice edge (southern contour), and define the ASZ. (ASZ: Antarctic Southern Zone)

Annual Mixed Layer Advective DIC Fluxes ($mol/m^2/yr$)

a) Advective Flux

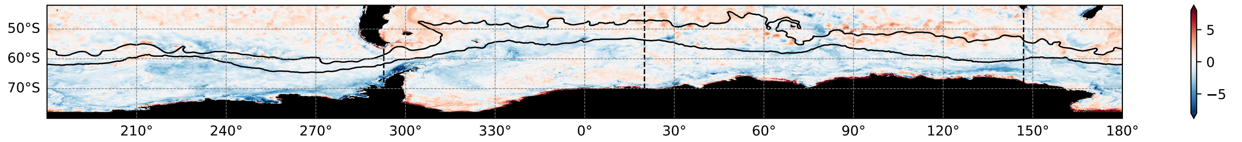

b) Horizontal Advective Flux

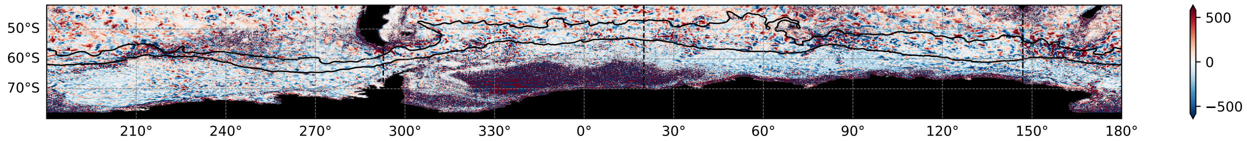

c) Vertical Advective Flux

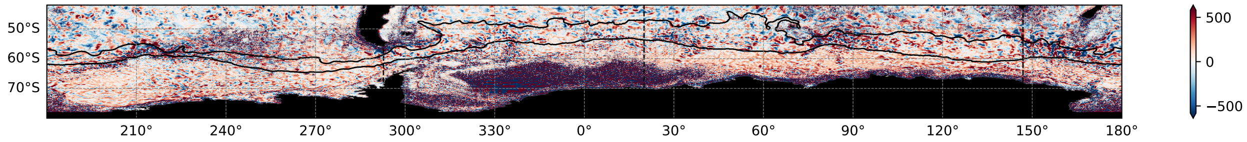

Figure G.3: Annually integrated mixed layer DIC a) net advection, b) horizontal advection and c) vertical advection. The contours plotted represent the Polar front (northern contour) and the sea ice edge (southern contour), and define the ASZ. (ASZ: Antarctic Southern Zone)

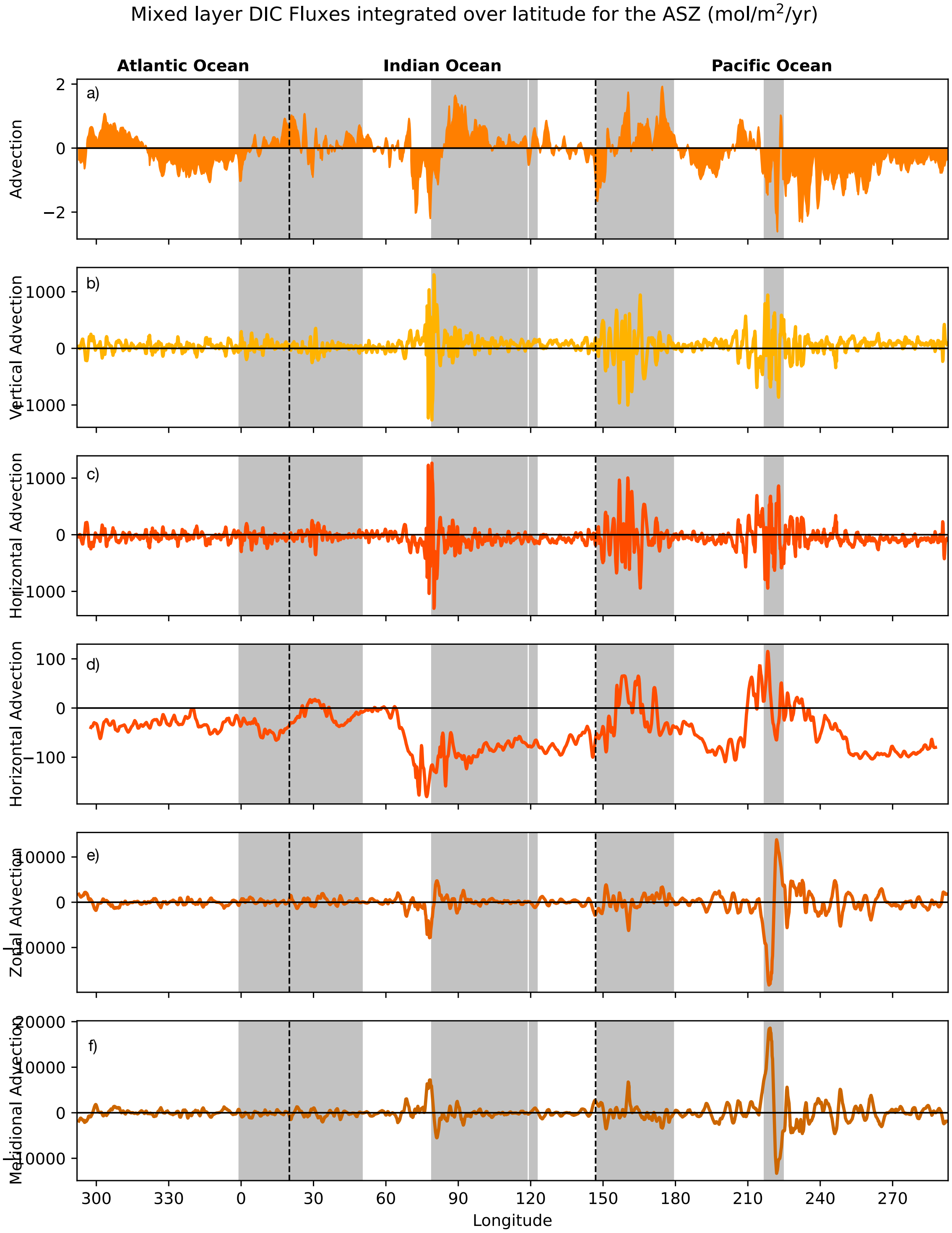

Figure G.4: Annually and latitudinally integrated mixed layer DIC a) net advection, b) vertical advection, c) horizontal advection, d) horizontal advection smoothed with a window witdh of 60 cells, e) zonal advection, f) meridional advection for the ASZ. (ASZ: Antarctic Southern Zone)

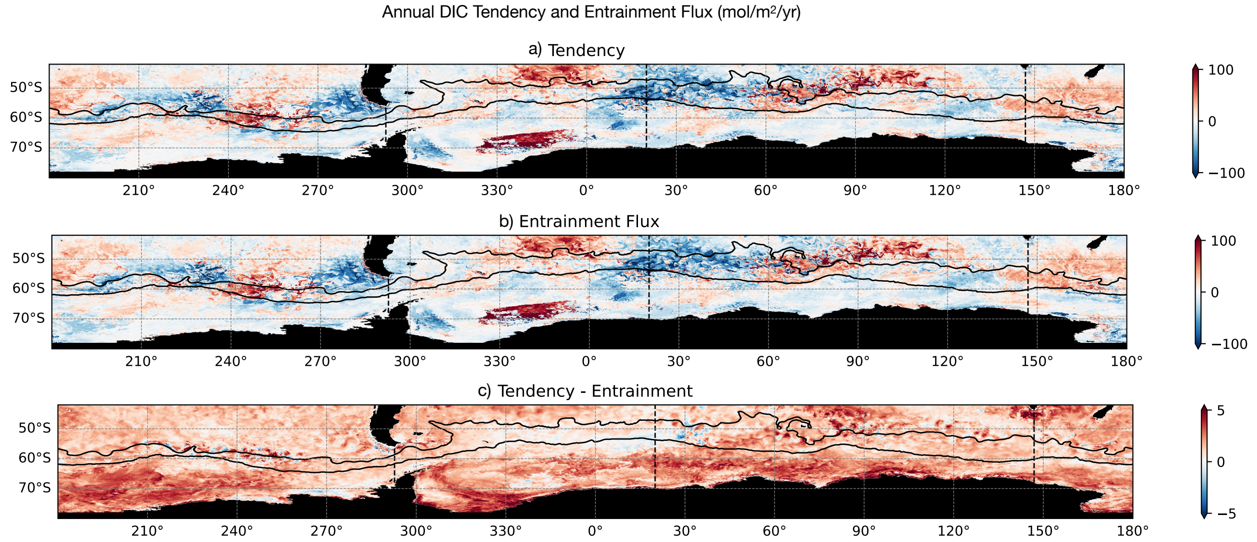

Figure G.5: Annually integrated mixed layer DIC a) tendency, b) entrainment flux and c) tendency minus entrainment flux. The tendency is the time derivative of the amount of DIC in the mixed layer. The tendency minus entrainment flux is equal to the temporal change in mixed layer DIC concentration multiplied by the mixed layer depth. The contours plotted represent the Polar front (northern contour) and the sea ice edge (southern contour), and define the ASZ. (ASZ: Antarctic Southern Zone)

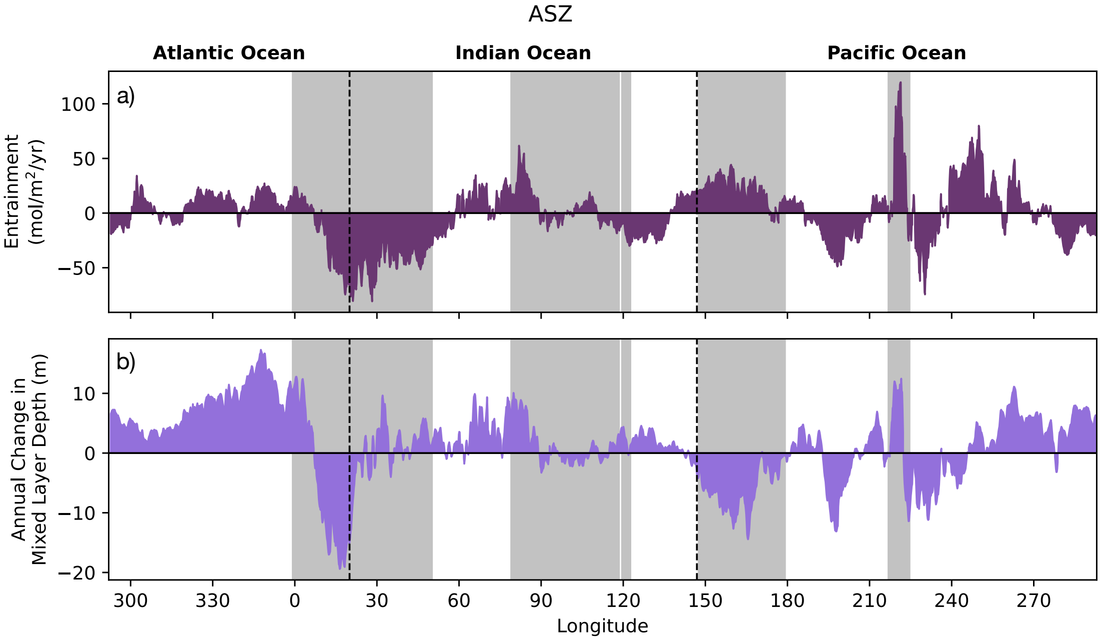

Figure G.6: a) Annually and latitudinally integrated mixed layer DIC entrainment flux for the ASZ. b) Latitudinally averaged annual change in mixed layer depth for the ASZ. (ASZ: Antarctic Southern Zone)

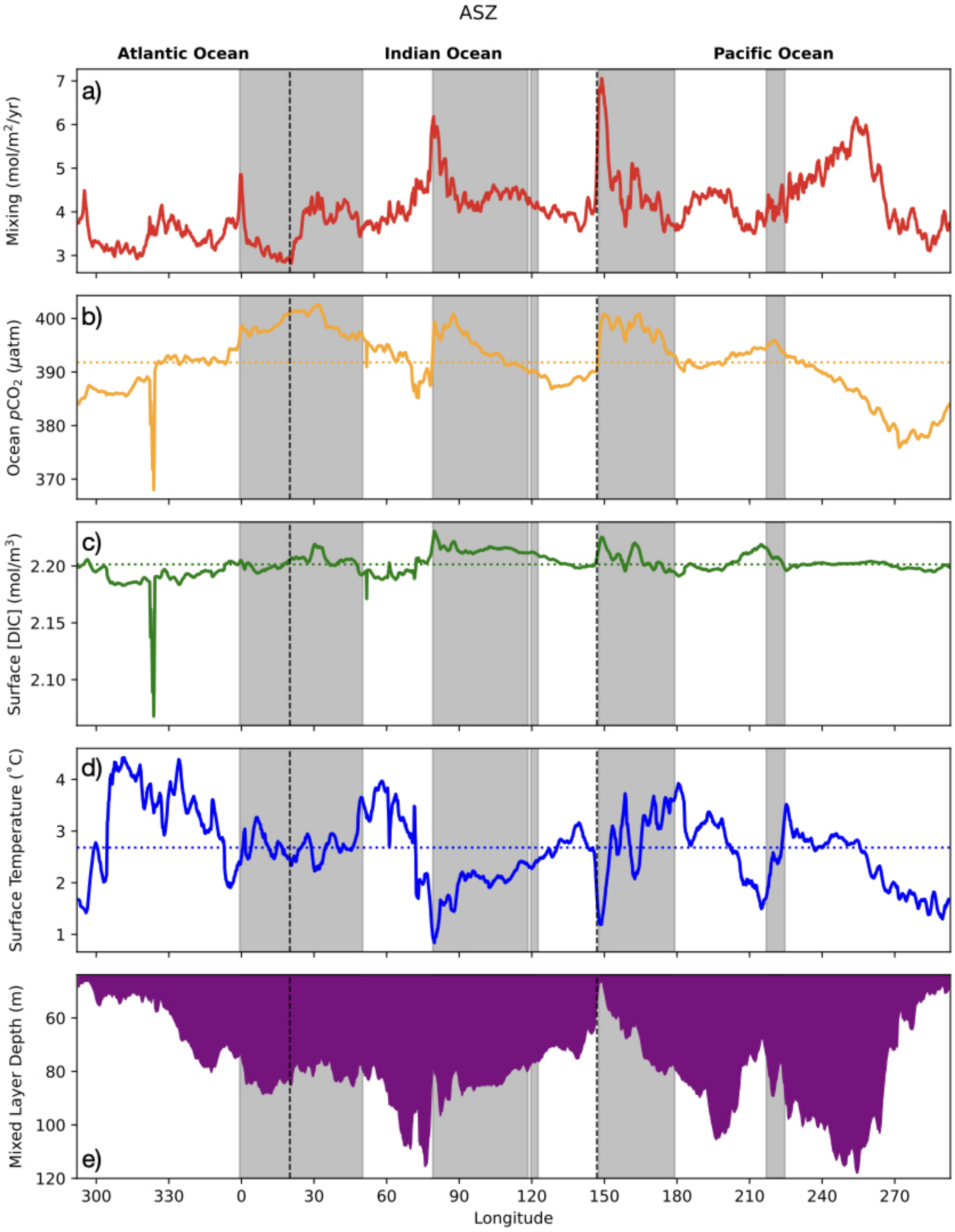

Figure G.7: a) Annually and latitudinally integrated mixed layer DIC mixing flux for the ASZ. b) Annually and latitudinally averaged surface ocean $p\mathrm{CO}_2$, c) surface ocean DIC concentration, d) surface ocean temperature for the ASZ, and e) mixed layer depth. The horizontal colored dotted lines correspond to the zonal average of the respective variable. (ASZ: Antarctic Southern Zone)